Luminescent Isocyanide Complexes of Mn(I) and Mo(0)

Inauguraldissertation

zur
Erlangung der Würde eines Doktors der Philosophie

vorgelegt der
Philosophisch-Naturwissenschaftlichen Fakultät
der Universität Basel

von

Patrick Sebastian Herr

aus Endingen am Kaiserstuhl

Basel, 2021

Genehmigt von der Philosophisch-Naturwissenschaftlichen Fakultät

auf Antrag von

Erstbetreuer: Prof. Dr. Oliver S. Wenger

Zweitbetreuerin: Prof. Dr. Catherine E. Housecroft

Externer Experte: Prof. Dr. Matthias Bauer

Basel, den 02. März 2021

_____

Prof. Dr. Marcel Mayor

Acknowledgement

First and foremost, I want to thank Prof. Dr. Oliver S. Wenger for all the support over the last four years. When I applied for a PhD position in Basel, I only knew about the research I was getting into, but nothing about my future supervisor or the Wenger group. It turned out that I could not have hoped for a more supportive supervisor and a more welcoming atmosphere in the group. I am also thankful for the opportunity to go to several conferences with you and all the memories I gathered there (like a karaoke night in Japan) as well as on several group trips.

I also want to thank Prof. Dr. Catherine Housecroft for co-examining this thesis and Prof. Dr. Matthias Bauer for accepting the role of an external expert.

A big thank you goes to everybody who keeps the department running and who oftentimes could help solve problems on short notice: the Werkstatt team, the analytics team, Daniel Häussinger and many more.

Furthermore, I want to acknowledge all the students that did their internship or Master's project (or both) with me. It was a pleasure to tutor you.

The warm and welcoming atmosphere in the Wenger group made my start in Basel very easy and pleasant. For that, I want to thank all the former and current members of the Wenger group. Apart from introducing me to all the new techniques I needed for my work, there were also all the fun Aperos, summer hikes, sledging trips, SOLA runs, Rheintreiben, countless coffee break card sessions and after work beers with cards against humanity that made the last four years unforgettable. Special thanks go to Chris, Christina, Mirjam, Lucius and Felix for proofreading this thesis.

The people in Lab304 made my everyday life at university enjoyable. I especially enjoyed the "awesome music" -Fridays, but also all the conferences we attended together in Oxford, Sendai, and Hong Kong.

I want to thank Lucius for introducing me to climbing as well as accompanying me on the "quick cross-country run" around Windgällenhütte. A sporty thank you goes to the whole running group, David, Luci, and Chris, for oftentimes pushing me to my limit.

Special thanks go to Chris for providing me guidance in the early stage of the isocyanide project as well as all the discussions on chemistry and the world we had throughout the years. I am really looking forward to having you back in Switzerland.

There are so many memories and things I could thank Mirjam for, that it would fill another whole page. In short: Thank you for being my friend and the kind person that you are.

Am Ende noch ein herzliches Dankeschön an Mama und Papa für all die Unterstützung, insbesondere in den letzten 11 Jahren. Dank euch, und natürlich auch Simon, Hannah und Julia, freue ich mich jedes Mal, wenn ich zurück nach Hause komme. Vielen Dank auch an Oma für die Unterstützung während dem Studium. Wer weiß, ob ich das ohne all die Schätze aus Omas Garten so gut durchgestanden hätte?

Ganz am Ende noch ein großes Dankeschön an Lena. Gibt es etwas Schöneres, als jeden Abend heim zu kommen und zu wissen, dass da jemand auf einen wartet?

Abstract

At the current rate, global warming will render large portions of our planet uninhabitable in the foreseeable future. Therefore, finding a clean and renewable energy source that can replace the current fossil reserve-based industry will be one of the major challenges of the 21st century. A worldwide industry based on solar power seems to be the obvious solution to this problem. The sun provides more than enough energy for our current needs and harnessing that power does not produce any pollutants, in stark contrast to fossil sources.

However, current technology is not advanced enough to fully replace conventional energy sources. In the energy sector, solar cells are used to produce electricity, but they are still expensive and lack the required high efficiencies. In other important industries, the required solar powered technologies are still underdeveloped. Among these are important fields such as CO_2 reduction, water splitting, or chemical reactions powered by light in general. The products of all these reactions are energy enriched substrates, so-called solar fuels, that can be used in the transport sector or at times when no sunlight is available.

Main investigations in these research fields are focusing on precious metal complexes. However, for a global scale application of photocatalyzed reactions, systems based on abundant, inexpensive elements are required.

The research presented in this thesis focuses on photoactive metal complexes based on inexpensive first- and second-row transition metal complexes of manganese and molybdenum. The underlying photophysical properties as well as current progress on photoactive first-row transition metal complexes will be discussed in chapter 2 of this thesis.

In chapter 3, two new isocyanide complexes of Mn(I) are presented. Both of these air-stable complexes exhibit MLCT luminescence in solution at room temperature. This represents not only the first report on MLCT luminescence from Mn(I) compounds, but these are also among the first examples of any first-row transition metal complex exhibiting MLCT luminescence (apart from Cu(I) complexes, whose electronic structure makes MLCT luminescence easier accessible). Both complexes were successfully employed as photosensitizers in energy and electron transfer reactions. Further interesting photophysical properties of these complexes, as well as their synthesis, will be discussed in this chapter.

The two publications presented in chapter 4 provide new insights into the properties and photocatalytic applications of Mo(0) isocyanide complexes. The introduction of bulky groups on the ligands leads to rigidification of the complex and more efficient shielding of the active metal centre from the chemical surrounding. This structural change increases the excited-state lifetime and the photoluminescence quantum yield by one order of magnitude compared to a previously reported analogue. These enhanced properties, in combination with the high exited state oxidation potential, enable the application of this complex in challenging photoreactions.

Chapter 5 provides a brief conclusion on low-valent isocyanide complexes of earth-abundant metals as well as possible future research and improvements in this area.

Finally, photoinduced electron transfer in oligo-1,2-naphthylene linked donor-acceptor compounds was investigated. Unusual distance dependencies of the electron transfer rate were found for different lengths of the helical 1,2-naphthylene linker units which can be explained by “shortcuts” through close noncovalent intramolecular contacts (appendix, chapter 6).

Contents

Abbreviations

BHAS	base-promoted homolytic aromatic substitution reactions
bpy	2,2’-bipyridine
^{t}Bu	*tert*-butyl
btz	3,3’-dimethyl-1,1’-bis(*p*-tolyl)-4,4’-bis(1,2,3-triazol-5-ylidene)
ddpd	*N,N*’-dimethyl-*N,N*’-dipyridine-2-ylpyridine-2,6-diamine
DFT	density-functional theory
dgpy	2,6-diguanidylpyridine
dgpz	2,6-diguanidylpyrazine
DSSC	dye-sensitised solar cell
Fc	ferrocene
HOMO	highest occupied molecular orbital
IC	internal conversion
ILCT	intraligand charge transfer
Iph	2,6-diisopropylphenyl
ISC	intersystem crossing
LC	ligand centred
LED	light-emitting devices
LLCT	ligand-to-ligand charge transfer
LMCT	ligand-to-metal charge transfer
MC	metal centred
Me	methyl
MMFF	Merck molecular force field
MLCT	metal-to-ligand charge transfer
NHC	*N*-heterocyclic carbenes
NIR	near infrared
$PhB(Melm)_3$	tris(3-methylimidazolin-2-ylidene)(phenyl)borate
phtmeimb	{phenyl[tris(3-methylimidazol-1-ylidene)] borate}$^{-}$
ppy	2,2’-phenylpyridine
SCE	saturated calomel electrode
$ThiaSO_2$	*p-tert*-butylsulphonylcalix[4]arene

UV	ultraviolet
Vis	visible
VR	vibrational relaxation

1 Perspective

Rapid technological advancement paired with a growing world population has led to a massive increase in global energy consumption over the last several decades. To date, more than ¾ of that energy still stems from fossil reserves such as oil, coal and gas.[1] Not only are these resources finite, but burning them also releases large amounts of polluting gases, including nitric oxides (NO_x), sulphur dioxide (SO_2) and large quantities of carbon dioxide (CO_2) – a major contributor to global warming responsible for approximately 26 % of the greenhouse effect (excluding water vapour even 65 %).[2]

Not least due to new record heatwaves each summer and a widespread lack of snow in winter,[3] there is a steadily growing awareness of global warming within the population and in politics.[4,5] In order to achieve the goals of the United Nations Paris Agreement – "holding the increase in the global average temperature to well below 2 °C above pre-industrial levels" – there is a strong need to find sustainable energy sources.

By far the highest potential for CO_2-free energy production stems from solar energy. The amount of solar power reaching Earth´s surface every hour is enough to supply humanity´s energy demand for a whole year.[6] Depending on weather conditions and only considering the usable amount of solar energy, this still amounts to 1500 - 49800 exajoule, which is far in excess of the current global energy consumption.[7]

Presently, solar energy is predominantly used to generate electricity through crystalline silicon solar panels. Despite the generally increasing share of energy from renewable sources, especially over the last decade,[8] solar energy conversion still faces some intrinsic problems. The most prominent are the high price of solar panels, the intermittent availability of solar energy, the fact that electricity only makes up a part of the total energy demand (23 % in the EU),[9] as well as the difficulties and cost of storing large amounts of electricity. While electricity can be used to produce hydrogen gas from water, a more efficient solution to the three latter problems would be the direct production of solar fuels. The feedstock for such a sustainable energy source could be derived from the fixation of atmospheric CO_2, essentially resulting in a carbon-neutral fuel. Such solar fuels could also be employed in the transport sector, which still constitutes the largest portion of global energy demand (e.g. 31 % in the EU).[9]

Nature already provides a blueprint on how to use the nearly unlimited energy of the sun to convert CO_2 into useful, high-energy molecules: photosynthesis. While natural photosynthesis from plants annually converts 120 Gt of carbon from CO_2 to biomass, the process is not very efficient, with less than 1 % of solar irradiance converted into stored biomass.[6,10] Outside of tropical latitudes with high irradiances (e.g. bioethanol production from sugar cane in Brazil), this process is not applicable and even there it competes with food production. In contrast, artificial photosystems have the potential to surpass their natural counterparts by more than one order of magnitude e.g. in a CO_2-to-CO reduction system that achieves an efficiency of

12.7 %.[11,12] Other photoinitiated reactions even have the potential to considerably exceed 100 % efficiency if radical chain processes are involved.[13]

The basic thermodynamic principle behind photosynthesis is the light-induced spatial separation of charges, creating a chemical potential. The kinetic challenge is to prevent charge recombination long enough for a chemical reaction to occur.[14] Analogous basic requirements – e.g. high yield of excited-state formation, sufficiently long lifetimes, reversible photophysics and tunability of excited-state properties – also hold true for artificial photocatalysts,[15] which can be used to propel chemical reactions with light instead of thermal energy. However, only a few groups of compounds fulfil these very stringent criteria as most chemical compounds rapidly convert their excited-state energy into heat. One class of such compounds that has received significant attention from researchers are metal complexes with a $4d^6$ or $5d^6$ valence electron configuration. Upon photoexcitation, complexes of e.g. Ru(II), Ir(III), Os(II) or Re(I) undergo a metal-to-ligand charge transfer (MLCT) transition, giving rise to a long-lived and luminescent excited state.[16,17]

Complexes of these metal ions have been utilised by researchers in a wide variety of fields such as dye-sensitised solar cells (DSSCs),[18] light-emitting devices (LEDs),[19] photoredox catalysis,[20] artificial photosynthesis[21] or phototherapy[22].

Despite their favourable properties and diverse area of possible applications, these metals are among the rarest in the Earth's crust, preventing their wide-spread utilisation. In order to accomplish global scale use, systems based on earth-abundant, inexpensive metals like most of the first-row and some of the second-row transition metals are necessary.[16] Possible abundant metal ions with the d^6 electronic configuration include Cr(0), Mo(0), Mn(I), Fe(II) and Co(III).

There has been considerable progress over the last years to synthesize luminescent complexes of iron – the most abundant of the transition metals.[17] Through different approaches and the use of sophisticated ligand designs, the excited-state lifetime could be increased by more than two orders of magnitude, from only 9 ps in 2013 to over 2 ns in 2019.[17,23,24] Despite these efforts, there are still no reports of MLCT luminescence of iron complexes under continuous-wave excitation, as typically observed with its heavier analogue, ruthenium. This is mainly due to low lying metal centred (MC) ligand field excited states, which promote rapid non-radiative deactivation of the excited MLCT state.[25,26]

Apart from iron, there are multiple examples of other luminescent first-row transition metal complexes e.g. of Cr(0), Cr(III), Co(III), Ni(II) or Cu(I).[27] Of these metal ions, only Co(III) and Cr(0) possess the desired $3d^6$ electron configuration and so far only complexes of Cr(0) have been reported to show MLCT emission.[28,29] In these complexes, bidentate isocyanide ligands were used to support the low-valent ions of Cr(0) and its heavier analogue Mo(0). The strong π-acceptor properties of isocyanide stabilise the metal in its zero-valent state via π-backbonding. This gives rise to MLCT luminescence with lifetimes long enough to enable photocatalytic applications.[29,30]

Following a detailed introduction to the photophysics of transition metal complexes and current research in this area (chapter 2), the first research part of this thesis will discuss new luminescent complexes of Mn(I) with multidentate isocyanide ligands (chapter 3). Manganese is the third most abundant transition metal (after iron and titanium) and Mn(I) has the desired $3d^6$ valence electron configuration. Surprisingly, Mn(I) has been hitherto overlooked in the search for a cheap substitute for Ru(II) and Ir(III). Adapting a similar strategy as previously used for luminescent Cr(0) complexes, the ligand design has been optimised by introducing thiophene linkers in the ligand backbone. The resulting bi- and tridentate isocyanide complexes (Figure 1) are the first Mn(I) complexes to exhibit room temperature luminescence in solution.

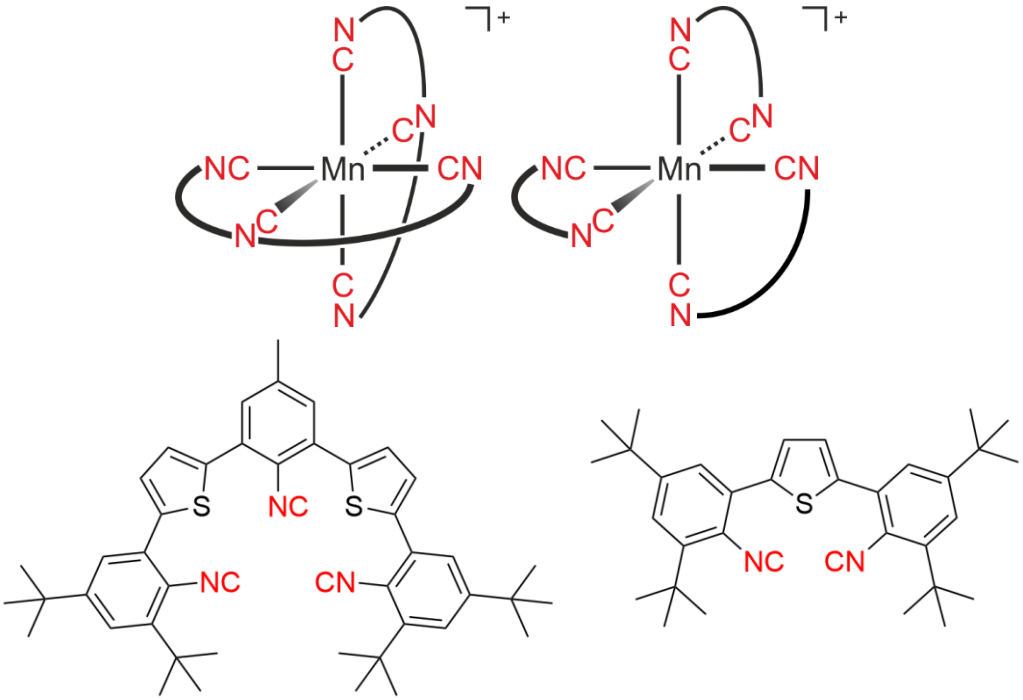

Figure 1: Structure of the two Mn(I) isocyanide complexes discussed in chapter 3 of this thesis (top) and their respective bi- and tridentate ligands (bottom).

In the second research part, an in-depth analysis of bidentate isocyanide complexes of Mo(0) and their application in challenging, base-promoted homolytic aromatic substitution reactions (BHAS) will be presented (chapter 4). One major insight gained from this work is that the introduction of sterically demanding groups on the terphenyl ligand (Figure 2) can shield the metal centre from the chemical surrounding, increasing luminescence lifetime and luminescence quantum yield by a full order of magnitude.

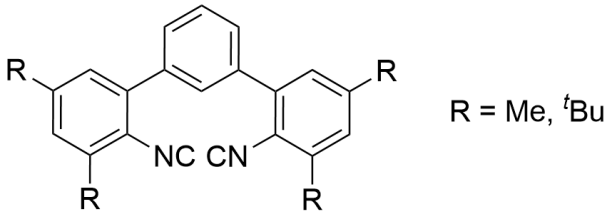

Figure 2: Structure of the isocyanide ligands used for the complexes discussed in chapter 4 of this thesis. Exchanging the Me substituents for bulkier ^{t}Bu groups drastically improves the photophysical properties of the resulting Mo(0) complex.

2 Introduction

2.1 Photophysics of Transition Metal Complexes

Transition metal complexes require specifically tailored photophysical and photochemical properties for their application in fields such as solar energy conversion or photoredox catalysis.[31] A thorough understanding of the underlying photophysical processes is necessary to predict and modify these properties towards the desired photochemical characteristics.[15,16,26]

To understand the influence of ligand modifications or different metal centres in a complex system, a close look at the relevant frontier molecular orbitals is required. The five energetically degenerate d-orbitals of a transition metal centre predominantly affect the interactions between metal and ligands as well as the photoredox properties of a complex. Due to their different spatial orientation, the d-orbitals do not interact with ligand orbitals to an equal extent. This results in splitting of the orbital energies in a ligand field. In an octahedral coordination geometry, this leads to splitting into three energetically lower lying t_{2g} orbitals, and two e_g orbitals, which are higher in energy (Figure 3).

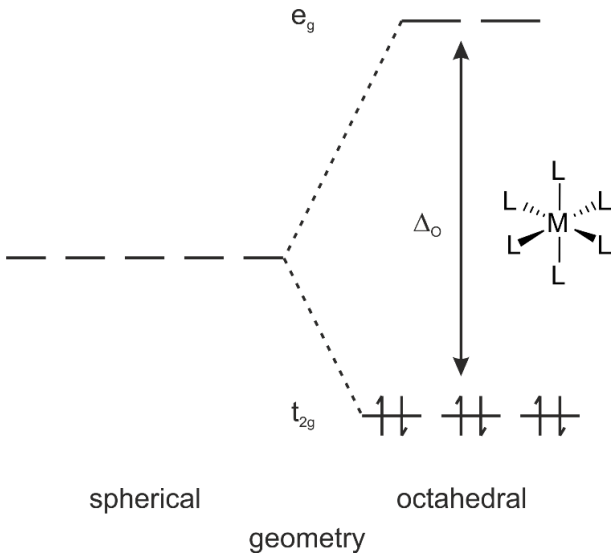

Figure 3: Simplified crystal field splitting of the d-orbitals in an octahedral coordination geometry for the low-spin d^6 electron configuration. Δ_O is the energy difference between the t_{2g} and e_g orbitals in an octahedral crystal field.

If the metal centre is a late transition metal or the ligands induce a strong field, the low-spin electron configuration with a maximum number of paired electrons as depicted in Figure 3 is favoured. All complexes discussed in this thesis have a d^6 metal centre and fulfil at least one of the above-mentioned conditions. Therefore, they adopt the low-spin electron configuration with paired electrons.

2.1.1 The Excited State

The most common interaction between a molecule and light is the absorption of one photon by one molecule.[32] In order to be absorbed and to trigger electronic transitions in a molecule, photons require a certain energy that usually ranges from the UV to the visible part of the electromagnetic spectrum (200 – 800 nm). Upon absorption of the photon, an electron is promoted from the molecule's ground state into an electronically excited state. The probability of light absorption at a given wavelength determines the intensity ε of an absorption band. There are two selection rules that predict the likelihood of an electronic transition: (1) LAPORTE or symmetry selection rule; (2) spin selection rule. The symmetry selection rule states that in centrosymmetric molecules, such as octahedral complexes, only transitions that change parity are allowed. Consequently, all transitions within the same set of orbitals (e.g. d → d) are forbidden. The spin selection rule only allows transitions that have no change in spin-multiplicity such as singlet → singlet or triplet → triplet. In reality, spin-forbidden transitions can also be observed due to vibronic coupling or the heavy atom effect, albeit generally with low ε values.[32]

The most relevant electronic states and transitions after photoexcitation can be depicted in a JABLONSKI diagram (Figure 4). It shows the states arranged vertically by energy level and horizontally by spin multiplicity. The vibrational ground state of each electronic state is represented by a bold horizontal line and the vibrationally excited states are depicted by thin horizontal lines. Radiative transitions are depicted as solid vertical arrows and non-radiative transitions as dotted arrows.

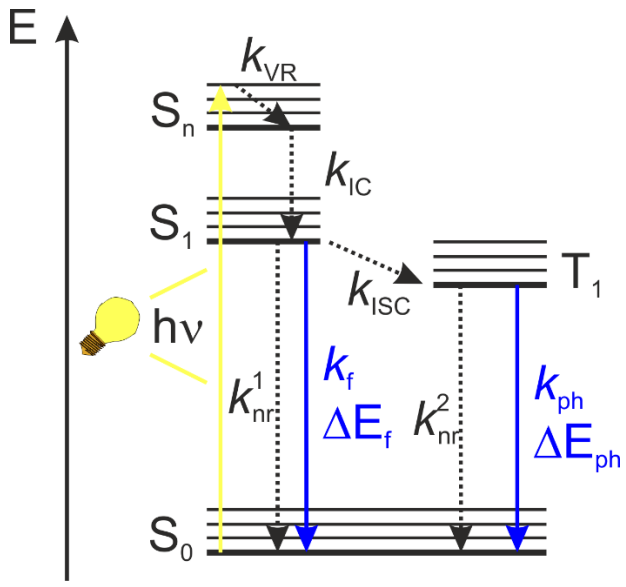

Figure 4: JABLONSKI diagram illustrating the relevant singlet (S) and triplet (T) states (black horizontal lines) and transitions upon light excitation (solid yellow vertical line). Dotted black lines depict non-radiative and solid blue lines radiative transitions. See main text for abbreviations.

A photon of sufficiently high energy can excite an electron from the ground state S_0 to a higher excited state S_n of the same spin multiplicity. This represents the most common

type of transition and results in strong absorption bands, as it is both spin and symmetry allowed.

From the S_n state, the electron rapidly loses energy via vibrational relaxation (VR) to the lowest vibrational state of S_n and via internal conversion (IC) to the S_{n-1} state until it reaches the vibrationally relaxed S_1 state. From there, multiple decay processes are possible. The electron can either relax to the ground state S_0 via a non-radiative pathway with the rate constant k_{nr}^1 or via emission of a photon with the energy ΔE_f and rate constant k_f. Spin-allowed emission, typically from singlet states, is called fluorescence.[32,33]

Intersystem crossing (ISC) is the third possible relaxation pathway from the S_1 state and represents a spin-forbidden transition. Especially in complexes of late transition metals with a pronounced heavy atom effect, ISC with the rate constant k_{ISC} can be the main transition, leading to efficient population of T_1 as the lowest excited state. Emission from triplet states is called phosphorescence and occurs with the energy ΔE_{ph} and rate constant k_{ph}. Phosphorescence usually has a significantly smaller decay rate constant compared to fluorescence ($k_{ph} < k_f$, resulting in longer excited-state lifetimes), as the transition back to S_0 changes the spin multiplicity and is therefore again a spin-forbidden process.[32,33]

KASHA´s rule states that radiative transitions only occur from the lowest energy excited state of a given spin multiplicity. This can be explained with the relative position of excited-state energy levels. The energetic difference between the ground state and the first excited state is typically larger than between the first and following excited-state levels. The resulting overlap of vibrational wavefunctions between different excited states leads to rapid non-radiative depletion of the higher excited states (IC). Once the lowest excited state S_1 is reached, fluorescence and ISC become kinetically competitive with non-radiative relaxation (IC) due to the higher energy gap to the electronic ground state (S_0).[32]

A small energy gap between the ground and the first excited state can also facilitate non-radiative deactivation processes. The energy gap law describes how the rate constant for non-radiative transitions increases with decreasing energy difference between two states. The reason is an overlap of the wavefunctions of the lowest vibrational level of S_1 or T_1 and higher vibrational states of the ground state S_0, facilitating non-radiative transitions.[34,35] This effect is more pronounced if the energy gap between ground and first excited state is low, e.g. for compounds which exhibit luminescence in the red and NIR regions of the electromagnetic spectrum. Non-radiative deactivation is usually an undesired process and can drastically limit the applicability of a luminophore by diminishing its luminescence quantum yield and excited-state lifetimes.

The inverse of the sum over all depletion pathway rate constants gives the lifetime of an excited state. The lifetimes of the lowest singlet and triplet excited states are calculated according to equations II.1 and II.2, respectively.

$$\tau_{S1} = \frac{1}{(k_f + k_{nr}^1 + k_{ISC})} \quad \text{(II.1)}$$

$$\tau_{T1} = \frac{1}{(k_{ph} + k_{nr}^2)} \quad \text{(II.2)}$$

The efficiencies of deactivation processes such as phosphorescence are determined by their quantum yields. The quantum yield ϕ is defined as the number of molecules undergoing a certain process divided by the number of photons absorbed by the molecule.[32] The quantum yield of a process *i* is linked to its decay rate constant and lifetime by equation II.3.

$$\phi_i = \frac{\text{number of molecules undergoing process } i}{\text{number of photons absorbed by the molecule}} = k_i \times \tau_i \quad \text{(II.3)}$$

The absorption spectrum of a complex consists of different absorbance bands, leading to different excited states. There are three kinds of possible electronic transitions that can occur in transition metal complexes.

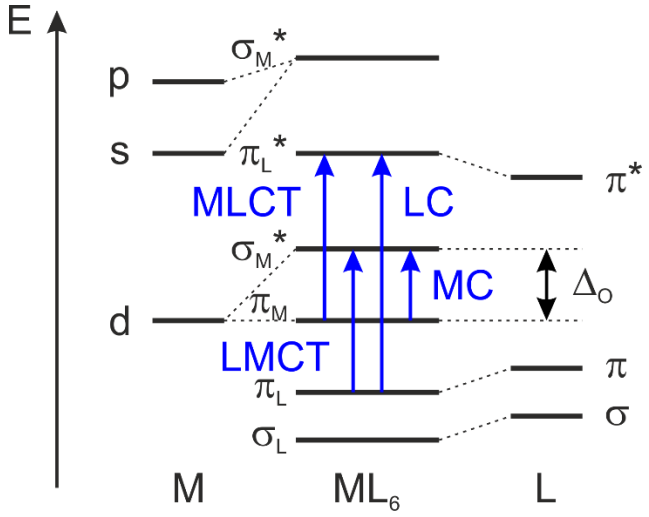

Figure 5: Schematic diagram of metal (M), ligand (L) and molecular orbitals for an octahedral complex of a transition metal adopted from reference [32]. The blue arrows depict possible transitions leading to absorbance bands in the UV and visible region of the electromagnetic spectrum. Δ_O is the energy difference between the t_{2g} and e_g orbitals in an octahedral crystal field (see Figure 3).

Metal centred transitions (MC in Figure 5) between two molecular orbitals with strong d character (forming ligand field excited states) are spin-forbidden and therefore only have low ε values. These transitions do not lead to charge redistribution between metal centre and ligand. MC transitions are often undesired as they can give rise to excited-state reactions such as ligand dissociation or substitution, and isomerisation reactions.[36] In most complexes of late transition metals, such as Ru or Mo, MC states are high enough in energy to minimize their involvement in excited-state photochemistry at relevant temperatures. However, in first-row transition metal complexes (e.g. of Fe, Cr or Mn), low lying metal centred states, due to the much lower ligand field splitting of these metals, can cause efficient non-radiative depopulation of the excited state. This results in

inefficient emission (with concomitantly short lifetimes) or complete absence thereof, as observed in complexes of Fe(II).[17]

The second possible transition occurs between two ligand-based orbitals (LC in Figure 5). These ligand centred transitions are typically $\pi \rightarrow \pi^*$ in character (but can also be $n \rightarrow \pi^*$) and can occur within the same ligand (intraligand charge transfer (ILCT)) or between different ligands of a complex (ligand-to-ligand charge transfer (LLCT)). These transitions cause intense absorption bands, typically in the blue or UV spectral range. Since these transitions do not involve the MC orbitals, their absorption bands are often similar in intensity, position and shape to those observed for the free ligand.[36]

The third kind of transition involves a charge transfer between the metal centre and the ligands (MLCT and LMCT in Figure 5). For most transition metal complexes, this is the most relevant type of transition and determines the photophysical behaviour. Depending on the direction of electron transfer, there are metal-to-ligand charge transfer (MLCT) and less common (with respect to photoactive complexes) ligand-to-metal charge transfer (LMCT) transitions. The metal and its oxidation state, as well as the type(s) of ligand(s) used, will determine the direction of electron transfer upon photoexcitation. Charge transfer transitions can vastly alter the redox properties of a complex, as will be discussed in the next subchapter.

2.1.2 Photocatalysis

Like natural photosynthesis in plants, artificial photocatalysis is able to combine two seemingly contradictory characteristics: mild reaction conditions and reactions with high activation barriers. This is possible because the energy of a photocatalytic reaction originates from the energetically high, light-induced excited state (of the photocatalyst), instead of elevated reaction temperatures, as in classic, thermal reactions. Hence, photocatalysis can be used to activate thermodynamically challenging compounds or to increase reaction selectivity due to the better control over the generated intermediates at lower temperatures.[32]

Figure 6 is a general depiction of the way photoreactions can overcome high reaction barriers or even enable endothermic reactions. In the simplest case of a photochemical reaction, a reactant A absorbs a photon and forms the excited-state species A*. Due to the higher energy of A* (compared to A), a subsequent unimolecular reaction to P is exothermic. In contrast, a thermal reaction with a similar reaction profile requires high temperatures to proceed. Examples of such simple photochemical reactions are the *cis*/*trans* isomerisation of double bonds or the elimination of nitrogen from azocompounds.[37] If the excited-state species A* encounters another molecule B, a bimolecular reaction can occur. Hydrogen abstraction by an excited ketone is a typical example for this case. However, these two simple cases require the reactant A to be able to (efficiently) absorb light.[38]

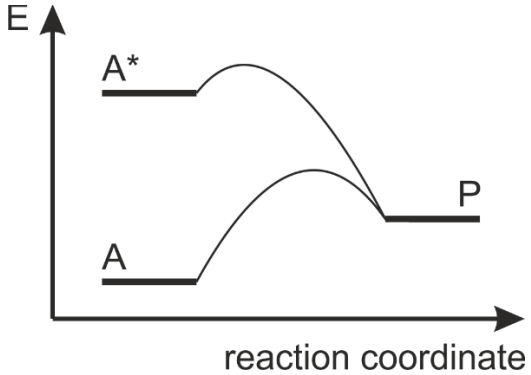

Figure 6: Schematic reaction energy profile depicting a reaction of substrate A to product P by thermal activation or light-induced activation via A*. Due to the high energy of the excited-state species A*, the reaction barrier is reduced, and/or the reaction becomes exergonic.

The separation of the light-absorption step from the consequent chemical reaction is the fundamental principle of photocatalysis. Therefore, a photocatalyst is employed to absorb light and promote further reactions of the substrate. Most photocatalytic processes either rely on photoinduced electron or energy transfer reactions as depicted in Figure 7. Initially, the photocatalyst C absorbs a photon and is promoted into the excited-state species C*. In a classic photoinduced electron transfer reaction, a consequent electron transfer from or to the substrate R forms the oxidised or reduced catalyst C’ and the intermediate product R’ (Figure 7a). R’ undergoes further reaction steps to form the desired product P_R. To close the catalytic cycle, C’ reacts with a second substrate D,

recovering C and generating D'. D is often a cheap (sacrificial) compound that is only used to regenerate C, while D' is a non-useful by-product of the catalytic cycle. The special case of a redox-neutral reaction (Figure 7b) is further discussed in chapter 4. In this case, R', which can transform to R'' in an intermediate, light-independent reaction step, also takes the role of D, recovering C and forming P_R at the same time. In the case of photosensitization (Figure 7c), only the excited-state energy is transferred from C* to R, and C is directly recovered. This reaction produces the excited-state species R*, which can undergo further reactions and/or loose the excited-state energy by emission of light.[32,38]

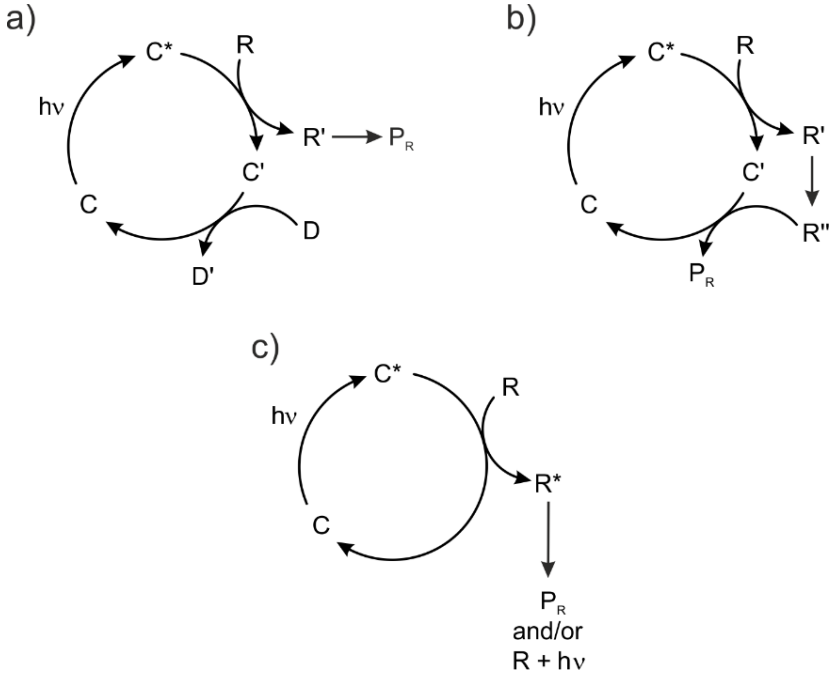

Figure 7: a) Catalytic cycle for a photoinduced electron transfer reaction. b) Catalytic cycle for a redox-neutral photoinduced electron transfer reaction. c) Catalytic cycle for a photosensitization reaction. C is a photocatalyst, C* its excited state and C' its oxidized or reduced form after reaction with R. R is a reactant, R' and R'' are its reaction intermediates, and R* its excited state. D is a second (sacrificial) reactant, D' its intermediate product after reaction with C' and P_R the product of the reaction. Adopted from references [32] and [38].

Due to their long-lived (triplet) excited states, octahedral complexes of d^6 metals such as Ru(II) or Ir(III) are commonly employed in photocatalysis.[39] Upon light-induced excitation, an electron is promoted from a t_{2g} orbital into a ligand centred orbital, which is typically lower in energy than the unoccupied metal e_g orbitals. Subsequent rapid ISC from the ^{1}MLCT excited state forms the ^{3}MLCT excited state. After the charge transfer from metal to ligand, the formally oxidised metal centre is a better oxidant compared to the ground state. At the same time, the formally reduced ligand is a better reductant than the ground state (Figure 8).

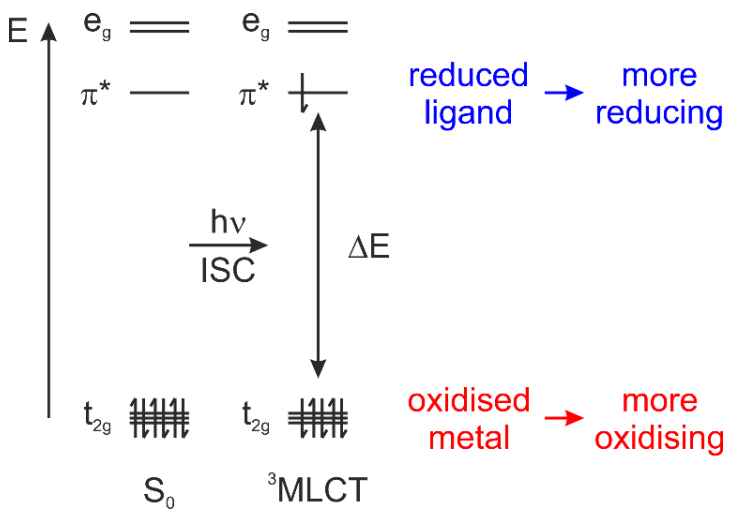

Figure 8: Energy diagram depicting excitation of an octahedral d^6 metal complex and formation of the ^{3}MLCT state. The charge-separated state is simultaneously a stronger oxidant and a stronger reductant than its corresponding ground state.

A LATIMER diagram (Figure 9) depicts the excited-state oxidation and reduction potentials of a compound and demonstrates how the excited state is simultaneously more oxidising and more reducing than its ground state. This resulting versatility is the reason complexes like $[Ru(bpy)_3]^{2+}$ (bpy = 2,2'-bipyridine) and its derivatives are so popular in photochemical applications, as in their excited state, they can be used as electron donors as well as acceptors for photoredox reactions.[20,40,41]

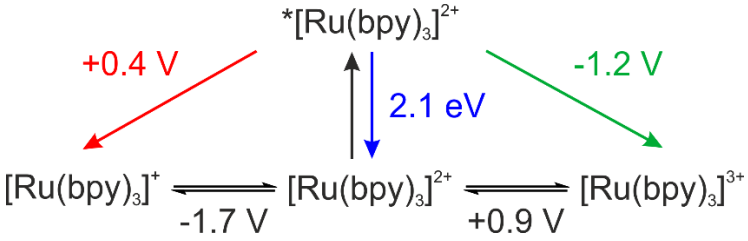

Figure 9: LATIMER diagram of $[Ru(bpy)_3]^{2+}$ used to calculate the excited-state oxidation and reduction potentials. Redox potentials are reported *vs* $Fc^{+/0}$ in acetonitrile.[42]

The excited-state oxidation and reduction potentials can be calculated from experimental data. Subtraction of the zero-phonon energy E_{00} (the energy difference between the ground and excited state; blue in Figure 9) from the ground state oxidation potential gives the excited-state oxidation potential (green in Figure 9), while addition of E_{00} to the ground state reduction potential gives the excited-state reduction potential (red in Figure 9).

2.2 Photoactive First-Row Metals

Due to the amount of research dedicated to second- and third-row d^6 transition metal complexes, there is a deep understanding of their advantageous photophysics and photochemistry. Complexes such as $[Ru(bpy)_3]^{2+}$ or $[Ir(ppy)_3]$ (ppy = 2,2'-phenylpyridine) and their derivatives have been utilised as photosensitizers or photocatalysts in countless examples.[39]

Nevertheless, the rarity of many popular metals prevents widespread application of such photocatalysts. The abundance of the two commonly used metals, ruthenium and iridium, is only 10^{-6} and 10^{-7} mass percent in Earth´s crust, respectively, leading to high prices of complexes using these metals.[43] In contrast, first-row transition metals are rather common, with abundances between 4.7 and 0.0024 mass percent for iron and cobalt, respectively.[43]

It would be desirable if all the knowledge and experience in the field of second- and third-row octahedral d^6 complexes could be transferred to luminescent first-row transition metal complexes. However, the initial design of such luminescent complexes is challenging, due to the aforementioned low lying MC states that enable fast, and typically radiation-less, relaxation in complexes of many first-row metals. Different concepts to obtain photoactive and luminescent first-row transition metal complexes have been explored. In the following section, selected current research and challenges in the design of luminescent (d^6) complexes of several first-row metals is presented.

2.2.1 Cobalt

Currently, there are not many examples of luminescent Co(III) complexes. Possibly the most relevant examples were reported in 2018 by the groups of Zysman-Colman and Hanan.[44] Due to large bite angles and strongly σ-donating nature of the ligands, their $[Co(dgpy)_2]^{3+}$ (dgpy = 2,6-diguanidylpyridine) and $[Co(dgpz)_2]^{3+}$ (dgpz = 2,6-diguanidylpyrazine) complexes (Figure 10) exhibit blue emission from a ^{3}LMCT state after (relatively) low-energy UV excitation. The reported (average) luminescence lifetimes of up to 5.5 ns and luminescence quantum yields of up to 0.7 % are among the highest reported values for charge transfer excited states of any first-row d^6 complexes. Both complexes were successfully applied as strong photooxidants for the trifluoromethylation of polycyclic aromatic hydrocarbons.

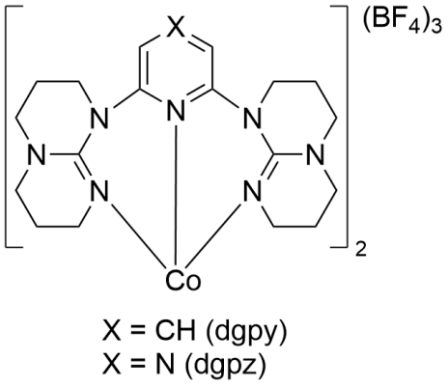

Figure 10: Structures of $[Co(dgpy)_2]^{3+}$ and $[Co(dgpy)_2]^{3+}$ investigated in reference [44].

In the same year, the group of Soper reported another Co(III)-CF_3 complex that allows the photoinduced homolysis and subsequent trifluoromethylation of C–H bonds in arenes.[45] However, this complex does not show any luminescence.

A recent paper from the groups of Wärnmark, Yartsev and Persson presents microsecond photoluminescence from the $[Co(III)(PhB(Melm)_3)_2]^+$ ($PhB(Melm)_3$ = tris(3-methylimidazolin-2-ylidene)(phenyl)borate) complex.[46] What makes this complex stand out is the luminescence from a MC excited state. MC excited-state luminescence in Co(III) has been known since 1979 for $[Co(CN)_6]^{3-}$, but with much shorter excited-state lifetimes.[47,48] After excitation of a deaerated solution of the $[Co(III)(PhB(Melm)_3)_2]^+$ complex at 266 nm, orange emission at 690 nm was observed. As expected from MC emission, the luminescence quantum yield is low (10^{-2} %). Due to the sensitivity of the emissive state to oxygen quenching, it was assigned as a ^{3}MC state. The tunability of σ- and π-properties of NHC ligands (in contrast to CN^-) enables future improvements in this compound class.

2.2.2 Iron

As the most abundant of the transition metals, iron-based complexes have received significant and ever increasing attention in recent years.[17] Compared to isoelectronic complexes of ruthenium, the ligand field induced by iron is much weaker, lowering the energy of the $^3T_{1g}$ and $^5T_{2g}$ MC states below that of the ^{3}MLCT state (depicted for $[Fe(bpy)_3]^{2+}$ in Figure 11b). This causes rapid, non-radiative deactivation of the excited state. There are two obvious countermeasures to suppress this deactivation pathway.[17] The first strategy targets stabilisation of the ^{3}MLCT state. However, lowering the energy of this state must be done within the limits of the energy-gap law as a too low lying energetic level increases non-radiative deactivation rates via vibrational coupling.[34,35] The second strategy aims towards pushing the MC states to higher energies. Higher MC state energies can be obtained with ligands that induce a strong ligand field. While MC states are highly dependent on the strength of the interaction between metal and ligand (Δ_O, see Figure 3), the energy of MLCT states mainly depends on the redox properties of metal centre and ligands.[14] The effect of an increase in the ligand field splitting parameter Δ_O can be illustrated in a TANABE-SUGANO diagram (Figure 11a).

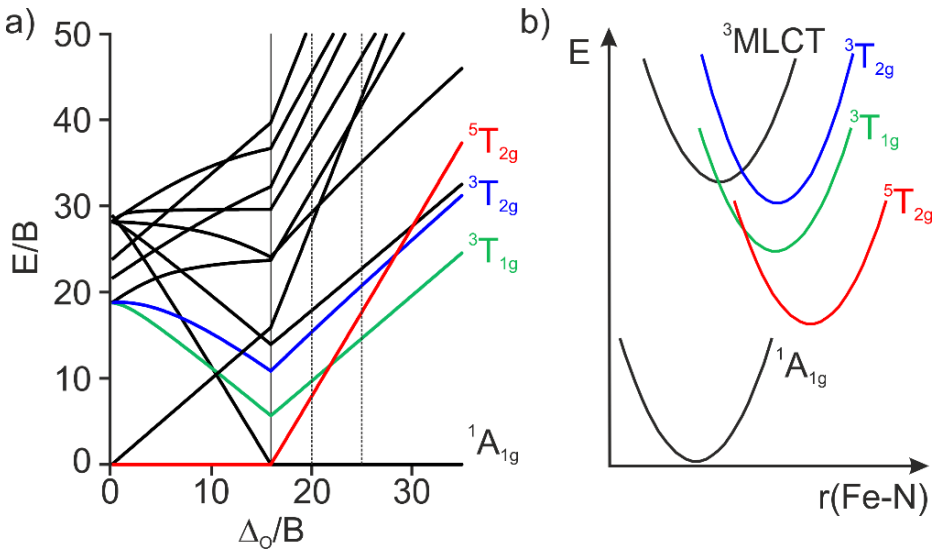

Figure 11: a) TANABE-SUGANO diagram for the low spin d^6 electron configuration with RACAH scaling parameter B = 827 cm^{-1}. The dotted vertical lines at 20 and 25 Δ_O/B depict approximate ligand field strength values for the complexes $[Fe(bpy)_3]^{2+}$ and $[Ru(bpy)_3]^{2+}$, respectively. b) Simplified potential energy diagram with the key electronic states in $[Fe(bpy)_3]^{2+}$, adopted from reference [17].

A larger value of Δ_O results in increasing energy levels of the $^3T_{1g}$ and $^5T_{2g}$ MC states (green and red in Figure 11, respectively). Depending on the choice of ligand, one of these two states is usually the lowest excited state in low-spin complexes of Fe(II). The stronger dependence of the $^5T_{2g}$ state on Δ_O (red in Figure 11a) arises from the excitation of two electrons into antibonding e_g orbitals (in contrast to one electron for $^3T_{1g}$).

The effect of a larger Δ_O is illustrated in Figure 11a by the exemplary complexes $[Fe(bpy)_3]^{2+}$ and $[Ru(bpy)_3]^{2+}$, represented by the two dotted vertical lines at 20 and

25 Δ_O/B, respectively. In the case of $[Fe(bpy)_3]^{2+}$, the position of the $^3T_{1g}$ and $^5T_{2g}$ states are notably below that of the ^{3}MLCT excited state (highlighted in Figure 11b), leading to an essentially barrier- and radiation-less deactivation of the ^{3}MLCT state within 50 fs.[49] In contrast, the heavier analogue $[Ru(bpy)_3]^{2+}$ shows a long-lived, luminescent excited-state, as the MC states are energetically above the ^{3}MLCT state due to the increase in ligand field strength. The energy level of the ^{3}MLCT state could be illustrated as a basically horizontal line in Figure 11a, due to the aforementioned virtual independence from Δ_O.[14] In the TANABE-SUGANO diagram, Δ_O and the energy E are scaled by the RACAH parameter B, which corresponds to d-electron repulsion.[33] A high degree of covalence in a metal-ligand bond reduces B (nephelauxetic effect) and is therefore another option to increase MC state energies.

To obtain a comparable situation for complexes of Fe(II), as in the prototypical $[Ru(bpy)_3]^{2+}$, many research groups use strong-field inducing ligands such as *N*-heterocyclic carbenes (NHC) to increase the energy of the deactivating MC states.

The first reported Fe(II) NHC complex (Figure 12) by Wärnmark and Sundström had a charge-transfer excited-state lifetime of 9 ps, exceeding the lifetime of $[Fe(bpy)_3]^{2+}$ by almost two orders of magnitude.[23]

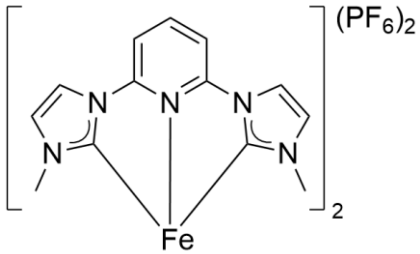

Figure 12: Structure of the first reported Fe(II) complex with NHC ligands from reference [23].

Density-functional theory (DFT) calculations by the groups of Jakubikova,[50] Monari[51] and Dixon,[52] as well as systematic studies as performed by the groups of Bauer and Lochbrunner,[53] increased the general understanding of the concepts required to enhance the lifetime of MLCT states over the following years.[17]

In a more recent study, the groups of Wärnmark and Sundström used mesoionic carbene ligands such as btz (Figure 13a, btz = 3,3'-dimethyl-1,1'-bis(*p*-tolyl)-4,4'-bis(1,2,3-triazol-5-ylidene)), which have both stronger σ-donor and π-acceptor capabilities than classic NHC ligands. The homoleptic complex $[Fe(btz)_3]^{2+}$ shows an excited-state lifetime of up to 528 ps that is ascribed to a ^{3}MLCT state.[54]

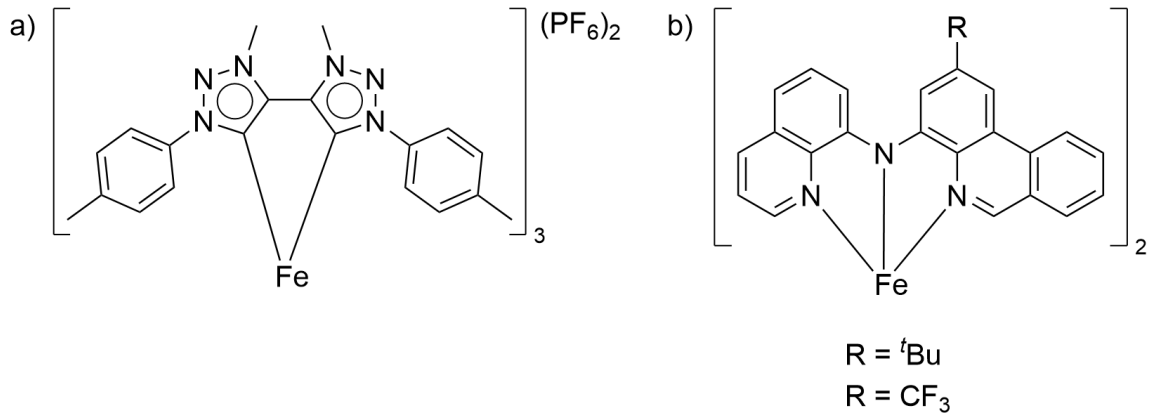

Figure 13: Structure of a) the mesoionic carbine complex $[Fe(btz)_3]^{2+}$reported in reference [54] b) the two [Fe((phenanthridin-4-yl)(quinolin-8-yl)amido$_2$] complexes from reference [24].

In 2019, the group of Herbert increased the MLCT excited-state lifetime to over 2 ns using a conceptually different "HOMO-inversion" strategy, with two Fe(II) complexes with benzannulated phenanthridine heterocycle ligands with amido donors (Figure 13b).[24] Despite all of the impressive progress in recent years, luminescence has not been reported from any complex of Fe(II).

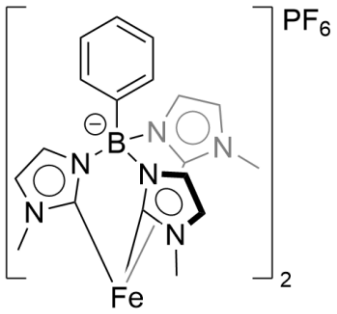

Figure 14: Structure of the luminescent complex $[Fe(phtmeimb)_2]^+$ reported in reference [55].

However, two recent publications reported LMCT emission in complexes of Fe(III).[55,56] In particular the $[Fe(phtmeimb)_2]^+$ (Figure 14, phtmeimb = {phenyl[tris(3-methylimidazol-1-ylidene)] borate}$^-$) complex reported in 2019 by the group of Wärnmark exhibits an impressive luminescence lifetime of 2 ns with a luminescence quantum yield of 2 %. This complex, as well as the $[Fe(btz)_3]^{3+}$ complex from the same group, exhibits spin-allowed fluorescence from a ^{2}LMCT state.

2.2.3 Manganese

A recent report on NIR emission in the solid state from a bis(tris(carbene)borate) Mn(IV) complex was inspired by luminescent Cr(III) complexes with d^3 electron configuration (*vide infra*). At 80 K, this complex mainly emits from a $^2E \rightarrow {}^4A_2$ transition at 828 nm, but also shows weak LMCT luminescence at 500 nm.[57]

There is a single report on luminescence in solution from a Mn(III) complex with a Schiff base ligand. However, the reported emission is purely ligand-based fluorescence in the blue spectral range.[58]

While solid state luminescence from Mn(II) complexes is rather common, there are only two reports on emission in solution. One of them describes an excitation wavelength dependent emission at 380, 440 or 495 nm. However, the origin of the longest wavelength luminescence in this complex could not be identified unambiguously.[59] The other report describes an orange emission from the polynuclear complex $[Mn_4(ThiaSO_2)_2F]^-$ ($ThiaSO_2$ = *p-tert*-butylsulphonylcalix[4]arene) in DMF at room temperature.[60]

There is only one report on emission from a Mn(I) compound. While the utilised polypyridine ligand functionalised with 1,3,4 oxadiozole and triarylamine moieties shows MLCT emission in a Re(I) complex, the emission for the respective Mn(I) complex (Figure 15), although with enhanced intensity, only has the same pure ILCT character as the free ligand.[61]

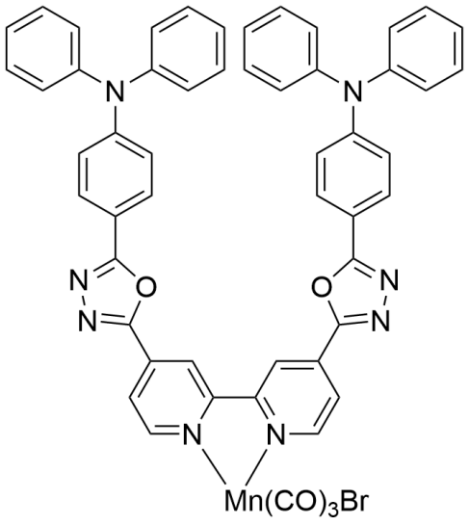

Figure 15: Structure of the Mn(I) complex that shows ILCT after excitation as reported in reference [61].

2.2.4 Chromium

Luminescence from Cr(III) complexes and application of photoactive Cr(III) compounds in the fields of solar cells or catalysis have been known for several decades.[62,63]
The Heinze group published several papers on luminescent "molecular ruby" complexes of Cr(III) over the last years.[64–67]

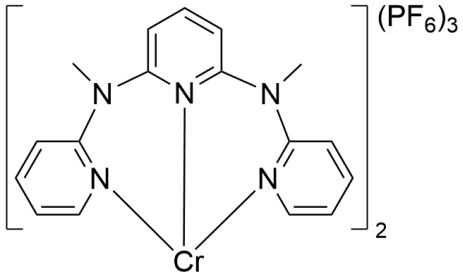

Figure 16: The "molecular ruby" complex $[Cr(ddpd)_2]^{3+}$, as reported in reference [64].

The high symmetry of these complexes with near ideal bite angles increases the relevant energy gap, decelerating non-radiative relaxations. This leads to very long excited-state lifetimes of close to 1 ms as for their $[Cr(ddpd)_2]^{3+}$ (ddpd = *N,N*'-dimethyl-*N,N*'-dipyridine-2-ylpyridine-2,6-diamine) complex (Figure 16), that exhibits $^2E_g \rightarrow {}^4A_{2g}$ spin-flip luminescence in the red spectral region in deaerated water at room temperature. This complex was also used as photosensitizer to produce $^1O_2$ via energy transfer, enabling subsequent reactions.[64] The deuterated version of this complex shows an even longer luminescence lifetime of 2.3 ms with a high luminescence quantum yield of 30 %.[65]
Reduction of $[Cr(ddpd)_2]^{3+}$ affords the corresponding Cr(II) complex, which exhibits thermally induced spin crossover. UV light excitation of this reduced complex gives rise to an excited state, which has a microsecond lifetime, but does not show luminescence.[68]
Büldt and Wenger reported a luminescent Cr(0) complex in 2017 (see also chapter 2.3).[29] In this complex, the use of strong-field inducing bidentate isocyanide ligands raises the energy of the relevant MC states, so that emission from the ^{3}MLCT state can compete with radiation-less deactivation. The emission lifetime of this complex is 2.2 ns in deaerated THF with a luminescence quantum yield of approximately 10^{-3} %. This is the first example of MLCT luminescence from a first-row d^6 transition metal complex.

Despite relevant results for other electronic configurations, there are currently only three examples of luminescence from first-row d^6 transition metal complexes. Complexes of Co(III) by the groups of Zysman-Colman and Hanan exhibit ^{3}LMCT luminescence.[44] A recent report by the groups of Wärnmark, Yartsev and Persson, as well as earlier reports on $[Co(CN)_6]^{3-}$ describe luminescence from a ^{3}MC state.[46–48] And an isocyanide complex of Cr(0) from the Wenger group is the first example of ^{3}MLCT luminescence.[29] Just a decade ago, many believed complexes of first-row transition metals (with the notable exception of the d^{10} metal Cu(I)) to be unusable as photoactive compounds due to their rapid excited-state deactivation.[69] Since then, excited-state lifetimes have increased by multiple orders of magnitude, e.g. from the sub-picosecond range to nanoseconds in complexes of Fe(II).[14,17] However, more research on relevant metals such as Cr(0), Mn(I), Fe(II) or Co(III) is required for further results and improvements of excited-state lifetimes and luminescence quantum yields as well as applications in photocatalyzed reactions.

2.3 Low-Valent Isocyanide Complexes

The (relative) stability of MLCT states in first-row transition metal complexes with a d^6 electron configuration can be improved by increasing the energy of low lying MC states with a strong ligand field. Possible ligands able to induce such a strong field include *N*-heterocyclic carbenes (NHC), carbonyls (CO) or isocyanides (RNC). For use in combination with metal centres in low oxidation states, the ligands further need to be able to stabilise the electron density on the metal via π-backbonding. NHCs are mainly σ-donors, while RNC and especially CO are also good π-acceptors. Due to the R-moiety, isocyanide ligands can easily be functionalised e.g. with aromatic groups, increasing their π-acceptor capabilities.[70,71] Their stronger σ-donation properties compared to the isolobal CO also helps to stabilise metal centres in higher oxidation states, which are typical intermediate states after photoinduced charge transfer.

Isocyanides have been used in early work from Mann and Gray to stabilise zero-valent group 6 metal centres of Cr, Mo and W. Of particular interest are the hexa(arylisocyanide) complexes of W(0) as they show strong emission with excited-state lifetimes of up to 80 ns at room temperature. The homoleptic Mo(0) and especially Cr(0) complexes with the same ligand were increasingly prone to ligand substitution reactions.[72,73]

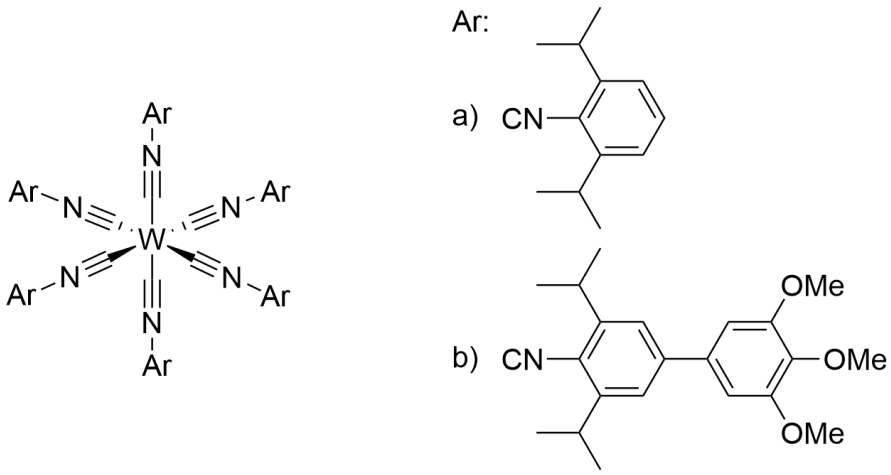

Figure 17: Luminescent hexa(isocyanide) complexes of W(0) as reported in references [74] and [75].

In two more recent publications of the same group, Sattler could show that $[W(CNIph)_6]$ (Iph = 2,6-diisopropylphenyl) (Figure 17a) can be used as a very powerful photoreductant.[74] Furthermore, it was described how extension of the ligand π-system (Figure 17b) could increase luminescence lifetimes (up to 1.83 µs) and quantum yields (up to 44 %).[75]

Ligands with multiple isocyanide coordination sites could reduce the extent of ligand dissociation and increase the shielding of the metal centre from coordination of solvent or nucleophiles. Due to the linear structure of the isocyanide M-C≡N-R motive, a distance

equivalent to at least 7 methylene groups between the isocyanide functionalities needs to be bridged for chelate formation.[76]

While several groups achieved the synthesis of multidentate isocyanide ligands, in most cases aliphatic bridging motifs were used (Figure 18).[77–84]

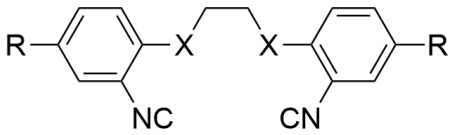

R = H, ^{t}Bu
X = O, NMe, CH_2S

M = Cr(0-II), Mn(I-II), Fe(II), Co(I-III), Ni(0), Cu(I), Rh(I), Pd(I)

Plummer, Sakata

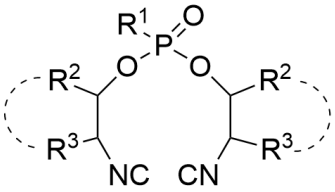

R^1 = Alkyl, aryl
R^2 = H, alkyl, aryl
R^3 = Alkyl, aryl

M = Pd(II), Cu(I), Rh(I), Ir(I)

Naik

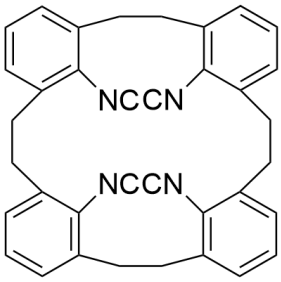

M = Cu(I), Co(II), Ni(0)

Ito

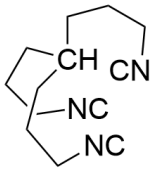

M = Cr(0), W(0)

Hahn

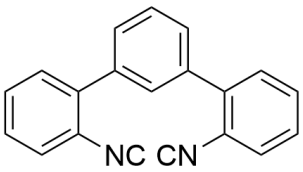

M = Ir(III)

Armaroli

Figure 18: Structures of chelating isocyanide ligands reported in references [77] - [84] with their respective metal ions used for the synthesis of transition metal complexes.

Plummer and Angelici even synthesised homoleptic, bidentate complexes of Mn(I), but did not report any luminescence properties.[77] Very likely, an aromatic ligand backbone is required to observe such behaviour. The group of Armaroli finally used an aromatic ligand backbone and reported the tuneable emission behaviour of the corresponding Ir(III) complex.[84] However, there are no reports from this group on using their ligand in combination with any other (more abundant) metal.

Finally, Büldt and Wenger used a similar ligand with aromatic terphenyl backbones in combination with low-valent Mo(0) and Cr(0) metal centres (Figure 19).[29,30] With these two complexes, they could observe luminescence upon visible-light excitation in solution at room temperature.

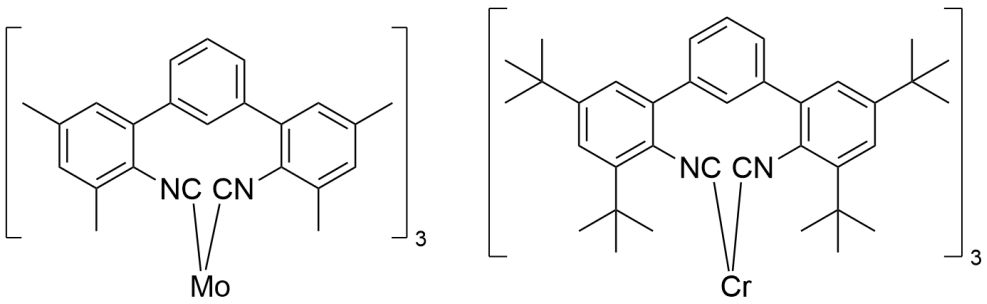

Figure 19: The luminescent [Mo(L^{Me})$_3$] and [Cr(L^{tBu})$_3$] complexes with chelating diisocyanide ligands reported by Büldt and Wenger.[29,30]

Both complexes exhibit broad MLCT absorption features from 350 nm up to approximately 550 nm and can be excited with green light. The reported Mo(0) complex has a luminescence lifetime of 225 ns in deaerated *n*-hexane and a luminescence quantum yield of 4.5 %.[30] The Cr(0) complex showed a lifetime of 2.2 ns in deaerated THF, with a quantum yield of 10^{-3} %.[29] Despite the short excited-state lifetime and low luminescence quantum yield, the Cr(0) complex was able to undergo triplet energy transfer to anthracene with subsequent triplet-triplet annihilation upconversion. Due to its high excited-state oxidation potential, the Mo(0) complex is able to catalyse the rearrangement of acyl cyclopropane to 2,3-dihydrofurane.

3 Manganese(I) Isocyanide Complexes with MLCT Luminescence and Photoreactivity

3.1 Design of new Isocyanide Ligands

As the Mo(0) isocyanide complex [Mo(L^{Me})$_3$] introduced in chapter 2.3 (Figure 19) exhibits limited stability upon light irradiation, a new ligand with a stronger chelate strength, due to its tridentate nature, was synthesised during the course of this PhD project (Figure 21). Initial Merck molecular force field (MMFF) calculations on possible structures for tridentate ligands showed that the bite angle induced by phenylene linkers in the ligand backbone (as in the complexes in Figure 19) would not be a good match for the intended coordination to Mn(I). Instead, thiophene units were used in the new tridentate ligand (Figure 20). According to the MMFF calculations, the complex geometry with the new thiophene based ligand is closer to an octahedral coordination geometry, with bite angles closer to 180°, more linear coordination modes and more linear isocyanide groups as displayed in the structures and table of Figure 20.

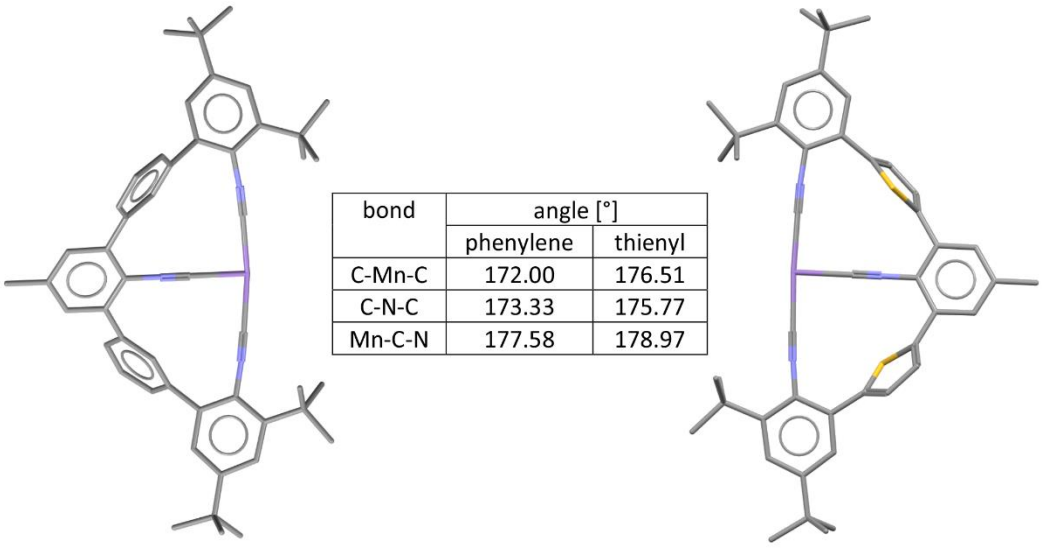

bond	angle [°]	
	phenylene	thienyl
C-Mn-C	172.00	176.51
C-N-C	173.33	175.77
Mn-C-N	177.58	178.97

Figure 20: MMFF calculated structures (only one ligand shown) for tridentate isocyanide Mn(I) complexes with either phenylene (left) or thienyl (right) linkers. The calculated bite angles (C-Mn-C), isocyanide angles (C-N-C) and coordination angles (Mn-C-N) are all closer to the optimal angle of 180° for the ligand with thienyl groups.

A recent publication from our group revealed that in isocyanide complexes of Mo(0), the introduction of thiophene units in the ligand backbone (in combination with an extension of the ligand π-system) leads to a red shift in emission by more than 100 nm.[85] In order to quantify the changes stemming from the introduction of the thienyl linker versus the

tridentate nature of the ligand, the corresponding bidentate ligand (Figure 21) was also synthesized according to a method previously used in the group.[86]

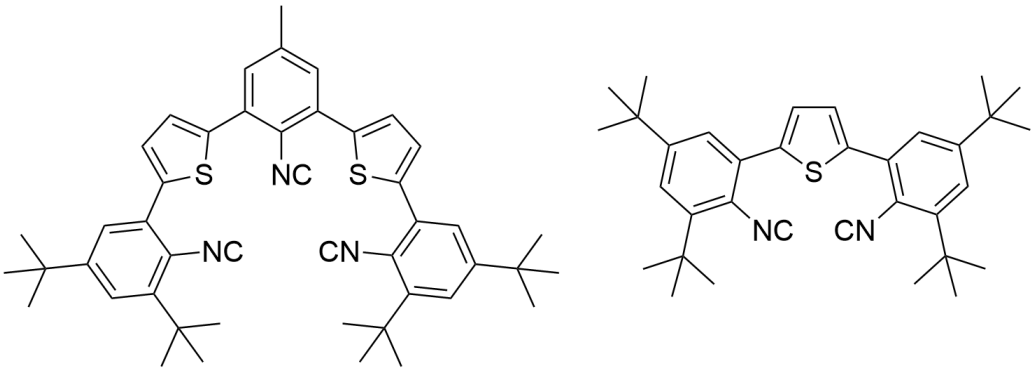

Figure 21: Multidentate isocyanide ligands used in this PhD project for the complexation of low-valent d^6 Mn(I).

3.2 New Isocyanide Complexes of Mn(I)

Homoleptic Mn(I) complexes of the bi- and tridentate thienyl ligands in Figure 21 were synthesised and their optical and electrochemical properties were thoroughly analysed. Mn(I) was used as the metal centre of choice as manganese is one of the most abundant transition metals in Earth's crust and is isoelectric to the d^6 metal Fe(II), which has been heavily researched in recent years.[17] Yet, there is only very little research dedicated towards finding an alternative to heavier transition metal complexes (such as $[Ru(bpy)_3]^{2+}$) based on Mn(I), despite its promising d^6 electronic configuration.
The synthesis of both complexes as well as their unexpected spectroscopic properties, and applications in energy and electron transfer reactions were submitted for publication:

- P. Herr, C. Kerzig, C. B. Larsen, D. Häussinger, O. S. Wenger "Manganese(I) complexes with metal-to-ligand charge transfer luminescence and photoreactivity" submitted **2020**.

Upon excitation with blue light, solutions of both homoleptic Mn(I) complexes show photoluminescence at 500 nm with lifetimes of up to 1.7 ns at room temperature. This marks only the second report of MLCT emission from a $3d^6$ metal complex and the first using manganese as metal centre. For isoelectronic Fe(II), no such emission could be observed to date, despite considerable effort.[17]
In frozen matrix, both Mn(I) complexes show two luminescence bands. This unexpected behaviour is attributed to the MLCT emission visible at room temperature as well as a second emission band originating from a ligand-based $^3\pi$- π^* state. In frozen matrix, the luminescence lifetime of this second band is in the range of 100-200 µs for both complexes, whereas it rapidly decays at room temperature, escaping observation.
Both excited states readily engage in photoreactions. Electron transfer reactions are accessible from the MLCT state whereas triplet energy transfer can occur from the $^3\pi$- π^*

state. This finding makes both Mn(I) complexes stand out from typical behaviour of precious metal-based photosensitizers, where the MLCT state is typically the only photochemically relevant state.

Author contributions

- P.H. carried out synthetic, spectroscopic, and electrochemical work, analysed data and wrote the manuscript.
- C.K. provided guidance in spectroscopic work, designed photochemical studies, and helped in data analysis and the preparation of the manuscript.
- C.B.L. provided guidance in synthetic, spectroscopic, and electrochemical work and helped in data analysis and the preparation of the manuscript.
- D.H. performed NMR studies and helped in the preparation of the manuscript.
- O.S.W. conceived the project, provided guidance, and wrote the manuscript.

Manganese(I) Complexes with Metal-to-Ligand Charge Transfer Luminescence and Photoreactivity

Patrick Herr, Christoph Kerzig, Christopher B. Larsen, Daniel Häussinger and Oliver S. Wenger*

Department of Chemistry, University of Basel, St. Johanns-Ring 19, 4056 Basel, Switzerland

Abstract

Precious metal complexes with the d^6 valence electron configuration often exhibit luminescent metal-to-ligand charge transfer (MLCT) excited states, which form the basis for many applications in lighting, sensing, solar cells, and synthetic photochemistry. Iron(II) has received much attention as a possible Earth-abundant alternative, but to date no iron(II) complex has been reported to show MLCT emission upon continuous-wave excitation. Manganese(I) has the same electron configuration as iron(II), but has been overlooked in the search for cheap MLCT luminophores until now. We discovered that novel isocyanide chelate ligands give access to air-stable manganese(I) complexes exhibiting MLCT luminescence in solution at room temperature, and these compounds were successfully employed as photosensitizers for energy and electron transfer reactions. Our study provides new guidelines for the design of photoactive complexes based on first-row transition metals, and it unravels fundamentally important differences in their photophysics compared to the well-known precious metal-based compounds.

Introduction

The long-lived MLCT excited states of many Ru(II) and Ir(III) complexes play key roles in light-emitting devices[1], dye-sensitized solar cells[2], photoredox catalysis[3], artificial photosynthesis[4] and photodynamic therapy[5]. There is a long-standing interest in replacing these precious and rare $4d^6$ and $5d^6$ ions by cheaper $3d^6$ elements, and until now essentially all efforts in that direction concentrated on Fe(II)[6]. However, the MLCT states of Fe(II) complexes deactivate on very rapid timescales, due to metal-centered (MC) excited states situated at much lower energies than in Ru(II) or Ir(III)[7-11]. Recently, these undesired deactivation processes were decelerated by innovative molecular design[12,13], yet no MLCT luminescence after continuous-wave excitation has been reported to date[14,15]. In the course of these efforts, ligand-to-metal charge transfer (LMCT) luminescence from Fe(III) ($3d^5$) complexes was discovered[16,17], but the direction of charge transfer is important for many applications hence emissive MLCT states of $3d^6$ complexes remain a strategic key target[18]. In particular, the development of $3d^6$ complexes resembling the prototypical $[Ru(bpy)_3]^{2+}$ compound (bpy = 2,2'-bipyridine) both structurally and functionally represents a grand challenge[19].

We recently reported a very weakly luminescent Cr(0) complex, but that compound suffered from sensitivity to air due to facile oxidation of Cr(0)[20]. For the present study, we turned to isoelectronic Mn(I), for which some air-stable complexes with π-acceptor ligands had been known[21-23]. After iron and titanium, manganese is the third most abundant transition metal element, exceeding the natural abundance of copper by a factor of 18, which seems noteworthy because copper has received much attention from the photophysics and photochemistry community[24-27]. The abundance and low cost combined with the prospect of obtaining compounds with low toxicity recently triggered

interest in Mn(I) complexes as catalysts for C-H activation[28] and other applications in organic chemistry[29,30], as well as for electrocatalytic CO_2 reduction related to artificial photosynthesis[31,32]. The photophysics of homoleptic Mn(I) complexes, however, is as yet essentially unexplored. Our Mn(I) photosensitizers complement recent important discoveries of LMCT luminophores made from Earth-abundant metals (including a Mn(IV) complex)[16,17,33-35], and they represent the first air-stable $3d^6$ complexes with luminescent MLCT states. The Mn(I) complexes presented herein furthermore have a low-lying ligand-centered $^3\pi$-π^* state, which leads to unexpectedly rich photophysics and photochemistry of this new class of compounds.

Results and discussion

Isocyanide ligands can stabilize metals in low oxidation states[36], and monodentate arylisocyanides provided access to emissive W(0) complexes in earlier studies[37,38]. Since chelate ligands usually give more robust coordination compounds, we previously developed bidentate isocyanide ligands with terphenyl backbones to obtain photoactive Cr(0) and Mo(0) complexes[20,39]. For the Mn(I) complexes reported herein (Fig. 1), we synthesized two new isocyanide chelates (SI pages S4/S5) with thiophene units in the backbone to optimize bite angles, one of them bidentate (L^{bi}) and the other tridentate (L^{tri}). The free ligands reacted with $Mn(CO)_5Br$ to the homoleptic complexes $[Mn(L^{bi})_3]^+$ and $[Mn(L^{tri})_2]^+$ (Fig. 1), which were characterized with all standard techniques (SI pages S6-S43) including ^{55}Mn NMR spectroscopy. The ^{55}Mn NMR shifts of $[Mn(L^{bi})_3]^+$ and $[Mn(L^{tri})_2]^+$ were determined as δ = –1225 and –1419 ppm, respectively, and fall both unambiguously in the range –1000 > δ > –1500 for Mn(I) complexes[40]. L^{tri} binds in meridional fashion, and the direct comparison of bis(tridentate) and tris(bidentate)

coordination environments allowed us to probe differences in robustness and photophysical behavior.

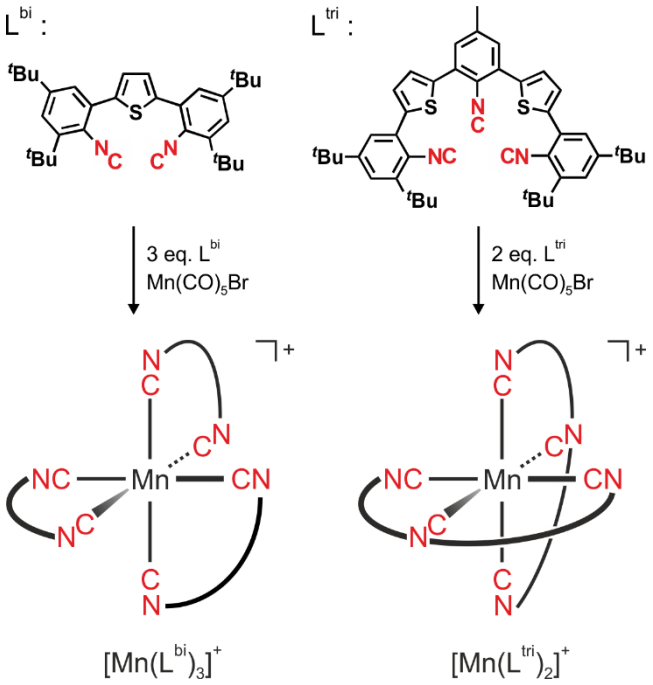

Figure 1. Molecular structures of the ligands and complexes (isolated as PF_6^- salts) explored in this work. Yields for complexation: 64% for $[Mn(L^{bi})_3]^+$, 41% for $[Mn(L^{tri})_2]^+$.

Both complexes are yellow due to an absorption band near 400 nm (solid purple lines in Figs. 2/S24), which tails to the deep blue region and is not present in the free ligands (dotted purple lines). Excitation into this absorption band causes solvatochromic luminescence, which red-shifts by roughly 1500 cm^{-1} between toluene and CH_3CN. In some solvents Raman-scattered excitation light is detectable (asterisks in Figs. 2/S24), but the emission bands are unstructured. The luminescence quantum yields (ϕ) in deaerated CH_3CN at 20 °C are 0.05% for $[Mn(L^{bi})_3]^+$ and 0.03% for $[Mn(L^{tri})_2]^+$ (SI page S61), which is more than one order of magnitude higher than for our recently reported Cr(0) complex emitting from a ^{3}MLCT state[20], whereas Fe(II) complexes are completely non-emissive

under comparable conditions. The presence of low-lying metal-centered (MC) excited states in the $3d^6$ configuration makes it much harder to establish luminescent charge-transfer excited states than in the $3d^0$ and $3d^{10}$ configurations, in which MC states are absent. Thus, the step from no luminescence (as in all previously studied Fe(II) complexes) to weak MLCT emission in our Mn(I) complexes represents an important breakthrough.

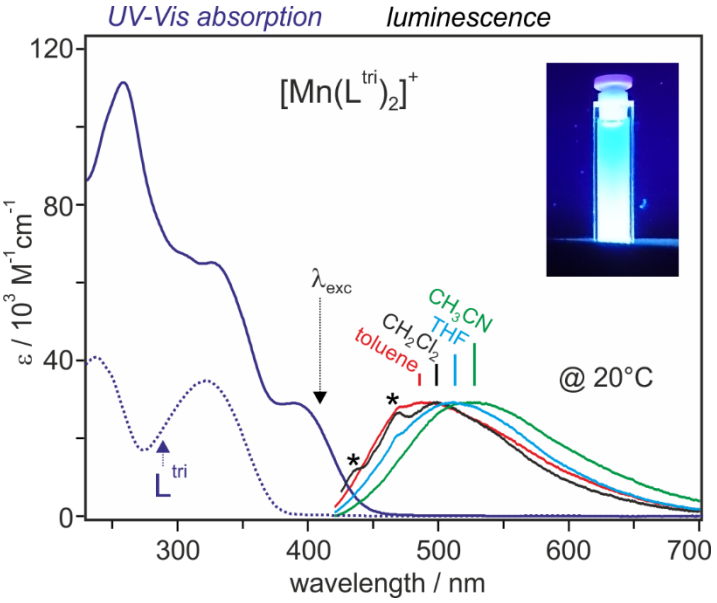

Figure 2. Steady-state absorption and emission spectroscopy. Left, purple lines: UV-Vis absorption spectra of $[Mn(L^{tri})_2]^+$ (solid) and L^{tri} (dotted) in CH_2Cl_2. Right: Luminescence spectra of $[Mn(L^{tri})_2]^+$ following excitation at 410 nm (λ_{exc}) in four different de-aerated solvents. The asterisks mark peaks caused by Raman scattered excitation light. Top right: Cuvette with a solution of $[Mn(L^{tri})_2]^+$ in CH_3CN irradiated from the bottom by a UV lamp for chromatography (λ_{exc} = 366 nm).

In picosecond transient absorption (ps-TA) spectroscopy a ground-state bleach (GSB) is observable near 400 nm (Figs. 3a/S25a) and an excited-state absorption (ESA) band appears at 470 nm. Following pulsed excitation, the ESA at 470 nm and the luminescence

at 460 nm show very similar decay behavior (Figs. 3d/S25d), indicating that both signals belong to the same excited state. MLCT states are formally comprised of an oxidized metal and a reduced ligand, whose individual spectral signatures are accessible via spectro-electrochemistry[41]. In our complexes, Mn(I) is oxidized reversibly to Mn(II) at ca. 1.0 V vs SCE (Figs. 3f/S25f), in line with expectation[21-23]. Reductive sweeps (Figs. 3e/S25e) contain several irreversible waves, the first one of which (at -1.9 V vs SCE) is attributable to the reduction of coordinated L^{tri}/L^{bi} to $(L^{tri})^{\bullet-}/(L^{bi})^{\bullet-}$. At a constant potential of -2.2 V vs SCE, the spectro-electrochemical $(L^{tri})^{\bullet-} - L^{tri}$ (Fig. 3b) and $(L^{bi})^{\bullet-} - L^{bi}$ (Fig. S25b) difference spectra are obtained. At a fixed potential of 1.2 V vs SCE, one obtains the spectro-electrochemical difference spectra in Figs. 3c/S25c, which correspond to the subtraction of spectra of Mn(I) from Mn(II) species. The ps-TA spectra (Figs. 3a/S25a) are essentially a linear combination of the difference spectra of metal oxidation (Figs. 3c/S25c) and ligand reduction (Figs. 3b/S25b), as expected for MLCT transitions[41]. This very good agreement between transient absorption and spectro-electrochemical data furthermore suggests limited admixture of π-π^* character to the emissive MLCT state.

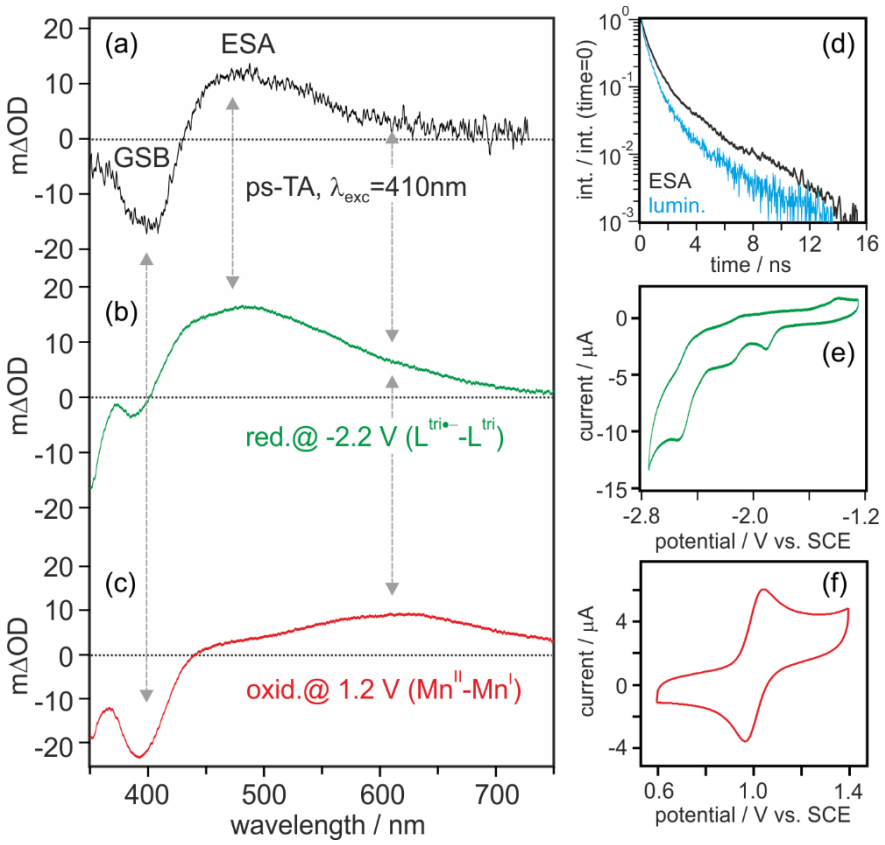

Figure 3. Time-resolved and (spectro-)electrochemical data for $[Mn(L^{tri})_2]^+$. (a) UV-Vis transient difference spectrum of 16 µM $[Mn(L^{tri})_2]^+$ in de-aerated CH_2Cl_2 at 20 °C, time-integrated over 2 ns following excitation at 410 nm with 30-ps laser pulses. (b) UV-Vis changes upon electrochemical (ligand-centered) reduction in CH_3CN. (c) UV-Vis changes upon electrochemical (metal-centered) oxidation in CH_3CN. (d) Decays of the excited-state absorption (ESA) signal at 470 nm (black, λ_{exc} = 410 nm) and the luminescence intensity at 460 nm (blue, λ_{exc} = 405 nm) in de-aerated CH_2Cl_2 at 20 °C. (e) Cyclic voltammogram (CV) showing ligand-based reduction in deaerated CH_3CN. (f) CV showing metal-based oxidation in CH_2Cl_2. The electrolyte was 0.1 M $TBAPF_6$.

Luminescence lifetimes are tri-exponential with weighted average lifetimes of 0.74 ns for $[Mn(L^{bi})_3]^+$ and 1.73 ns for $[Mn(L^{tri})_2]^+$ in deaerated CH_3CN at 20 °C (Table 1), close to some of the longest lifetimes for (dark) MLCT states in Fe(II) complexes[12,13], and similar to the

MLCT lifetime (2.2 ns) of our recently reported Cr(0) isocyanide complex[20]. The backbones of our ligands L^{tri} and L^{bi} contain sequences of ArNC-thiophene-ArNC units, and flipping of the central thiophene unit with respect to the neighboring ArNC (arylisocyanide) units can lead to different conformers (SI pages S80-S83), and this causes the multi-exponential decay behavior[39]. All three decay components (τ_1, τ_2, τ_3) have identical luminescence spectra (Figs. S32/S33), which is in line with a single emissive state in different conformers.

Table 1. Electrochemical and photophysical parameters[a].

	$[Mn(L^{bi})_3]^+$	$[Mn(L^{tri})_2]^+$
E^0 ($Mn^{II/I}$) vs SCE [b]	1.05 V	1.00 V
E^0 (($L^{tri/bi}$)/($L^{tri/bi}$)$^{\bullet-}$) vs SCE	-1.94 V	-1.91 V
τ_{avg} / ns	0.74	1.73
τ_1, τ_2, τ_3 / ns [c]	0.374 (79.2%), 1.84 (19.3%), 5.85 (1.5%)	0.635 (56.4%), 2.07 (33.6%), 6.74 (10.0%)
ϕ	0.05%	0.03%

[a] In de-aerated CH_3CN at 20 °C unless otherwise noted. [b] In CH_2Cl_2 at 20 °C. $L^{tri/bi}$ denotes coordinated ligands.

[c] Values in parentheses indicate relative importance.

In isoelectronic $[Fe(bpy)_3]^{2+}$, excitation into the ^{1}MLCT absorption band is followed by intersystem crossing (ISC) to the lowest ^{3}MLCT excited state within less than 20 fs[42], and from this perspective it seems plausible that the emissive MLCT states of our Mn(I) complexes (at 2.9 eV) are triplets. However, upon addition of excess naphthalene (with a

triplet energy (E_T) of 2.64 eV) or *p*-terphenyl (E_T = 2.52 eV) the characteristic triplet ESA signatures of these polyaromatic hydrocarbons (PAHs) are not observable, even though rate constants for triplet-triplet energy transfer (TTET) typically reach the diffusion-limit when the driving-force is 0.2 eV or greater[43]. Only when PAHs with lower triplet energies such as pyrene (E_T = 2.10 eV, SI page S66) or anthracene (E_T = 1.85 eV, see further below) are used, there is clear evidence for TTET. Thus, it looks as if our Mn(I) complexes have a (dark) triplet excited state below 2.52 eV (*p*-terphenyl) but above 2.10 eV (pyrene). However, upon direct excitation of the Mn(I) complexes in solution at 20°C, we were unable to detect long-lived excited states other than the MLCT in Figs. 3a/S25a.

To get direct insight into the electronic structures of our coordinated ligands (and possible low-lying ligand-centered triplet states), we explored the [$ZnCl_2(L^{bi})$] complex (SI pages S21, S45, S70-S77). Expectedly, the UV-Vis spectrum of [$ZnCl_2(L^{bi})$] (Fig. S44) closely resembles that of uncoordinated L^{bi}, as the MLCT absorption bands observable for the Mn(I) complexes at 400 nm (Fig. 2/S24) are absent for Zn(II). In solution at 20 °C, [$ZnCl_2(L^{bi})$] exhibits luminescence with a band maximum at 440 nm (Fig. S44), blue-shifted more than 50 nm relative to the MLCT emissions in Figs. 2/S24. This luminescence with a lifetime of 1.24 ns (Fig. S45) is attributed to fluorescence from a $^1\pi$-π^* state at 3.2 eV (Fig. 4e). In our search for a low-lying $^3\pi$-π^* state, we explored one Ru(II) and three Ir(III) complexes with well-defined triplet energies as sensitizers for TTET to [$ZnCl_2(L^{bi})$] (SI pages S73-S75). Selective excitation of the Ir(III) complexes with E_T values between 2.4 and 2.7 eV in presence of excess Zn(II) complex yields a long-lived (τ_T > 50 μs) photoproduct that can be assigned to triplet-excited [$ZnCl_2(L^{bi})$] (Fig. S47), whilst the Ru(II) complex with E_T = 2.2 eV fails to provide this photoproduct. From this we conclude that coordinated L^{bi} has $^3\pi$-π^* state at ca. 2.3 eV (Fig. 4e), and given the structural similarity between L^{bi} and L^{tri}, it

seems reasonable to assume that this is also the case for the tridentate ligand (for which we have been unable to isolate a stable Zn(II) complex). It follows that there must be a ligand-centered $^3\pi$-π^* state at ca. 2.3 eV in $[Mn(L^{bi})_3]^+$ and $[Mn(L^{tri})_2]^+$ (Fig. 4d).

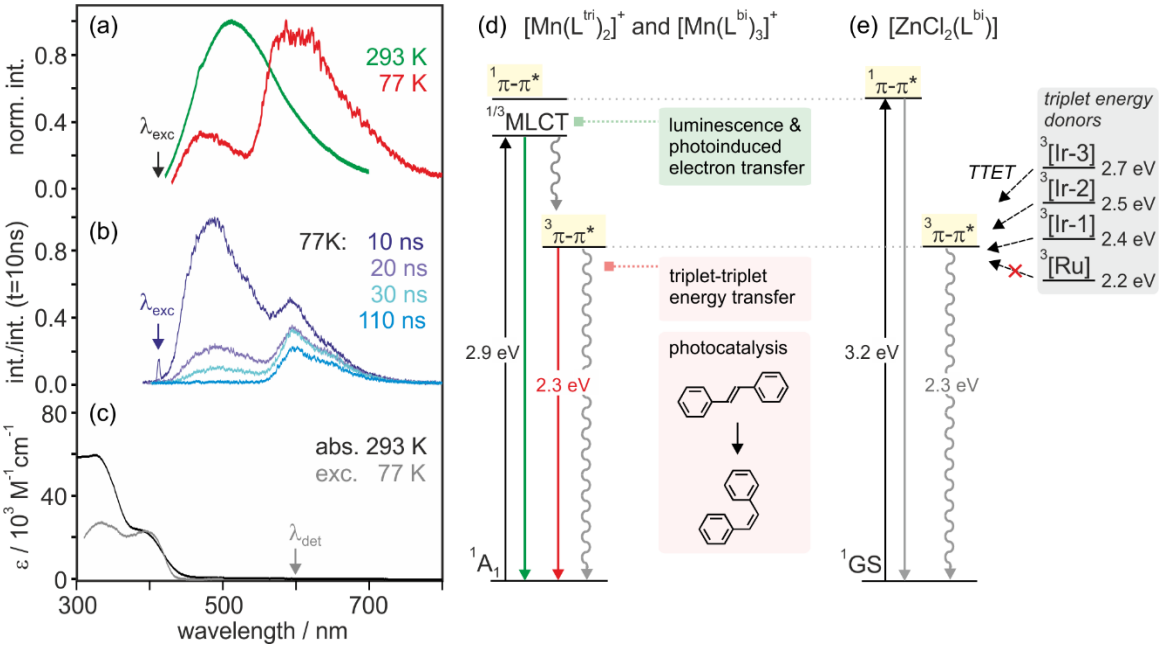

Figure 4. Dual emission at 77 K, different excited states and their photo-reactivities. (a) Luminescence of $[Mn(L^{tri})_2]^+$ (25 µM) after cw-excitation at 410 nm in de-aerated THF (293 K) and 2-methyl-THF (77 K). (b) Luminescence at 77 K after pulsed excitation of $[Mn(L^{tri})_2]^+$ (25 µM) at 410 nm and different detection delay times but constant integration times of 1 µs. (c) Black: UV-Vis spectrum of $[Mn(L^{tri})_2]^+$ in THF at 293 K. Gray: Excitation spectrum monitoring the 600-nm emission of $[Mn(L^{tri})_2]^+$ in 2-methyl-THF at 77 K. (d) Energy-level scheme for the Mn(I) complexes; colored arrows represent emissions observed at 20 °C (green) and 77 K (red), respectively. Wavy arrows denote nonradiative relaxation processes. (e) Energy-level scheme for the $[ZnCl_2(L^{bi})]$ reference complex. Determination of the $^3\pi$-π^* energy occurred with one ruthenium- and three iridium-based triplet sensitizers with well-defined triplet energies between 2.2 and 2.7 eV.

Indeed, when exciting the Mn(I) complexes in frozen 2-methyl-THF at 77 K, one observes dual emission (red trace in Fig. 4a/S26a), with two bands with maxima at 475 and 605 nm. The higher energy band resembles the room temperature emission (green trace), but the additional low-energy band is more prominent at 77 K. In time-gated experiments at 77 K (Figs. 4b/S26b), the intensity ratio between the two bands depends strongly on the time delay used for detection, because they have very disparate decay behavior. Whilst the 475-nm emission decays within the instrumental limit (10 ns), the 605-nm luminescence has a lifetime of 118 μs for $[Mn(L^{bi})_3]^+$ and 213 μs for $[Mn(L^{tri})_2]^+$ at 77 K (Fig. S34). This low-energy emission clearly originates from the Mn(I) complexes, as the excitation spectra in Figs. 4c/S26c confirm. All of these data are in line with an MLCT state at 2.9 eV, which is responsible for the room temperature emission, and a ligand-centered $^3\pi$-π^* state at ca. 2.3 eV, which only emits at low temperatures (Fig. 4d). At 20 °C, the $^3\pi$-π^* state in the Mn(I) complexes deactivates rapidly and escapes direct detection by transient absorption spectroscopy, as noted above. Possibly, ^{3}MC states deactivate the $^3\pi$-π^* state at 20 °C.

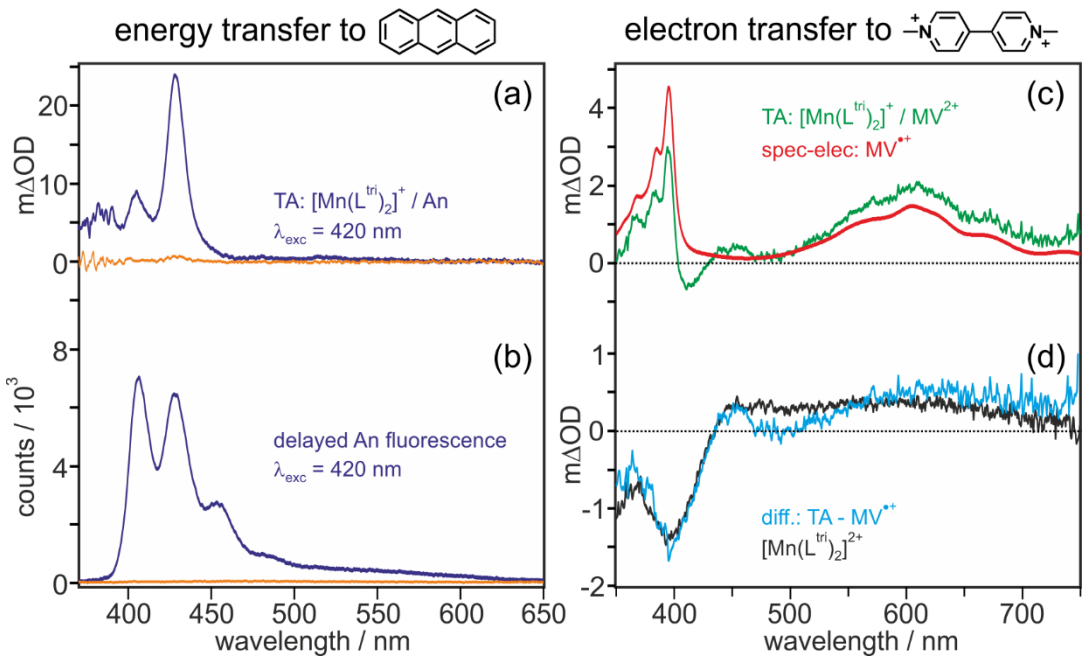

Figure 5. Photoinduced energy and electron transfer. (a) Purple: Transient absorption (TA) spectrum after excitation of $[Mn(L^{tri})_2]^+$ (25 µM) at 420 nm in presence of 40 mM anthracene (An) in de-aerated toluene. Orange: spectrum obtained under identical conditions without $[Mn(L^{tri})_2]^+$. (b) Luminescence of the two solutions used in (a). (c) Green: TA spectrum after 420-nm excitation of $[Mn(L^{tri})_2]^+$ (25 µM) in presence of 80 mM methyl viologen (MV^{2+}) in de-aerated CH_3CN. Red: UV-Vis difference spectrum upon electrochemical reduction of MV^{2+} to $MV^{\bullet+}$. (d) Blue: Difference between the red and the green spectra in (c); scaling factor chosen such that the difference between the TA spectrum of $MV^{\bullet+}$ and the spectrum of the oxidized complex was as small as possible. Black: TA difference spectrum resulting from oxidation of $[Mn(L^{tri})_2]^+$ to $[Mn(L^{tri})_2]^{2+}$, obtained after 410-nm excitation of $[Mn(L^{tri})_2]^+$ (20 µM) in presence of 1 M CCl_4 in de-aerated CH_3CN. All spectra measured at 20 °C, using pulse durations and energies of 10 ns and 6 mJ, respectively. Delay and integration times were 200 ns / 200 ns for (a), 200 ns / 500 µs for (b), 10 ns / 200 ns for (c) and (d).

With their luminescent MLCT states at 2.9 eV and ligand-centered $^3\pi$-π^* states at 2.3 eV, the new family of Mn(I) complexes resembles special cases of Ru(II) polypyridine compounds, in which there are non-equilibrated MLCT and $^3\pi$-π^* excited states (see SI pages S78-S79 for a broader discussion)[44,45]. Given this electronic structure, it seemed interesting to explore their photo-reactivities. After 420-nm excitation of the Mn(I) complexes in presence of 80 mM methyl viologen (MV^{2+}) in CH_3CN, they undergo electron transfer to form Mn(II) and $MV^{\bullet+}$ (Figs. 5c/S27c). Subtraction of the $MV^{\bullet+}$ contribution (red traces) from the transient absorption spectra (green traces) yields the blue traces in Figs. 5d/S27d. The latter are in agreement with transient difference spectra from a separate experiment, in which the Mn(I) complexes were photo-oxidized to Mn(II) in presence of CCl_4 (black traces)[46]. Based on Mn(I/II) potentials of ca. 1.0 V vs SCE (Table 1) and an energy of ca. 2.9 eV for the luminescent state (Figs. 2/S24), the excited-state oxidation potentials of $[Mn(L^{bi})_3]^+$ and $[Mn(L^{tri})_2]^+$ are ca. -1.9 V vs SCE, leading to roughly 1 eV driving-force for photoinduced electron transfer to MV^{2+}. The reductive dechlorination of CCl_4 implies that very challenging photoreductions are within reach. The MLCT luminescence of $[Mn(L^{tri})_2]^+$ is quenched with a rate constant on the order of $3 \cdot 10^9$ M^{-1} s^{-1} by MV^{2+} (SI page S63), indicating that photoinduced electron transfer to this acceptor occurs from the MLCT excited state (green box in Fig. 4d). Furthermore, we expect that the photoreduction of CCl_4 also proceeds from the MLCT (rather than the $^3\pi$-π^*) state for thermodynamic reasons, though we have been unable to perform analogous MLCT luminescence quenching studies due to the irreversibility of the electron transfer in this case.

In toluene solutions containing 40 mM anthracene and 25 μM of $[Mn(L^{bi})_3]^+$ or $[Mn(L^{tri})_2]^+$, photoinduced energy transfer is observable (Figs. 5a/S27a). Selective excitation of the

Mn(I) complexes results in the well-known triplet absorption spectrum of anthracene, which decays with lifetimes of 52-73 μs (Fig. S37). Moreover, delayed anthracene fluorescence is detectable as a consequence of triplet-triplet annihilation (Figs. 5b/S27b)[47]. These findings, together with our control experiments, provide unambiguous evidence for triplet-triplet energy transfer. Based on relative actinometry experiments with $[Ru(bpy)_3]^{2+}$ (SI pages S64-S65), the quantum efficiency of triplet energy transfer under these conditions is 9.4% for $[Mn(L^{bi})_3]^+$ and 12.1% for $[Mn(L^{tri})_2]^+$. The MLCT emission of the Mn(I) complexes remains virtually unquenched, indicating that the energy transfer to anthracene does not directly involve the MLCT state, but instead occurs from the $^3\pi$-π^* state at 2.3 eV (pink box in Fig. 4d).

In preparation of lab-scale photocatalysis experiments with our complexes, we performed photostability studies under long-term LED irradiation at 405 nm (SI page S62). In CH_2Cl_2, $[Mn(L^{bi})_3]^+$ is considerably more photo-robust than $[Mn(L^{tri})_2]^+$, and it seems possible that this is related to differences in metal-ligand bonding strengths between the two complexes. In particular, π-backbonding is significantly stronger in $[Mn(L^{bi})_3]^+$ than in $[Mn(L^{tri})_2]^+$ according to infrared spectroscopy, which shows C≡N stretches of 2120 cm^{-1} for both free ligands, compared to 2064 cm^{-1} for $[Mn(L^{bi})_3]^+$ and 2081 cm^{-1} for $[Mn(L^{tri})_2]^+$ (SI pages S53-S54). Under 440-nm irradiation of 2 mM $[Mn(L^{bi})_3]^+$ in a deaerated CD_2Cl_2 solution containing 50 mM *trans*-stilbene (with a triplet energy of 2.14 eV), the photoisomerization to *cis*-stilbene was completed to 80% in 5 hours (SI pages S68-S69), whilst a reference solution containing no Mn(I) complex did not show significant conversion. This represents successful proof-of-concept for lab-scale photocatalysis and paves the way for further applications in synthetic photochemistry[48].

Conclusions

The family of Mn(I) isocyanide complexes introduced herein have their lowest MLCT states at significantly higher energies (ca. 0.8 eV) than a recently explored (isoelectronic) Cr(0) isocyanide complex[20], mostly due to the higher metal oxidation state. The development of chelating isocyanide ligands has led to the long-sought MLCT emission from $3d^6$ metal complexes, which has been far more difficult to obtain than in Cu(I) compounds, where the lack of metal-centered excited states eliminates an important nonradiative decay channel.

The photoactive excited states of our Mn(I) isocyanides are sufficiently long-lived for bimolecular reactions, they readily engage in photoinduced electron and energy transfer reactions, and the proof-of-concept for applications in sensitized triplet-triplet annihilation and photocatalysis is made. The observable electron transfer photoreactivity can occur from the emissive MLCT state, whilst the triplet energy transfer photoreactivity originates from a ligand-centered $^3\pi$-π^* state. Unlike the previously studied Cr(0), Mo(0) and W(0) isocyanides[20,37,39,49] the Mn(I) complexes are air-stable, and regeneration of their initial state after photo-oxidation is possible with common sacrificial reagents. This opens greater perspectives for photoredox catalysis and applications in artificial photosynthesis, for example photochemical water reduction or CO_2 fixation. Further developments of Mn(I) coordination chemistry and photophysics seem desirable for this, but the foundations are now laid. The high abundance, low cost and comparatively low toxicity of many of its compounds make manganese a very attractive element.

The finding that MLCT and ligand-centered $^3\pi$-π^* states of our Mn(I) complexes can both be photoactive, including dual emission at 77 K, is unexpected and contrasts typical behavior of precious metal based compounds, where only the MLCT state is usually

emissive and photochemically relevant[50]. This fundamental insight complements recent unexpected discoveries concerning the photophysical behavior of first-row transition metal complexes, for example luminescent LMCT states in Fe(III) complexes[16,17] or dual emission from V(III) complexes[51]. It seems that the photophysics and the photochemistry of coordination chemistry is at the verge of a new era, with important implications for diverse fields and applications, ranging from light-emitting devices and dye-sensitized solar cells to synthetic photochemistry, solar fuels production, and phototherapy.

Data availability

All characterization data of new substances and pertinent experimental procedures are provided in this article and its Supplementary Information. Additional data are also available from the corresponding author on reasonable request.

References

1 Costa, R. D. *et al.* Luminescent ionic transition-metal complexes for light-emitting electrochemical cells. *Angew. Chem. Int. Ed.* **51**, 8178-8211 (2012).

2 Hagfeldt, A., Boschloo, G., Sun, L. C., Kloo, L. & Pettersson, H. Dye-sensitized solar cells. *Chem. Rev.* **110**, 6595-6663 (2010).

3 Twilton, J. *et al.* The merger of transition metal and photocatalysis. *Nat. Rev. Chem.* **1**, 0052 (2017).

4 Magnuson, A. *et al.* Biomimetic and microbial approaches to solar fuel generation. *Acc. Chem. Res.* **42**, 1899-1909 (2009).

5 Heinemann, F., Karges, J. & Gasser, G. Critical overview of the use of Ru(II) polypyridyl complexes as photosensitizers in one-photon and two-photon photodynamic therapy. *Acc. Chem. Res.* **50**, 2727-2736 (2017).

6 McCusker, J. K. Electronic structure in the transition metal block and its implications for light harvesting. *Science* **363**, 484-488 (2019).

7 Liu, Y. Z., Persson, P., Sundström, V. & Wärnmark, K. Fe N-heterocyclic carbene complexes as promising photosensitizers. *Acc. Chem. Res.* **49**, 1477-1485 (2016).

8 Zhang, W. K. *et al.* Tracking excited-state charge and spin dynamics in iron coordination complexes. *Nature* **509**, 345-348 (2014).

9 Auböck, G. & Chergui, M. Sub-50-fs photoinduced spin crossover in $Fe(bpy_3)^{2+}$. *Nat. Chem.* **7**, 629-633 (2015).

10 Carey, M. C., Adelman, S. L. & McCusker, J. K. Insights into the excited state dynamics of Fe(II) polypyridyl complexes from variable-temperature ultrafast spectroscopy. *Chem. Sci.* **10**, 134-144 (2019).

11 Zhang, K., Ash, R., Girolami, G. S. & Vura-Weis, J. Tracking the metal-centered triplet in photoinduced spin crossover of $Fe(phen)_3^{2+}$ with tabletop femtosecond M-edge X-ray absorption near-edge structure spectroscopy. *J. Am. Chem. Soc.* **141**, 17180-17188 (2019).

12 Chábera, P. *et al.* Fe^{II} hexa N-heterocyclic carbene complex with a 528 ps metal-to-ligand charge-transfer excited-state lifetime. *J. Phys. Chem. Lett.* **9**, 459-463 (2018).

13 Braun, J. D. *et al.* Iron(II) coordination complexes with panchromatic absorption and nanosecond charge-transfer excited state lifetimes. *Nat. Chem.* **11**, 1144-1150 (2019).

14 Duchanois, T. *et al.* NHC-based iron sensitizers for DSSCs. *Inorganics* **6**, 63, doi: 10.3390/inorganics6020063 (2018).

15 Förster, C. & Heinze, K. Photophysics and photochemistry with earth-abundant metals – fundamentals and concepts. *Chem. Soc. Rev.* **49**, 1057-1070 (2020).

16 Chábera, P. *et al.* A low-spin Fe^{III} complex with 100-ps ligand-to-metal charge transfer photoluminescence. *Nature* **543**, 695-699 (2017).

17 Kjær, K. S. *et al.* Luminescence and reactivity of a charge-transfer excited iron complex with nanosecond lifetime. *Science* **363**, 249-253 (2019).

18 Wood, C. J. *et al.* A comprehensive comparison of dye-sensitized NiO photocathodes for solar energy conversion. *Phys. Chem. Chem. Phys.* **18**, 10727-10738 (2016).

19 Young, E. R. & Oldacre, A. Iron Hits the Mark. *Science* **363**, 225-226 (2019).

20 Büldt, L. A., Guo, X., Vogel, R., Prescimone, A. & Wenger, O. S. A tris(diisocyanide)chromium(0) complex is a luminescent analog of Fe(2,2'-bipyridine)$_3^{2+}$. *J. Am. Chem. Soc.* **139**, 985-992 (2017).

21 Mann, K. R. *et al.* Electronic structures and spectra of hexakisphenylisocyanide complexes of Cr^0, Mo^0, W^0, Mn^I, and Mn^{II}. *Inorg. Chim. Acta* **16**, 97-101 (1976).

22 Plummer, D. T. & Angelici, R. J. Synthesis and characterization of homoleptic complexes of the chelating bidentate isocyano ligand *tert*-BuDiNC. *Inorg. Chem.* **22**, 4063-4070 (1983).

23 Treichel, P. M., Firsich, D. W. & Essenmacher, G. P. Manganese(I) and chromium(0) complexes of phenyl isocyanide. *Inorg. Chem.* **18**, 2405-2409 (1979).

24 Hamze, R. *et al.* Eliminating nonradiative decay in Cu^I emitters: >99% quantum efficiency and microsecond lifetime. *Science* **363**, 601-606 (2019).

25 Hossain, A., Bhattacharyya, A. & Reiser, O. Copper's rapid ascent in visible-light photoredox catalysis. *Science* **364**, 450-461 (2019).

26 Di, D. W. *et al.* High-performance light-emitting diodes based on carbene-metal-amides. *Science* **356**, 159-163 (2017).

27 Gernert, M. *et al.* Cyclic (amino)(aryl)carbenes enter the field of chromophore ligands: expanded π system leads to unusually deep red emitting Cu^{I} compounds. *J. Am. Chem. Soc.* **142**, 8897-8909 (2020).

28 Liu, W. P. & Ackermann, L. Manganese-catalyzed C–H activation. *ACS Catal.* **6**, 3743-3752 (2016).

29 Elangovan, S. *et al.* Efficient and selective N-alkylation of amines with alcohols catalysed by manganese pincer complexes. *Nat. Commun.* **7**, 8 (2016).

30 Mukherjee, A. *et al.* Manganese-catalyzed environmentally benign dehydrogenative coupling of alcohols and amines to form aldimines and H_2: a catalytic and mechanistic study. *J. Am. Chem. Soc.* **138**, 4298-4301 (2016).

31 Sampson, M. D. *et al.* Manganese catalysts with bulky bipyridine ligands for the electrocatalytic reduction of carbon dioxide: eliminating dimerization and altering catalysis. *J. Am. Chem. Soc.* **136**, 5460-5471 (2014).

32 Bourrez, M., Molton, F., Chardon-Noblat, S. & Deronzier, A. Mn(bipyridyl)$(CO)_3$Br : an abundant metal carbonyl complex as efficient electrocatalyst for CO_2 Reduction. *Angew. Chem. Int. Ed.* **50**, 9903-9906 (2011).

33 Zhang, Y. *et al.* Delayed fluorescence from a zirconium(IV) photosensitizer with ligand-to-metal charge-transfer excited states. *Nat. Chem.* **12**, 345-352 (2020).

34 Pal, A. K., Li, C. F., Hanan, G. S. & Zysman-Colman, E. Blue-emissive cobalt(III) complexes and their use in the photocatalytic trifluoromethylation of polycyclic aromatic hydrocarbons. *Angew. Chem. Int. Ed.* **57**, 8027-8031 (2018).

35 Harris, J. P. *et al.* Near-infrared $^2E_g \rightarrow {}^4A_{2g}$ and visible LMCT luminescence from a molecular bis-(tris(carbene)borate) manganese(IV) complex. *Can. J. Chem.* **95**, 547-552 (2017).

36 Drance, M. J. *et al.* Terminal coordination of diatomic boron monofluoride to iron. *Science* **363**, 1203-1205 (2019).

37 Sattler, W., Henling, L. M., Winkler, J. R. & Gray, H. B. Bespoke photoreductants: tungsten arylisocyanides. *J. Am. Chem. Soc.* **137**, 1198-1205 (2015).

38 Mann, K. R., Gray, H. B. & Hammond, G. S. Excited-state reactivity patterns of hexakisarylisocyano complexes of chromium(0), molybdenum(0), and tungsten(0). *J. Am. Chem. Soc.* **99**, 306-307 (1977).

39 Herr, P., Glaser, F., Büldt, L. A., Larsen, C. B. & Wenger, O. S. Long-lived, strongly emissive, and highly reducing excited states in Mo(0) complexes with chelating isocyanides. *J. Am. Chem. Soc.* **141**, 14394-14402 (2019).

40 Harris, R. K. & Mann, B. E. *NMR and the Periodic Table*. (Academic Press, 1978).

41 Brown, A. M., McCusker, C. E. & McCusker, J. K. Spectroelectrochemical identification of charge-transfer excited states in transition metal-based polypyridyl complexes. *Dalton Trans.* **43**, 17635-17646 (2014).

42 Gawelda, W. *et al.* Ultrafast nonadiabatic dynamics of $Fe^{II}(bpy)_3^{2+}$ in solution. *J. Am. Chem. Soc.* **129**, 8199-8206 (2007).

43 Murtaza, Z. *et al.* Energy-Transfer in the Inverted Region - Calculation of Relative Rate Constants by Emission Spectral Fitting. *J. Phys. Chem.* **98**, 10504-10513 (1994).

44 Baba, A. I., Shaw, J. R., Simon, J. A., Thummel, R. P. & Schmehl, R. H. The photophysical behavior of d^6 complexes having nearly isoenergetic MLCT and ligand localized excited states. *Coord. Chem. Rev.* **171**, 43-59 (1998).

45 Taffarel, E., Chirayil, S., Kim, W. Y., Thummel, R. P. & Schmehl, R. H. Coexistence of Ligand Localized and MLCT Excited States in a 2-(2‘-Pyridyl)benzo[g]quinoline Complex of Ruthenium(II). *Inorg. Chem.* **35**, 2127-2131 (1996).

46 Anne, A., Hapiot, P., Moiroux, J., Neta, P. & Savéant, J. M. Oxidation of 10-methylacridan, a synthetic analog of NADH, and deprotonation of its cation radical - convergent application of laser flash-photolysis and direct and redox catalyzed electrochemistry to the kinetics of deprotonation of the cation radical. *J. Phys. Chem.* **95**, 2370-2377 (1991).

47 Singh-Rachford, T. N. & Castellano, F. N. Photon upconversion based on sensitized triplet-triplet annihilation. *Coord. Chem. Rev.* **254**, 2560-2573 (2010).

48 Strieth-Kalthoff, F., James, M. J., Teders, M., Pitzer, L. & Glorius, F. Energy transfer catalysis mediated by visible light: principles, applications, directions. *Chem. Soc. Rev.* **47**, 7190-7202 (2018).

49 Kvapilova, H. *et al.* Electronic excited states of tungsten(0) arylisocyanides. *Inorg. Chem.* **54**, 8518-8528 (2015).

50 Arias-Rotondo, D. M. & McCusker, J. K. The photophysics of photoredox catalysis: a roadmap for catalyst design. *Chem. Soc. Rev.* **45**, 5803-5820 (2016).

51 Dorn, M. *et al.* A vanadium(III) complex with blue and NIR-II spin-flip luminescence in solution. *J. Am. Chem. Soc.* **142**, 7947-7955 (2020).

Acknowledgements

O. S. W. thanks the Swiss National Science Foundation (grant number 200021_178760) for financial support. C. K. acknowledges a Novartis University of Basel Excellence Scholarship for Life Sciences.

Author contributions

P. H. carried out synthetic, spectroscopic and electrochemical work and analyzed data, C. K. provided guidance in spectroscopic work, designed photochemical studies, and helped in data analysis, C. B. L. provided guidance in synthetic, spectroscopic and electrochemical work, D. H. performed NMR studies, O. S. W. conceived the project and provided guidance. All authors contributed to the writing and editing of the manuscript and have given approval to its final version.

Supporting Information to:

Manganese(I) complexes with metal-to-ligand charge transfer luminescence and photoreactivity

Patrick Herr, Christoph Kerzig, Christopher B. Larsen, Daniel Häussinger and Oliver S. Wenger*

Department of Chemistry, University of Basel, St. Johanns-Ring 19, 4056 Basel, Switzerland

Table of contents

Reaction schemes

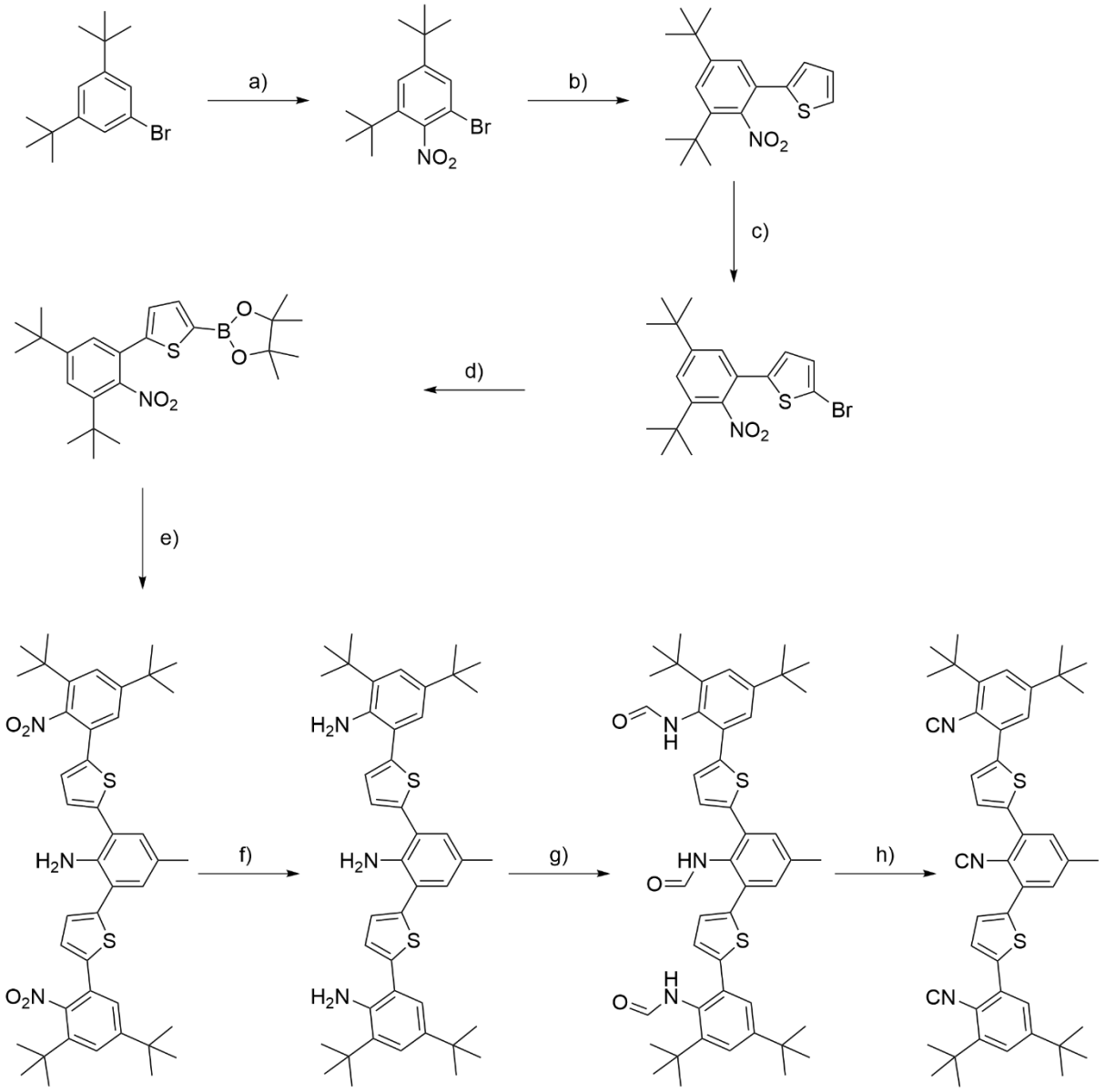

Scheme S1. Synthesis of the tridentate ligand $\mathbf{L^{tri}}$: a) AcOH, H_2SO_4 and HNO_3 (fuming), 80 °C, 1.5 h; b) thiophene-2-boronic acid pinacol ester, K_2CO_3, $[Pd(dppf)Cl_2]\cdot CH_2Cl_2$ in a mixture of toluene, EtOH and H_2O, microwave, 140 °C, 30 min; c) NBS in DMF, 60 °C, 16 h; d) bis(pinacolato)diboron, KOAc, $[Pd(dppf)Cl_2]\cdot CH_2Cl_2$ in DMSO, 85 °C, 16 h; e) 2,6-dibromo-4-methylaniline, K_2CO_3, $[Pd(dppf)Cl_2]\cdot CH_2Cl_2$ in a mixture of toluene, EtOH and H_2O; f) Zn, $N_2H_4\cdot H_2O$ in MeOH, 70 °C, 3 days; g) Ac_2O, formic acid, 100 °C, 16 h; h) $POCl_3$, NEt_3 in CH_2Cl_2, rt, 16 h.

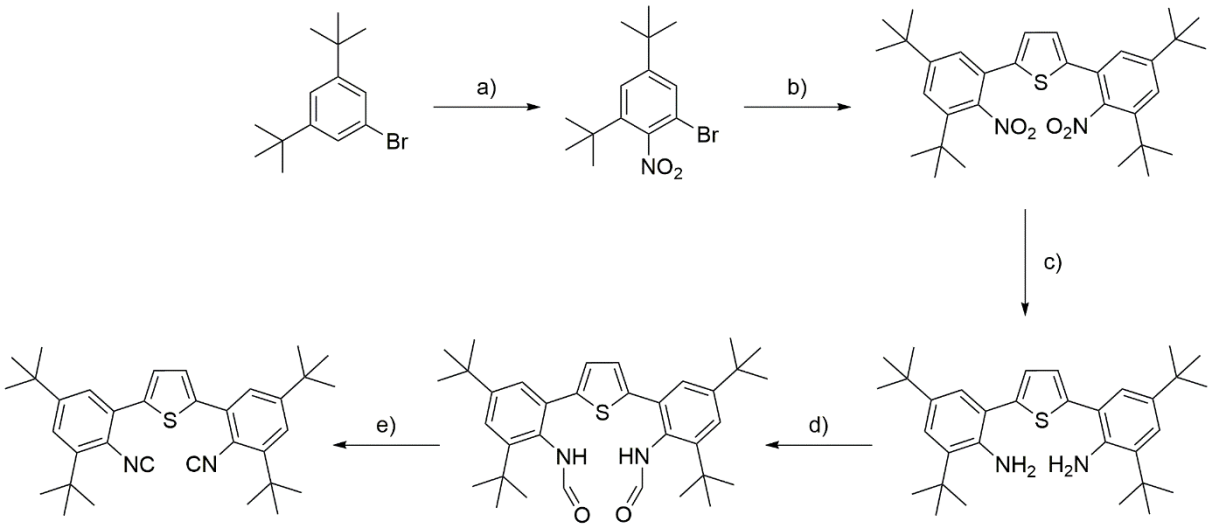

Scheme S2. Synthesis of the bidentate ligand $\mathbf{L^{bi}}$: a) AcOH, H_2SO_4 and HNO_3 (fuming), 80 °C, 1.5 h; b) 2,5-bis(tri-*n*-butylstannyl)thiophene, $[Pd(dppf)Cl_2]\cdot CH_2Cl_2$ in xylene, 140 °C, 16 h; c) Zn, $N_2H_4\cdot H_2O$ in MeOH, 70 °C, 16 h; d) Ac_2O, formic acid, 100 °C, 16 h; e) $POCl_3$, di(iso-propyl)amine in CH_2Cl_2, rt, 3 h.

Synthesis

1-bromo-3,5-di-*tert*-butyl-2-nitrobenzene **1**

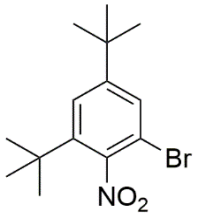

Following a previously published method[1], 1-bromo-3,5-di-*tert*-butylbenzene (15 g, 55.7 mmol) was dissolved in a mixture of glacial acetic acid (150 mL) and concentrated sulfuric acid (84 mL) at 50 °C. Fuming nitric acid (10 mL) was added and the solution was stirred at 80 °C for 90 min. The reaction mixture was poured into ice water and extracted with dichloromethane. The organic phase was washed with water and dried over anhydrous Na_2SO_4. The solvent was removed under reduced pressure. **1** (12.3 g, 39 mmol, 70 %) was obtained by crystallization from ethanol as a white solid.

^{1}H-NMR (400 MHz, $CDCl_3$): δ 7.50 (d, J = 2.0 Hz, 1 H), 7.49 (d, J = 2.0 Hz, 1 H), 1.38 (s, 9 H), 1.32 (s, 9 H) ppm.

2-(3,5-di-*tert*-butyl-2-nitrophenyl)thiophene **2**

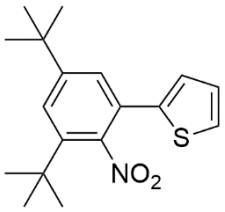

1 (1.5 g, 4.77 mmol), 4,4,5,5-tetramethyl-2-(2-thienyl)-1,3,2-dioxaborolan (1.1 g, 5.25 mmol) and K_2CO_3 (3.3 g, 23.9 mmol) were dissolved in a mixture of toluene (10 mL), water (5 mL) and ethanol (2.5 mL). The solution was bubbled with nitrogen for 10 min before $[Pd(dppf)Cl_2]\cdot CH_2Cl_2$ (39 mg, 48 µmol) was added. The mixture was heated to 140 °C for 30 min under microwave conditions. The reaction mixture was quenched with a sat. aq. NH_4Cl solution. The organic phase was separated, dried over Na_2SO_4 and filtered through a short silica column. The solvent was removed under reduced pressure to afford **2** (1.5 g, 4.7 mmol, 99 %) as a pale yellow solid.

^{1}H-NMR (400 MHz, $CDCl_3$): δ 7.56 (d, *J* = 2.1 Hz, 1 H), 7.37 (dd, *J* = 5.0, 1.3 Hz, 1 H), 7.34 (d, *J* = 2.1 Hz, 1 H), 7.07 – 7.03 (m, 2 H), 1.42 (s, 9 H), 1.35 (s, 9 H) ppm.

^{13}C-NMR (126 MHz, $CDCl_3$): δ 152.4, 147.7, 140.1, 137.7, 127.6, 127.5, 127.2, 127.0, 126.9, 125.2, 36.3, 35.2, 31.3, 31.1 ppm.

IR: ν 2964.6 (m), 2872.0 (w), 1527.6 (m), 1365.6 (m), 1244.1 (w), 1203.6 (w), 881.5 (w), 856.4 (w), 842.9 (m), 831.3 (m), 702.1 (m), 694.4 (m) cm^{-1}.

ESI-HRMS (*m/z*) calcd for $C_{18}H_{23}NO_2S+Na^+$: 340.1342. Found: 340.1336.

Anal. calcd for $C_{18}H_{23}NO_2S$: C, 68.11; H, 7.30; N, 4.41. Found: C, 67.81; H, 7.45; N, 4.55.

mp: 102 °C.

2-bromo-5-(3,5-di-*tert*-butyl-2-nitrophenyl)thiophene **3**

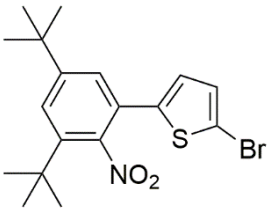

2 (4.44 g, 14 mmol) and *N*-bromosuccinimide (3.24 g, 18.2 mmol) were dissolved in DMF (60 mL) and stirred at 60 °C for 16 h. The reaction mixture was poured into water. The precipitate was collected by filtration and washed with water. After drying, **3** (5.25 g, 13.5 mmol, 97 %) was obtained as a beige solid.

^{1}H-NMR (400 MHz, $CDCl_3$): δ 7.57 (d, *J* = 2.0 Hz, 1 H), 7.28 (d, *J* = 2.0 Hz, 1 H), 6.99 (d, *J* = 3.9 Hz, 1 H), 6.81 (d, *J* = 3.9 Hz, 1 H), 1.41 (s, 9 H), 1.34 (s, 9 H) ppm.

^{13}C-NMR (126 MHz, $CDCl_3$): δ 152.6, 147.5, 140.3, 139.2, 130.5, 127.6, 126.8, 126.6, 125.8, 113.5, 36.3, 35.2, 31.3, 31.1 ppm.

IR: ν 2960.7 (m), 2926.0 (w), 2872.0 (w), 1587.4 (w), 1525.7 (m), 1442.8 (w), 1365.6 (m), 1242.2 (w), 1201.7 (w), 964.4 (m), 883.4 (w), 842.9 (w), 804.3 (m), 796.6 (m), 655.8 (w), 613.4 (w), 594.1 (w), 497.6 (w) cm^{-1}.

ESI-HRMS (*m/z*) calcd for $C_{18}H_{22}NO_2BrS+NH_4^+$: 413.0893. Found: 413.0886.

Anal. calcd for $C_{18}H_{22}NO_2BrS$: C, 54.55; H, 5.60; N, 3.53. Found: C, 54.83; H, 5.65; N, 3.72.

mp: 121 °C.

2-(5-(3,5-di-*tert*-butyl-2-nitrophenyl)thiophen-2-yl)-4,4,5,5-tetramethyl-1,3,2-dioxaborolane **4**

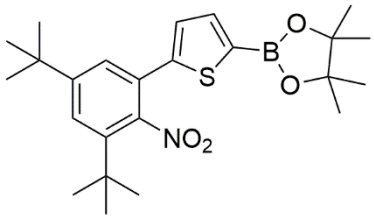

3 (7.52 g, 19 mmol), bis(pinacolato)diboron (6.26 g, 24.7 mmol) and KOAc (9.3 g, 95 mmol) were dissolved in dry DMSO (80 mL) in a dried flask. The solution was bubbled with nitrogen for 15 min before $[Pd(dppf)Cl_2]\cdot CH_2Cl_2$ (310 mg, 380 µmol) was added. The reaction mixture was heated to 85 °C for 16 h before it was poured into water. The precipitate was collected by filtration and washed with water. The crude product was dissolved in dichloromethane, dried over Na_2SO_4 and filtered over a short silica column. The solvent was removed under reduced pressure to afford **4** (8.33 g, 18.8 mmol, 99 %) as a beige solid.

^{1}H-NMR (500 MHz, CD_2Cl_2): δ 7.62 (d, *J* = 2.0 Hz, 1 H), 7.51 (d, *J* = 3.6 Hz, 1 H), 7.39 (d, *J* = 1.9 Hz, 1 H), 7.12 (d, *J* = 3.6 Hz, 1 H), 1.42 (s, 9 H), 1.36 (s, 9 H), 1.35 (s, 12 H) ppm.

^{13}C-NMR (126 MHz, CD_2Cl_2): δ 153.1, 147.6, 145.0, 140.5, 137.7, 128.6, 127.6, 127.3, 126.0, 84.7, 36.5, 35.5, 31.3, 31.1, 25.0 ppm.

IR: ν 2966.5 (m), 2872.0 (w), 1527.6 (m), 1467.8 (m), 1373.3 (m), 1365.6 (m), 1309.7 (m), 1269.2 (w), 1138.0 (m), 1074.4 (w), 883.4 (w), 846.8 (m), 819.8 (m), 665.4 (m) cm^{-1}.

ESI-HRMS (*m/z*) calcd for $C_{24}H_{34}NO_4BS+Na^+$: 466.2194. Found: 466.2195.

Anal. calcd for $C_{24}H_{34}NO_4BS$: C, 65.01; H, 7.73; N, 3.16. Found: C, 65.24; H, 7.68; N, 3.54.

mp: 125 °C.

2,6-bis(5-(3,5-di-*tert*-butyl-2-nitrophenyl)thiophen-2-yl)-4-methylaniline **5**

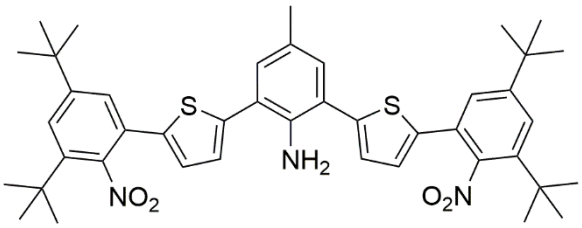

4 (1.35 g, 3.04 mmol), 2,6-dibromo-4-methylaniline (403 mg, 1.52 mmol) and K_2CO_3 (1.05 g, 7.6 mmol) were dissolved in a mixture of toluene (10 mL), water (5 mL) and ethanol (2.5 mL). The solution was bubbled with nitrogen for 10 min before $[Pd(dppf)Cl_2]\cdot CH_2Cl_2$ (50 mg, 61 µmol) was added. The mixture was heated to 140 °C for 30 min under microwave conditions. The reaction was quenched with a sat. aq. NH_4Cl solution. The organic phase was separated, dried over Na_2SO_4 and filtered through a short silica column. The product was purified by column chromatography (silica, gradient from 2:1 (v/v) pentanes/dichloromethane to pure dichloromethane). The solvent was removed under reduced pressure to afford **5** (0.67 g, 0.91 mmol, 60 %) as a light yellow, fluffy solid.

^{1}H-NMR (400 MHz, CD_2Cl_2): δ 7.61 (d, *J* = 1.9 Hz, 2 H), 7.43 (d, *J* = 1.9 Hz, 2 H), 7.19 (d, *J* = 3.6 Hz, 2 H), 7.14 (s, 2 H), 7.06 (d, *J* = 3.6 Hz, 2 H), 2.29 (s, 3 H), 1.43 (s, 18 H), 1.37 (s, 18 H) ppm.

^{13}C-NMR (126 MHz, $CDCl_3$): δ 152.5, 147.5, 142.5, 140.3, 139.1, 137.8, 131.8, 127.9, 127.5, 127.3, 127.0, 126.9, 125.3, 120.6, 36.3, 35.3, 31.3, 31.1, 20.4 ppm.

IR: ν 2962.7 (m), 2872.0 (w), 1589.3 (w), 1529.6 (m), 1462.0 (m), 1373.3 (m), 1365.6 (m), 842.9 (m), 819.8 (m), 657.7 (w) cm^{-1}.

ESI-HRMS (*m/z*) calcd for $C_{43}H_{51}N_3O_4S_2+H^+$: 738.3394. Found: 738.3389.

Anal. calcd for $C_{43}H_{51}N_3O_4S_2$: C, 69.98; H, 6.97; N, 5.69. Found: C, 69.97; H, 7.22; N, 5.54.

mp: 124 °C.

6,6'-((2-amino-5-methyl-1,3-phenylene)bis(thiophene-5,2-diyl))bis(2,4-di-*tert*-butylaniline) **6**

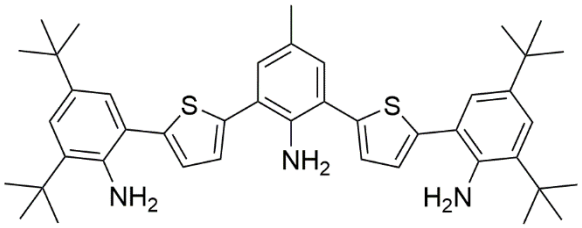

A suspension of **5** (1.40 g, 1.9 mmol), freshly activated zinc powder (496 mg, 7.6 mmol) and hydrazine (3.54 mL, 65 %wt, 47.4 mmol) in methanol was stirred at 70 °C for 3 days. The reaction mixture was quenched with brine and extracted with dichloromethane. The organic phase was filtered over celite, dried over Na_2SO_4 and the solvent was removed under reduced pressure to afford **6** (1.25 g, 1.84 mmol, 97 %) as a brown, fluffy powder.

^{1}H-NMR (400 MHz, CD_2Cl_2): δ 7.32 (d, *J* = 2.3 Hz, 2 H), 7.26 (d, *J* = 3.6 Hz, 2 H), 7.19 - 7.18 (m, 4 H), 7.15 (s, 2 H), 4.47 (s, 2 H), 4.23 (s, 4 H), 2.30 (s, 3 H), 1.47 (s, 18 H), 1.30 (s, 18 H) ppm.

^{13}C-NMR (126 MHz, CD_2Cl_2): δ 142.7, 141.4, 140.6, 140.5, 140.0, 133.9, 131.6, 127.7, 127.4, 127.0, 126.5, 124.5, 121.0, 120.9, 35.1, 34.5, 31.7, 30.0, 20.4 ppm.

IR: ν 3491.2 (w), 3379.3 (w), 2958.8 (m), 287.01 (w), 1612.5 (m), 1591.3 (m), 1529.6 (m), 1462.0 (m), 1442.8 (m), 1363.7 (m), 1240.2 (m), 1197.8 (w), 881.5 (w), 819.8 (m), 812.0 (m) cm^{-1}.

ESI-HRMS (*m/z*) calcd for $C_{43}H_{55}N_3S_2+H^+$: 678.3910. Found: 678.3903.

Anal. calcd for $C_{43}H_{55}N_3S_2 \cdot 0.5H_2O$: C, 75.17; H, 8.22; N, 6.12. Found: C, 75.34; H, 8.20; N, 6.11.

mp: 132 °C.

N,N'-(((2-formamido-5-methyl-1,3-phenylene)bis(thiophene-5,2-diyl))bis(4,6-di-*tert*-butyl-2,1-phenylene))diformamide **7**

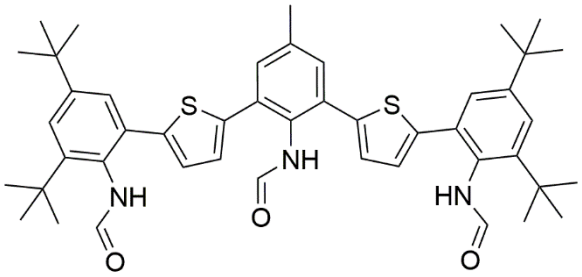

Formic acid (10.5 mL) was slowly added to acetic anhydride (21 mL) at 0 °C. The mixture was stirred at 50 °C for 2 h. After cooling to 0 °C, **6** (1.25 g, 1.84 mmol) was added and the reaction mixture was stirred at 100 °C for 16 h. Ice water was added and the precipitate was collected by filtration. After washing with water, the crude product was dissolved in dichloromethane. The organic phase was dried over Na_2SO_4 and the solvent was removed under reduced pressure. ESI-MS showed two mass peaks: **7**+Na^+ (*m/z* = 784.0, minor) and **7**+CO+Na^+ (m/z = 812.0, major), indicating the installment of 3 formamides (mass peak at 784.0) and additional (undesired) formylation of one formamide group (mass peak at 812.0).

This crude material was stirred in a mixture of formic acid (40 mL) and water (2 mL) at 80 °C for 16 h to remove the additional (undesired) formyl group of the **7**+CO product detected by mass spectrometry. Ice water was added and the precipitate was collected by filtration. After washing with water, the crude product was dissolved in dichloromethane. The organic phase was dried over Na_2SO_4 and the solvent was removed under reduced pressure to afford **7** (1.33 g, 1.75 mmol, 95 %) as a brown, fluffy solid. The product was used without further purification. Due to different possible rotamers for each of the three formamide groups, NMR spectra show a complicated mixture of isomers.

^{1}H-NMR (400 MHz, CD_2Cl_2): δ 8.88 - 7.00 (m, 16 H), 2.45 - 2.24 (m, 3 H), 1.46 - 1.32 (m, 36 H) ppm.

^{13}C-NMR (126 MHz, CD_2Cl_2): δ 166.3, 166.2, 166.1, 166.0, 165.9, 165.8, 165.5, 163.4, 163.3, 163.1, 162.9, 162.7, 162.2, 151.3 - 151.0 (multiple signals), 148.4 - 148.0 (multiple signals), 143.7, 143.0 - 141.6 (multiple signals), 140.9, 140.3, 140.1, 139.8, 138.6 - 138.4 (multiple signals), 135.3 - 134.1 (multiple signals), 133.2, 132.8, 131.8, 131.6, 131.1 - 130.9 (multiple signals), 129.9 - 129.4 (multiple signals), 128.6 - 126.4

(multiple signals), 125.1 - 124.9 (multiple signals), 120.9, 120.8, 120.7, 36.2 - 36.0 (multiple signals), 35.3, 35.2, 21.2 ppm.

IR: ν 3485.4 (w), 3373.5 (w), 3236.6 (w), 2958.8 (m), 2906.7 (w), 2870.1 (w), 1680.0 (m), 1593.2 (w), 1529.6 (m), 1464.0 (m), 1363.7 (m), 1242.2 (w), 1200.0 (w), 879.5 (w), 810.1 (w), 590.2 (w) cm^{-1}.

ESI-HRMS (*m/z*) calcd for $C_{46}H_{55}N_3O_3S_2+Na^+$: 784.3577. Found: 784.3567.

Anal. calcd for $C_{46}H_{55}N_3O_3S_2 \cdot 0.5H_2O$: C, 71.65; H, 7.32; N, 5.45. Found: C, 71.54; H, 7.50; N, 5.38.

mp: 184 °C.

5,5'-(2-isocyano-5-methyl-1,3-phenylene)bis(2-(3,5-di-*tert*-butyl-2-isocyanophenyl)thiophene) **L^{tri}**

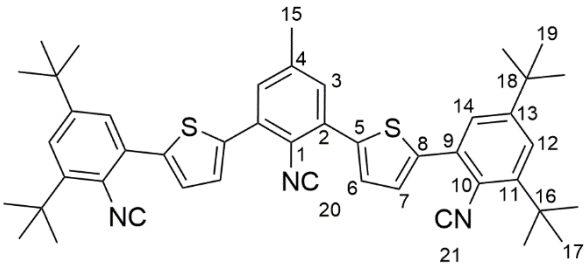

7 (150 mg, 0.2 mmol) was dissolved in dry dichloromethane (10 mL) under an argon atmosphere. Dry triethylamine (0.68 mL, 4.9 mmol) was added and the solution was cooled to 0 °C. $POCl_3$ (0.37 mL, 3.9 mmol) was added dropwise. The reaction mixture was stirred at rt for 16 h before it was quenched with an aqueous Na_2CO_3 solution. The aqueous phase was extracted with dichloromethane. The organic phase was dried over Na_2SO_4 and the solvent was removed under reduced pressure. The crude product was purified by column chromatography (silica, gradient from 3:1 (v/v) pentanes/dichloromethane to 1:2 (v/v) pentanes/dichloromethane). **L^{tri}** (98 mg, 0.14 mmol, 70 %) was obtained as a light beige, fluffy solid.

^{1}H-NMR (400 MHz, CD_2Cl_2): δ 7.60 (d, *J* = 3.8 Hz, H-7, 2 H), 7.52 (d, *J* = 2.1 Hz, H-12, 2 H), 7.47 (d, *J* = 2.1 Hz, H-14, 2 H), 7.45 (s, H-3, 2 H), 7.44 (d, *J* = 3.8 Hz, H-6, 2 H), 2.46 (s, H-15, 3 H), 1.58 (s, H-17, 18 H), 1.37 (s, H-19, 18 H) ppm.

^{13}C-NMR (126 MHz, CD_2Cl_2): δ 174.65 (C-21), 173.67 (C-20), 152.82 (C-13), 146.91 (C-11), 141.71 (C-8), 140.72 (C-4), 139.82 (C-5), 133.33 (C-9), 132.86 (C-2), 131.06 (C-3), 129.17 (C-6), 129.05 (C-7), 126.58 (C-14), 124.62 (C-12), 121.28 (C-10), 119.42 (C-1, from HMBC cross signal), 36.16 (C-16), 35.60 (C-18), 31.40 (C-19), 29.65 (C-17), 21.62 (C-15) ppm.

IR: ν 2962.2 (m), 2873.0 (w), 2109.7 (m), 1594.0 (w), 1469.1 (w), 1434.1 (w), 1407.8 (w), 1365.1 (w), 1281.7 (w), 1242.4 (w), 1202.3 (w), 885.6 (w), 859.4 (w), 804.5 (m), 755.9 (w), 657.6 (w), 622.0 (w) cm^{-1}.

ESI-HRMS (*m/z*) calcd for $C_{46}H_{49}N_3S_2+Na^+$: 730.3260. Found: 730.3262.

Anal. calcd for $C_{46}H_{49}N_3S_2 \cdot 0.5H_2O$: C, 77.05; H, 7.03; N, 5.86. Found: C, 76.79; H, 7.10; N, 5.46.

mp: 96 °C.

$[Mn(L^{tri})_2]PF_6$

L^{tri} (52.8 mg, 74.5 µmol) and $[Mn(CO)_5Br]$ (10 mg, 36.4 µmol) were dissolved in THF (5 mL) under an inert gas atmosphere. The reaction mixture was heated to reflux for 16 h. A saturated aqueous solution of KPF_6 was added and the precipitate was separated by filtration. The crude product was washed with water and dissolved in dichloromethane. The organic phase was separated, dried over Na_2SO_4 and the solvent was removed under reduced pressure. The product was purified by recrystallization from cyclohexane to afford $[Mn(L^{tri})_2]PF_6$ (24 mg, 15 µmol, 41 %) as a yellow to light orange solid.

^{1}H-NMR (600 MHz, CD_2Cl_2): δ 7.58 (s, H-3, 4 H), 7.43 (d, *J* = 2.2 Hz, H-14, 4 H), 7.39 (d, *J* = 2.2 Hz, H-12, 4 H), 7.08 (d, *J* = 3.5 Hz, H-6, 4 H), 7.00 (d, *J* = 3.5 Hz, H-7, 4 H), 2.59 (s, H-15, 6 H), 1.29 (s, H-19, 36 H), 1.28 (s, H-17, 36 H) ppm.

^{13}C-NMR (151 MHz, CD_2Cl_2): δ 180.85 (C-20), 178.59 (C-21), 152.24 (C-13), 146.56 (C-11), 141.22 (C-8), 139.95 (C-4), 139.35 (C-5), 133.63 (C-9), 132.98 (C-2), 130.27 (C-3), 128.76 (C-6), 127.43 (C-7), 125.63 (C-14), 125.20 (C-1), 124.78 (C-12), 124.00 (C-10), 36.02 (C-16), 35.56 (C-18), 31.33 (C-19), 30.01 (C-17), 21.87 (C-15).

^{55}Mn-NMR (148.5 MHz, CD_2Cl_2): δ -1419 (s, 1 Mn) ppm.

IR: ν 2961.1 (w), 2927.6 (w), 2871.2 (w), 2108.5 (w), 2073.7 (m), 1593.5 (w), 1465.7 (w), 1431.7 (w), 1364.8 (w), 1243.1 (w), 1202.6 (w), 884.6 (w), 840.1 (m), 805.7 (m), 756.6 (w), 700.8 (w), 656.4 (w) cm^{-1}.

ESI-HRMS (*m/z*) calcd for $C_{92}H_{98}N_6MnS_4^+$: 1469.6144. Found: 1469.6136.

Anal. calcd for $C_{92}H_{98}N_6F_6MnPS_4$: C, 68.38; H, 6.11; N, 5.20. Found: C, 67.97; H, 6.64; N, 5.46.

mp: > 250 °C.

2,5-bis(3,5-di-tert-butyl-2-nitrophenyl)thiophene **8**

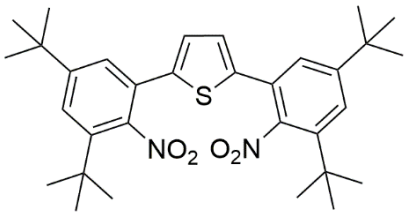

1 (1.22 g, 3.89 mmol) was dissolved in xylene (20 mL) and the solution was bubbled with nitrogen. 2,5-Bis(tri-*n*-butylstannyl)thiophene (1.00 g, 1.55 mmol, 0.86 mL) and $[Pd(dppf)Cl_2]\cdot CH_2Cl_2$ (63 mg, 0.07 mmol) were added to the reaction mixture. The mixture was stirred at 140 °C for 16 h. The solvent was removed and the crude product was purified by column chromatography (silica, gradient from pentanes to 1:1 (v/v) pentanes/dichloromethane) to afford **8** (834 mg, 1.51 mmol, 98 %) as a bright yellow solid.

^{1}H-NMR (400 MHz, CD_2Cl_2): δ 7.62 (d, *J* = 1.9 Hz, 2 H), 7.41 (d, *J* = 1.9 Hz, 2 H), 6.98 (s, 2 H), 1.43 (s, 18 H), 1.37 (s, 18H) ppm.

^{13}C-NMR (101 MHz, CD_2Cl_2): δ 153.3, 147.8, 140.7, 139.7, 127.8, 127.5, 127.2, 126.2, 36.7, 35.6, 31.4, 31.2 ppm.

IR: ν 2960.7 (m), 2872.0 (w), 1525.7 (m), 1469.8 (w), 1365.6 (m), 1246.0 (w), 881.5 (m), 844.8 (m), 815.9 (w), 615.3 (w) cm^{-1}.

ESI-HRMS (*m/z*) calcd for $C_{32}H_{42}N_2O_4S+Na^+$: 573.2757. Found: 573.2756.

Anal. calcd for $C_{32}H_{42}N_2O_4S\cdot 0.5H_2O$: C, 68.66; H, 7.74; N, 5.00. Found: C, 68.89; H, 7.64; N, 5.14.

mp: 242 °C.

6,6'-(thiophene-2,5-diyl)bis(2,4-di-tert-butylaniline) **9**

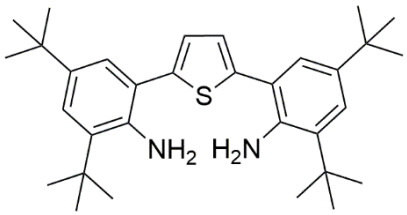

Hydrazine monohydrate (1.86 g, 37.2 mmol, 1.80 mL) was added to a suspension of **8** (755 mg, 1.45 mmol) and zinc powder (388 mg, 5.88 mmol) in dry MeOH (5 mL). The mixture was heated to reflux for 16 h. The yellow suspension was diluted with dichloromethane, filtered over celite and washed with brine. The light green organic phase was dried over Na_2SO_4 and the solvent was removed under reduced pressure to afford **9** (708 mg, 1.44 mmol, 99 %) as a green-yellow solid. **9** was used without further purification.

^{1}H-NMR (400 MHz, CD_2Cl_2): δ 7.32 (d, *J* = 2.3 Hz, 2 H), 7.18 (d, *J* = 2.3 Hz, 2 H), 7.16 (s, 2 H), 4.24 (s, 4 H), 1.48 (s, 18 H), 1.31 (s, 18 H) ppm.

^{13}C-NMR (101 MHz, CD_2Cl_2): δ 142.7, 140.8, 140.5, 133.9, 127.3, 126.6, 124.5, 121.2, 35.3, 34.6, 31.9, 30.1 ppm.

IR: ν 3498.9 (w), 3394.7 (w), 2956.9 (m), 2906.7 (w), 2870.1 (w), 1612.5 (m), 1599.0 (w), 1477.5 (w), 1462.0 (w), 1440.8 (m), 1361.7 (w), 1259.5 (w), 1240.2 (m), 1195.9 (w), 883.4 (w), 808.2 (w), 642.3 (w) cm^{-1}.

ESI-HRMS (*m/z*) calcd for $C_{32}H_{46}N_2S+H^+$: 491.3454. Found: 491.3457.

Anal. calcd for $C_{32}H_{46}N_2S \cdot 1H_2O$: C, 75.54; H, 9.51; N, 5.51. Found: C, 75.76; H, 9.38; N, 5.51.

mp: 198 °C.

N,N'-(thiophene-2,5-diylbis(4,6-di-tert-butyl-2,1-phenylene))diformamide **10**

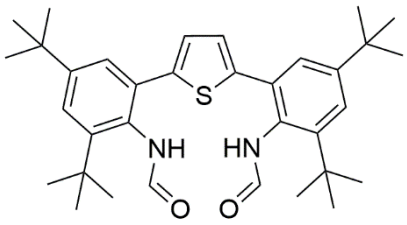

Formic acid (7.80 mL, 207 mmol) was added dropwise to acetic anhydride (15.6 mL, 165 mmol) within 10 min at 0 °C. The mixture was allowed to warm to rt and stirred at 50 °C for 2 h. After reaching rt, the mixture was cooled to 0 °C and **9** (708 mg, 1.44 mmol) was added. The mixture was stirred at 100 °C for 16 h. Ice water (45 mL) was added, the precipitate collected by filtration and washed with water (300 mL). The precipitate was dissolved in dichloromethane. The organic phase was dried over Na_2SO_4 and the solvent was removed under reduced pressure to afford **10** (612mg, 1.12 mmol, 80 %) as a white solid.

The product was isolated as a mixture of isomers (formamide rotamers) leading to a complex NMR spectrum.

^{1}H-NMR (400 MHz, CD_2Cl_2): δ 9.04 - 6.74 (m, 10 H), 1.46 - 1.33 (m, 36 H) ppm.

^{13}C-NMR (126 MHz, CD_2Cl_2): δ 165.7, 162.4, 151.3, 151.1, 148.5, 148.4, 148.0, 147.8, 143.3, 142.6, 141.6, 135.3, 134.8, 134.5, 129.8, 129.6, 128.3, 127.9, 127.6, 127.1, 126.8, 126.6, 126.5, 125.1, 124.9, 36.7, 36.2, 36.1, 35.3, 35.2, 31.5 - 31.2 (multiple signals) ppm.

IR: ν 3174.8 (w), 2960.7 (m), 2906.7 (w), 2870.1 (w), 1678.1 (m), 1477.5 (w), 1363.7 (w), 1288.5 (w), 1246.0 (w), 1201.7 (w), 1166.9 (w), 879.5 (w), 819.8 (w), 725.2 (w), 653.9 (w), 493.8 (w) cm^{-1}.

ESI-HRMS (*m/z*) calcd for $C_{34}H_{46}N_2O_2S+Na^+$: 569.3172. Found: 569.3172.

Anal. calcd for $C_{34}H_{46}N_2O_2S \cdot 1H_2O$: C, 72.30; H, 8.57; N, 4.96. Found: C, 72.57; H, 8.27; N, 4.85.

mp: 148 °C.

2,5-bis(3,5-di-tert-butyl-2-isocyanophenyl)thiophene **L^{bi}**

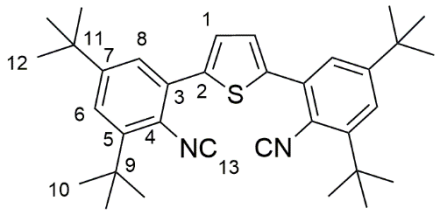

10 (612 mg, 1.12 mmol) was dissolved in dry dichloromethane (35 mL) under an argon atmosphere. Di(iso-propyl)amine (1.06 mL, 7.84 mmol) was added and the mixture cooled to 0 °C. $POCl_3$ (0.42 mL, 3.9 mmol) was added dropwise. The solution turned dark yellow and was allowed to warm to rt. After stirring for 3 h, a solution of Na_2CO_3 in water (1.5 M, 26.4 mL) was added and the biphasic system was vigorously stirred for 16 h. Saturated aqueous $NaHCO_3$ solution (23.2 mL) was added and the aqueous phase was extracted with dichloromethane. The organic phase was dried over Na_2SO_4 and the solvent removed under reduced pressure. The crude product was purified by column chromatography (silica, gradient from 20:1 (v/v) pentanes/DCM to 1:1 (v/v) pentanes/DCM) to afford **L^{bi}** (260 mg, 0.510 mmol, 45 %) as a yellow oil, which slowly solidifies to form a light yellow solid.

^{1}H-NMR (400 MHz, CD_2Cl_2): δ 7.50 (d, *J* = 2.1 Hz, 6-H, 2 H), 7.45 (d, *J* = 2.1 Hz, 8-H, 2 H), 7.42 (s, 1-H, 2 H), 1.57 (s, 10-H, 18 H), 1.35 (s, 12-H, 18 H) ppm.

^{13}C-NMR (101 MHz, CD_2Cl_2): δ 174.5 (C-13), 152.8 (C-7), 146.9 (C-5), 141.1 (C-3), 133.6 (C-2), 128.8 (C-1), 126.5 (C-8), 124.5 (C-6), 121.2 (C-4, from HMBC cross peak), 36.1 (C-9), 35.6 (C-11), 31.4 (C-12), 29.7 (C-10) ppm.

IR: ν 2961.8 (m), 2874.0 (w), 2113.1 (m), 1593.2 (w), 1409.0 (w), 1364.7 (m), 1281.7 (w), 1247.0 (w), 886.3 (m), 798.0 (m), 762.9 (w), 657.7 (m) cm^{-1}.

ESI-HRMS (m/z) calcd for $C_{34}H_{42}N_2S+Na^+$: 533.2961. Found: 533.2958.

Anal. calcd for $C_{34}H_{42}N_2S$: C, 79.95; H, 8.29; N, 5.48. Found: C, 79.54; H, 8.50; N, 5.39.

mp: 88 °C.

$[Mn(L^{bi})_3]PF_6$

L^{bi} (94.8 mg, 282 µmol) and $[Mn(CO)_5Br]$ (25 mg, 91 µmol) were dissolved in THF (5 mL) under an inert gas atmosphere. The reaction mixture was heated to reflux for 16 h. A saturated aqueous solution of KPF_6 was added and the precipitate was separated by filtration. The crude product was washed with water and dissolved in dichloromethane. The organic phase was separated, dried over Na_2SO_4 and the solvent was removed under reduced pressure. The product was purified by recrystallization from cyclohexane to afford $[Mn(L^{tri})_2]PF_6$ (69 mg, 58 µmol, 64 %) as a yellow to light orange solid.

^{1}H-NMR (600 MHz, CD_3OD): δ 7.56 (d, *J* = 2.2 Hz, H-6, 6 H), 7.51 (d, *J* = 2.2 Hz, H-8, 6 H), 7.14 (s, H-1, 6 H), 1.37 (s, H-12, 54 H), 1.36 (s, H-10, 54 H) ppm.

^{13}C-NMR (151 MHz, CD_3OD): δ 174.3 (C-13), 153.4 (C-7), 147.1 (C-5), 141.2 (C-3), 135.4 (C-2), 129.5 (C-1), 126.5 (C-8), 125.6 (C-6), 124.8 (C-4), 37.0 (C-9), 36.2 (C-11), 31.6 (C-12), 31.4 (C-10) ppm.

^{55}Mn-NMR (148.5 MHz, CD_3OD): δ -1225 (s, 1 Mn) ppm.

IR: ν 2955.0 (w), 2924.1 (w), 2870.1 (w), 2058.1 (m), 1363.7 (w), 1241.2 (w), 883.4 (w), 839.1 (w), 804.3 (w), 758.0 (w), 699.2 (w), 655.8 (w), 584.4 (m), 557.4 (w), 501.5 (w) cm^{-1}.

ESI-HRMS (*m/z*) calcd for $C_{102}H_{126}N_6MnS_3^+$: 1585.8615. Found: 1585.8615.

Anal. calcd for $C_{102}H_{126}N_6F_6MnPS_3 \cdot C_6H_{12}$: C, 71.42; H, 7.66; N, 4.63. Found: C, 71.78; H, 7.84; N, 4.98.

mp: > 250 °C.

$[ZnCl_2(L^{bi})]$

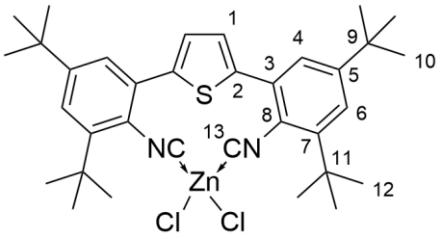

L^{bi} (60 mg, 117.4 µmol) was dissolved in dry hexane (3 mL). A solution of $ZnCl_2$ (84 µL, 58.7 µmol, 0.7 M in THF) was added and the reaction mixture was stirred at 90 °C for 90 min in a closed vessel. The precipitate was collected by filtration, washed with hexane and used without further purification.

$[ZnCl_2(L^{bi})]$ is stable as a solid at rt, but rapidly loses the isocyanide ligand upon contact with coordinating solvents such as THF, MeCN or water.

^{1}H-NMR (400 MHz, CD_2Cl_2): δ 7.60 (d, *J* = 2.0 Hz, H-6, 4 H), 7.51 (d, *J* = 2.0, H-4, 4 H), 7.19 (s, H-1, 4 H), 1.53 (s, H-12, 36 H), 1.37 (s, H-10, 36 H) ppm.

^{13}C-NMR (126 MHz, $CDCl_3$): 155.8 (C-5), 148.6 (C-13), 148.0 (C-7), 140.0 (C-2), 135.9 (C-3), 129.5 (C-1), 126.9 (C-4), 125.5 (C-6), 119.9 (C-8), 36.2 (C-11), 35.8 (C-9), 31.1 (C-10), 29.8 (C-12) δ ppm.

IR: ν 2959.8 (m), 2871.1 (w), 1944.3 (m), 1590.3 (m), 1464.0 (m), 1411.9 (w), 1364.7 (m), 1201.7 (m), 1151.5 (m), 1051.2 (w), 884.4 (m), 797.6 (m), 658.7 (m), 534.3 (w) cm^{-1}.

MALDI-MS (*m/z*) calcd for $C_{34}H_{42}N_2ClSZn$: 609.205. Found: 609.378.

Anal. calcd for $C_{34}H_{42}N_2Cl_2SZn$: C, 63.11; H, 6.54; N, 4.33. Found: C, 63.09; H, 6.43; N, 4.43.

mp: 227 °C.

Single crystals of $[ZnCl_2(L^{bi})\cdot 0.5C_2H_4Cl_2]$ were obtained by vapor diffusion of of *n*-hexane into a solution of $[ZnCl_2(L^{bi})]$ in 1,2-dichloroethane. Table S1 contains the crystal data of $[ZnCl_2(L^{bi})\cdot 0.5C_2H_4Cl_2]$ and Figure S23 displays the X-ray crystal structure with 50 % probability ellipsoids. The file CCDC 2047767 contains the supplementary crystallographic data for $[ZnCl_2(L^{bi})\cdot 0.5C_2H_4Cl_2]$. This data is provided free of charge by The Cambridge Crystallographic Data Centre.

Table S1. Crystallographic data for $[ZnCl_2(L^{bi})\cdot 0.5C_2H_4Cl_2]$.

Formula	$C_{34}H_{42}N_2Cl_2SZn\cdot 0.5C_2H_4Cl_2$
$D_{calc.}$/ g cm^{-3}	1.306
μ/mm^{-1}	2.436
Formula Weight	696.50
Colour	colourless
Shape	block
Size/mm^3	0.22×0.19×0.14
T/K	150
Crystal System	triclinic
Space Group	P-1
a/Å	10.8241(7)
b/Å	11.5193(7)
c/Å	15.5295(9)
α/°	100.376(5)
β/°	99.516(5)
γ/°	107.069(5)
V/Å^3	1771.1(2)
Z	2
Z'	1
Wavelength/Å	1.34143
Radiation type	GaK_α
Θ_{min}/°	2.587
Θ_{max}/°	58.248
Measured Reflections	37115
Independent Reflections	7361
Reflections I≥2 σ(I)	7002
R_{int}	0.0486
Parameters	391
Restraints	0
Largest Peak	0.894
Deepest Hole	-0.449
GooF	1.031
wR_2 (all data)	0.1315
wR_2	0.1291
R_1 (all data)	0.0487
R_1	0.0470

NMR Spectra

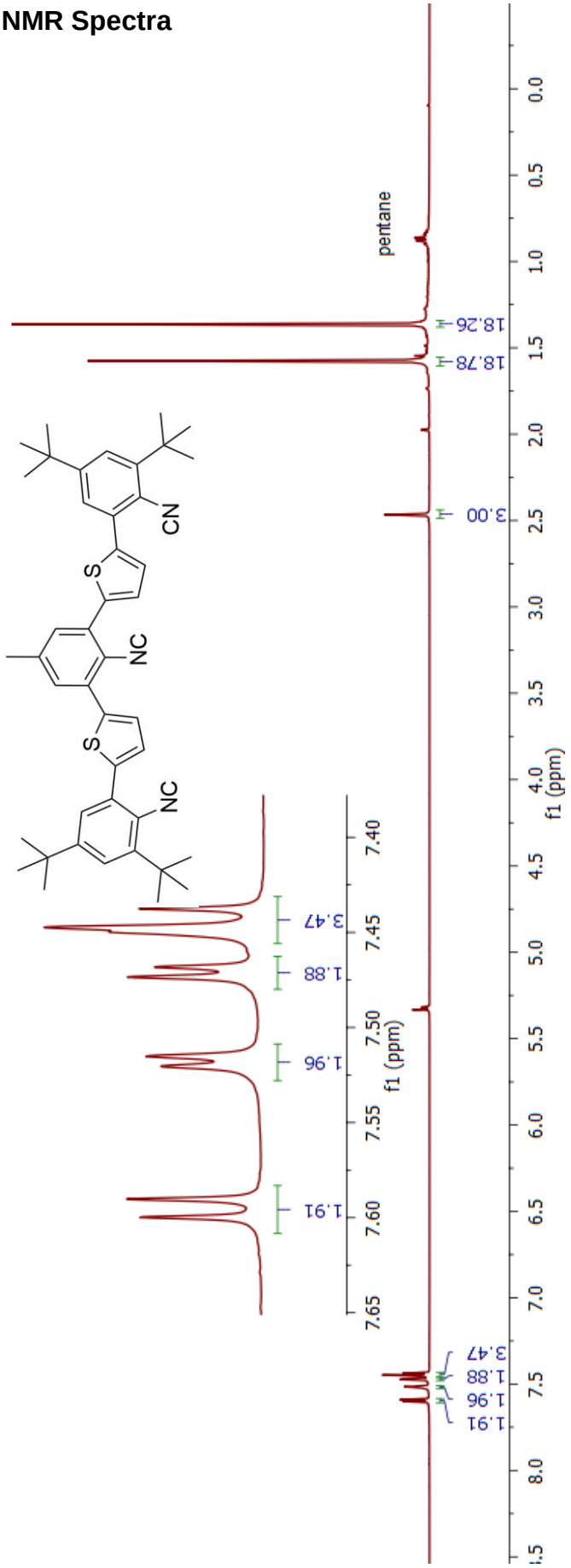

Figure S1. ^{1}H-NMR spectrum (400 MHz) of $\mathbf{L^{tri}}$ in CD_2Cl_2.

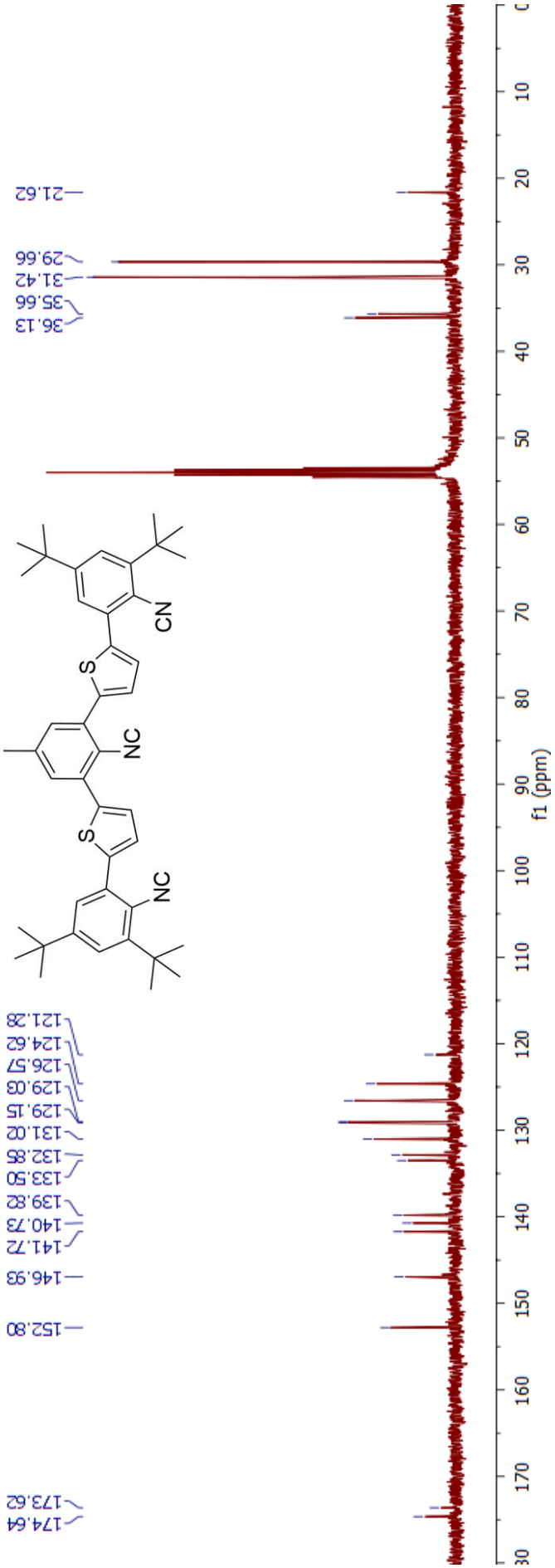

Figure S2. ^{13}C-NMR spectrum (126 MHz) of $\mathbf{L^{tri}}$ in CD_2Cl_2.

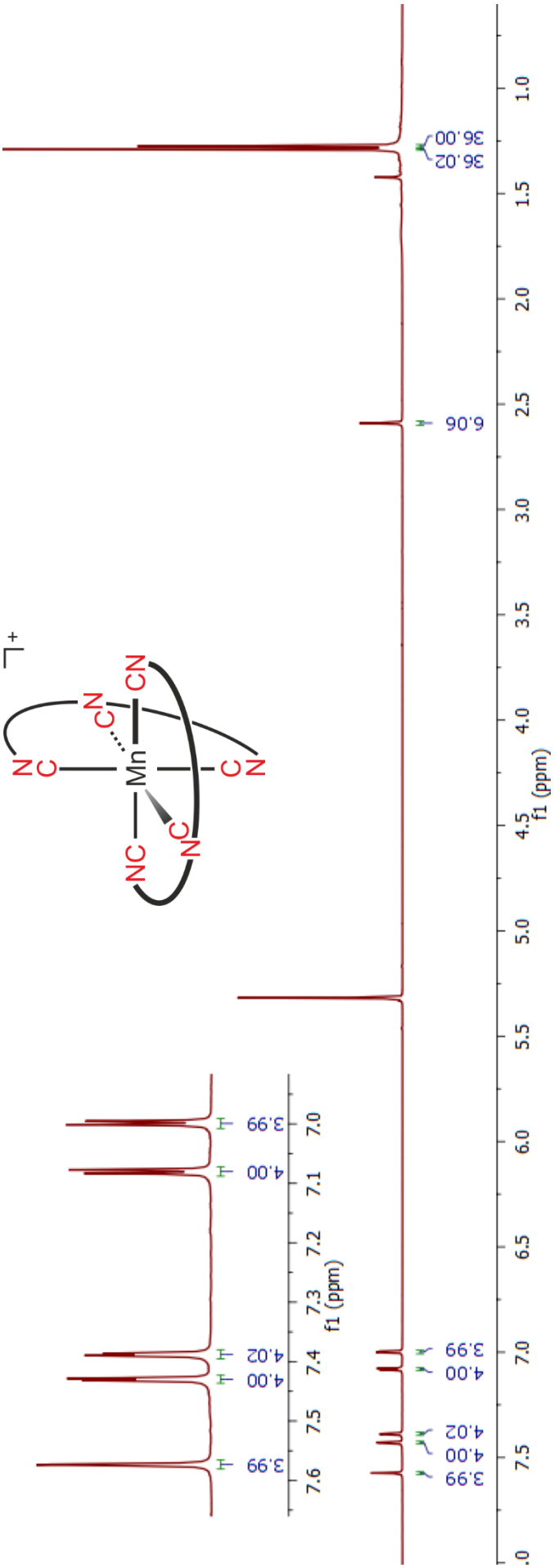

Figure S3. ^{1}H-NMR spectrum (600 MHz) of $[Mn(L^{tri})_2]PF_6$ in CD_2Cl_2.

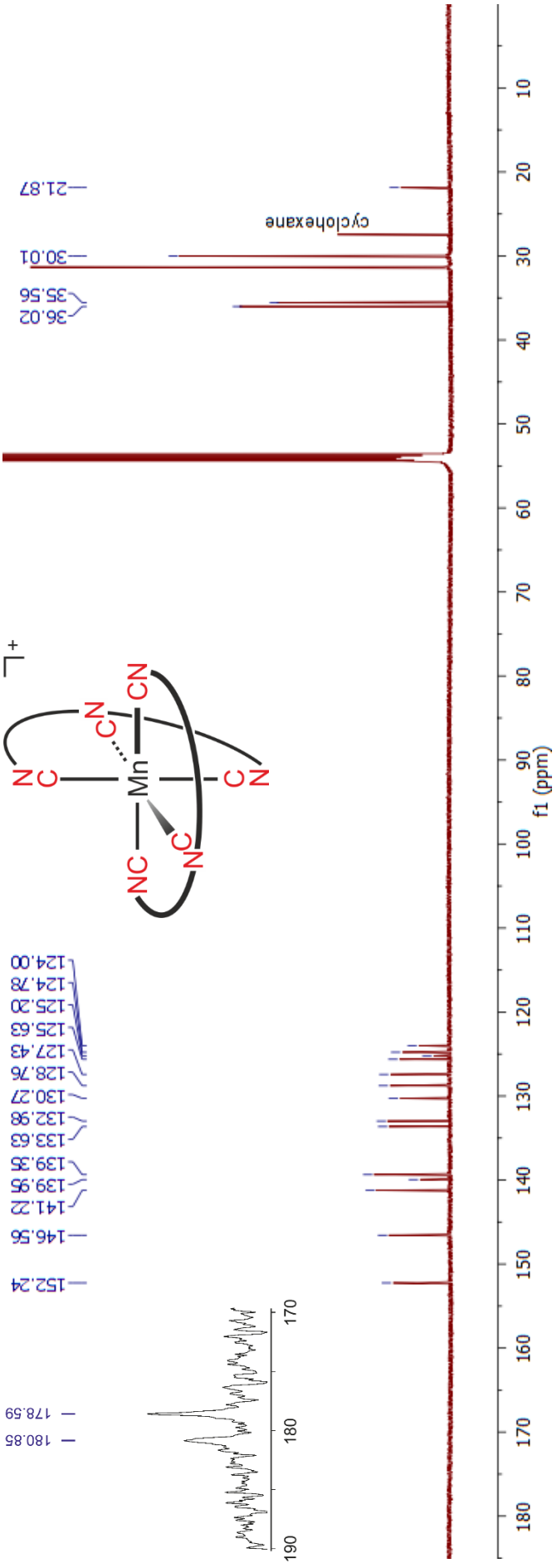

Figure S4. ^{13}C-NMR spectrum (151 MHz) of $[Mn(L^{tri})_2]PF_6$ in CD_2Cl_2.

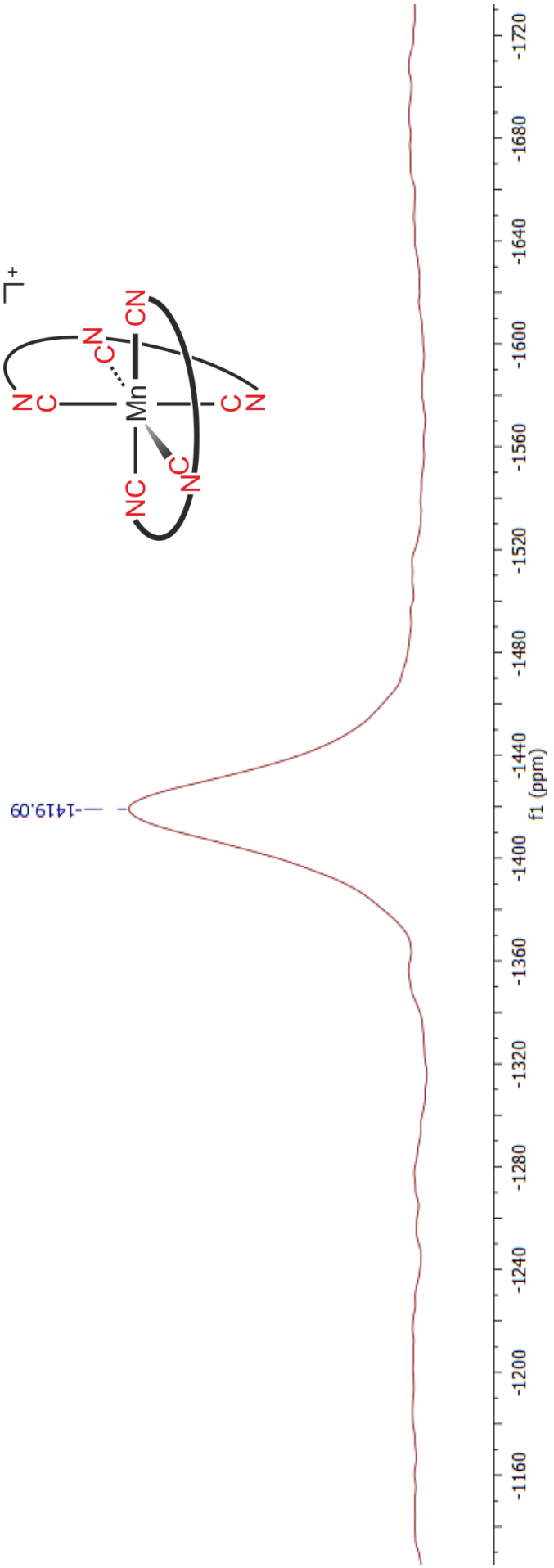

Figure S5. ^{55}Mn-NMR spectrum (148.5 MHz) of $[Mn(L^{tri})_2]PF_6$ in CD_2Cl_2.

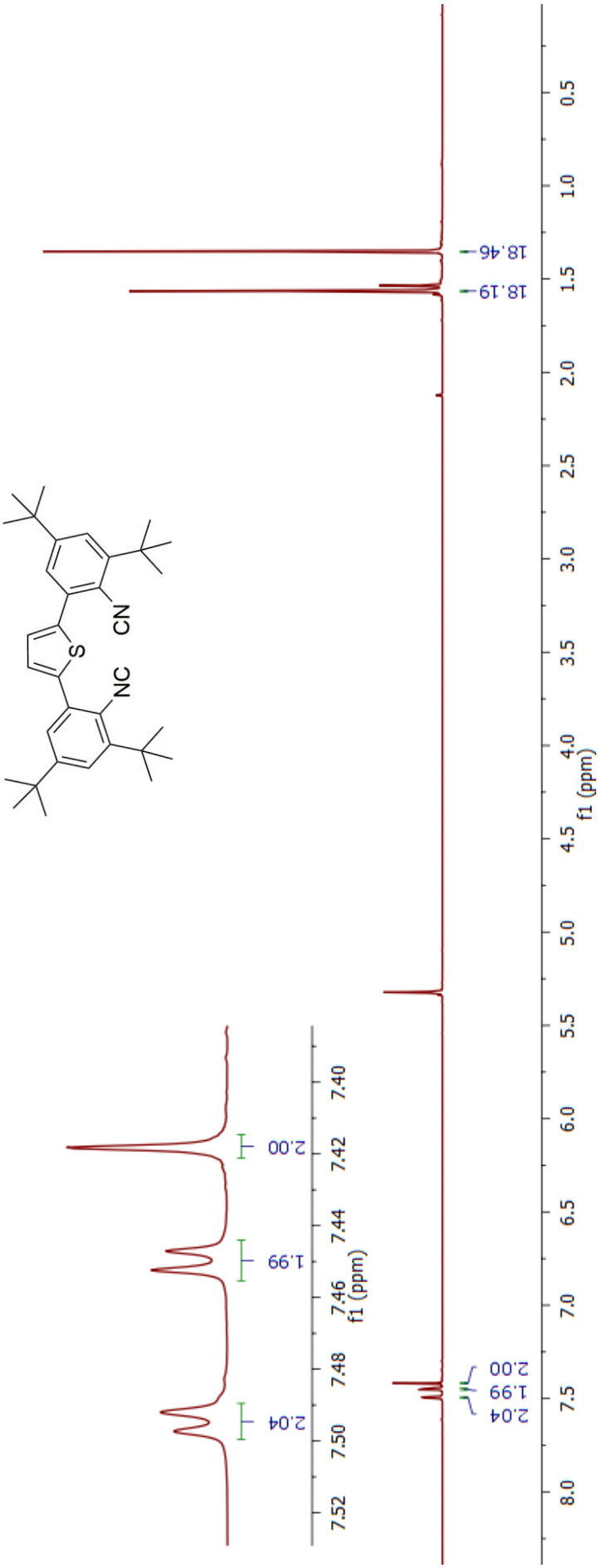

Figure S6. ^{1}H-NMR spectrum (400 MHz) of $\mathbf{L^{bi}}$ in CD_2Cl_2.

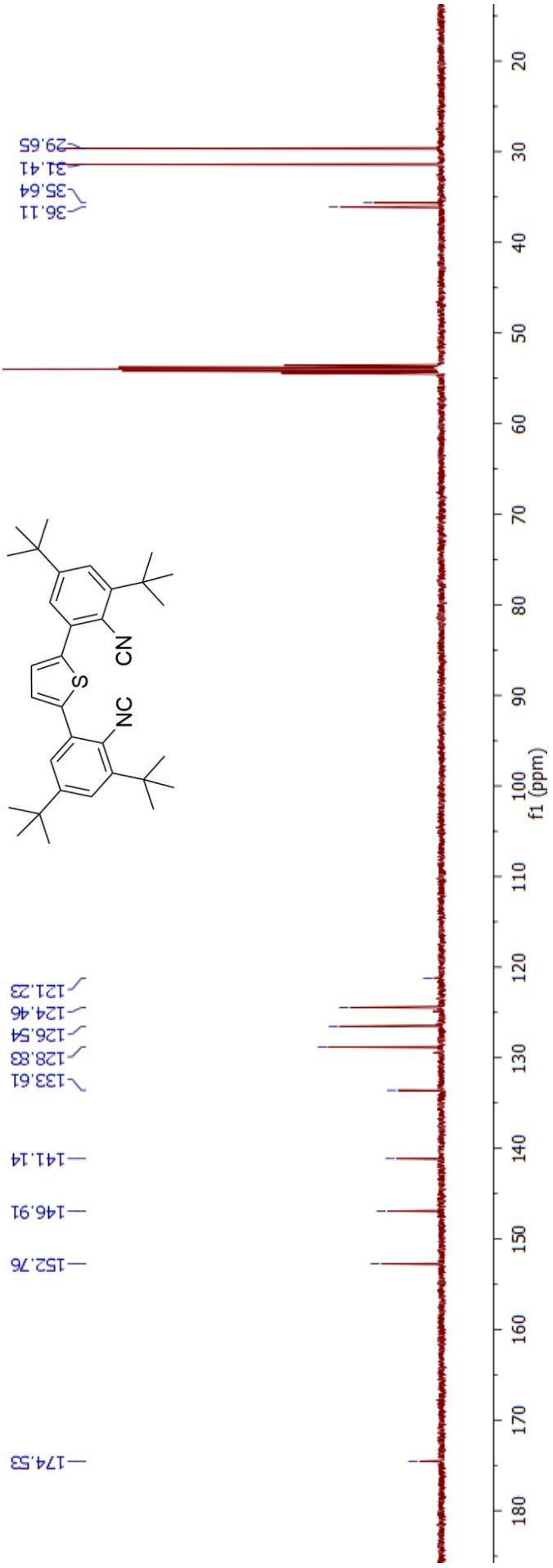

Figure S7. ^{13}C-NMR spectrum (126 MHz) of $\mathbf{L^{bi}}$ in CD_2Cl_2.

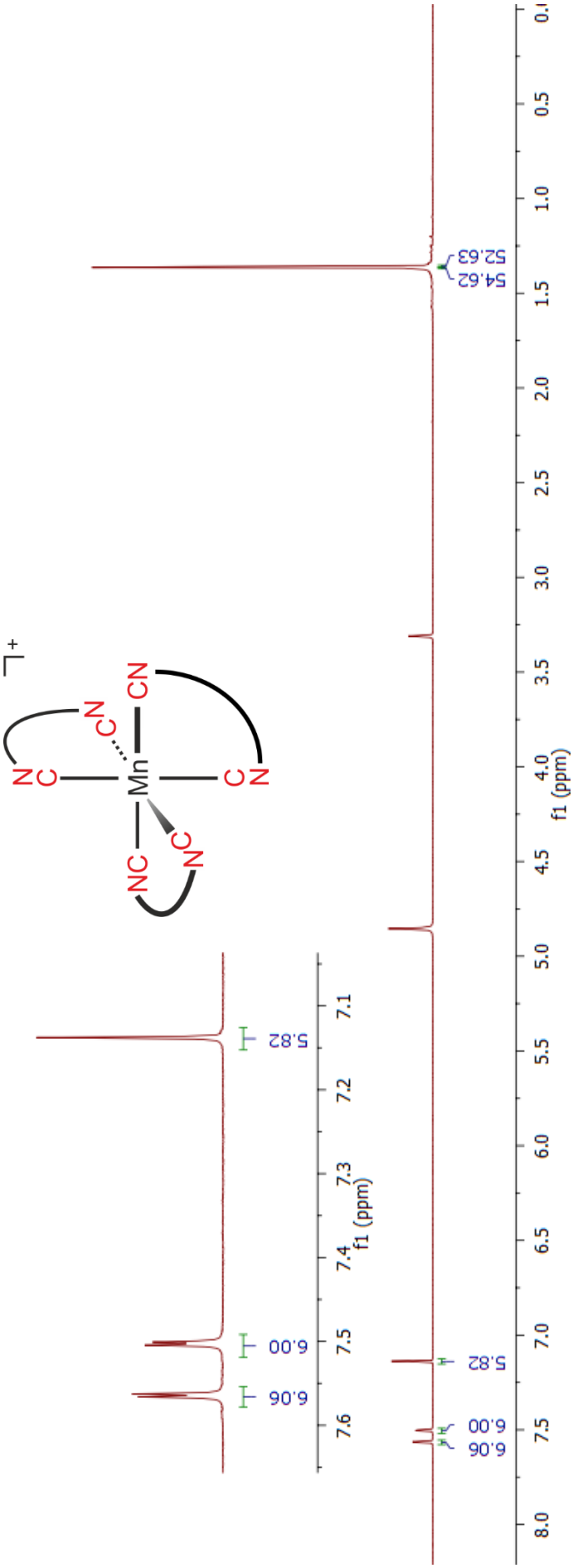

Figure S8. ^{1}H-NMR spectrum (600 MHz) of $[Mn(L^{bi})_2]PF_6$ in CD_3OD.

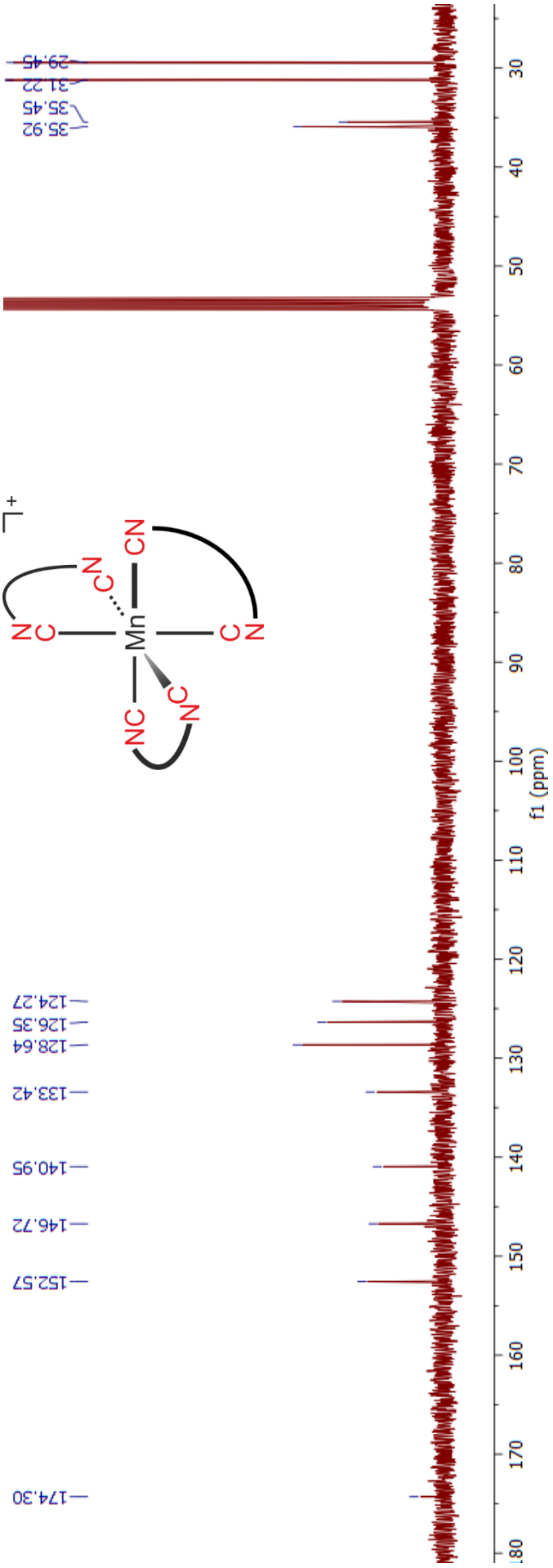

Figure S9. ^{13}C-NMR spectrum (151 MHz) of $[Mn(L^{bi})_2]PF_6$ in CD_3OD.

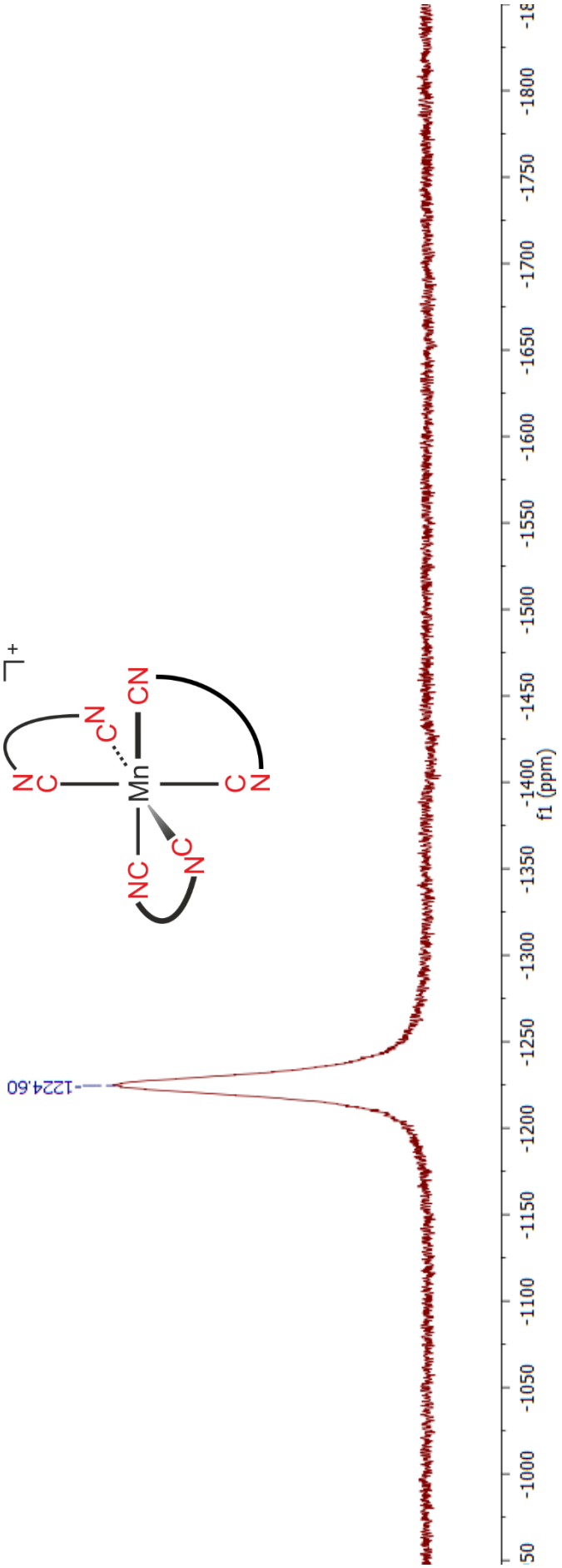

Figure S10. ^{55}Mn-NMR spectrum (148.5 MHz) of $[Mn(L^{bi})_2]PF_6$ in CD_3OD.

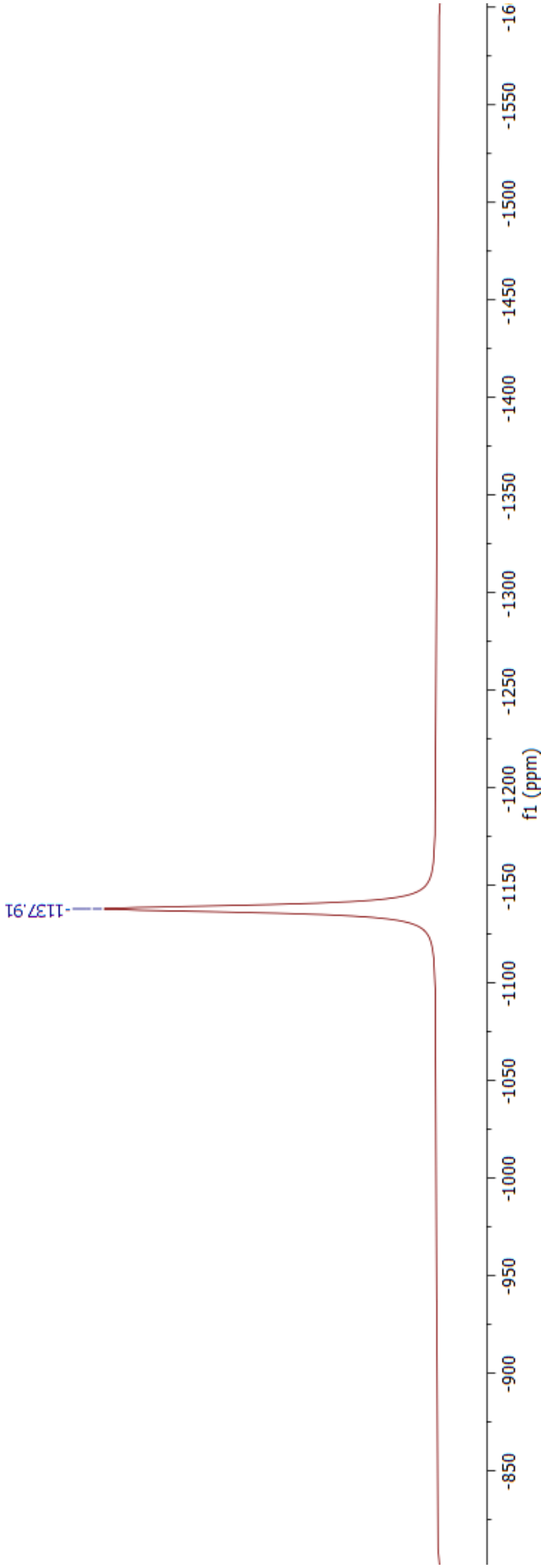

Figure S11. ^{55}Mn-NMR spectrum (148.5 MHz) of $[Mn(CO)_5Br]$ in CD_2Cl_2.

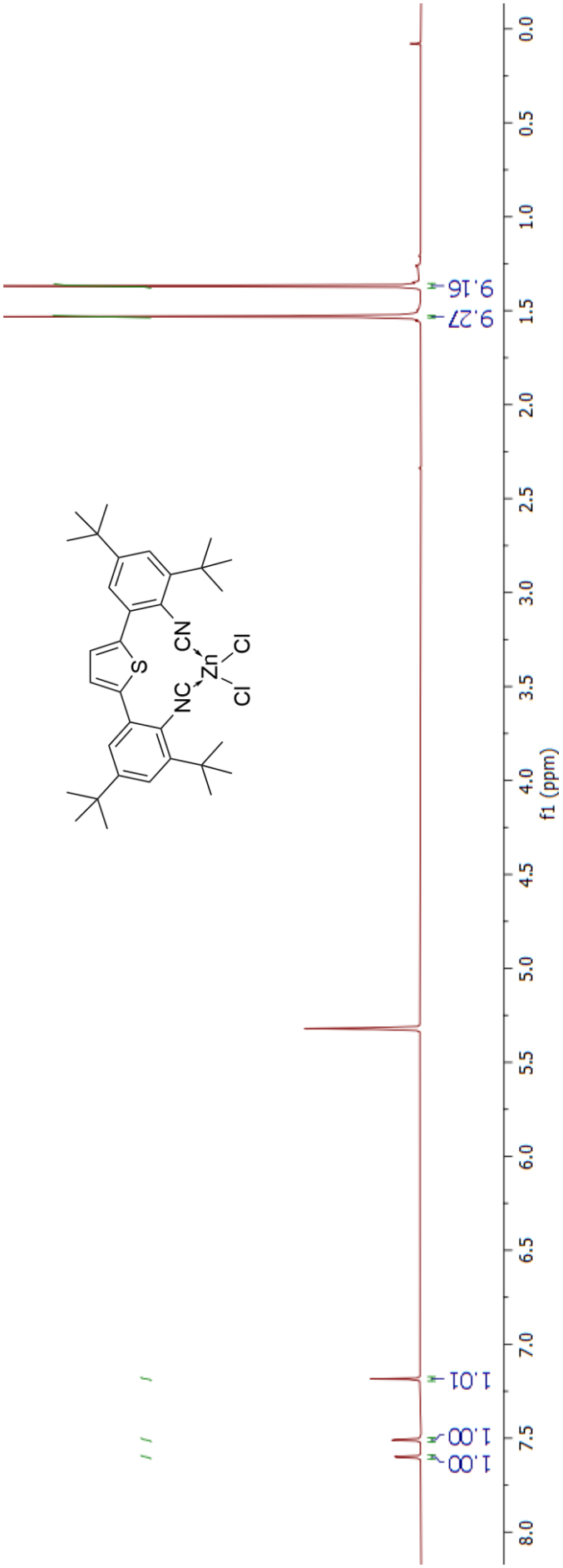

Figure S12. ^{1}H-NMR spectrum (400 MHz) of $ZnCl_2(L^{bi})$ in CD_2Cl_2.

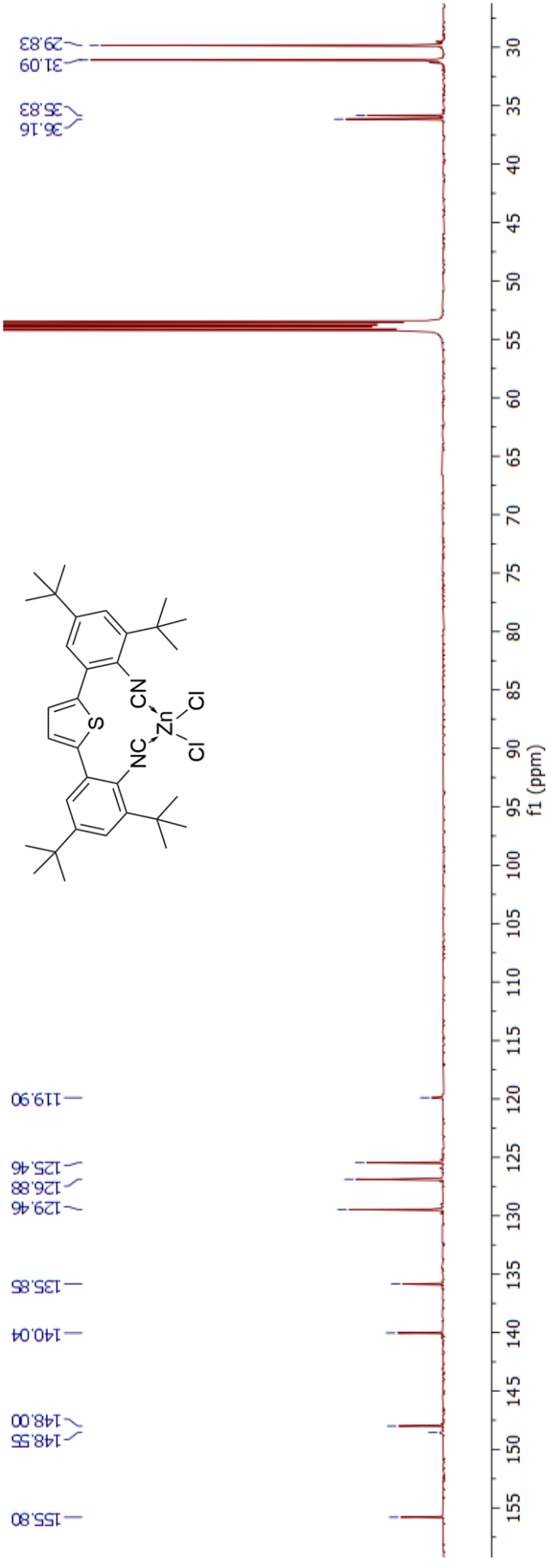

Figure S13. ^{13}C-NMR spectrum (148.5 MHz) of $ZnCl_2(L^{bi})$ in CD_2Cl_2.

Mass spectra

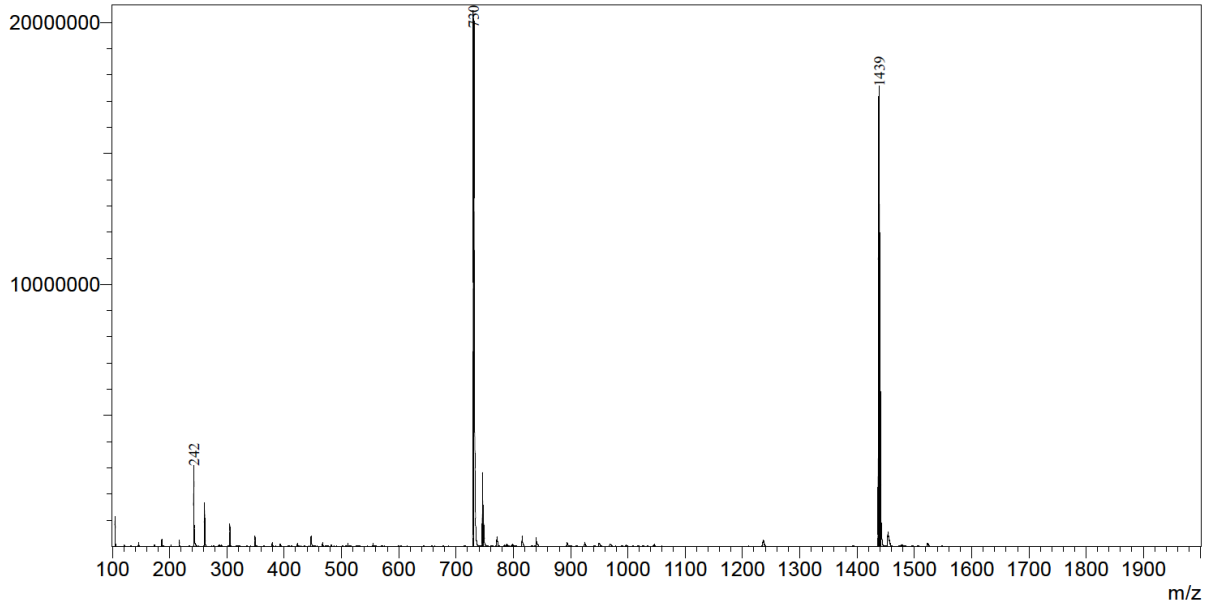

Figure S14. ESI-MS of $\mathbf{L^{tri}}$: Main peaks: $M+Na^+$ (m/z = 730) and $2M+Na^+$ (m/z = 1439).

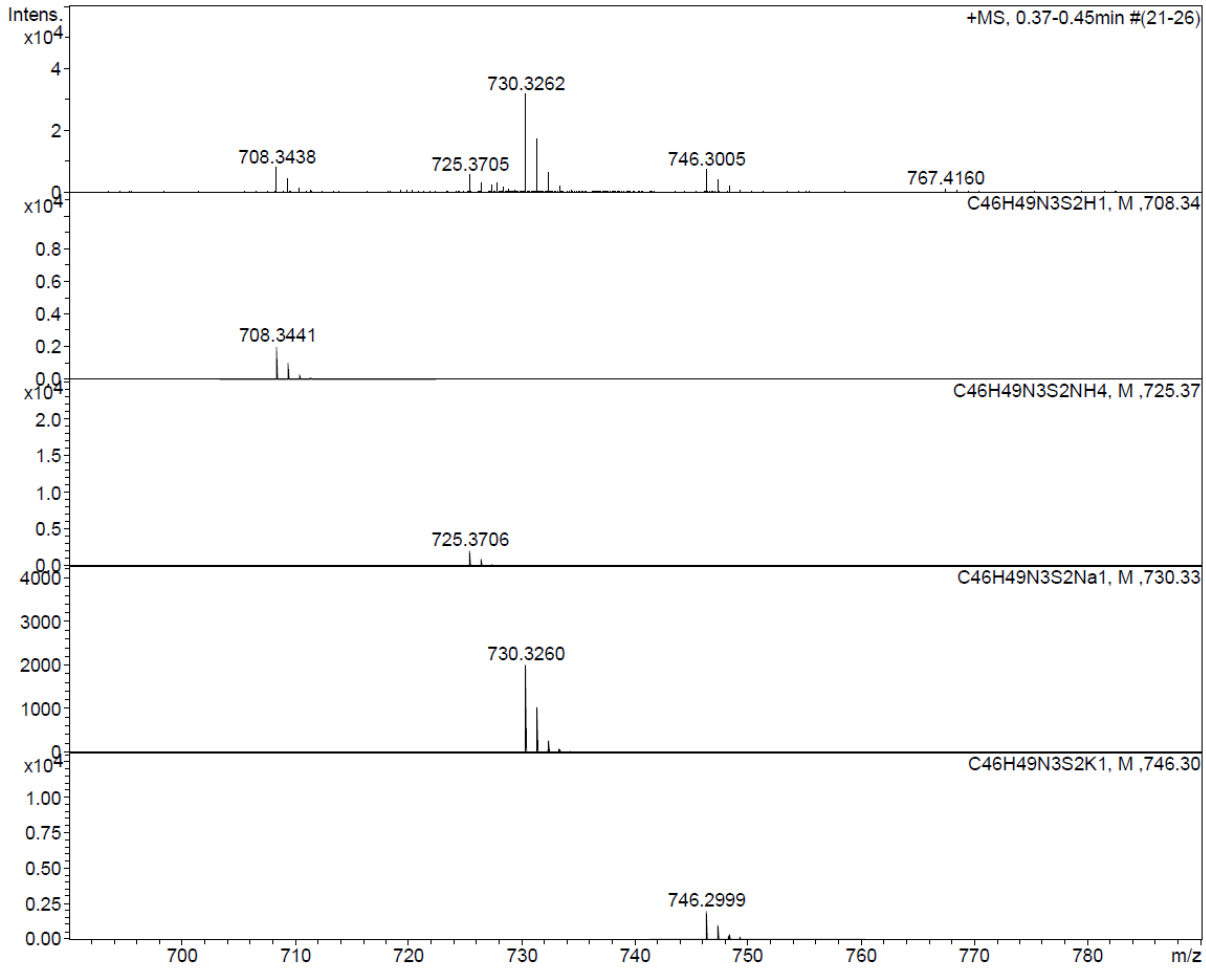

Figure S15. Top: Experimental ESI-HRMS of $\mathbf{L^{tri}}$: Below (from top to bottom): Simulations for $M+H^+$ (708.3341), $M+NH_4^+$ (725.3706), $M+Na^+$ (730.3260), and $M+K^+$ (746.2999).

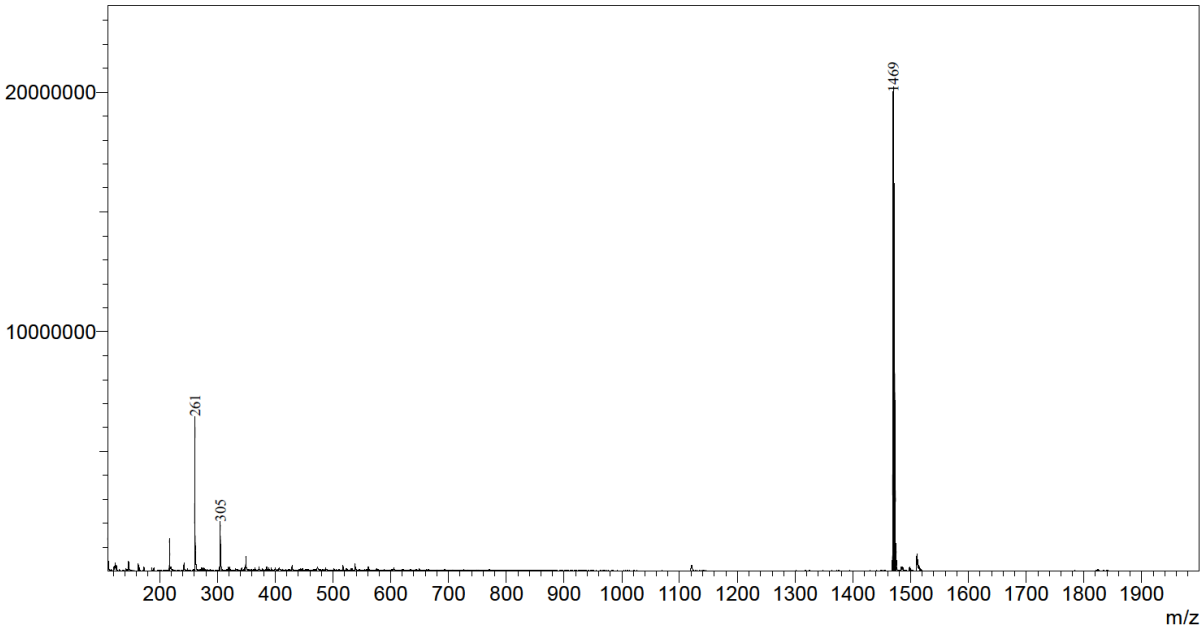

Figure S16. ESI-MS of $[Mn(L^{tri})_2]PF_6$. Main peak: M^+ (m/z = 1469).

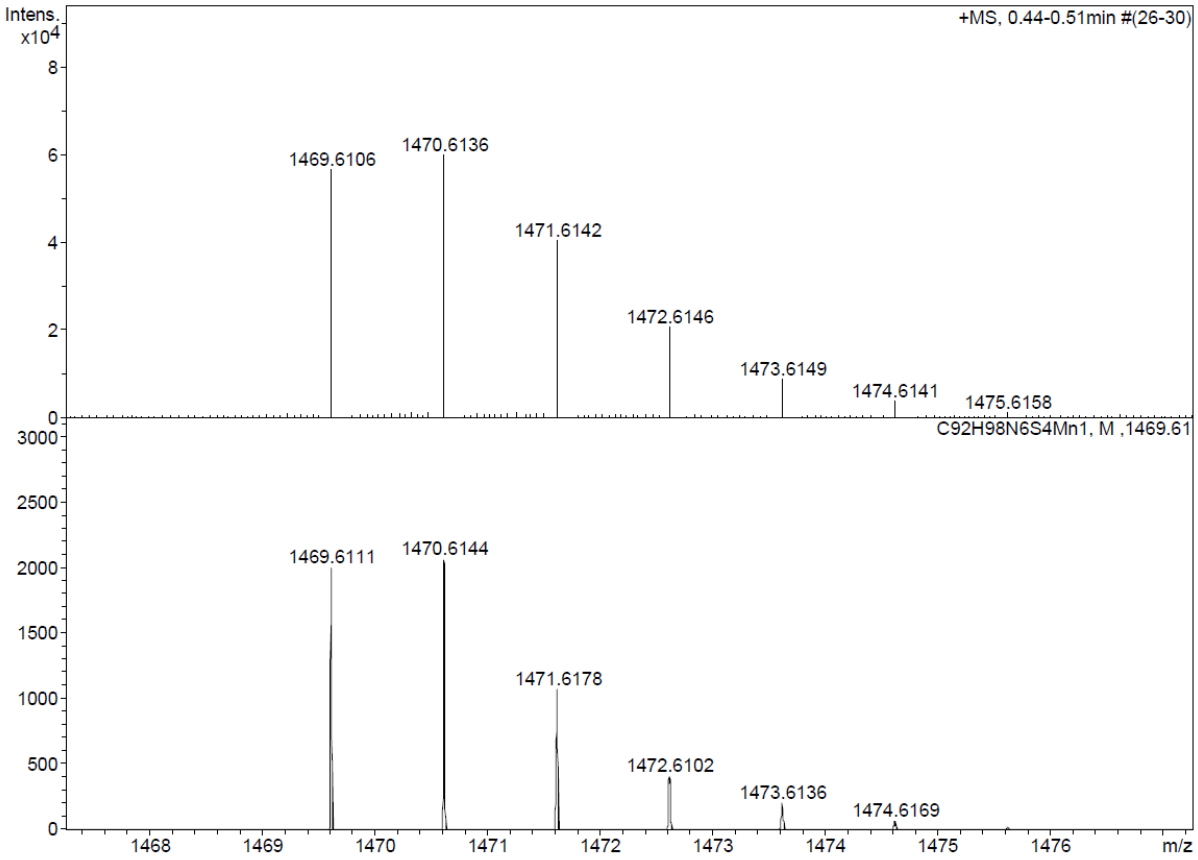

Figure S17. Top: Experimental ESI-HRMS of $[Mn(L^{tri})_2]PF_6$. Bottom: simulated spectrum for $[Mn(L^{tri})_2]^+$.

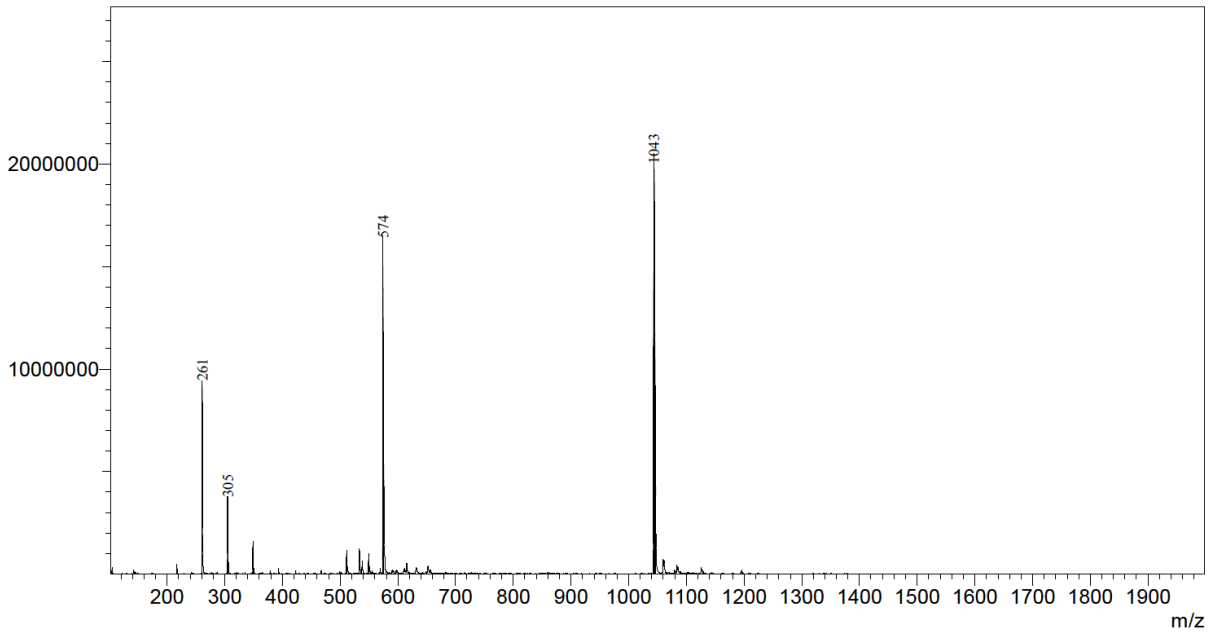

Figure S18. ESI-MS of $\mathbf{L^{bi}}$. Main peaks: $M+CH_3CN+Na^+$ (m/z = 574) and $2M+Na^+$ (m/z = 1043).

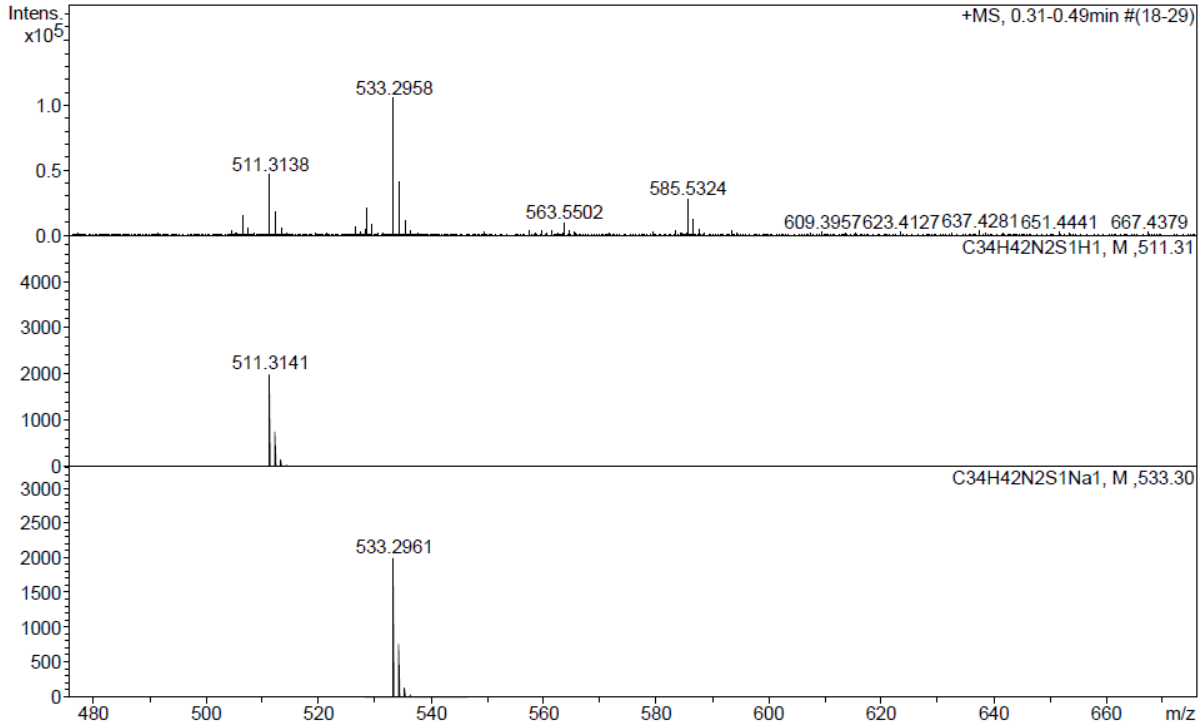

Figure S19. Top: Experimental ESI-HRMS of $\mathbf{L^{bi}}$; middle: simulated spectrum for $M+H^+$; bottom: simulated spectrum for $M+Na^+$.

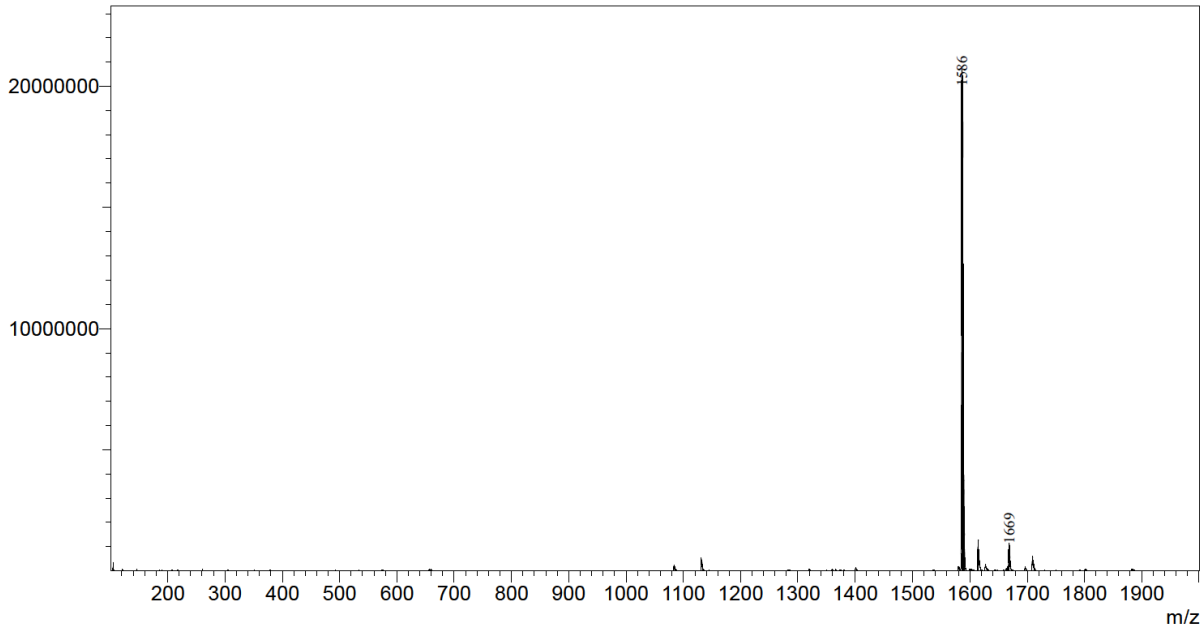

Figure S20. ESI-MS of $[Mn(L^{bi})_3]PF_6$. Main peak: M^+ (m/z = 1586).

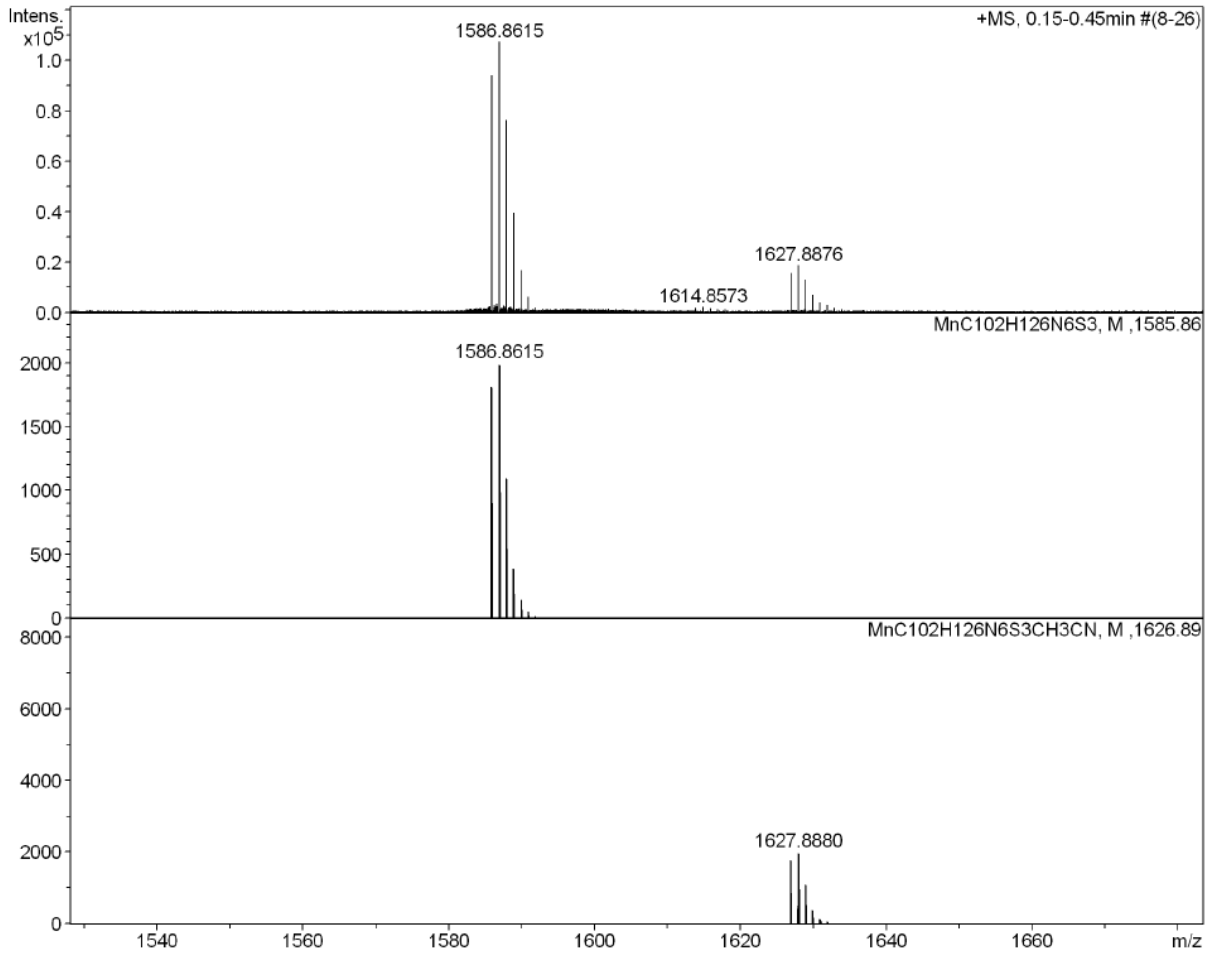

Figure S21. Top: Experimental ESI-HRMS of $[Mn(L^{bi})_3]PF_6$. Middle: simulated spectrum for $[Mn(L^{bi})_3]^+$. Bottom: simulated spectrum for $[Mn(L^{bi})_3]^+ + CH_3CN$.

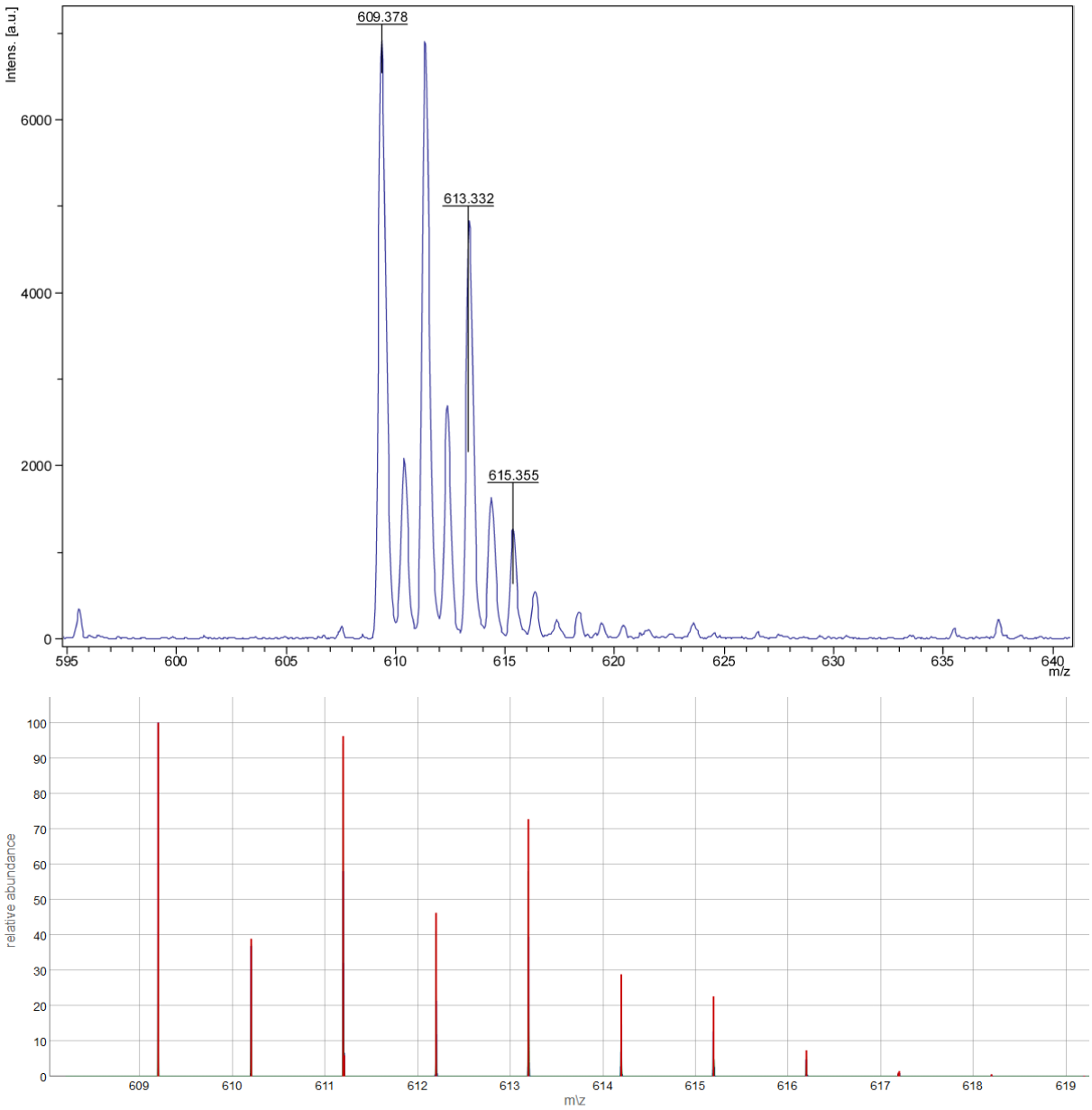

Figure S22. Top: Experimental MALDI-MS spectrum of $[ZnCl_2(L^{bi})]$. Bottom: Simulated spectrum for $[ZnCl(L^{bi})]^+$ (m/z = 609).

Crystal structure

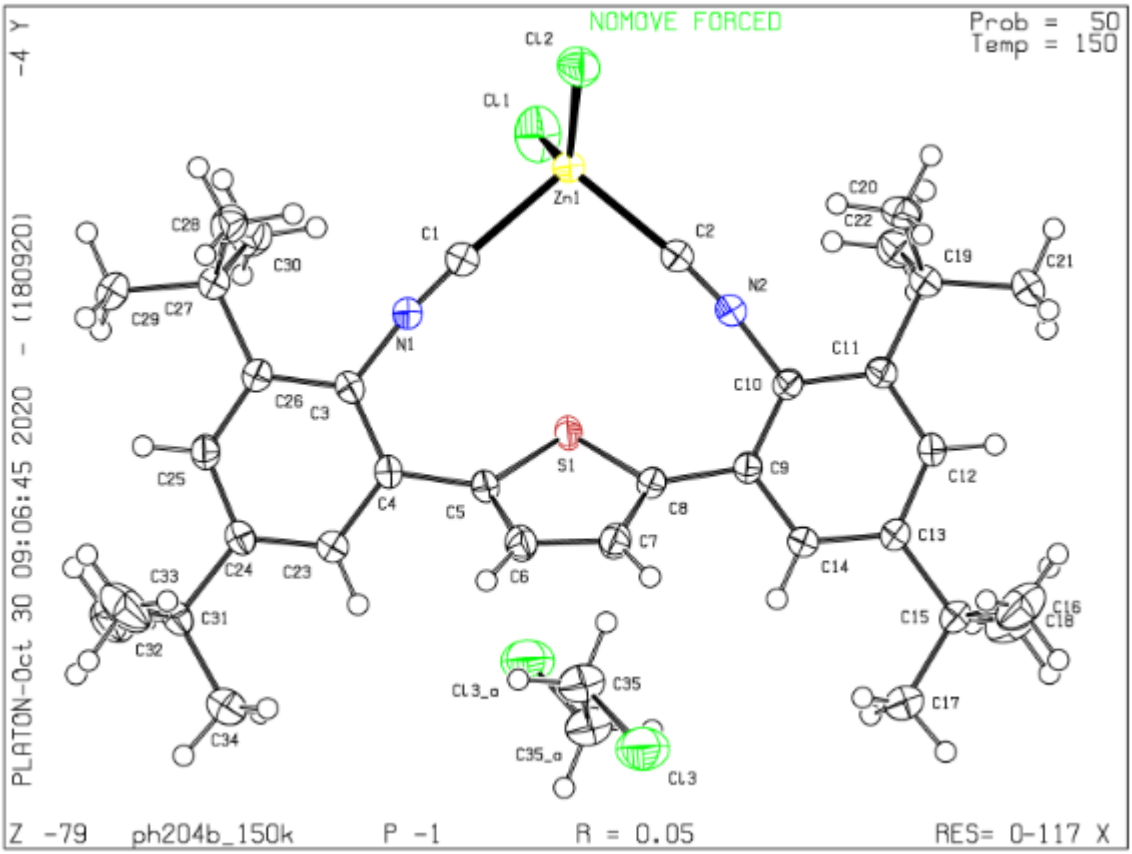

Figure S23. Crystal structure of $[ZnCl_2(L^{bi})]$. CCDC 2047767 contains the full supplementary crystallographic data for $[ZnCl_2(L^{bi})\cdot 0.5C_2H_4Cl_2]$. This data is provided free of charge by The Cambridge Crystallographic Data Centre.

Equipment and methods

All ^{1}H and ^{13}C NMR experiments were performed at a temperature of 298 K on Bruker Avance III NMR spectrometers operating at 400, 500 or 600 MHz.
All chemical shifts are reported in δ values in ppm referred to protons of the residual non-perdeuterated solvent used or its carbon atoms, respectively.
The ^{55}Mn (I = 5/2) NMR experiments were performed on a 14.1 T instrument at a frequency of 148.559259 MHz using a broadband direct observe probe (BBFO). The transmitter offset was chosen as –1400 ppm and a spectral width of 990 ppm (147 kHz) was applied. The 90° pulse was 13 µs at a power level of 100 W. We used a 90° excitation, an acquisition time of 323.8 ms and a recycling delay of 100 ms. 36 k scans were acquired and multiplied with an exponential line broadening function (lb = 1000 Hz) before Fourier transformation. The ^{55}Mn chemical shifts were referenced to a saturated solution of $KMnO_4$ in D_2O as δ = 0.00 ppm[2]. The recommended reference concentration of 0.82 mol/kg (13% w/w) is more than twice higher than the solubility in water at rt and cannot be correct.
ESI-MS spectra were measured on a Shimadzu LC-MS 8030 Plus mass spectrometer. HRMS spectra were measured on a Bruker maxis 4G HiRes ESI mass spectrometer.
Matrix-assisted laser desorption/ionization (MALDI) measurements were performed using a MALDI plate MSP 96 target ground steel on a Bruker Microflex mass spectrometer with trans-2-[3-(4-tert-butylphenyl)-2-methyl-2-propenylidene]malononitrile (DCTB) as a matrix.
Elemental analysis was conducted on an Elementar Vario MICRO Cube instrument.
Crystal structures were measured on a STOE STADIVARI diffractometer equipped with an Oxford Cryosystems low-temperature device operating at T = 150 K. Single colorless block crystals of $[ZnCl_2(L^{bi})]$ were used as supplied. A suitable crystal with dimensions 0.22 × 0.19 × 0.14 mm^3 was selected and mounted on a mylar loop in perfluoroether oil. The crystal was kept at a steady T = 150 K during data collection. The structure was solved with the ShelXT [3] solution program using dual methods and by using Olex2 [4] as the graphical interface. The model was refined with ShelXL 2018/3 [3] using full matrix least squares minimization on F2.

Cyclic voltammetry was performed using a Versastat3-200 or a Versastat4-200 potentiostat from Princeton Applied Research. For oxidative measurements, a glassy carbon disk electrode served as a working electrode, a silver wire as counter electrode and an SCE as reference electrode. For reductive measurements, a glassy carbon disk electrode served as a working electrode and two silver wires as counter and pseudo-reference electrode. Ferrocene was added as internal reference. The solvent was dry de-aerated acetonitrile or CH_2Cl_2 with 0.1 M $TBAPF_6$ (tetra-*n*-butylammonium hexafluorophosphate) as an electrolyte. Potential sweep rates were 0.1 V/s.

Optical absorption spectra were recorded on a Cary 5000 instrument from Varian. Steady-state luminescence spectra were measured on a Fluorolog-322 from Horiba Jobin-Yvon.

ATR-IR spectroscopy was performed with a Varian 800 FT-IR Scimitar Series instrument and a Shimadzu IRTracer-100. IR spectroscopy in solution was performed on a Bruker Vertex 70v instrument.

An LP920-KS instrument from Edinburgh Instruments was employed for nanosecond transient absorption spectroscopy and time-resolved luminescence spectroscopy. The frequency-doubled output of a Quantel Brilliant b laser served as an excitation source. The laser pulse duration was ~10 ns and the pulse frequency was 10 Hz. The typical pulse energy used for the nanosecond transient absorption studies was 6-7 mJ. Detection of transient absorption spectra occurred on an iCCD camera from Andor. Single-wavelength kinetics were recorded using a photomultiplier tube.

Transient absorption studies with sub-nanosecond time resolution were performed using a TRASS instrument from Hamamatsu and a mode-locked picosecond Nd:YVO_4/YAG laser (model PL2251B-20-SH/TH/FH with PRETRIG option) as an excitation source. The laser pulse duration was ~30 ps and the pulse frequency was 10 Hz. The laser pulse energy of 8 mJ at 355 nm powers an Ekspla PG402-264 OPA with an energy output of 0.9 mJ at 410 nm. High optical densities (OD) were required to afford good data quality. Best results for $[Mn(L^{tri})_2]PF_6$ were obtained with OD = 0.35 and OD = 1.00 for $[Mn(L^{bi})_3]PF_6$ at 410 nm. This in turn required the use of CH_2Cl_2 as solvent for the picosecond transient absorption

studies, because the solubility of the Mn(I) complexes in that solvent is significantly higher than in CH_3CN.

Luminescence lifetimes were recorded with an Edinburgh Instruments Lifespec II with a 313 nm pulsed LED or a 405 nm picosecond pulsed diode laser (pulse width 900 and 60 ps, respectively) and a pulse period of 50 ns.

Continuous-wave photo-irradiation was carried out at room temperature using either a 405 nm (665 mW power output) collimated LED with attached heat sink purchased from ThorLabs, or a 440 nm PR160-440 collimated LED (power consumption 45 W) from Kessil.

Most of the measurements were performed in CH_3CN, but for certain experiments other solvents were necessary. For instance, picosecond transient absorption studies had to be performed in CH_2Cl_2 (see above), and investigations of photoinduced energy transfer to anthracene were performed in toluene to ensure sufficiently high solubility of all components. Photostability studies were performed in CH_2Cl_2 because the lab-scale stilbene isomerization experiment required long irradiation times, and the substrate was particularly well soluble in CH_2Cl_2.

In ^{55}Mn-NMR spectroscopy, the slightly more upfield resonance signal for $[Mn(L^{tri})_2]^+$ indicates a larger electron density on this complex compared to $[Mn(L^{bi})_3]^+$, a finding that is confirmed by the slightly lower oxidation potential of the former (c.f. Table 1). The significantly larger linewidth of the ^{55}Mn resonance in $[Mn(L^{tri})_2]^+$ (5900 Hz vs. 2100 Hz) reflects the lower symmetry of this complex.

Additional optical spectroscopic and electrochemical data

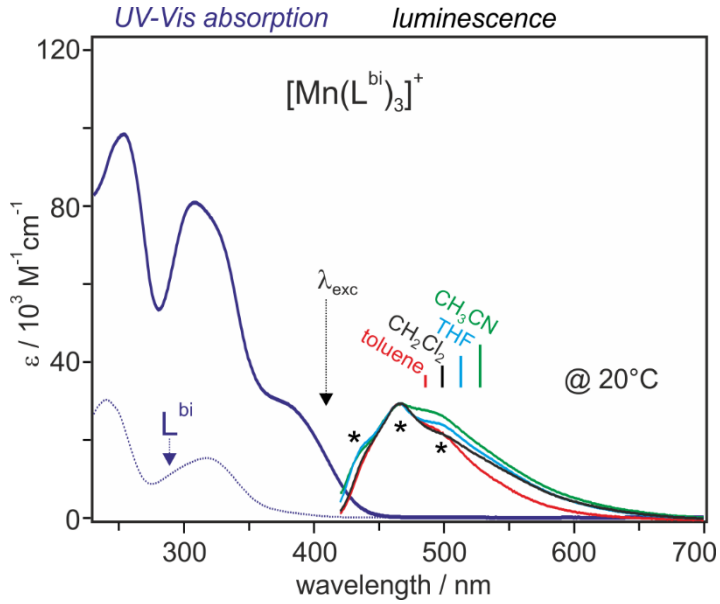

Figure S24. Steady-state absorption and emission spectroscopy. Left, purple lines: UV-Vis absorption spectra of $[Mn(L^{bi})_3]^+$ (solid) and **L^{bi}** (dotted) in CH_2Cl_2. Right: Luminescence spectra of $[Mn(L^{bi})_3]^+$ following excitation at 410 nm (λ_{exc}) in four different de-aerated solvents. The asterisks mark peaks caused by Raman scattered excitation light.

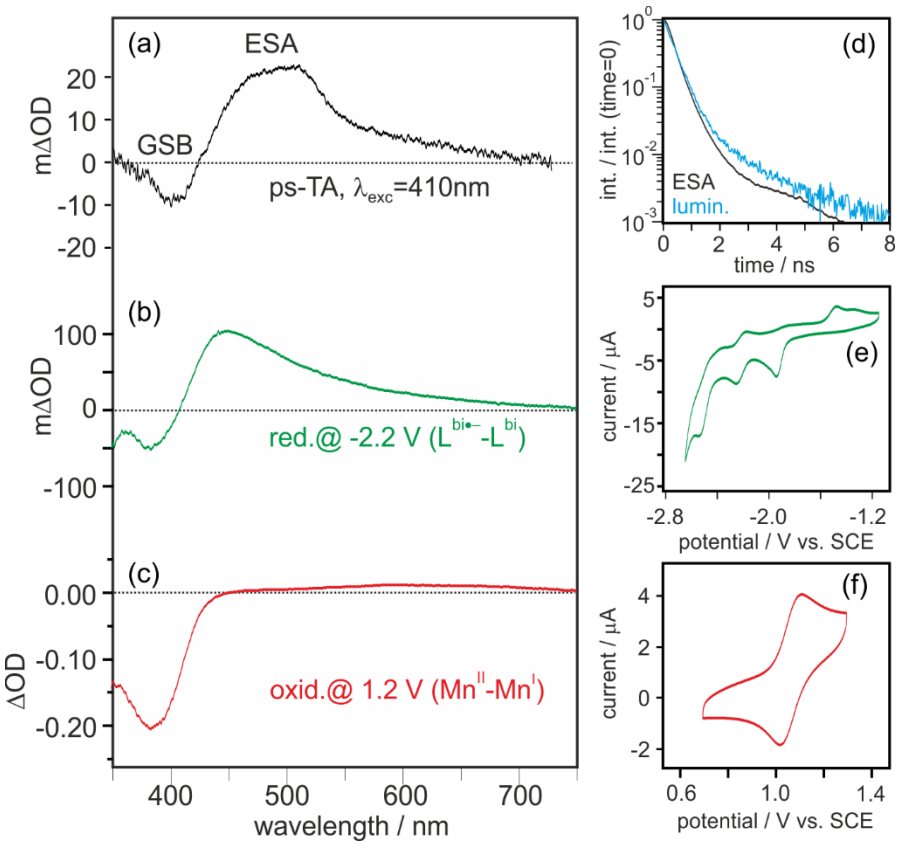

Figure S25. Time-resolved and (spectro-)electrochemical data. (a) UV-Vis transient difference spectrum of 67 µM $[Mn(L^{bi})_3]^+$ in de-aerated CH_2Cl_2 at 20 °C, time-integrated over 2 ns following excitation at 410 nm with 30-ps laser pulses. (b) UV-Vis changes upon electrochemical (ligand-centered) reduction in CH_3CN. (c) UV-Vis changes upon electrochemical (metal-centered) oxidation in CH_3CN. (d) Decays of the excited-state absorption (ESA) signal at 470 nm (black, λ_{exc} = 410 nm) and the luminescence intensity at 460 nm (blue, λ_{exc} = 405 nm) of $[Mn(L^{bi})_3]^+$ in de-aerated CH_2Cl_2 at 20 °C. (e) Cyclic voltammogram (CV) showing ligand-based reduction in deaerated CH_3CN. (f) CV showing metal-based oxidation in CH_2Cl_2. The electrolyte was 0.1 M $TBAPF_6$.

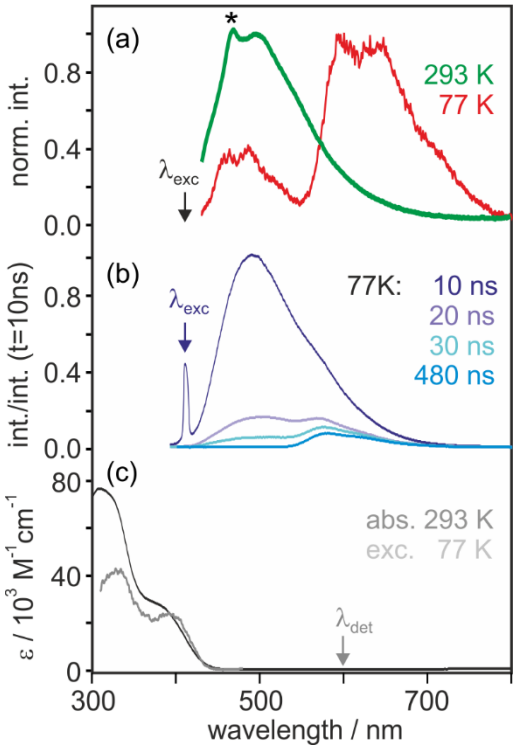

Figure S26. Dual luminescence at 77 K. (a) Luminescence of $[Mn(L^{bi})_3]^+$ (25 µM) after cw-excitation at 410 nm in de-aerated THF (green, 293 K) and 2-methyl-THF (red, 77 K). The asterisk marks a peak caused by Raman scattered excitation light. (b) Luminescence at 77 K after pulsed excitation of $[Mn(L^{bi})_3]^+$ (25 µM) at 410 nm and different detection delay times but constant integration times of 1 µs. (c) Black: UV-Vis spectrum of $[Mn(L^{bi})_3]^+$ in THF at 293 K. Gray: Excitation spectrum monitoring the 600-nm luminescence of $[Mn(L^{bi})_3]^+$ in 2-methyl-THF at 77 K.

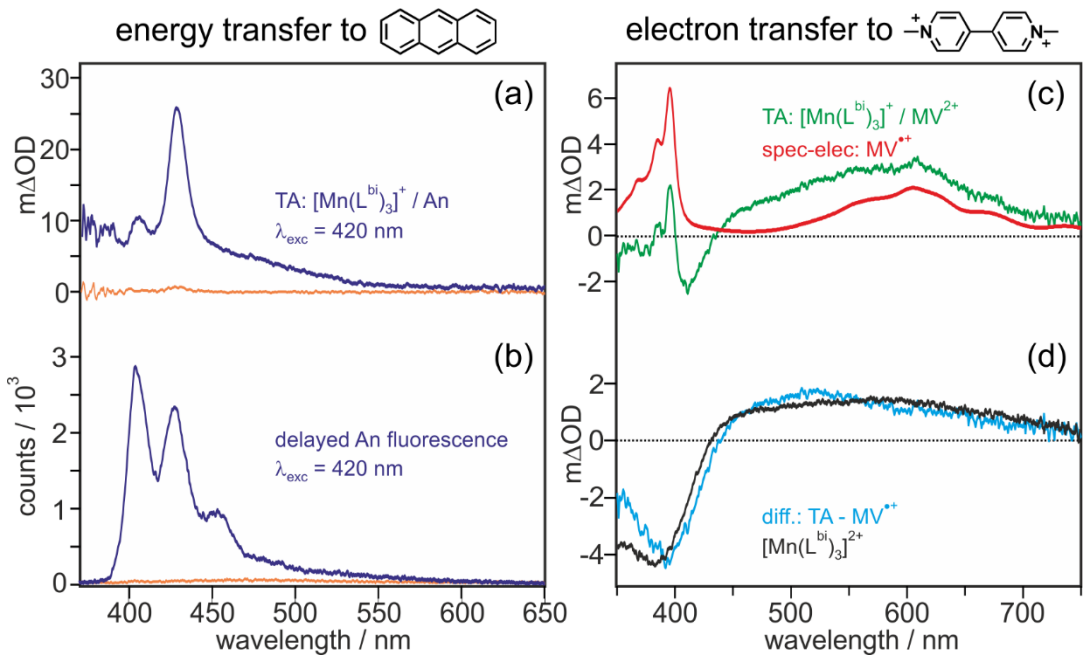

Figure S27. Photoinduced energy and electron transfer. (a) Purple: Transient absorption (TA) spectrum after excitation of $[Mn(L^{bi})_3]^+$ (25 µM) at 420 nm in presence of 40 mM anthracene (An) in de-aerated toluene. Orange: spectrum obtained under identical conditions without $[Mn(L^{bi})_3]^+$. (b) Luminescence of the two solutions used in (a). (c) Green: TA spectrum after 420-nm excitation of $[Mn(L^{bi})_3]^+$ (25 µM) in presence of 80 mM methyl viologen (MV^{2+}) in de-aerated CH_3CN. Red: UV-Vis difference spectrum upon electrochemical reduction of MV^{2+} to $MV^{\bullet+}$. (d) Blue: Difference between the red and the green spectra in (c); scaling factor chosen such that the difference between the TA spectrum of $MV^{\bullet+}$ and the spectrum of the oxidized complex was as small as possible. Black: TA difference spectrum resulting from oxidation of $[Mn(L^{bi})_3]^+$ to $[Mn(L^{bi})_3]^{2+}$, obtained after 410-nm excitation of $[Mn(L^{bi})_3]^+$ (20 µM) in presence of 1 M CCl_4 in de-aerated CH_3CN. All spectra measured at 20 °C, using pulse durations and energies of 10 ns and 6 mJ, respectively. Delay and integration times were 200 ns / 200 ns for (a), 200 ns / 500 µs for (b), 10 ns / 200 ns for (c) and (d).

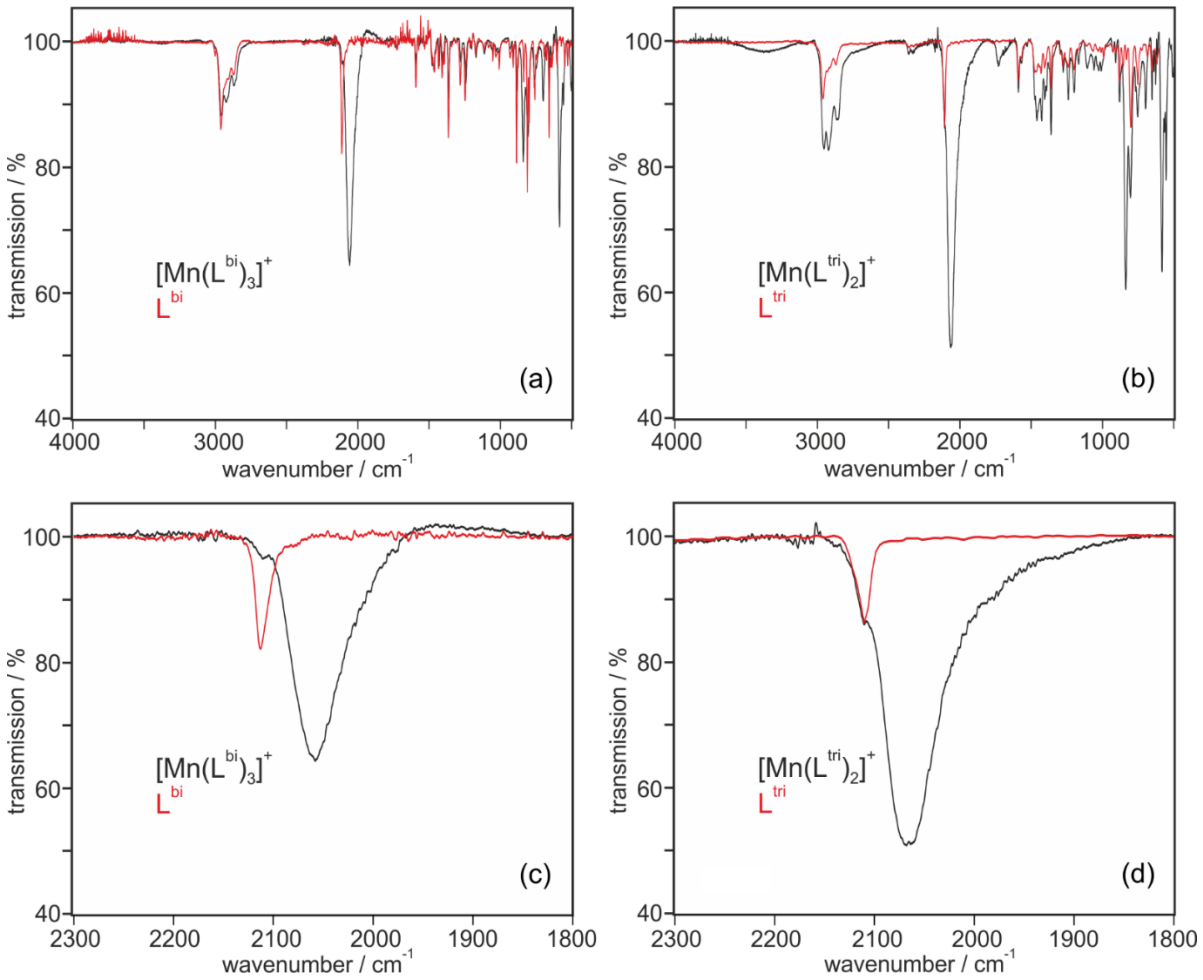

Figure S28. Solid state infrared spectra of complexes (black traces) and ligands (red traces): (a) $[Mn(L^{bi})_3]^+$ and L^{bi}; (b) $[Mn(L^{tri})_2]^+$ and L^{tri}. (c, d) Spectral region of the isocyanide (C≡N) stretching vibration on enlarged scales.

The isocyanide stretch frequency (υ_{CN}) for L^{bi} is 2120 cm^{-1} and shifts to 2064 cm^{-1} in $[Mn(L^{bi})_3]^+$. For L^{tri}, υ_{CN} is identical as for L^{bi} (2120 cm^{-1}), and in $[Mn(L^{tri})_2]^+$ it shifts to 2081 cm^{-1}. This indicates that π-backbonding is stronger in $[Mn(L^{bi})_3]^+$ than in $[Mn(L^{tri})_2]^+$, as noted in the main paper.

Mn-C vibrations ($\upsilon_{Mn\text{-}C}$) are observable at 568 cm^{-1} for $[Mn(L^{bi})_3]^+$ and at 584 cm^{-1} for $[Mn(L^{tri})_2]^+$.

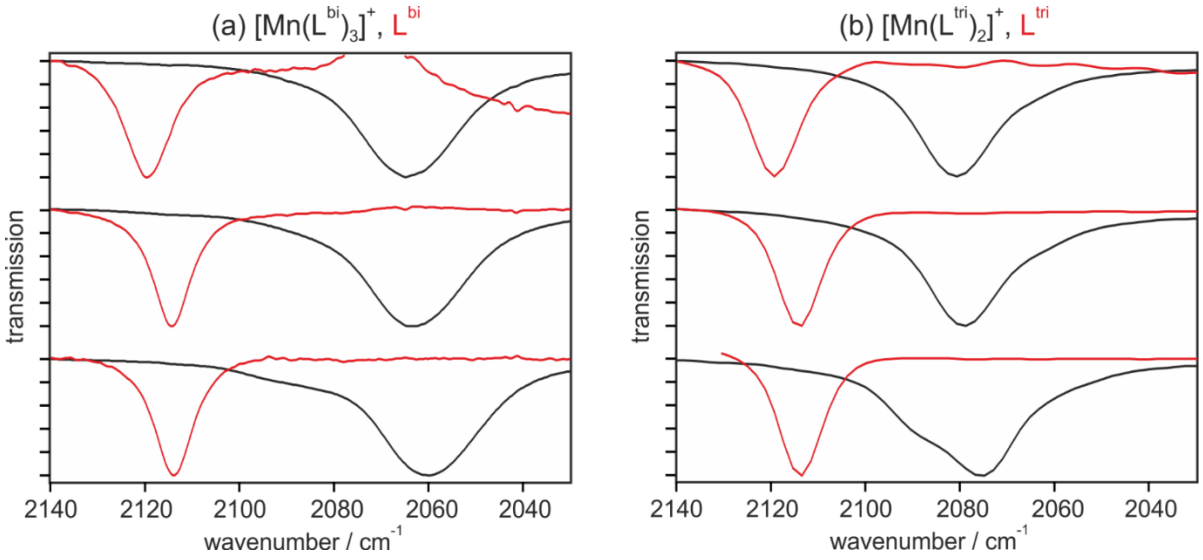

Figure S29. Infrared spectra of complexes (black traces) and ligands (red traces) in CH_3CN (top), THF (middle) and toluene (bottom) at 20 °C: (a) $[Mn(L^{bi})_3]^+$ and L^{bi}; (b) $[Mn(L^{tri})_2]^+$ and L^{tri}.

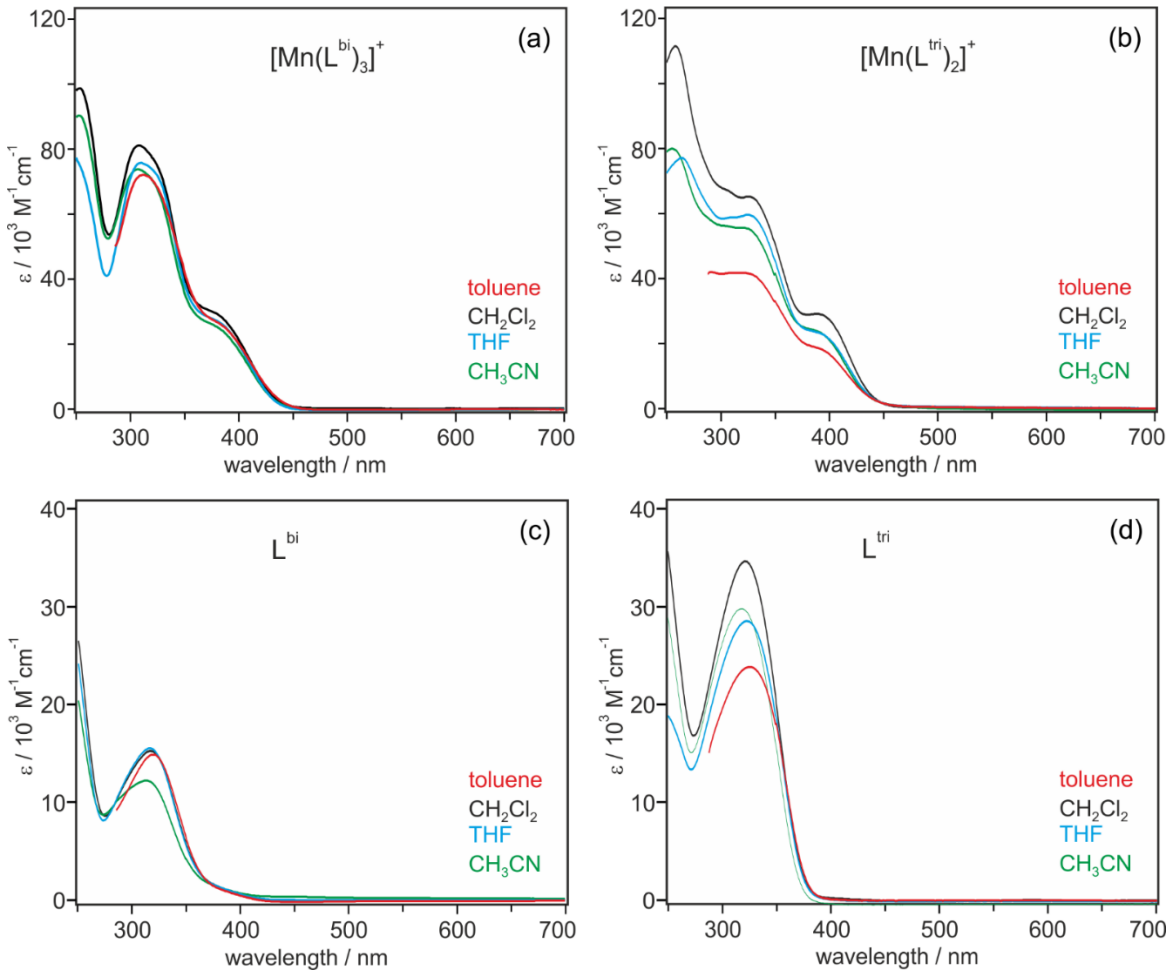

Figure S30. UV-Vis absorption spectra of (a) $[Mn(L^{bi})_3]^+$, (b) $[Mn(L^{tri})_2]^+$, (c) L^{bi}, and (d) L^{tri} in different solvents at 20 °C.

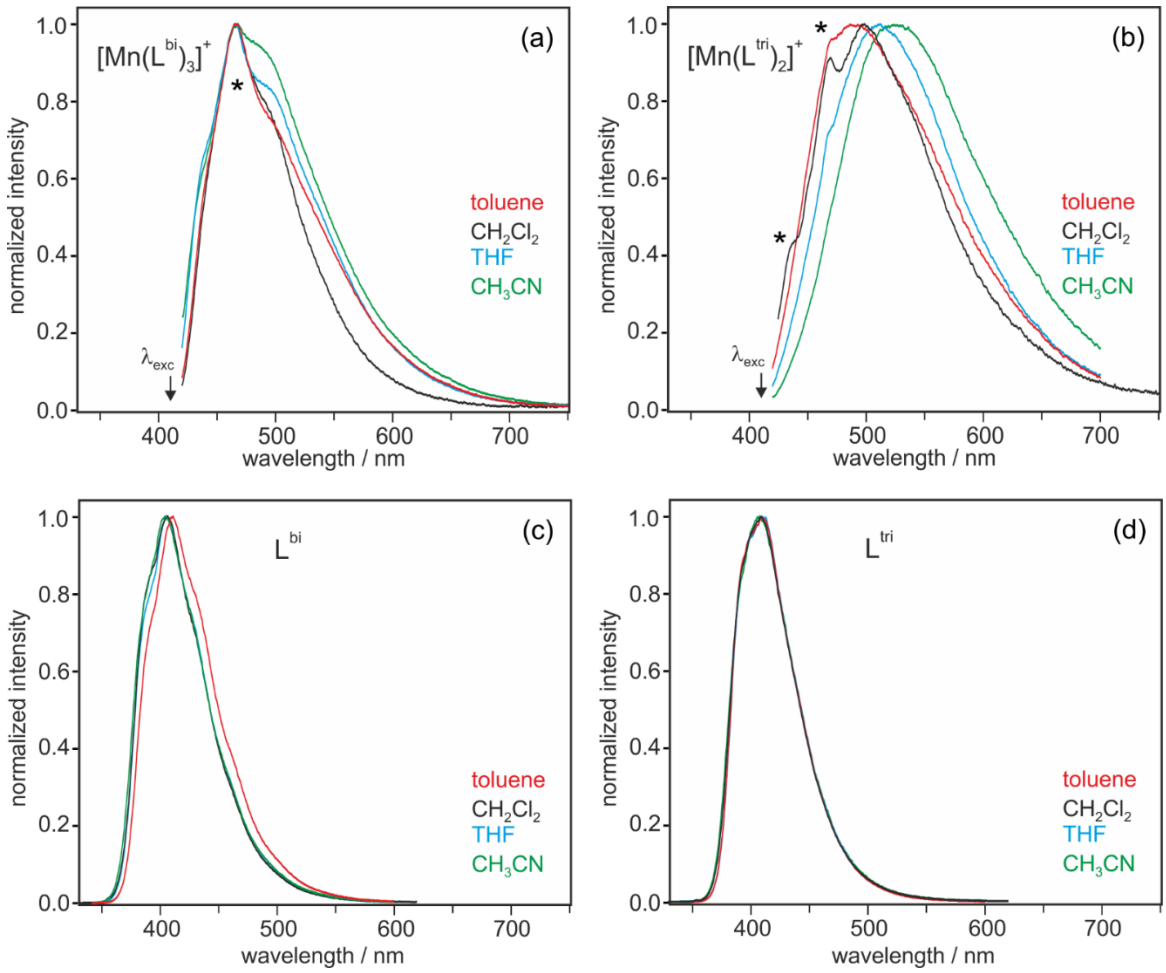

Figure S31. Luminescence spectra of (a) $[Mn(L^{bi})_3]^+$, (b) $[Mn(L^{tri})_2]^+$, (c) L^{bi}, and (d) L^{tri} in different de-aerated solvents at 20 °C. Excitation of the Mn^I complexes occurred at 410 nm (arrows), the free ligands were excited at 320 nm. The asterisks mark peaks that are due to Raman-scattered excitation light.

Table S2. Maxima of major absorption bands of $[Mn(L^{bi})_3]^+$, **L^{bi}**, $[Mn(L^{tri})_2]^+$ and **L^{tri}** (with extinction coefficients) as well as emission maxima after excitation at 410 nm (complexes) or 320 nm (free ligands).

	$[Mn(L^{bi})_3]^+$	**L^{bi}**	$[Mn(L^{tri})_2]^+$	**L^{tri}**
$\lambda_{max, abs}$ [nm][a]	307	313	325	318
(ε [$M^{-1}cm^{-1}$])[a]	(73500)	(12200)	(55200)	(29800)
	385		395	
	(23800)		(22500)	
$\lambda_{max, em}$ [nm][a]	485	404	525	408
$\lambda_{max, em}$ [nm][b]	480		480	
	620		600	

[a] in MeCN at 20 °C; [b] in 2-methyl-THF at 77K.

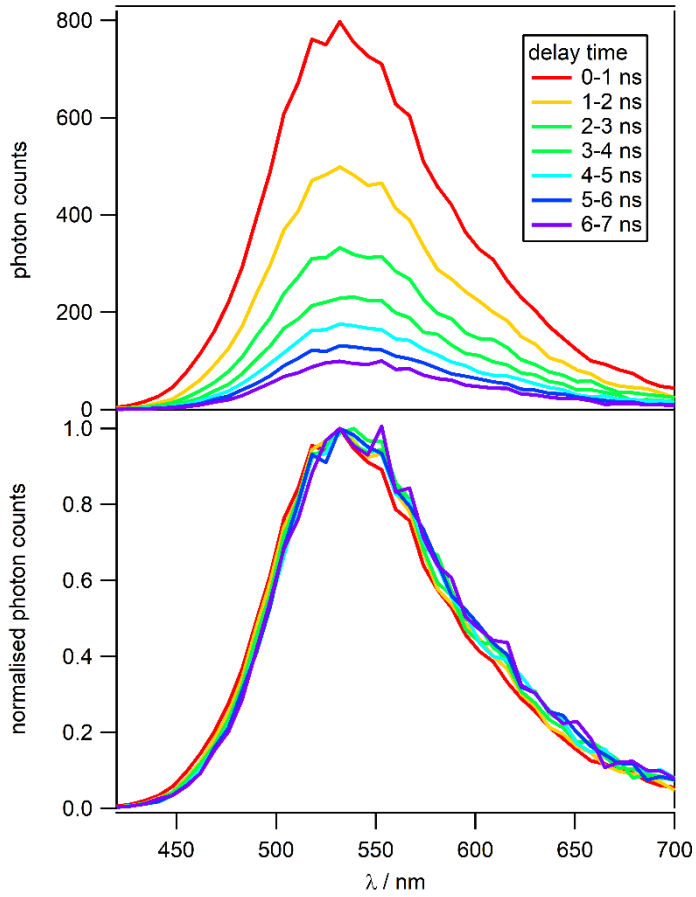

Figure S32. Time-gated luminescence spectra (from TCSPC measurements) of $[Mn(L^{tri})_2]^+$ in de-aerated MeCN at 20 °C following excitation at 405 nm. Emission decay curves were measured over a 50-ns time window at wavelengths between 430 and 700 nm (in 7-nm increments). The photon counts of the individual decay curves at the times indicated in the inset (0-7 ns, integrated over 1 ns) were then plotted as a function of detection wavelength to obtain the emission spectra. The upper panel contains the raw data, in the lower panel all spectra are normalized to the same maximum.

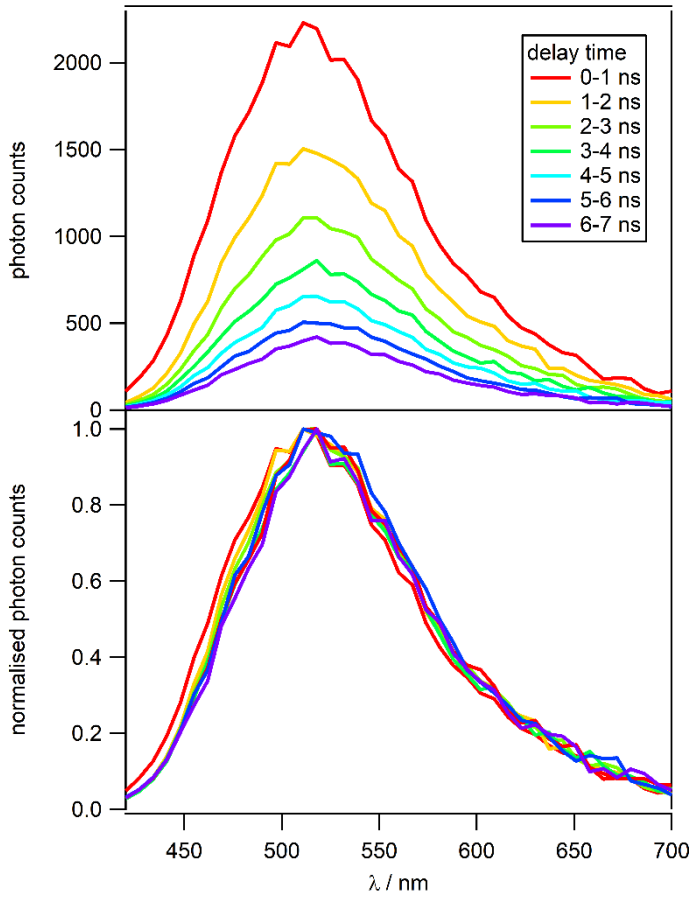

Figure S33. Time-gated luminescence spectra (from TCSPC measurements) of $[Mn(L^{bi})_3]^+$ in de-aerated MeCN at 20 °C following excitation at 405 nm. Emission decay curves were measured over a 50-ns time window at wavelengths between 430 and 700 nm (in 7-nm increments). The photon counts of the individual decay curves at the times indicated in the inset (0-7 ns, integrated over 1 ns) were then plotted as a function of detection wavelength to obtain the emission spectra. The upper panel contains the raw data, in the lower panel all spectra are normalized to the same maximum.

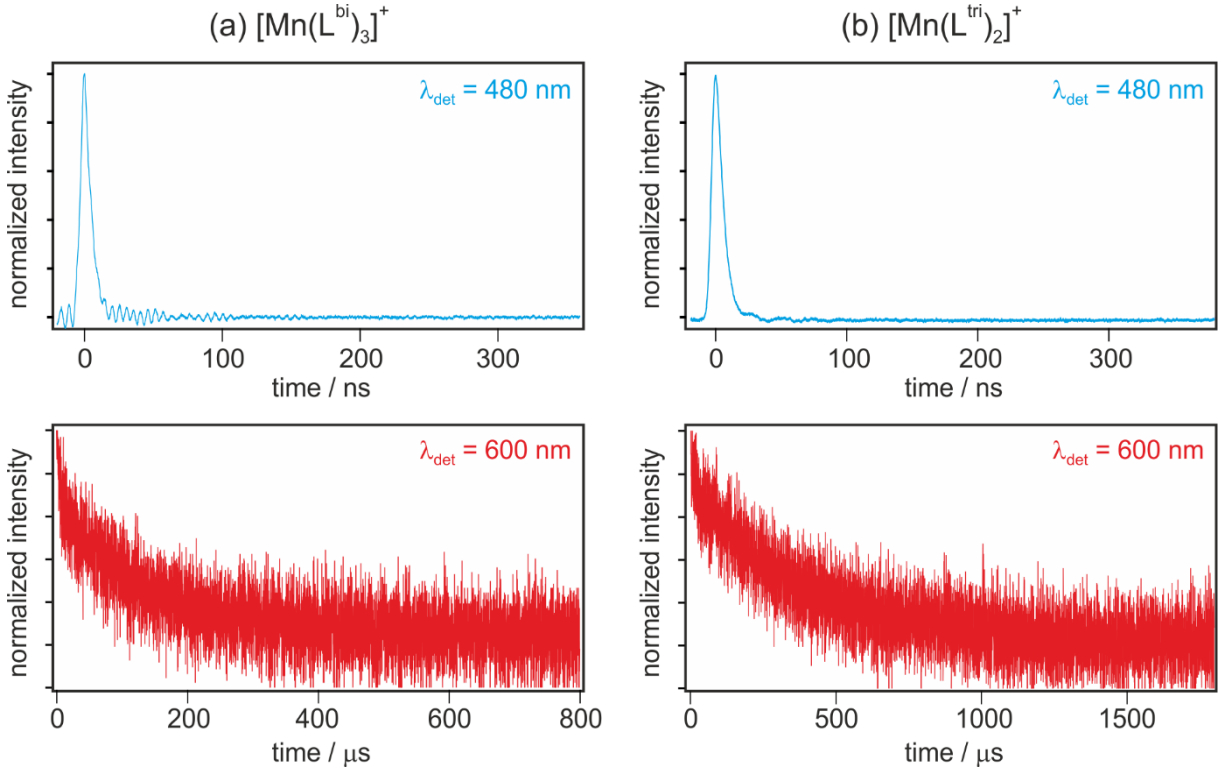

Figure S34. Luminescence decays measured for (a) $[Mn(L^{bi})_3]^+$ and (b) $[Mn(L^{tri})_2]^+$ in de-aerated 2-methyl-THF at 77 K. Excitation occurred at 410 nm, detection was at 480 nm (blue traces) and at 600 nm (red traces).

Luminescence quantum yields Φ of $[Mn(L^{bi})_3](PF_6)$ and $[Mn(L^{tri})_2](PF_6)$ in degassed CH_3CN at 20 °C were determined by a comparative method relative to $[Ru(bpy)_3](PF_6)_2$ in aerated CH_3CN ($\Phi_R = 0.018$)[5]. Double determinations at three different excitation wavelengths were performed. Optical densities for the Mn(I) complexes were ca. 0.1 (at 405 nm) while the concentration of $[Ru(bpy)_3](PF_6)_2$ was as high as possible (highest OD at excitation wavelength, 0.051) without the resulting emission exceeding the detector limit. Under these conditions, two concentrations of $[Ru(bpy)_3](PF_6)_2$ were chosen: at the higher concentration, the entrance and exit slits of the spectrometer were 3 nm each while at the lower concentration they were 5 nm (for all compounds of each series).

When using the same solvent (CH_3CN) for all compounds, the luminescence quantum yield (Φ) of the Mn(I) complexes can be determined from equation S4 (where Φ_R is the known luminescence quantum yield of the $[Ru(bpy)_3](PF_6)_2$ reference, see above).

$$\Phi = \Phi_R \times \frac{I}{OD} \times \frac{OD_R}{I_R} \qquad \text{(eq. S4)}$$

Using the experimentally determined optical densities of the Mn(I) complexes (OD) and the $[Ru(bpy)_3](PF_6)_2$ reference (OD_R) at the excitation wavelength, the luminescence quantum yields Φ reported in Table S3 were determined as the average of the values obtained at 405, 410 and 415 nm.

Table S3. Luminescence quantum yields for the Mn(I) complexes in degassed CH_3CN. [a] higher concentration of $[Ru(bpy)_3](PF_6)_2$ with slit width of 3 nm. [b] lower concentration of $[Ru(bpy)_3](PF_6)_2$ with slit width of 5 nm, see text above for further details.

	Φ [%]			$\Phi_{average}$ [%]
	λ_{exc} = 405	λ_{exc} = 410	λ_{exc} = 415	
$[Mn(L^{bi})_3](PF_6)$[a]	0.051	0.048	0.049	0.049
$[Mn(L^{bi})_3](PF_6)$[b]	0.044	0.041	0.042	0.042
				0.046 ±
$[Mn(L^{tri})_2](PF_6)$[a]	0.027	0.028	0.033	0.029
$[Mn(L^{tri})_2](PF_6)$[b]	0.023	0.024	0.029	0.025

0.027 ±

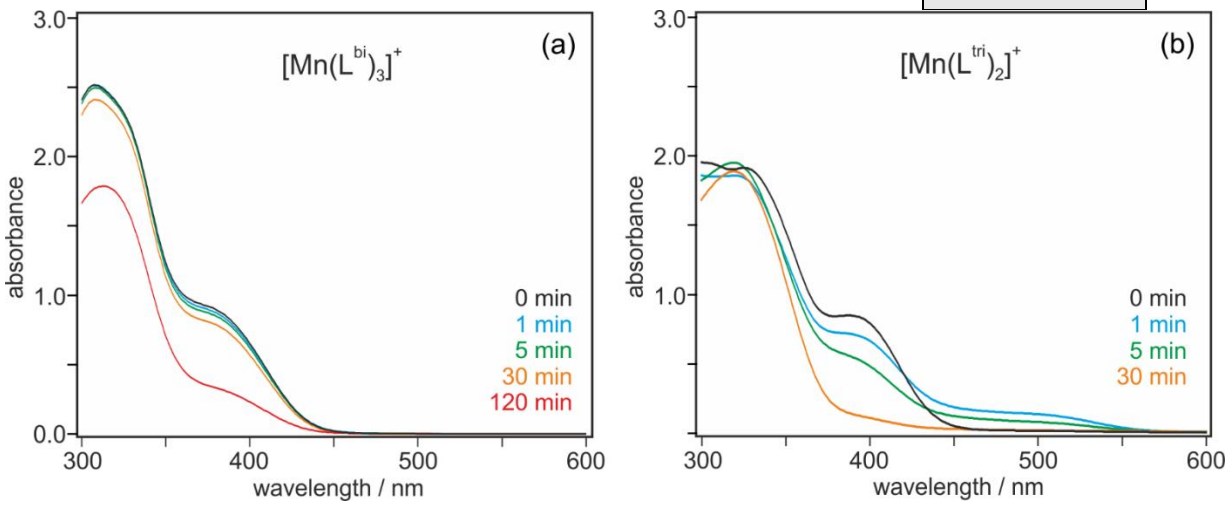

Figure S35. Photostability experiments: UV-Vis absorption spectra of (a) $[Mn(L^{bi})_3]^+$ and (b) $[Mn(L^{tri})_2]^+$ in de-aerated CH_2Cl_2 at 20 °C after different times of irradiation with a 665 mW collimated LED at 405 nm.

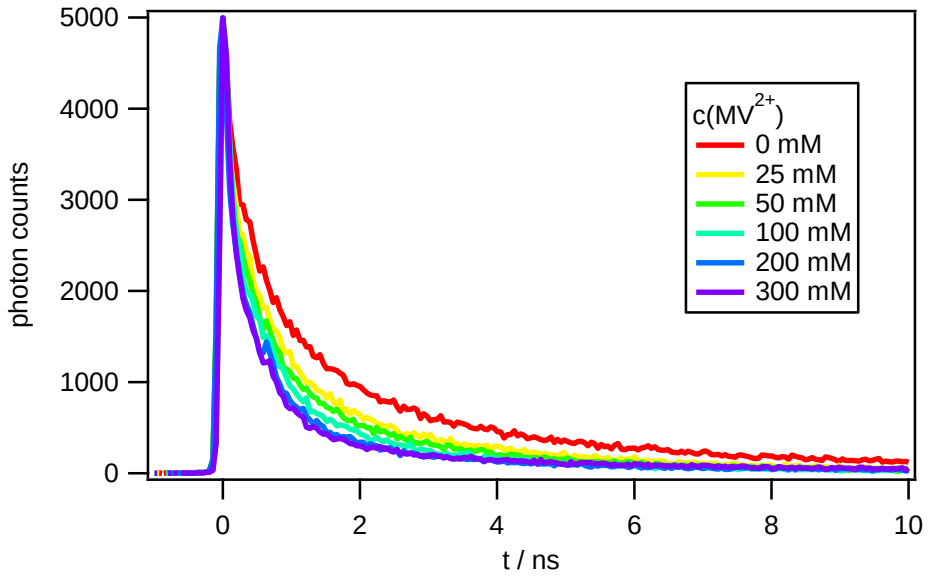

Figure S36. Luminescence decays of $[Mn(L^{tri})_2]^+$ (20 µM) detected at 510 nm after excitation at 405 nm in the absence (red trace) and in the presence of different concentrations of methyl viologen (MV^{2+}, see inset) in de-aerated MeCN at 20 °C.

As noted in the main paper (Table 1) and as discussed on page S78, the luminescence decays are tri-exponential, and this renders Stern-Volmer analysis of the data in Figure S36 difficult. The mean MLCT excited-state lifetime of $[Mn(L^{tri})_2]^+$ in de-aerated CH_3CN at 20 °C is 1.73 ns (with individual decay components featuring lifetimes in the range from 0.374 to 5.82 ns (Table 1)), which corresponds to a mean MLCT decay rate constant of $5.8 \cdot 10^8$ s^{-1}. The fact that substantial (about 50 %) MLCT luminescence quenching is observable at a MV^{2+} concentration of 0.3 M therefore indicates that under these conditions the inherent MLCT excited-state decay rate and the rate for electron transfer from MLCT-excited $[Mn(L^{tri})_2]^+$ to MV^{2+} are on the same order of magnitude, roughly $5 \cdot 10^8$ s^{-1} to 10^9 s^{-1}.

For the rate constant of bimolecular photoinduced electron transfer (k_{ET}) between $[Mn(L^{tri})_2]^+$ and MV^{2+}, we therefore estimate that $k_{ET} \approx 10^9$ s^{-1} / 0.3 M $\approx 3 \cdot 10^9$ M^{-1} s^{-1}. This is below the diffusion limit of $1.9 \cdot 10^{10}$ M^{-1} s^{-1} for CH_3CN at 25 °C, but electrostatic repulsion between monocationic $[Mn(L^{tri})_2]^+$ and dicationic MV^{2+} could account for sub-diffusion limit kinetics in spite of favorable reaction thermodynamics (driving force of ca. 1 eV for photoinduced electron transfer).

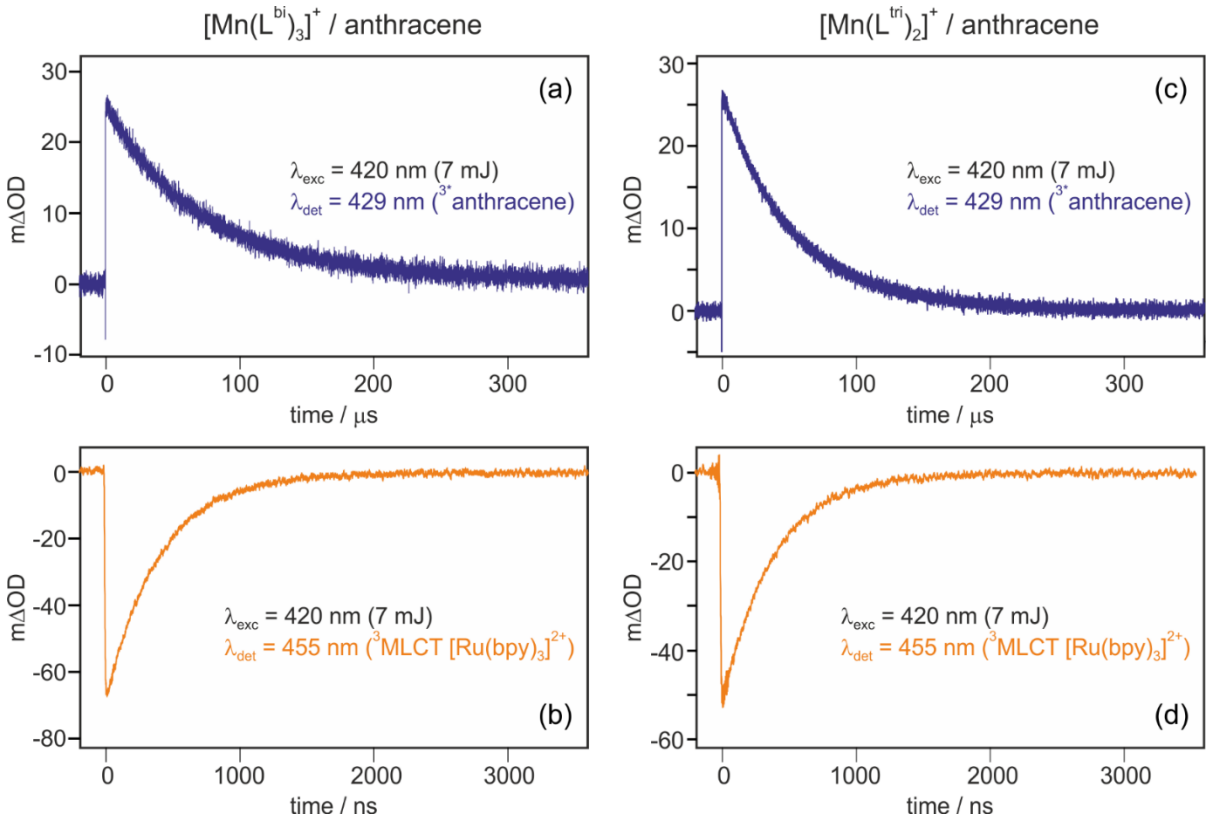

Figure S37. Relative actinometry experiments: (a) Formation and decay of the anthracene T_1 state (^{3*}anthracene) following excitation of $[Mn(L^{bi})_3]^+$ (25 µM) in presence of 40 mM anthracene in de-aerated toluene at 20 °C. (b) Bleach (and recovery) of the MLCT absorption of $[Ru(bpy)_3]Cl_2$ in de-aerated water under identical conditions; the concentration of the ruthenium complex was adjusted such that the solution had the same absorbance at the excitation wavelength as the solution from (a). (c) Analogous data set as in (a) for $[Mn(L^{tri})_2]^+$ (20 µM) in presence of 40 mM anthracene in de-aerated toluene at 20 °C. (d) Analogous data set as in (b), with the $[Ru(bpy)_3]Cl_2$ concentration adjusted such that the solution had the same absorbance at the excitation wavelength as the solution from (c). Excitation (λ_{exc}) and detection wavelengths (λ_{det}) are indicated in the insets.

Table S4. Data extracted from the relative actinometry experiments in Figure S37, using

$\Delta\varepsilon = -10'100\ M^{-1}\ cm^{-1}$ for $[Ru(bpy)_3]^{2+}$ in water at 455 nm[6], and $\varepsilon = 45'500\ M^{-1}\ cm^{-1}$ for the anthracene T_1 state at 429 nm[7]. The efficiency of energy transfer (η) corresponds to the ratio between the concentration of anthracene in the T_1 state and the concentration of $[Ru(bpy)_3]^{2+}$ in ^{3}MLCT state.

	$[Mn(L^{bi})_3]^+$	$[Mn(L^{tri})_2]^+$
$[Ru(bpy)_3]^{2+}$ MLCT bleach at 455 nm	-0.069	-0.054
conc. of $[Ru(bpy)_3]^{2+}$ in ^{3}MLCT state	6.83 µM	5.35 µM
absorbance of anthracene in T_1 state at 430 nm	0.0257	0.0260
conc. of anthracene in T_1 state	0.565 µM	0.571 µM
efficiency (η) of energy transfer	8.3%	10.7%
efficiency ($\eta_{TTET,exp}$) of energy transfer, corrected for differences in refractive indices (toluene vs. water)	9.4%	12.1%

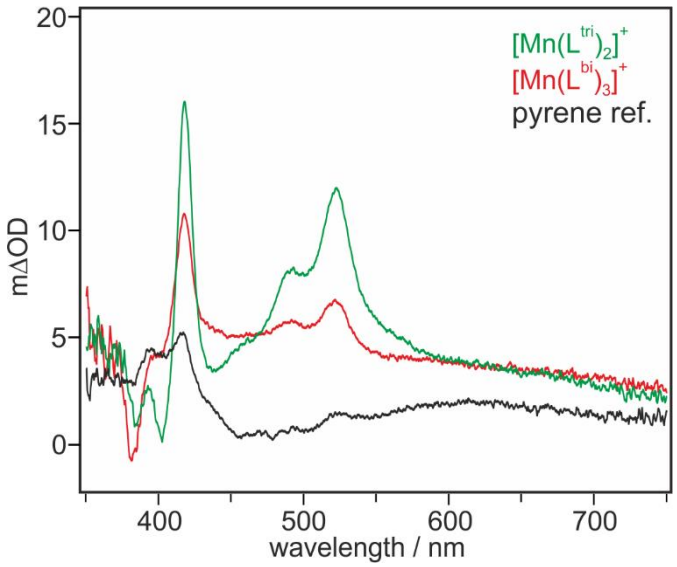

Figure S38. Transient absorption (TA) spectra after excitation of $[Mn(L^{bi})_3]^+$ (red trace, 25 µM) and $[Mn(L^{tri})_2]^+$ (green trace, 25 µM) at 420 nm in presence of 40 mM pyrene in de-aerated CH_2Cl_2 at 20 °C. Reference spectrum of 40 mM pyrene in de-aerated CH_2Cl_2 at 20 °C (black trace). All spectra were integrated over 200 ns after a detection delay of 200 ns.

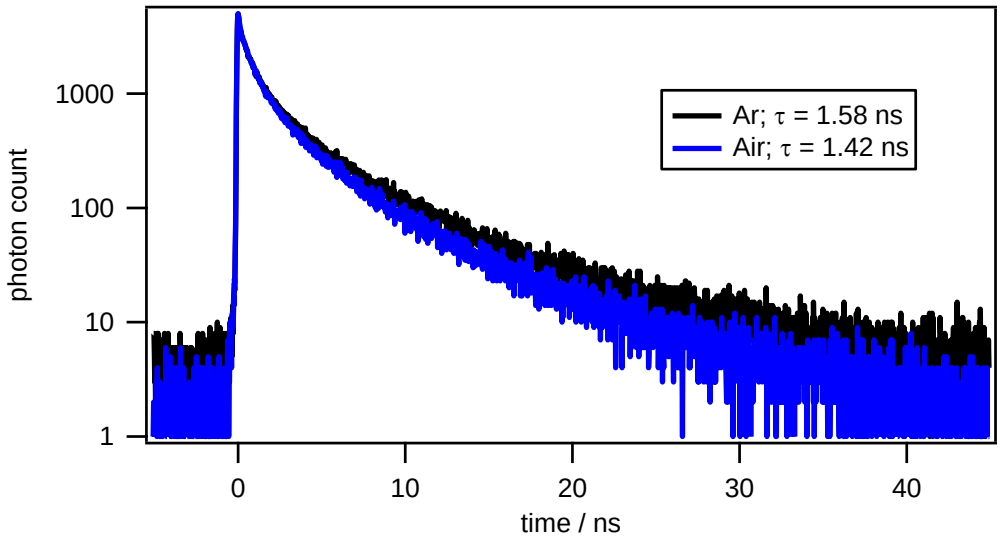

Figure S39. Luminescence decay and average luminescence lifetimes of $[Mn(L^{tri})_2]^+$ after excitation at 405 nm in aerated MeCN (blue) and under Ar atmosphere (black) at 20 °C. The indicated average lifetimes (τ) are weighted averages from triexponential fits.

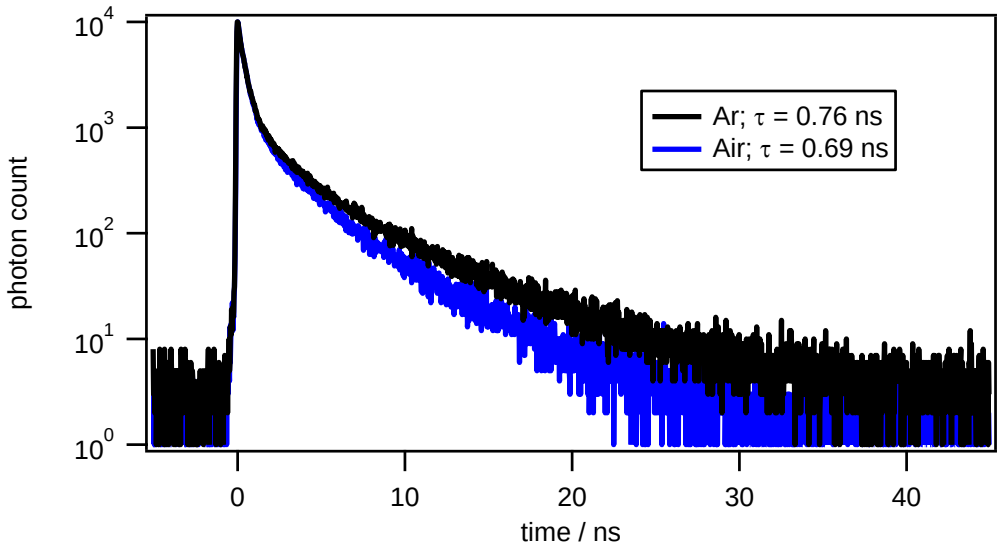

Figure S40. Luminescence decay and average luminescence lifetimes of $[Mn(L^{bi})_3]^+$ after excitation at 405 nm in aerated MeCN (blue) and under Ar atmosphere (black) at 20 °C. The indicated average lifetimes (τ) are weighted averages from triexponential fits.

These oxygen quenching experiments are inconclusive as far as the question whether the emissive MLCT state at 2.9 eV is singlet or triplet, because that state is sufficiently reducing (E_{ox}^* = -1.9 V vs SCE) for generation of superoxide radical

anion such that both energy and electron transfer quenching pathways are feasible.

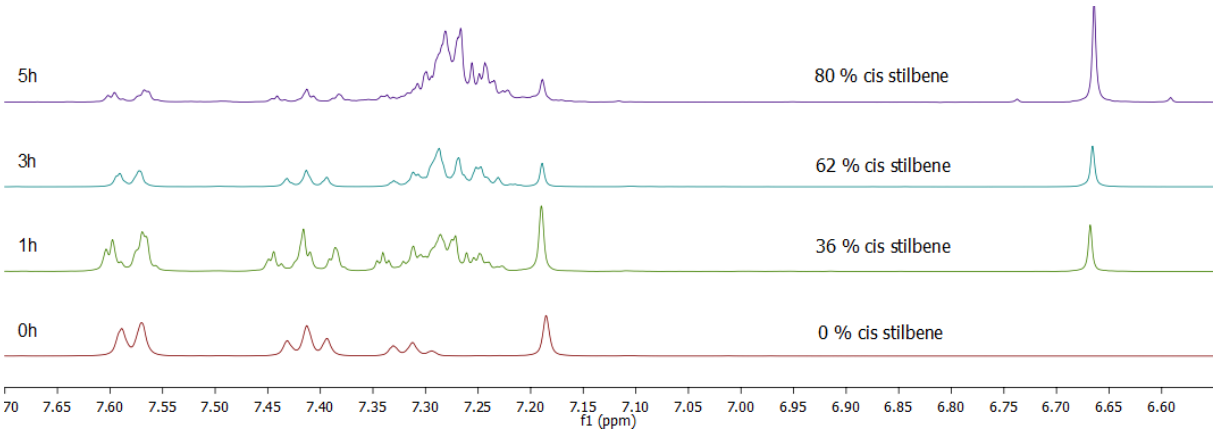

Figure S41. Photo-isomerization experiments: ^{1}H-NMR spectra obtained after different irradiation times from a solution containing 2 mM $[Mn(L^{bi})_3]^+$ and 50 mM *trans*-stilbene in de-aerated CD_2Cl_2. Irradiation occurred with a 45 W (power input) LED at 440 nm.

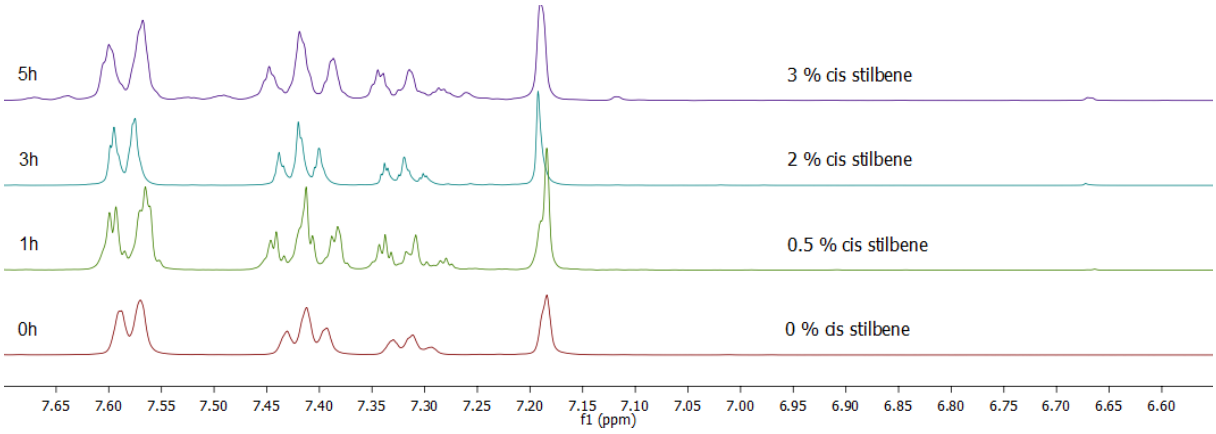

Figure S42. Reference experiment to the photo-isomerization in Figure S41: ^{1}H-NMR spectra obtained after different irradiation times from a solution containing 50 mM *trans*-stilbene (but no $[Mn(L^{bi})_3]^+$) in de-aerated CD_2Cl_2. Irradiation occurred with the same light source as in Fig S44.

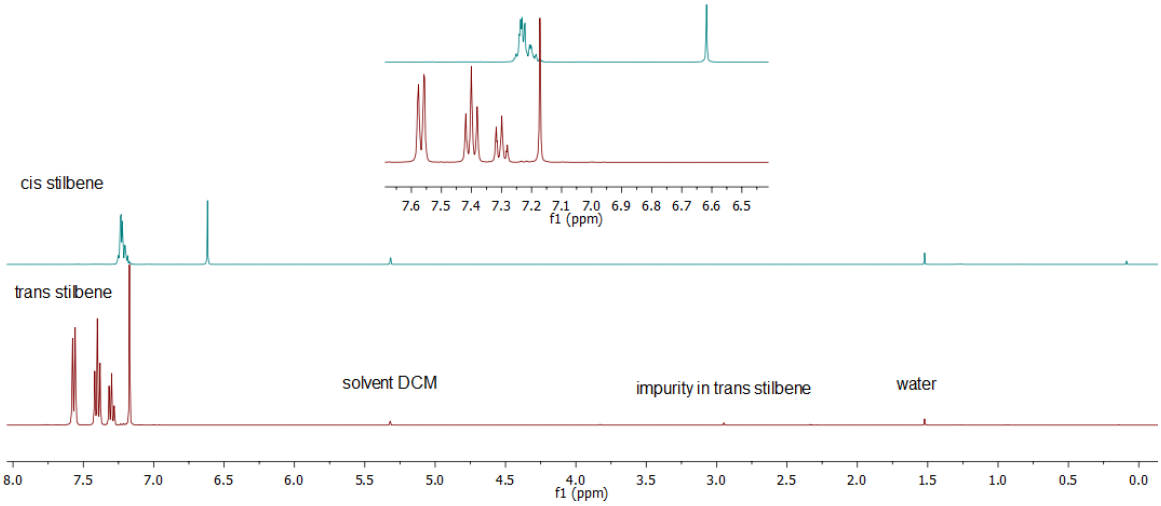

Figure S43. ^{1}H-NMR spectra of neat *cis*- and *trans*-stilbene in CD_2Cl_2.

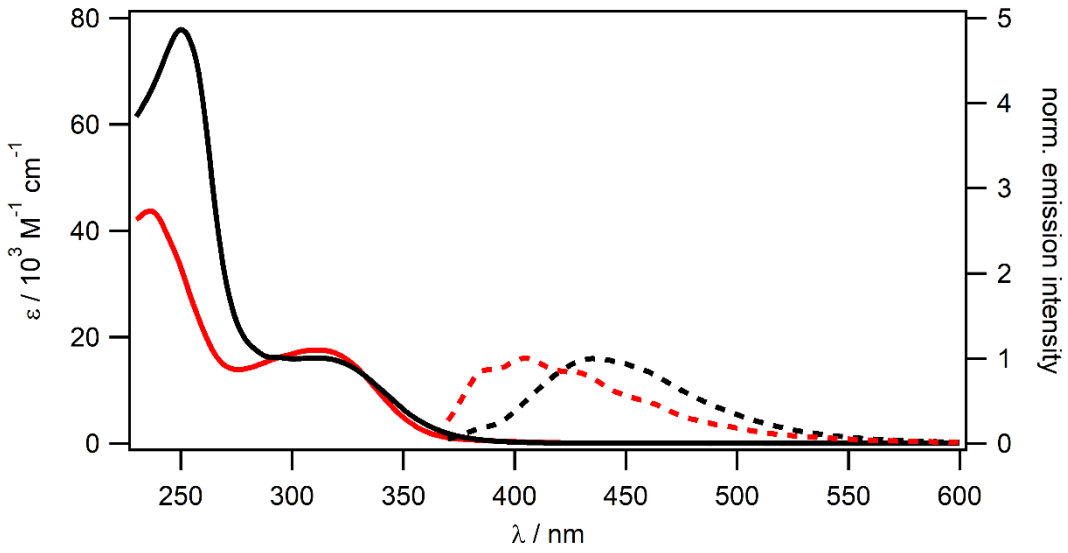

Figure S44. Absorption (solid lines) and normalized luminescence spectra (dashed lines) of [$ZnCl_2(L^{bi})$] (black) and **L^{bi}** (red) in a 1:1 mixture of isopentane and DCM at 20 °C. Luminescence was recorded after excitation at 355 nm.

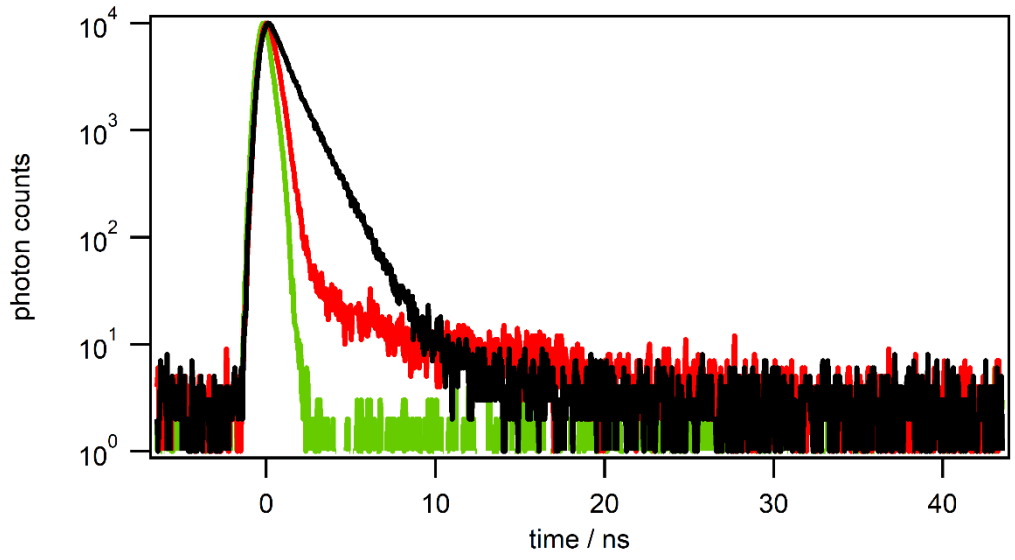

Figure S45. Luminescence decays of [$ZnCl_2(L^{bi})$] (black) and **L^{bi}** (red) in a 1:1 mixture of isopentane and DCM after excitation with a 313 nm laser (in a TCSPC setup) at 20 °C. The luminescence lifetime of [$ZnCl_2(L^{bi})$] under these conditions is 1.24 ns and 0.3 ns for **L^{bi}**. Both lifetimes were obtained using a reconvolution fit with the instrument response function (IRF, green) of the TCSPC setup.

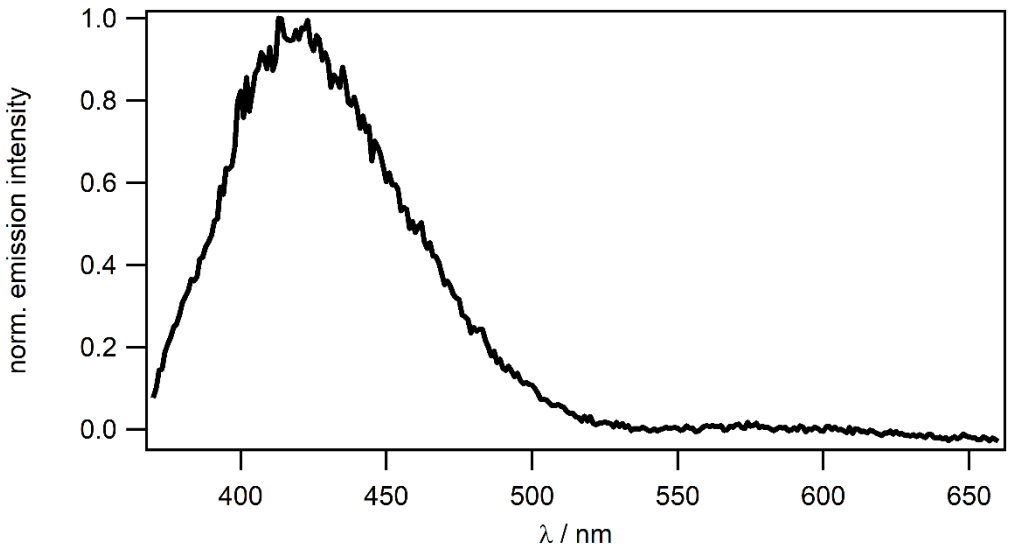

Figure S46. Normalized luminescence of [$ZnCl_2(L^{bi})$] at 77 K in a 1:1 mixture of isopentane and DCM after 355 nm excitation. The luminescence lifetime is instrumentally limited on the available LP920-KS setup.

The luminescence spectrum in Figure S46 shows a prominent band centered at 420 nm, which is attributed to fluorescence from the same $^1\pi$-π^* excited state as the room temperature emission in Figure S44 (dashed black trace). There is no clear evidence for phosphorescence from a $^3\pi$-π^* excited state, suggesting that intersystem crossing in [$ZnCl_2(L^{bi})$] is inefficient. Due to the absence of a clear phosphorescence signal, the energy of the lowest $^3\pi$-π^* excited state in this Zn(II) complex was determined using the triplet-triplet energy transfer experiments presented below (Figure S47).

The lack of ligand field stabilization in the $3d^{10}$ electron configuration makes the Zn(II) complex inherently less stable than the low-spin $3d^6$ Mn(I) complexes. Consequently, [$ZnCl_2(L^{bi})$] is considerably more substitution-labile than the Mn(I) complexes. Only non-coordinating solvents can be used for [$ZnCl_2(L^{bi})$], whilst solvents such as THF, CH_3CN or water cannot be employed. 1:1 (v:v) mixtures of isopentane and CH_2Cl_2 provide a good compromise between stability and solubility, and furthermore this mixture can be used for 77 K measurements.
Furthermore, [$ZnCl_2(L^{bi})$] does not absorb in the visible spectral range due to lack of MLCT absorption bands (Figure S44). Under UV-irradiation the Zn(II) complex is substantially less photo-robust than the Mn(I) complexes under visible excitation,

and consequently no photoreactions following direct excitation of the Zn(II) complex could be investigated. A further complication of photoreactions in which $[ZnCl_2(L^{bi})]$ is designed to act as photosensitizer (present at micromolar concentrations) is the fact that many possible reaction partners (for example triplet energy acceptors, typically present in millimolar concentrations) have non-negligible molar extinction coefficients at 355 nm.

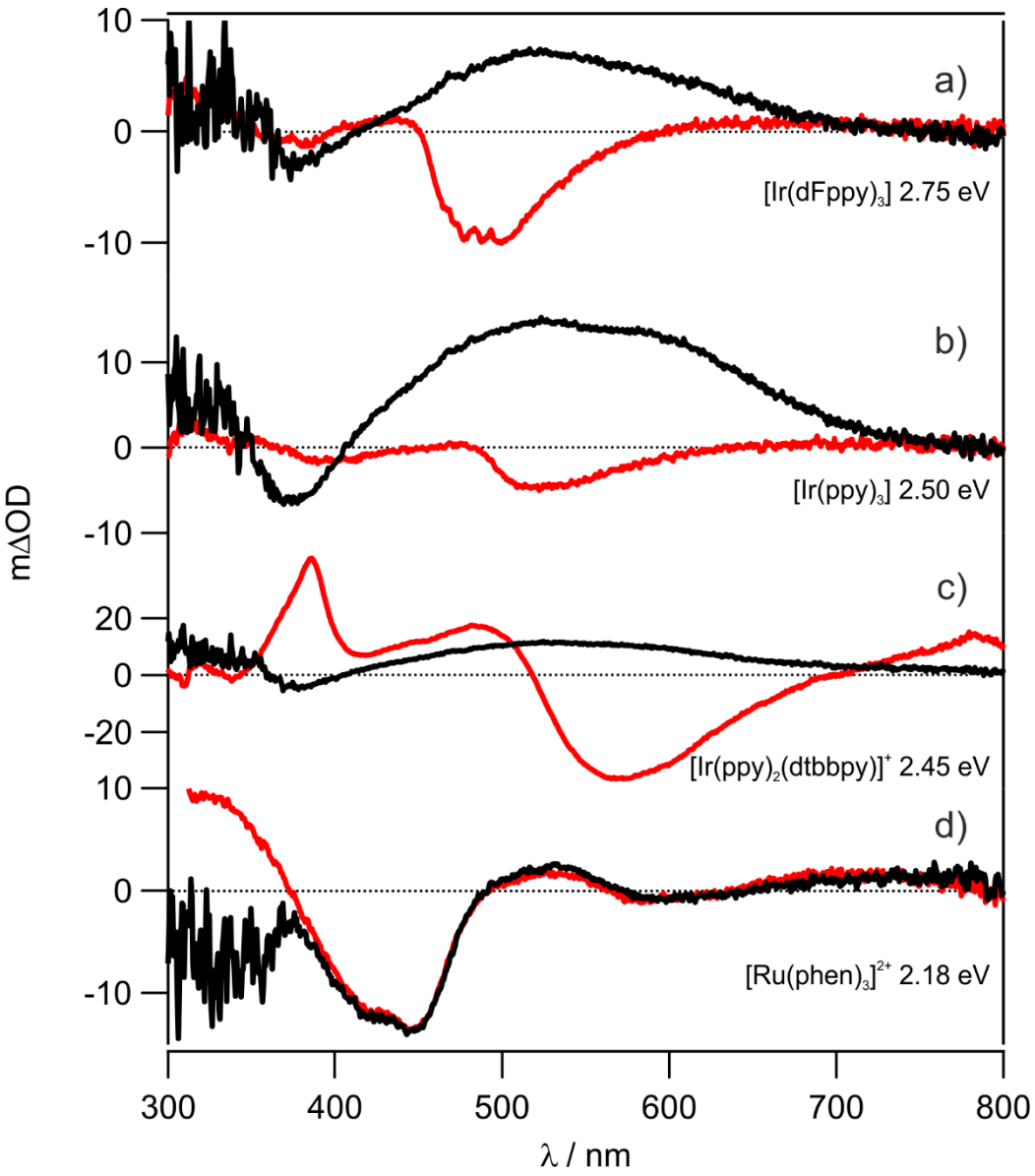

Figure S47. Transient absorption spectra after triplet-triplet energy transfer (TTET) from different photosensitizers to [$ZnCl_2(L^{bi})$]. De-aerated dichloromethane solutions contained 20 μM photosensitizer and 1 mM [$ZnCl_2(L^{bi})$] (black traces) or only 20 μM photosensitizer without any Zn(II) complex (red traces), measurements occurred after (selective) excitation of the Ir/Ru photosensitizers at 410 nm (for (a) and (b)), 420 nm (c) and 450 nm (d) at 20 °C. Black traces were recorded with a delay of 4 μs after excitation with pulses of ca. 10 ns duration. (a) *fac*-[$Ir(dFppy)_3$] photosensitizer (dFppy = 2-(2,4-difluorophenyl)-pyridine) with a triplet energy (E_T) of 2.75 eV[8,9]; (b) *fac*-[$Ir(ppy)_3$] photosensitizer (ppy = 2-phenylpyridine) with E_T = 2.50 eV[8,10]; (c) $[Ir(ppy)_2(dtbbpy)]^+$ photosensitizer (dtbbpy = 4,4'-di-*tert*-butyl-2,2'-

bipyridine) with E_T = 2.45 eV (see below); (d) $[Ru(phen)_3]^{2+}$ photosensitizer (phen = 1,10'-phenanthroline) with E_T = 2.18 eV[8].

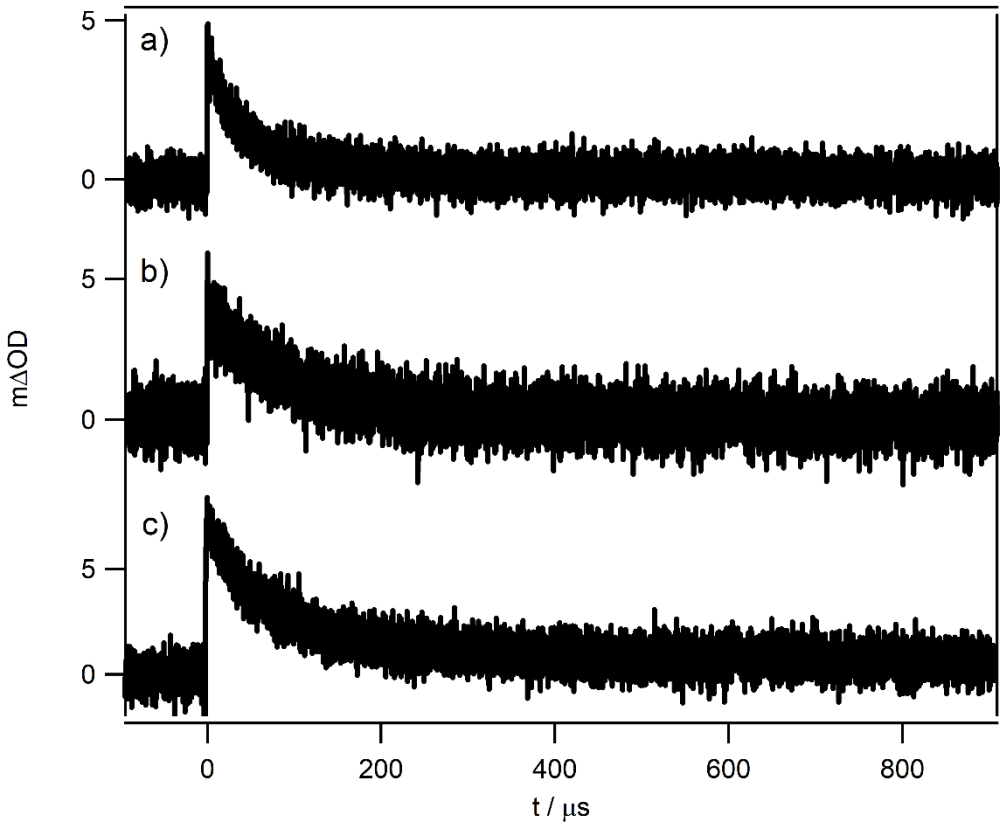

Figure S48. Excited state absorption decay at 600 nm of a de-aerated dichloromethane solution of a) $[Ir(dFppy)_3]$ (20 µM); b) $[Ir(ppy)_3]$ (20 µM); c) $[Ir(ppy)_2(dtbbpy)]^+$ (20 µM) each with $[ZnCl_2(L^{bi})]$ (1 mM) after photoexcitation at 410 nm (for a) and b)) and 420 nm (for c)) (Figure S47a-c). The excited state absorption signals decay with lifetimes of 48, 99 and 86 µs, respectively, at 20 °C.

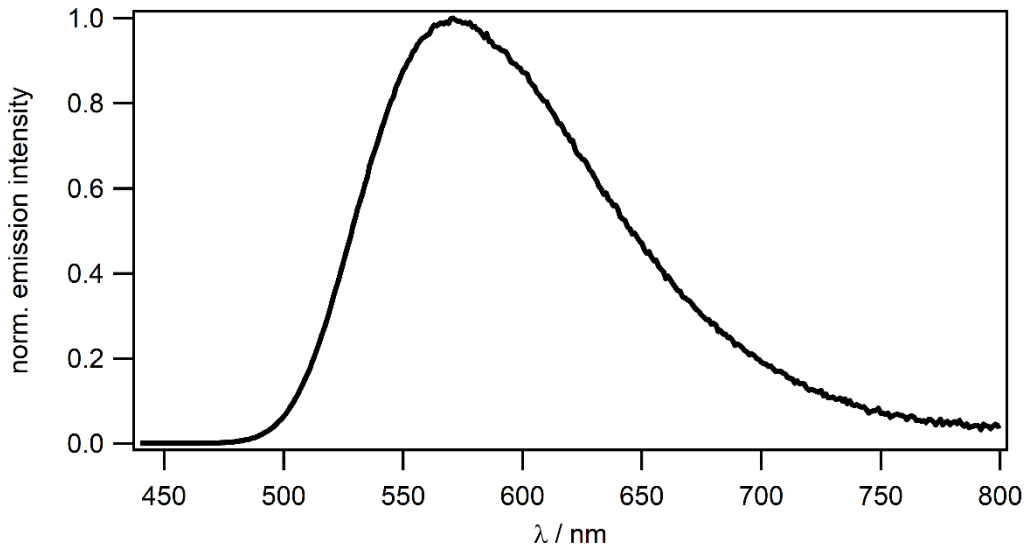

Figure S49. Luminescence of $[Ir(ppy)_2(dtbbpy)]PF_6$ (20 µM) in de-aerated dichloromethane at 20 °C after excitation at 420 nm. The triplet energy (E_T) was estimated from the wavelength on the high-energy side of the spectrum at which the intensity corresponds to 10 % of the maximum emission intensity. Previously reported triplet energies for this compound seem inaccurate[8,11], because the wavelength of the emission band maximum was used as approximation.

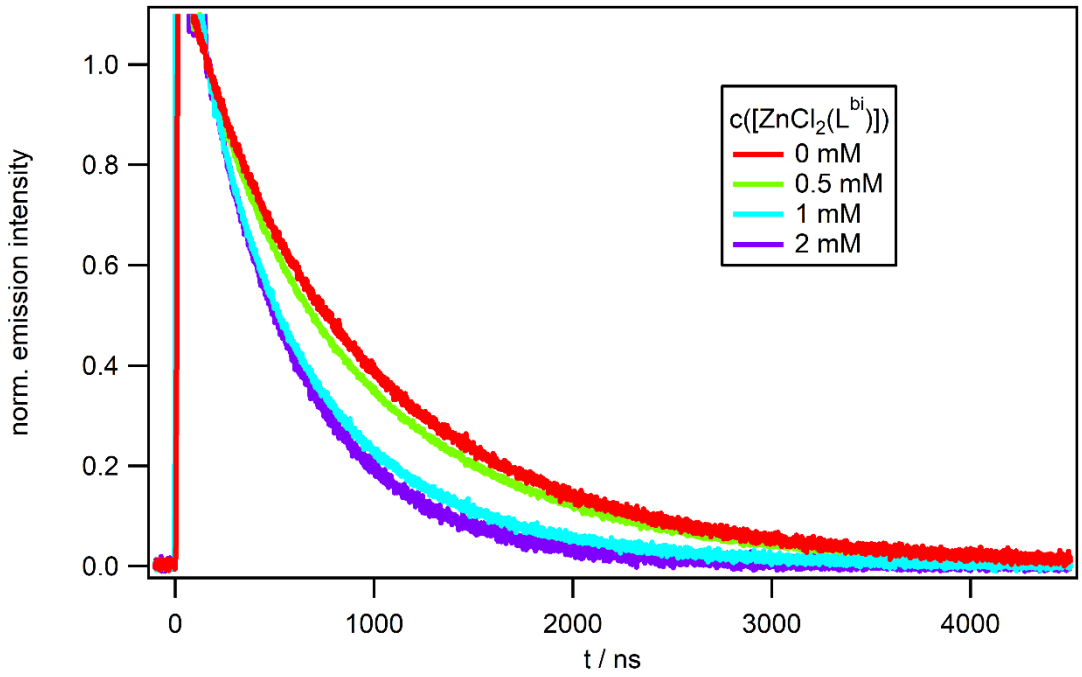

Figure S50. Luminescence lifetime quenching of *fac*-[Ir(dFppy)$_3$] (20 µM) with different concentrations of [ZnCl$_2$(L^{bi})] as quencher in de-aerated dichloromethane at 20 °C. Selective excitation of *fac*-[Ir(dFppy)$_3$] occurred at 410 nm with laser pulses of ca. 10 ns duration, the emission signal was detected at 600 nm. Single-exponential fits to these decay data provided the lifetimes used for the Stern-Volmer plot in Figure S51.

The green, cyan and purple traces in Figure S50 contain an initial rapid decay in the time window between 0 and ca. 150 ns, which we tentatively attribute to a luminescent impurity present in the [ZnCl$_2$(L^{bi})] material. Whilst this compound is analytically pure (see above), traces of strongly emissive impurities could become detectable in this experiment.

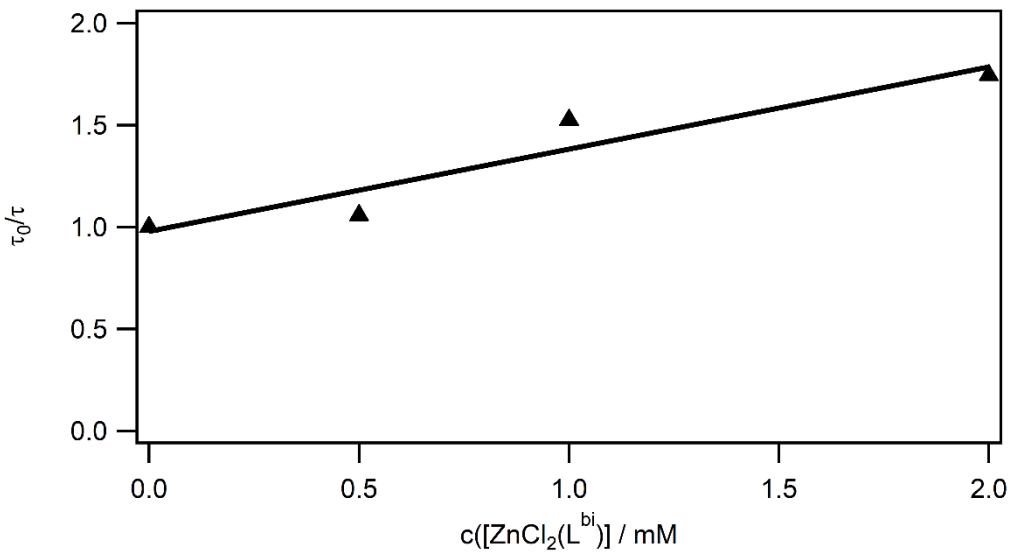

Figure S51. Stern-Volmer plot based on the luminescence decay data from Figure S50. A linear regression fit to the experimental data (solid line) yields a Stern-Volmer constant K_{SV} of 403 M^{-1}. Based on this value and the natural excited-state lifetime (τ_0) of 897 ns for *fac*-[Ir(dFppy)$_3$] in de-aerated dichloromethane at 20 °C, a rate constant of $4.5 \cdot 10^8$ $M^{-1}s^{-1}$ is obtained.

Alternative interpretations of the electronic structure of the Mn(I) complexes

In addition to the favored scenario described in the main paper (depicted in Figure S52a below), several other scenarios are in principle conceivable for the electronic structures of $[Mn(L^{tri})_2]^+$ and $[Mn(L^{bi})_3]^+$ (Figure S52b-d). Common to all four scenarios is an emissive MLCT excited state at 2.9 eV, and this interpretation is strongly supported by the combined transient absorption, spectro-electrochemical and time-resolved luminescence data (Figures 3 and S25). Furthermore, all four scenarios feature a ligand-centered $^3\pi$-π^* excited state at 2.3 eV, based on the investigation of the $[ZnCl_2(L^{bi})]$ reference complex. (As noted in the main paper, the underlying assumption here is that both ligands (L^{tri} and L^{bi}) have such a $^3\pi$-π^* state at 2.3 eV. This assumption seems reasonable given the structural similarity between these two ligands; unfortunately we were unable to isolate a stable Zn(II) complex with L^{tri} to test this hypothesis. Preliminary DFT calculations (not included) indicate that the lowest excited state of the $[Mn(L^{tri})_2]^+$ complex features electron redistributions that primarily occur on one of the two ArNC-thiophene-ArNC branches of the tridentate ligand, indicating that L^{tri} behaves in fact similarly as L^{bi}, and thus justifying the above assumption of a common $^3\pi$-π^* state at 2.3 eV for both ligands).

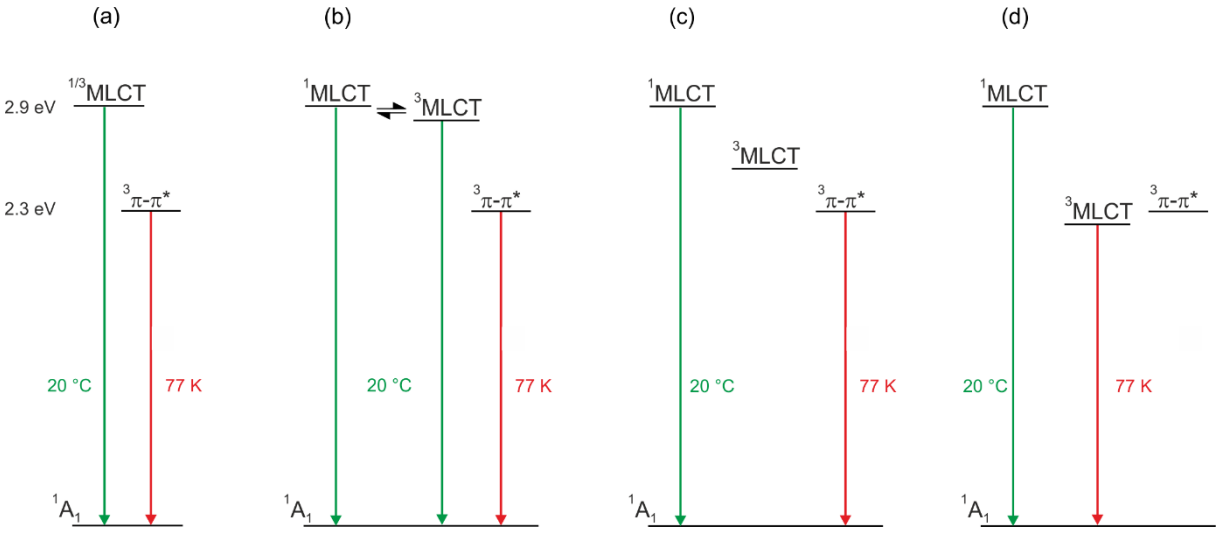

Figure S52. Different conceivable relative orders of excited-state energy levels for $[Mn(L^{tri})_2]^+$ and $[Mn(L^{bi})_3]^+$. The scenario in (a) corresponds to the favored interpretation discussed in the main paper.

In the favored scenario (Figure S52a), the ^{1}MLCT and ^{3}MLCT excited states are energetically close, similar to isoelectronic Fe(II) complexes, in which the singlet-triplet energy gap is small[12]. Furthermore, by analogy to $[Fe(bpy)_3]^{2+}$, in which intersystem crossing (ISC) from ^{1}MLCT to ^{3}MLCT occurs within less than 20 fs, one would expect ISC to be fast (and complete) in our Mn(I) complexes[12]. There exist some Ru(II) polypyridine complexes, in which there is both an emissive ^{3}MLCT state and a (dark) long-lived ligand-centered $^3\pi$-π^* excited state, for example $[Ru(bpy)_2(dmpbq)]^{2+}$ (dmpbq = 3,3‘-dimethylene-2-(2‘-pyridyl)benzo[*g*]quinoline)[13,14]. In that compound, the ^{3}MLCT and the $^3\pi$-π^* state seemed to be so weakly electronically coupled that non-radiative relaxation occurred without significant internal conversion between them, leading to a situation with two non-equilibrated excited states. A similar situation is conceivable for the Mn(I) complexes investigated herein.

In the second scenario (Figure S52b), the ^{1}MLCT and ^{3}MLCT states are in equilibrium, and possibly contribute to the multi-phasic decays, though the available experimental evidence as well as prior studies of Mo(0) isocyanide complexes[15] suggest that the multi-exponential decays are rather due to different conformers, as discussed on pages S58-S59 and on pages S80-S83.

In the third scenario (Figure S52c), the ^{1}MLCT and ^{3}MLCT states are energetically distant and hence no longer in equilibrium. This scenario would require much slower ISC than in Fe(II) polypyridines, such that the ^{1}MLCT state at 2.9 eV is not completely quenched and can in fact luminesce with a lifetime on the order of 1-2 nanoseconds. Thus, scenario (c) is in conflict with prior knowledge gained on Fe(II) complexes, in which ISC is ultrafast.

In the fourth scenario (Figure S52d), the ^{3}MLCT state is energetically (slightly) below the ligand-centered $^3\pi$-π^* state at 2.3 eV and becomes the phosphorescent state at 77 K. However, this would necessitate an unusually large energy gap between ^{1}MLCT and ^{3}MLCT, and unusually slow ISC. This is in conflict with prior knowledge gained on Fe(II) complexes[12], but it can better explain why the phosphorescent state is very short-lived at 20 °C (< 10 ns) in the Mn(I) complexes: Internal conversion from a ^{3}MLCT excited state to a ^{3}MC state is expected to be more efficient than internal conversion from a $^3\pi$-π^* state to a ^{3}MC state due to more significant orbital overlap.

The ^{3}MC state is not included in Figure S52 because its energetic position is currently unclear. Early studies suggested that Mn(I) isocyanide complexes have their lowest MC states above 25000 cm^{-1} [16]. Regardless, it is evident that the triplet manifold in these Mn(I) complexes is highly convoluted.

Schematic representation of all possible isomers of $[Mn(L^{tri})_2]^+$ and $[Mn(L^{bi})_3]^+$

From the X-ray crystal structure in Figure S23, it is evident that upon chelation, the thiophene ring of L^{bi} becomes rotated out of the ligand plane. This is consistent with previous reports of structurally related complexes with terphenyl ligand backbones[17,18]. As a consequence of this ring rotation, $[Mn(L^{bi})_3]^+$ and $[Mn(L^{tri})_2]^+$ can adopt multiple conformers in which the thiophene sulfur atoms orient in different directions out of the ligand plane. For $[Mn(L^{bi})_3]^+$, two unique conformers can be identified (Figure S53): one where all sulfurs orient in the same direction (clockwise or anticlockwise, depending on the molecular orientation), and one where one sulfur is oriented in the opposite direction. It should be noted that each conformer of $[Mn(L^{bi})_3]^+$ also exists in both Δ and Λ enantiomers. Unlike $[Mn(L^{bi})_3]^+$, $[Mn(L^{tri})_2]^+$ is not chiral. However, the additional thiophene ring results in six identifiable unique conformers (Figure S54).

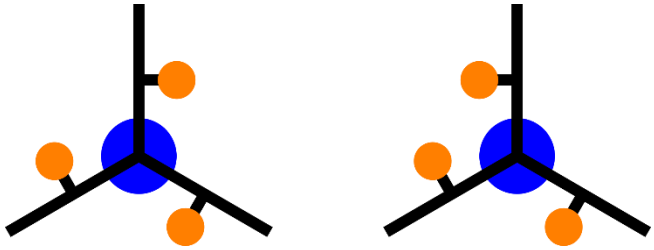

Figure S53. Newman projection-like schematic representations for both possible isomers of $[Mn(L^{bi})_3]^+$. The blue circle represents the Mn center, and the orange circles represent the directions in which the thienyl sulfurs point out of the ligand plane.

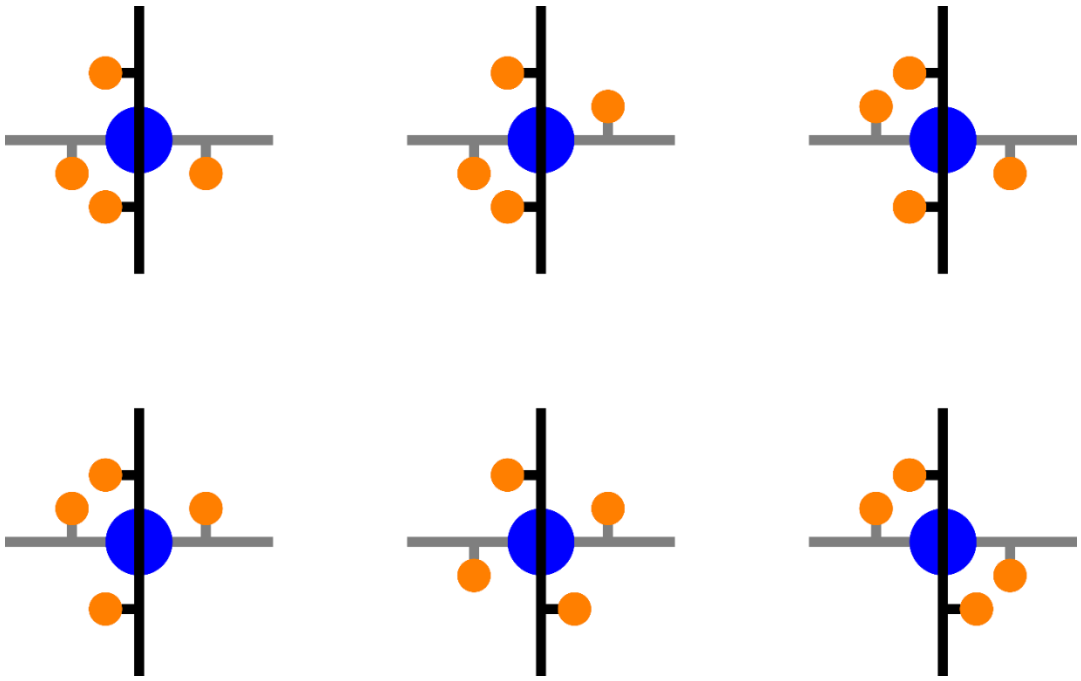

Figure S54. Newman projection-like schematic representations for all six possible conformers of $[Mn(L^{tri})_2]^+$. The blue circle represents the Mn center, and the orange circles represent the directions in which the thienyl sulfurs point out of the ligand plane.

MMFF calculations were employed to roughly gauge relative conformer and transition-state energies (Figures S55 and S56). As conformer interchange is achieved through 'flipping' of a thiophene ring, a conformation in which the thiophene ring lies within the ligand plane must occur during conformer interchange, and it is reasonable to assume this conformation represents the energetic maximum along the interchange coordinate, i.e. the transition-state. Within the context of the MMFF calculations, the transition-state is crudely approximated by constraining one thiophene ring to be coplanar with its neighboring phenylene rings. Obtained energies are likely exaggerated due to the crude approximations and the low level of theory employed, but it is clearly evident that both complexes exhibit multiple stable conformations with large energy barriers for conformational interchange.

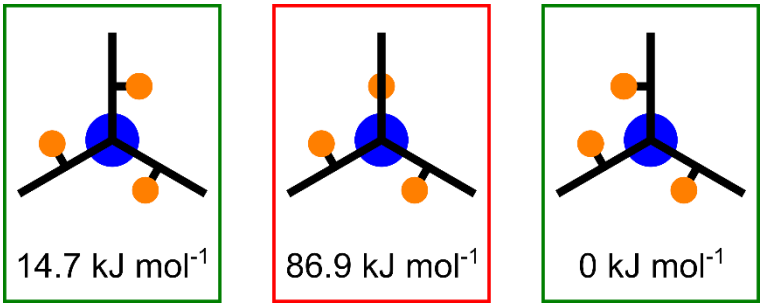

Figure S55. Conformer (green boxes) and transition-state (red box) energies relative to the lowest energy conformer for $[Mn(L^{bi})_3]^+$, obtained from MMFF geometry optimization calculations. Transition states have one thiophene ring constrained to coplanar with respect to its neighboring phenylene rings, with the sulfur atom directed towards the Mn center.

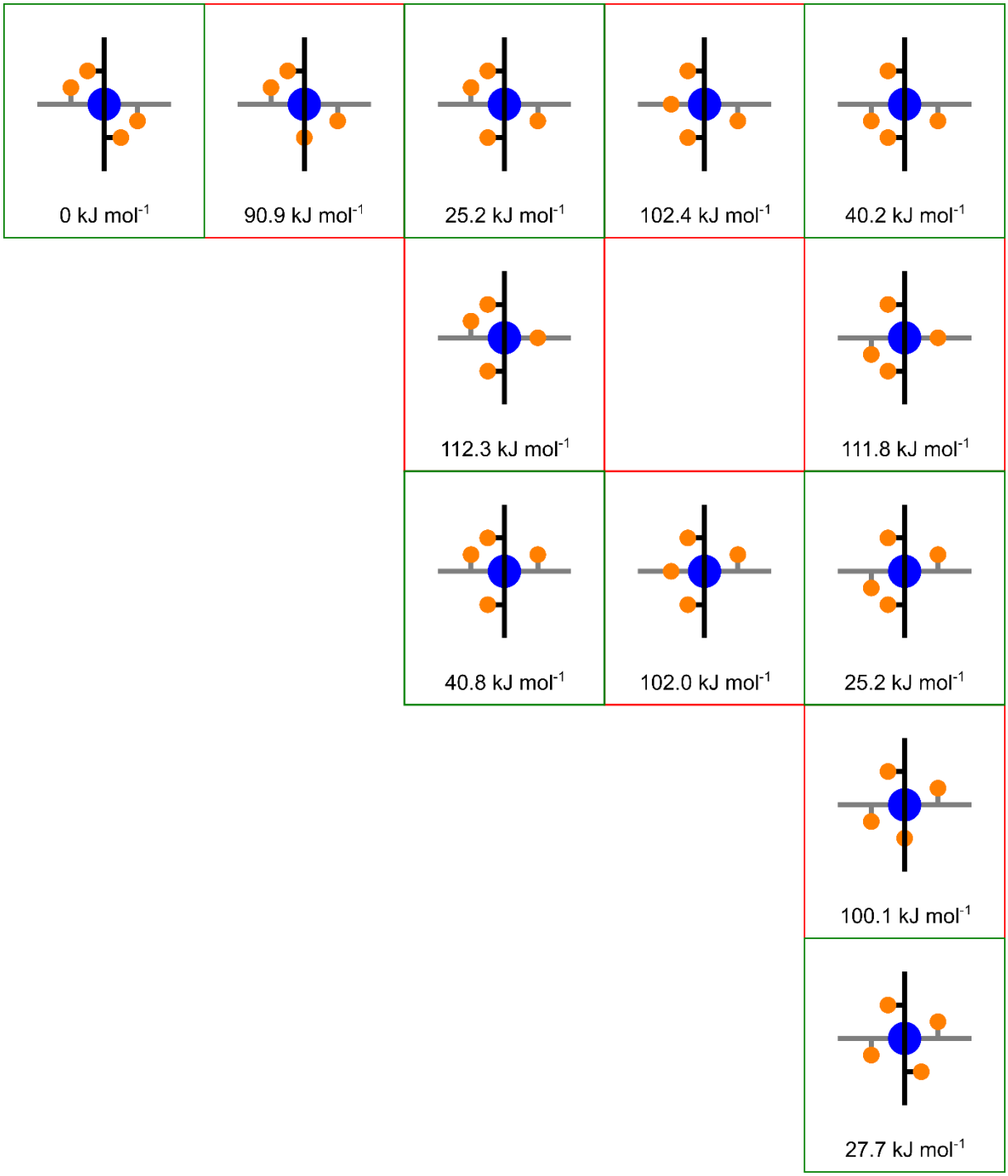

Figure S56. Conformer (green boxes) and transition-state (red boxes) energies relative to the lowest energy conformer for $[Mn(L^{tri})_2]^+$, obtained from MMFF geometry optimization calculations. Transition states have one thiophene ring constrained to coplanar with respect to its neighboring phenylene rings, with the sulfur atom directed towards the Mn center.

References

1. Rundel, W. Notiz über die Nitrierung von 3.5-Di-tert.-butyl-brombenzol. *Chem. Ber.* **96**, 636–637 (1963).

2. Harris, R. K., Becker, E. D., Cabral de Menezes, S. M., Goodfellow, R. & Granger, P. NMR nomenclature. Nuclear spin properties and conventions for chemical shifts. *Pure Appl. Chem.* **73**, 1795–1818 (2001).

3. Sheldrick, G. M. Crystal structure refinement with SHELXL. *Acta Crystallogr. C* **71**, 3–8 (2015).

4. Dolomanov, O. V., Bourhis, L. J., Gildea, R. J., Howard, J. A. K. & Puschmann, H. OLEX2: A complete structure solution, refinement and analysis program. *J. Appl. Crystallogr.* **42**, 339–341 (2009).

5. Suzuki, K. *et al.* Reevaluation of absolute luminescence quantum yields of standard solutions using a spectrometer with an integrating sphere and a back-thinned CCD detector. *Phys. Chem. Chem. Phys.* **11**, 9850–9860 (2009).

6. Goez, M., Kerzig, C. & Naumann, R. An 'all-green' catalytic cycle of aqueous photoionization. *Angew. Chem. Int. Ed.* **53**, 9914–9916 (2014).

7. Bensasson, R. & Land, E. J. Triplet-triplet extinction coefficients via energy transfer. *Trans. Faraday Soc.* **67**, 1904–1915 (1971).

8. Koike, T. & Akita, M. Visible-light radical reaction designed by Ru- and Ir-based photoredox catalysis. *Inorg. Chem. Front.* **1**, 562–576 (2014).

9. Strieth-Kalthoff, F., James, M. J., Teders, M., Pitzer, L. & Glorius, F. Energy transfer catalysis mediated by visible light: principles, applications, directions. *Chem. Soc. Rev.* **47**, 7190–7202 (2018).

10. Arias-Rotondo, D. M. & McCusker, J. K. The photophysics of photoredox catalysis: a roadmap for catalyst design. *Chem. Soc. Rev.* **45**, 5803–5820 (2016).

11. Slinker, J. D. *et al.* Efficient Yellow Electroluminescence from a Single Layer of a Cyclometalated Iridium Complex. *J. Am. Chem. Soc.* **126**, 2763–2767 (2004).

12. Gawelda, W. *et al.* Ultrafast nonadiabatic dynamics of $[Fe^{II}(bpy)_3]^{2+}$ in solution. *J. Am. Chem. Soc.* **129**, 8199–8206 (2007).

13. Taffarel, E., Chirayil, S., Kim, W. Y., Thummel, R. P. & Schmehl, R. H. Coexistence of Ligand Localized and MLCT Excited States in a 2-(2′-Pyridyl)benzo[*g*]quinoline Complex of Ruthenium(II). *Inorg. Chem.* **35**, 2127–2131 (1996).

14. Baba, A. I., Shaw, J. R., Simon, J. A., Thummel, R. P. & Schmehl, R. H. The photophysical behavior of d^6 complexes having nearly isoenergetic MLCT and ligand localized excited states. *Coord. Chem. Rev.* **171**, 43–59 (1998).

15. Herr, P., Glaser, F., Büldt, L. A., Larsen, C. B. & Wenger, O. S. Long-Lived, Strongly Emissive, and Highly Reducing Excited States in Mo(0) Complexes with Chelating Isocyanides. *J. Am. Chem. Soc.* **141**, 14394–14402 (2019).

16. Mann, K. R. *et al.* Electronic Structures and Spectra of Hexakisphenylisocyanide Complexes of Cr(0), Mo(0), W(0), Mn(I) and Mn(II). *Inorg. Chim. Acta* **16**, 97–101 (1976).

17. Büldt, L. A., Guo, X., Prescimone, A. & Wenger, O. S. A Molybdenum(0) Isocyanide Analogue of $[Ru(2,2'\text{-Bipyridine})_3]^{2+}$: A Strong Reductant for Photoredox Catalysis. *Angew. Chem. Int. Ed.* **55**, 11247–11250 (2016).

18. Büldt, L. A., Guo, X., Vogel, R., Prescimone, A. & Wenger, O. S. A Tris(diisocyanide)chromium(0) Complex is a Luminescent Analog of $[Fe(2,2'\text{-Bipyridine})_3]^{2+}$. *J. Am. Chem. Soc.* **139**, 985–992 (2017).

4 Comprehensive Studies on Mo(0) Complexes with Bidentate Isocyanide Ligands

4.1 Enhancing the Photophysical Properties of Mo(0) Isocyanide Complexes and their Application in a Series of BHAS Reactions

The Mo(0) isocyanide complex [Mo(L^{Me})$_3$] introduced in chapter 2.3 shows two impressive characteristics for an earth-abundant metal complex. First are the compound's relatively good photophysical properties with a long luminescence lifetime of 225 ns and a high photoluminescence quantum yield of up to 4.5 % in *n*-hexane. But what makes this compound really stand out is its high reducing power with an excited-state oxidation potential of -2.2 V *vs* SCE. There are only a limited number of compounds based on earth-abundant metal complexes that can initiate photoreactions that require such a strongly reducing catalyst.[87,88] The widely used *fac*-[Ir(ppy)$_3$] only has an excited-state oxidation potential of -1.7 V *vs* SCE, limiting its application in challenging reactions.[15,89]
However, [Mo(L^{Me})$_3$] has one major drawback. In reactions that release nucleophiles, e.g. I^- from an initial dehalogenation of the substrate, we were not able to afford high product yields. Our hypothesised reason for the incomplete reaction was a lack of shielding of the oxidised metal centre against nucleophiles, resulting in deactivation of the catalyst. An obvious solution to this problem is the use of a ligand with increased steric demand. Such a ligand, L^{tBu}, was already at hand from the work related to the Cr(0) complex also reported in chapter 2.3. The resulting new complex, [Mo(L^{tBu})$_3$], and its application in challenging BHAS reactions are reported in:

- P. Herr, F. Glaser, L. A. Büldt, C. B. Larsen, O. S. Wenger "Long-Lived, Strongly Emissive, and Highly Reducing Excited States in Mo(0) Complexes with Chelating Isocyanides" *J. Am. Chem. Soc.* **2019**, *141*, 14394-14402.

Introduction of sterically demanding ^{t}Bu groups in the ortho-position to the ligating isocyanides can stabilise low-valent transition metals and protects the metal centre from the chemical environment. We further found that the bulkier ligands increase the rigidity of the [Mo(L^{tBu})$_3$] complex, decelerating non-radiative excited-state decay by one order of magnitude relative to the previously reported [Mo(L^{Me})$_3$]. This increases the luminescence lifetime of [Mo(L^{tBu})$_3$] into the microsecond range and the photoluminescence quantum

yield to 20 % in deaerated toluene. The luminescence quantum yield of the popular $[Ru(bpy)_3]^{2+}$ is 9.5 % in deaerated CH_3CN, [90] more than a factor of two lower than that of $[Mo(L^{tBu})_3]$.

The enhanced shielding of the metal centre shines in photocatalyzed BHAS reactions. Despite the formation of nucleophilic I^-, an intramolecular aryl-aryl coupling reaction can be completed with quantitative yield within one hour of irradiation. The stability of the new complex is further highlighted in reactions that require an initial debromination step. Although the overall reaction is slow in this case, the complex is still catalytically active and shows photoluminescence even after weeks of continuous irradiation.

The influence of structural and electronic variations on the performance of light driven BHAS reactions was systematically determined with a range of selected substrates.

Author Contributions

- P.H. resynthesised the Mo(0) complexes and fully characterised them, repeated and completed photophysical characterisation and did the initial photoreactions (Scheme 2 and Table 3). He contributed equally to data analysis and the preparation of the manuscript.
- F.G. carried out the photocatalytic substrate scope (Table 4) and contributed equally to data analysis and the preparation of the manuscript.
- L.A.B. carried out the initial synthesis of the Mo(0) complexes and did first photophysical characterisations.
- C.B.L. contributed equally to data analysis and preparation of the manuscript.
- O.S.W. conceived research and contributed equally to data analysis and the preparation of the manuscript.

JACS
JOURNAL OF THE AMERICAN CHEMICAL SOCIETY
Article
Cite This: J. Am. Chem. Soc. 2019, 141, 14394−14402
pubs.acs.org/JACS

Long-Lived, Strongly Emissive, and Highly Reducing Excited States in Mo(0) Complexes with Chelating Isocyanides

Patrick Herr,[†] Felix Glaser,[†] Laura A. Büldt,[†] Christopher B. Larsen, and Oliver S. Wenger*

Department of Chemistry, University of Basel, St. Johanns-Ring 19, 4056 Basel, Switzerland

Supporting Information

ABSTRACT: Newly discovered tris(diisocyanide)molybdenum(0) complexes are Earth-abundant isoelectronic analogues of the well-known class of $[Ru(\alpha\text{-diimine})_3]^{2+}$ compounds with long-lived ^{3}MLCT (metal-to-ligand charge transfer) excited states that lead to rich photophysics and photochemistry. Depending on ligand design, luminescence quantum yields up to 0.20 and microsecond excited state lifetimes are achieved in solution at room temperature, both significantly better than those for $[Ru(2,2'\text{-bipyridine})_3]^{2+}$. The excited Mo(0) complexes can induce chemical reactions that are thermodynamically too demanding for common precious metal-based photosensitizers, including the widely employed *fac*-[Ir(2-phenylpyridine)$_3$] complex, as demonstrated on a series of light-driven aryl−aryl coupling reactions. The most robust Mo(0) complex exhibits stable photoluminescence and remains photoactive after continuous irradiation exceeding 2 months. Our comprehensive optical spectroscopic and photochemical study shows that Mo(0) complexes with diisocyanide chelate ligands constitute a new family of luminophores and photosensitizers, which is complementary to precious metal-based 4d^6 and 5d^6 complexes and represents an alternative to nonemissive Fe(II) compounds. This is relevant in the greater context of sustainable photophysics and photochemistry, as well as for possible applications in lighting, sensing, and catalysis.

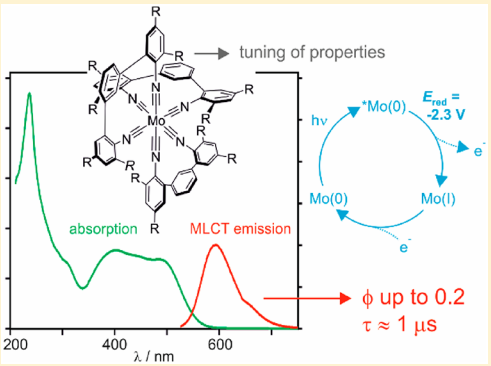

INTRODUCTION

The long-lived luminescent metal-to-ligand charge transfer (MLCT) excited states of complexes with precious d^6 metals such as Ru(II), Ir(III), Os(II), or Re(I) form the basis for many photophysical and photochemical applications, for example in luminescent devices,[1] sensing,[2,3] solar energy conversion,[4] and photoredox catalysis.[5] There is a long-standing interest in obtaining complexes with similarly favorable electronic structures made from cheaper first-row transition metal elements.[6−8] Fe(II) is an obvious and much explored target,[9−15] because iron is the most abundant and cheapest transition metal in Earth's crust. However, such 3d^6 complexes have energetically low-lying metal-centered (MC) excited states that deactivate the MLCT states very efficiently.[16−18] Different concepts have been explored to lengthen ^{3}MLCT lifetimes in Fe(II) complexes, including the optimization of metal coordination geometries,[19−21] the use of push−pull ligand environments,[22,23] and the enhancement of ligand fields with N-heterocyclic[24−27] or mesoionic carbenes.[28] Recently, these efforts culminated in the discovery of two Fe(III) complexes that luminesce from a ligand-to-metal charge transfer (LMCT) excited state[29,30] and an Fe(II) complex with a ^{3}MLCT lifetime of 528 ps in solution at room temperature.[31]

Building on early studies of group 6 d^6 metal complexes with isocyanide ligands[32,33] and recent reports of luminescent W(0) complexes with monodentate isocyanides,[34,35] we recently discovered that chelating diisocyanide ligands give access to Cr(0) and Mo(0) complexes with emissive ^{3}MLCT excited states.[36] The Cr(0) complex exhibited an excited-state lifetime of 2.2 ns and a luminescence quantum yield of ca. 10^{-5} in tetrahydrofuran (THF) solution at room temperature,[37] while the Mo(0) complex had a ^{3}MLCT lifetime of 166 ns and a quantum yield of 0.023 in toluene.[38] Herein, we report how improved ligand design can enhance both of these properties in Mo(0) complexes by an order of magnitude, and it becomes evident that the initially communicated single example is not merely an academic curiosity, but instead tris(diisocyanide)-molybdenum(0) complexes represent a new family of robust 4d^6 complexes with very favorable photophysical properties. Moreover, we demonstrate that excitation of these complexes can induce chemical reactions that are thermodynamically too challenging for typical precious metal-based photosensitizers, such as the well-known *fac*-[Ir(ppy)$_3$] complex. For this purpose, we investigated base-promoted homolytic aromatic substitution (BHAS) reactions,[39] which were performed in an intramolecular fashion on a series of substrates specifically designed to elucidate the catalytic properties of the Mo(0) complexes.

Our study complements ongoing research on photoactive complexes with other Earth-abundant metal elements such as

Received: July 11, 2019
Published: August 29, 2019

DOI: 10.1021/jacs.9b07373
J. Am. Chem. Soc. 2019, 141, 14394−14402

Fe,[9−15] Cu,[40−50] Cr,[51−54] Co,[55] Ni,[56−58] Zr,[59,60] W,[34,35,61−63] and Ce,[64] as well as current research on new metal-free organic photosensitizers.[65−69]

RESULTS AND DISCUSSION

Synthesis and Infrared Spectroscopy. Monodentate isocyanide ligands play an important role in organometallic chemistry as alternatives to CO that can be further functionalized,[70,71] and one attractive option is to create polydentate chelating isocyanides.[72−80] In our initial communication, we reported that a *m*-terphenyl backbone is useful to obtain a diisocyanide ligand that binds Mo(0) in chelating fashion, giving access to a homoleptic complex (Scheme 1a, $[Mo(L^{Me})_3]$) that is structurally and electronically similar to $[Ru(bpy)_3]^{2+}$ (bpy = 2,2′-bipyridine).[38] Sterically demanding groups in α-position to the ligating isocyanides usually stabilize low-valent transition metal species, rendering them less susceptible to electrophilic attack.[71,81] We therefore reasoned that bulkier *tert*-butyl (rather than methyl) substituents could minimize interactions between the Mo(0) center and the solvent, as well as rigidifying the complex, potentially leading to decreased nonradiative ^{3}MLCT deactivation. In the resulting new $[Mo(L^{tBu})_3]$ complex (Scheme 1b), this is indeed the case, as our detailed comparative photophysical study with $[Mo(L^{Me})_3]$ will show. We had previously used L^{tBu} to obtain a luminescent Cr(0) complex,[37] and the synthesis of L^{Me} was reported in our initial Mo(0) communication.[38] The new $[Mo(L^{tBu})_3]$ complex was prepared by stirring a solution of $[MoCl_2(THF)_4]$ and 3 equiv of L^{tBu} in THF over Na/Hg (see Supporting Information page S2 for details). The complex was isolated as a red powder that can be handled under air.

Scheme 1. Molecular Structures of (a) $[Mo(L^{Me})_3]$ and (b) $[Mo(L^{tBu})_3]$

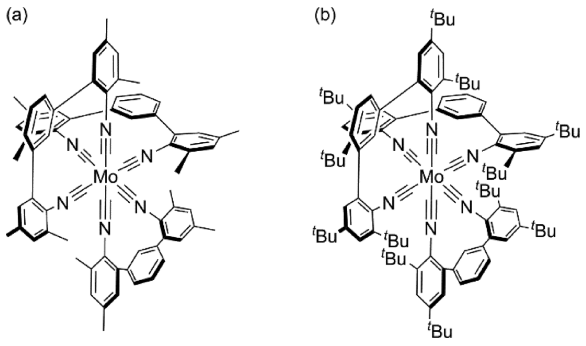

The C≡N stretch frequencies in the free L^{Me} and L^{tBu} ligands are 2113 and 2112 cm^{-1} (Figure S4), respectively. In the $[Mo(L^{Me})_3]$ and $[Mo(L^{tBu})_3]$ complexes, the C≡N vibrations are broad and intense, and their maxima are shifted to 1939 and 1951 cm^{-1}, respectively, due to π-backbonding.[82]

Electrochemistry. In cyclic voltammetry, oxidation of Mo(0) to Mo(I) in deaerated THF with 0.1 M $TBAPF_6$ results in quasi-reversible waves from which potentials of −0.02 and −0.08 V vs saturated calomel electrode (SCE) can be determined for $[Mo(L^{Me})_3]$ and $[Mo(L^{tBu})_3]$, respectively (Figure 1). These potentials are shifted anodically by 0.2−0.3 V relative to those for previously reported Mo(0) complexes with monodentate arylisocyanides (Table 1).[83]

In principle, this shift could be due to either stabilization of the Mo(0) state or destabilization of the Mo(I) form in the chelate complexes.[85] It seems likely that the latter effect is dominant, because the bite angle of the chelating L^{Me} and L^{tBu} ligands is expected to become less favorable with increasing oxidation state due to decreasing Mo−C bond distances. Sweeps over greater potential ranges than those in Figure 1 produce lower-quality voltammograms, and ligand reduction was undetectable. However, the observable Mo(0/I) redox wave is the most important one, because it is directly relevant for the photochemistry of $[Mo(L^{Me})_3]$ and $[Mo(L^{tBu})_3]$ presented below.

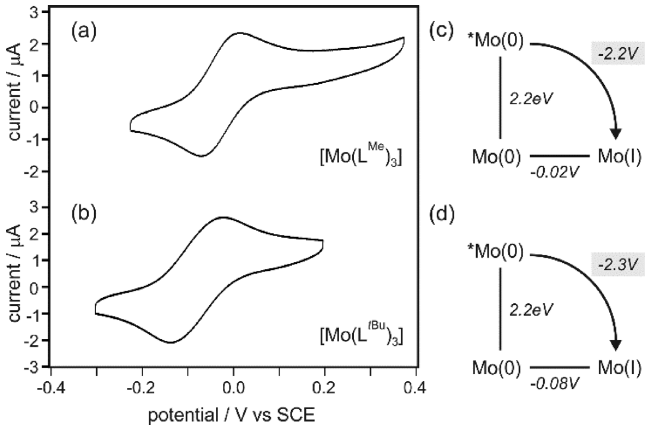

Figure 1. Cyclic voltammograms of (a) $[Mo(L^{Me})_3]$ and (b) $[Mo(L^{tBu})_3]$ recorded in deaerated THF with 0.1 M $TBAPF_6$ at 20 °C. The potential scan rates were 0.1 and 0.2 V/s, respectively. The differences in anodic and cathodic peak currents are 86 mV (a) and 116 mV (b). (c, d) Latimer diagrams for $[Mo(L^{Me})_3]$ and $[Mo(L^{tBu})_3]$, based on an energy of 2.2 eV for the emissive ^{3}MLCT excited state (Figure S7b).

Table 1. Electrochemical Potentials (in V vs SCE) in the Electronic Ground State and in the Long-Lived ^{3}MLCT Excited State

	E^0 (M^+/M^0)	E^0 ($M^+/{}^*M^0$)
$[Mo(L^{tBu})_3]^a$	−0.08	−2.3
$[Mo(L^{Me})_3]^{a,b}$	−0.02	−2.2
$[Mo(CN\text{-}C_6H_5)_6]^c$	−0.24	
$[Mo(CN\text{-}^{2,6\text{-}iPr}C_6H_5)_6]^c$	−0.32	
fac-$[Ir(ppy)_3]^d$	0.77	−1.7

[a]This work, measured in THF with 0.1 M $TBAPF_6$ (Figure 1). [b]From ref 38, measured in THF with 0.1 M $TBAPF_6$. [c]From ref 83, measured in THF with 0.1 M $TBAPF_6$ versus Ag/AgCl. [d]From ref 84.

UV−Vis Absorption, Luminescence, and Transient Absorption Spectroscopy. The UV−vis spectra of $[Mo(L^{Me})_3]$ and $[Mo(L^{tBu})_3]$ exhibit MLCT absorptions between 350 and 550 nm (Figure 2a and b) that cause the orange−red color of these complexes. Ligand-based $\pi-\pi^*$ transitions appear at shorter wavelengths, and thus the overall spectra are reminiscent of that of isoelectronic $[Ru(bpy)_3]^{2+}$.[36] However, the MLCT absorptions in $[Mo(L^{Me})_3]$ and $[Mo(L^{tBu})_3]$ are broader and have higher extinction coefficients by factors of approximately 1.5 and 2.0, respectively.

Upon excitation at 500 nm, both Mo(0) complexes luminesce in deaerated solution at room temperature (Figure 2c and d). The emission is broad and unstructured, and there is a sizable red shift of the emission band maximum when increasing the solvent polarity from *n*-hexane to toluene and THF (540 cm^{-1} in total for $[Mo(L^{Me})_3]$ and 410 cm^{-1} for $[Mo(L^{tBu})_3]$). These observations are compatible with MLCT

DOI: 10.1021/jacs.9b07373
J. Am. Chem. Soc. 2019, 141, 14394−14402

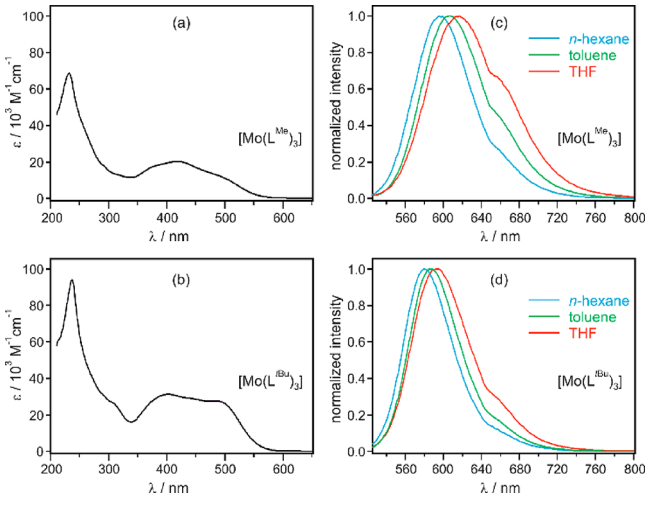

Figure 2. UV–vis absorption spectra of (a) $[Mo(L^{Me})_3]$ and (b) $[Mo(L^{tBu})_3]$ in THF at 20 °C. Normalized photoluminescence spectra of (c) $[Mo(L^{Me})_3]$ and (d) $[Mo(L^{tBu})_3]$ in deaerated solvents at 20 °C. Excitation occurred at 500 nm.

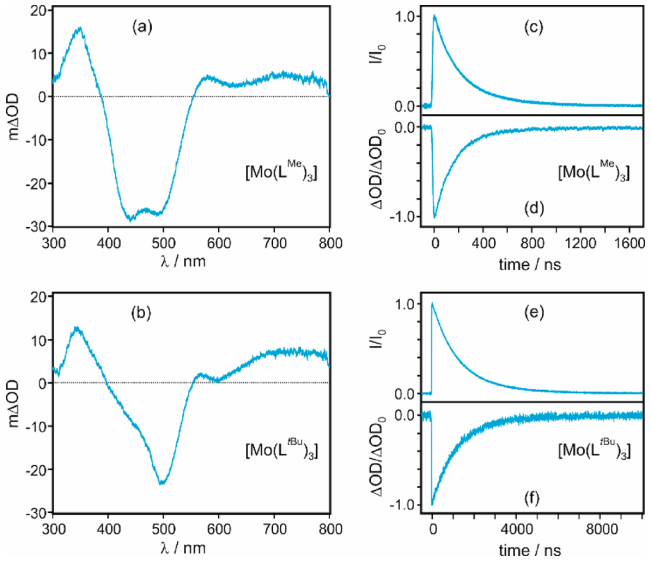

Figure 3. Transient absorption spectra measured after excitation of 10^{-5} M solutions of (a) $[Mo(L^{Me})_3]$ and (b) $[Mo(L^{tBu})_3]$ in deaerated toluene at 532 nm with laser pulses of ~10 ns duration. The signals were time-integrated over 200 ns immediately after excitation. Luminescence decays (c, e) recorded from these solutions at 595/615 nm and recoveries of the MLCT bleaches (d, f) at 485 nm. See Figures S8 and S10 for analogous data recorded in other solvents.

emission, in analogy to $[Ru(bpy)_3]^{2+}$. A key finding is that the luminescence quantum yield (ϕ) of the $[Mo(L^{tBu})_3]$ complex is much higher than that of $[Mo(L^{Me})_3]$ in all investigated solvents. For example, in deaerated toluene at 20 °C, the complex with the more sterically demanding *tert*-butyl-substituted diisocyanide ligand exhibits ϕ = 0.203, whereas the complex with the methyl substituents only has ϕ = 0.023 (Table 2). This shows that the aforementioned design principle, according to which better shielding of the metal center from the chemical environment and enhanced complex rigidity should lead to improved photophysical properties, is indeed successful. $[Ru(bpy)_3]^{2+}$ has a luminescence quantum yield of 0.095 under optimized conditions in deaerated CH_3CN, more than a factor of 2 lower than $[Mo(L^{tBu})_3]$.[86] Such strong luminescence is remarkable for a d^6 MLCT emitter made from an Earth-abundant transition metal and compares very favorably to most Cu(I) diimine complexes.[43,87−89] The latter represent an extremely well investigated class of compounds for which similar luminescence quantum yields required many optimization attempts.

Time-resolved luminescence and transient UV/vis absorption spectroscopy were used to explore the decay characteristics of the emissive excited states and to confirm their MLCT nature. The transient absorption spectra in Figure 3a and b were averaged over a period of 200 ns immediately after excitation at 532 nm with laser pulses of ca. 10 ns duration. In both cases a negative signal (ground-state bleach) is detected near 500 nm, coincident with the lowest-energy ^{1}MLCT absorption bands in Figure 2a and b. Additionally, excited-state absorption bands near 345 nm are observed for both complexes, reminiscent of the absorption bands near 370 nm for ^{3}MLCT-excited $[Ru(bpy)_3]^{2+}$, which are caused by π–π^* transitions on the transiently reduced bpy ligand.[90] Such short-wavelength excited-state absorption bands combined with ground-state ^{1}MLCT bleaches are in fact diagnostic features of MLCT excited states in photoactive Ru(II) and Fe(II) complexes.[22,31]

As expected, the MLCT luminescence at 595/615 nm and the MLCT bleach at 485 nm exhibit the same decay for a given complex (Figure 3c/d and e/f), confirming that the same excited state is monitored by emission and transient absorption spectroscopies. However, the MLCT lifetimes (τ) extractable from these data sets are markedly different for $[Mo(L^{tBu})_3]$ and $[Mo(L^{Me})_3]$ in all investigated solvents (Figure S10). For instance, in deaerated toluene at 20 °C, τ = 166 ns for $[Mo(L^{Me})_3]$, while for the $[Mo(L^{tBu})_3]$ complex, a biexponential decay with τ_1 = 1110 ns (85%) and τ_2 = 2330 ns (15%) is observed (Table 2). Thus, the factor-of-10 increase in luminescence quantum yield when going from $[Mo(L^{Me})_3]$ to $[Mo(L^{tBu})_3]$ (see earlier) is accompanied by an equivalent increase in excited-state lifetime, compatible with the view that the rate for radiative decay from the emissive MLCT states is similar in both complexes, whereas the rate for nonradiative decay is decreased by an order of magnitude in $[Mo(L^{tBu})_3]$. This is additional confirmation for the success of the design concept outlined in the Introduction, and it is evident that the bulkier *tert*-butyl substituents lead to much improved photophysical properties relative to the methyl substituents.

Table 2. ^{3}MLCT Excited-State Lifetimes (τ) and Luminescence Quantum Yields (ϕ) in Deaerated Solvents at 20 °C

	n-hexane			toluene			THF		
	τ_1 (ns)	τ_2 (ns)	ϕ	τ_1 (ns)	τ_2 (ns)	ϕ	τ_1 (ns)	τ_2 (ns)	ϕ
$[Mo(L^{tBu})_3]^a$	1040 (76%)	2370 (24%)	0.190	1110 (85%)	2330 (15%)	0.203	610 (73%)	1610 (27%)	0.058
$[Mo(L^{Me})_3]^b$	225 (100%)		0.045	166 (100%)		0.023	74 (100%)		0.006

[a]This work, extracted from the data in Figure S10; determined using $[Ru(bpy)_3]^{2+}$ in aerated CH_3CN as standard (ϕ = 0.018).[86] [b]From ref 38.

DOI: 10.1021/jacs.9b07373
J. Am. Chem. Soc. 2019, 141, 14394−14402

In all investigated solvents, the luminescence decays and MLCT bleach recoveries are consistently monoexponential for $[Mo(L^{Me})_3]$, while for $[Mo(L^{tBu})_3]$ biexponential kinetics were observed in all experiments. The biexponential decays are tentatively attributed to the presence of different conformers in the latter. In our previously published crystal structure of $[Cr(L^{tBu})_3]$, the three L^{tBu} ligands are not equivalent,[37] and interconversion between different conformations seems to be sterically hindered by the *tert*-butyl substituents. In $[Mo(L^{Me})_3]$, the methyl substituents impose less hindrance, and interconversion between different conformers can therefore occur on a faster time scale, leading to single-exponential MLCT decays. Related dynamic interconversions have been observed for some Ru(II) complexes.[91]

Going from toluene to THF, the MLCT lifetimes and luminescence quantum yields decrease in parallel in both complexes (Table 2). Qualitatively, this can be understood in the framework of the energy gap law,[92] because the MLCT state is energetically stabilized in more-polar THF (red shifts observable in Figure 2c and d), leading to a smaller energy gap to the ground state and consequent faster nonradiative relaxation. Different propensities for energy dissipation via molecular vibrations of the various solvents could further contribute to the observable lifetime and quantum yield changes between *n*-hexane, toluene, and THF. It is likely that the solvent nucleophilicity also plays a role with respect to the excited-state lifetime, especially for $[Mo(L^{Me})_3]$, with more nucleophilic solvents more efficiently deactivating the excited state. However, nucleophilicity and energy-gap law effects are difficult to disentangle in low-polarity solvents. The MLCT lifetimes of both complexes are strongly oxygen-sensitive, confirming the triplet nature of these excited states.

For the photoredox investigations below, the excited-state oxidation potential (E_{ox}*) is relevant, and this in turn requires knowledge of the energy of the photoactive ^{3}MLCT state. Therefore, in addition to the emission experiments reported earlier, luminescence spectra were measured at 77 K (Figure S7) to estimate the energy of the electronic origin (E_{00}) of the ^{3}MLCT emission more accurately. This procedure yields an E_{00} value of 2.2 eV for both complexes, leading to excited-state oxidation potentials of −2.2 and −2.3 V vs SCE for $[Mo(L^{Me})_3]$ and $[Mo(L^{tBu})_3]$, respectively, as indicated in Figure 1c and d (gray shaded areas). Thus, both complexes should be far stronger photoreductants than isoelectronic $[Ru(bpy)_3]^{2+}$ (E_{ox}* = −0.9 V vs SCE) and *fac*-$[Ir(ppy)_3]$ (E_{ox}* = −1.73 V vs SCE).[84]

Photochemical Studies. In our preliminary communication we reported that the $[Mo(L^{Me})_3]$ complex is able to photocatalyze the rearrangement of an acylcyclopropane substrate to a 2,3-dihydrofuran product,[38] but we noticed that the presence of nucleophiles in the reaction mixture caused degradation of the Mo complex over time. We speculated that this degradation is caused by ligation of nucleophiles to the metal center in Mo(I) intermediates formed transiently in the course of the photocatalysis reaction cycle; seven-coordinate molybdenum isocyanide complexes are well-known.[93,94] We will now show that in the new $[Mo(L^{tBu})_3]$ complex this problem no longer persists, presumably because the bulkier *tert*-butyl substituents more efficiently shield the metal from the chemical environment.

The main purpose of the studies below was to explore the photochemical properties of this new family of d^6 MLCT emitters and to test their robustness in the presence of nucleophiles over extended irradiation times, rather than to develop new photoredox reactions. Toward this end, we concentrated on net redox-neutral cross-coupling between aryl halides and arenes, which can be considered electron-catalyzed reactions.[39] A specific example is the intramolecular reaction between an aryl iodide and pyrrole (Scheme 2). Base-promoted homolytic aromatic substitution (BHAS) reactions of this type have been identified as a viable alternative to Pd- and Rh-based C−C bond formation, but they often require harsh conditions involving high temperatures and strong bases.[95−100] Photochemical approaches to BHAS not relying on UV excitation have been relatively scarce so far.[101−106]

Scheme 2. Intramolecular Base-Promoted Homolytic Aromatic Substitution (BHAS) via Photoredox Catalysis

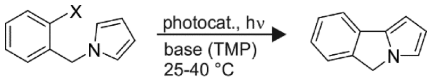

1a: X = I
2a: X = Br

1b

First, we tested the performance of the $[Mo(L^{Me})_3]$ complex as a photocatalyst for the reaction in Scheme 2, which can be conveniently followed by monitoring the benzylic ^{1}H NMR resonances of substrate and product (Figure S13). Using 50 mM substrate **1a** in deaerated C_6D_6, 2 equiv of 2,2,6,6-tetramethylpiperidine (TMP) as base, and a photocatalyst loading of 5 mol % in a flame-sealed NMR tube at room temperature, 19% of the substrate was converted to product **1b** after irradiation at 470 nm with a light-emitting diode (LED) (ca. 14 W; see Supporting Information page S16 for details) for 1 h (Table 3, entry 1). Maximum conversion of 31% was observed after 18 h (Table 3, entry 2; Figure S13). Catalyst-based luminescence could not be detected after this time, implying decomposition of $[Mo(L^{Me})_3]$. The new $[Mo(L^{tBu})_3]$ complex, however, catalyzed the reaction to completion within 1 h (Table 3, entry 3; Figure S14). In comparison, use of *fac*-$[Ir(ppy)_3]$ (E_{ox}* = −1.73 V vs SCE) under identical conditions resulted in nearly negligible conversion over the same time period (Table 3, entry 4; Figure S15), and reactions did not reach conclusion even after >100 h of continuous irradiation. As *fac*-$[Ir(ppy)_3]$ absorbs weakly at wavelengths longer than 450 nm and may therefore create a biased comparison, the experiments with *fac*-$[Ir(ppy)_3]$ were repeated under 405 nm irradiation, which showed little difference to the results obtained with 470 nm irradiation (Figure S16).

Table 3. Performance of $[Mo(L^{Me})_3]$, $[Mo(L^{tBu})_3]$, and *fac*-$[Ir(ppy)_3]$ in the Light-Driven BHAS Reaction of Scheme 2[a]

entry	substrate	complex	irradiation time/h	conversion/%
1	**1a**	$[Mo(L^{Me})_3]$	1	19
2	**1a**	$[Mo(L^{Me})_3]$	18	31
3	**1a**	$[Mo(L^{tBu})_3]$	1	100
4	**1a**	*fac*-$[Ir(ppy)_3]$	1	4
5	**2a**	$[Mo(L^{tBu})_3]$	18	7

[a]Conditions: 50 mM substrate, 5 mol % metal complex, and 2 equiv of 2,2,6,6-tetramethylpiperidine (TMP) in deaerated C_6D_6 at ca. 40 °C. Irradiation at 470 nm with 14 W LED. See Supporting Information pages S16−S19.

DOI: 10.1021/jacs.9b07373
J. Am. Chem. Soc. 2019, 141, 14394−14402

The photochemical BHAS reaction is initiated by a reductive dehalogenation step (see below), and the promising results observed above for $[Mo(L^{tBu})_3]$ encouraged us to explore the reaction of Scheme 2 with a bromo-substituted substrate (**2a**), which is more difficult to reduce than the iodoarene of **1a**. However, only very modest conversion was observable, and it required extremely long irradiation times (Table 3, entry 5; Figure S17). Over the course of these experiments, we found that the $[Mo(L^{tBu})_3]$ complex still exhibited stable photoluminescence and was catalytically active after continuous irradiation exceeding 2 months.

A proposed mechanism for the photochemical BHAS reaction with $[Mo(L^{tBu})_3]$ is presented in Scheme 3. Due to its high reducing power (E_{ox}^* = −2.3 V vs SCE, Figure 1d), the ^{3}MLCT-excited Mo(0) complex is able to induce the initial reductive dehalogenation of iodobenzene substrate **1a** ($E_{red} \approx -2.2$ eV)[107] in an efficient manner. In contrast, the photoexcited *fac*-$[Ir(ppy)_3]$ complex is substantially less reducing (E_{ox}^* = −1.73 V vs SCE),[84] and this is likely the main reason for its comparatively poor performance as a catalyst of the reaction in Scheme 2 (Table 3, entry 4). Bromobenzene has a reduction potential of ca. −2.4 V vs SCE (in dimethylformamide (DMF));[107] hence, reductive dehalogenation of substrate **2a** becomes inefficient even for photoexcited $[Mo(L^{tBu})_3]$ (Table 3, entry 5), especially in nonpolar C_6D_6. Photodriven reductive dehalogenation reactions are increasingly well-investigated,[108−111] and the general observation is that aryl bromides are substantially more difficult to reduce than aryl iodides,[107,112] and aryl chlorides are even more challenging.[106,113−115] The liberation of I^- in this initial step (and ligation of I^- to Mo(I), see earlier)[38] is likely responsible for the rather rapid degradation of $[Mo(L^{Me})_3]$ and the modest conversion achievable with this first-generation complex (Table 3, entries 1 and 2). Aryl radicals usually have very short lifetimes, but in the specific case of aryl radical A (Scheme 3), intramolecular reaction with the radical interceptor pyrrole to form the cyclic intermediate B is rather efficient.[116] Oxidation of intermediate B by Mo(I) then reinstates the photosensitizer to its initial (electronic ground) state and leads to radical cation C, which can be subsequently deprotonated to afford the final cyclization product. An important difference to thermal BHAS reactions is the presence of a weak base (TMP) rather than ^{t}BuOK, and it seems plausible that this renders deprotonation of intermediate B inefficient, making oxidation of B to C necessary before the proton can be abstracted by TMP. With ^{t}BuOK the reverse order of steps is commonly observed (deprotonation followed by oxidation), and this can give rise to a radical chain mechanism because the radical anion intermediate formed after the deprotonation step is strongly reducing (see Supporting Information page S15 for further details).[100] In the mechanism of Scheme 3, the neutral radical intermediate B is not sufficiently reducing to propagate a radical chain via electron donation to another equivalent of substrate.

To gain further insight into the photochemical performance of $[Mo(L^{tBu})_3]$, we explored the carefully selected range of substrates in Table 4, allowing us to probe the influence of structural and electronic variations on the light-driven BHAS reaction in a systematic manner. Substrate **3a** differs from **1a** by the length of the alkyl linker, and the resulting increased conformational flexibility causes a need for longer reaction times (Table 4, entries 1 and 2; Figure S19). Substrate **4a** has the same ethylene linker as **3a**, but the reaction time had to be lengthened further from 4 to 145 h to reach a similar level of conversion (Table 4, entry 3; Figure S20). This can be attributed to the fact that *tert*-butylphenyl is a far less efficient interceptor for the aryl radical than pyrrole,[116] rendering the step from A to B in Scheme 3 inefficient. Substrate **5a** (Table 4, entry 4) has essentially the same linker length as **4a**, but one CH_2 group has been replaced by an O atom. This makes the reaction even slower, now requiring 450 h instead of 145 h (Figure S21). The reason for this is likely the electron-donating nature of the alkoxy linker, rendering the reduction potential of the iodobenzene unit more negative and making reductive deiodination in the initial reaction step more difficult. In substrate **6a** (Table 4, entry 5) the alkoxy linker is reversed compared to **5a**, with the O atom connected to the *tert*-butylphenyl rather than the iodobenzene unit. This reduces the

Scheme 3. Proposed Mechanism for the Light-Driven Base-Promoted Homolytic Aromatic Substitution (BHAS) Reaction of Scheme 2[a]

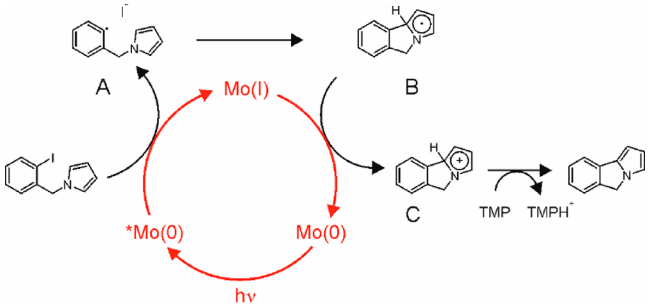

[a]Mo(0), *Mo(0), and Mo(I) denote the $[Mo(L^{tBu})_3]$ complex in its initial ground state, its long-lived ^{3}MLCT-excited state, and its one-electron oxidized form, respectively. TMP is 2,2,6,6-tetramethylpiperidine.

Table 4. BHAS Reactions To Explore the Photochemical Reactivity of $[Mo(L^{tBu})_3]$[a]

entry	reaction	conversion	duration
1		98%	2h
2		91%	4h
3	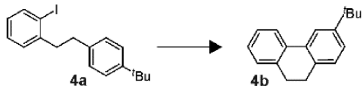	93%	145h
4	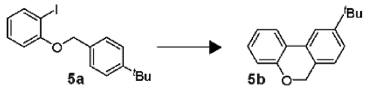	93%	450h
5	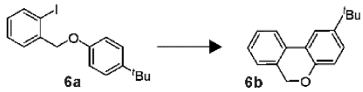	81%	7h

[a]Conditions were similar to those given in Table 3, but using a photoreactor with active cooling to stabilize the temperature of the reaction mixture at 25 °C throughout the complete irradiation process. See Supporting Information pages S16−S21 for details.

DOI: 10.1021/jacs.9b07373
J. Am. Chem. Soc. 2019, 141, 14394−14402

necessary reaction time to 7 h (for 81% conversion; Figure S22), likely because the electron-donating nature of the alkoxy linker now mostly acts on the *tert*-butylphenyl unit, making the deiodination of **6a** less difficult and the oxidation step converting intermediate B to C (Scheme 3) more facile. The reactivities observable for the range of substrates **1a**−**6a** thus seem compatible with the mechanism in Scheme 3. Evidently the $[Mo(L^{tBu})_3]$ complex is much more robust in these photochemical experiments than $[Mo(L^{Me})_3]$, making the new *tert*-butylated complex far superior not just in terms of photophysical properties (see earlier) but also for photochemical applications involving challenging reduction steps not feasible with $[Ru(bpy)_3]^{2+}$ or *fac*-$[Ir(ppy)_3]$.

SUMMARY AND CONCLUSIONS

Octahedrally coordinated low-spin d^6 complexes made from precious metals such as Ru, Os, Re, or Ir have attracted interest for more than 40 years, yet to date only a handful of such complexes made from Earth-abundant metals are known to emit from MLCT excited states.[117] Notably, the struggle to identify an MLCT-luminescent Fe(II) complex continues.[11] The present study establishes Mo(0) complexes with chelating diisocyanide ligands as a new family of photoactive compounds that are structurally and electronically closely related to Ru(II) polypyridines. Their photophysical properties can be tuned through ligand modification to a point where their luminescence quantum yield surpasses that achievable for $[Ru(bpy)_3]^{2+}$ by more than a factor of 2. Shielding of the metal center from the chemical environment and rigidifying the complex by introducing steric congestion at the ligand periphery is the key to this favorable behavior. In this manner, it has been possible to reduce the rate for nonradiative excited-state decay by more than an order of magnitude between $[Mo(L^{Me})_3]$ and $[Mo(L^{tBu})_3]$, leading to microsecond MLCT lifetimes and luminescence quantum yields as high as 0.203. This design principle furthermore improved the photochemical robustness enormously, making the high reducing power of the ^{3}MLCT-excited $[Mo(L^{tBu})_3]$ complex suitable for photochemical transformations that cannot be performed with the widely employed *fac*-$[Ir(ppy)_3]$ complex. Specifically, the inertness against nucleophilic attack at transiently oxidized Mo(I) metal centers seems of key importance, now permitting photoirradiation over very long periods (days to weeks) without significant complex degradation. A range of base-promoted homolytic aromatic substitution (BHAS) reactions with substrates specifically designed to underpin the photochemical mechanism was explored, demonstrating possibilities and limitations for application of the Mo(0) complexes for these overall redox-neutral reactions involving a thermodynamically challenging reductive dehalogenation and a C−H activation step.

ASSOCIATED CONTENT

Supporting Information

The Supporting Information is available free of charge on the ACS Publications website at DOI: 10.1021/jacs.9b07373.

Synthetic protocols, characterization data, additional spectroscopic data, and details regarding photochemical experiments (PDF)

AUTHOR INFORMATION

Corresponding Author

*oliver.wenger@unibas.ch

ORCID

Oliver S. Wenger: 0000-0002-0739-0553

Author Contributions

†P.H., F.G., and L.A.B. contributed equally.

Notes

The authors declare no competing financial interest.

ACKNOWLEDGMENTS

Funding from the Swiss National Science Foundation through Grant no. 200021_178760 is gratefully acknowledged.

REFERENCES

(1) Baldo, M. A.; Thompson, M. E.; Forrest, S. R. High-Efficiency Fluorescent Organic Light-Emitting Devices using a Phosphorescent Sensitizer. *Nature* **2000**, *403*, 750−753.

(2) Li, A.; Turro, C.; Kodanko, J. J. Ru(II) Polypyridyl Complexes Derived from Tetradentate Ancillary Ligands for Effective Photocaging. *Acc. Chem. Res.* **2018**, *51*, 1415−1421.

(3) Mari, C.; Pierroz, V.; Ferrari, S.; Gasser, G. Combination of Ru(II) Complexes and Light: New Frontiers in Cancer Therapy. *Chem. Sci.* **2015**, *6*, 2660−2686.

(4) Hagfeldt, A.; Grätzel, M. Molecular Photovoltaics. *Acc. Chem. Res.* **2000**, *33*, 269−277.

(5) Yoon, T. P.; Ischay, M. A.; Du, J. N. Visible Light Photocatalysis as a Greener Approach to Photochemical Synthesis. *Nat. Chem.* **2010**, *2*, 527−532.

(6) Gray, H. B.; Maverick, A. W. Solar Chemistry of Metal-Complexes. *Science* **1981**, *214*, 1201−1205.

(7) McCusker, J. K. Electronic Structure in the Transition Metal Block and its Implications for Light Harvesting. *Science* **2019**, *363*, 484−488.

(8) Young, E. R.; Oldacre, A. Iron Hits the Mark. *Science* **2019**, *363*, 225−226.

(9) Liu, Y. Z.; Persson, P.; Sundström, V.; Wärnmark, K. Fe N-Heterocyclic Carbene Complexes as Promising Photosensitizers. *Acc. Chem. Res.* **2016**, *49*, 1477−1485.

(10) Duchanois, T.; Liu, L.; Pastore, M.; Monari, A.; Cebrian, C.; Trolez, Y.; Darari, M.; Magra, K.; Frances-Monerris, A.; Domenichini, E.; Beley, M.; Assfeld, X.; Haacke, S.; Gros, P. C. NHC-Based Iron Sensitizers for DSSCs. *Inorganics* **2018**, *6*, 63.

(11) Wenger, O. S. Is Iron the New Ruthenium? *Chem. - Eur. J.* **2019**, *25*, 6043−6052.

(12) Steube, J.; Burkhardt, L.; Päpcke, A.; Moll, J.; Zimmer, P.; Schoch, R.; Wölper, C.; Heinze, K.; Lochbrunner, S.; Bauer, M. Excited-State Kinetics of an Air-Stable Cyclometalated Iron(II) Complex. *Chem. - Eur. J.* **2019**, DOI: 10.1002/chem.201902488.

(13) Dixon, I. M.; Boissard, G.; Whyte, H.; Alary, F.; Heully, J. L. Computational Estimate of the Photophysical Capabilities of Four Series of Organometallic Iron(II) Complexes. *Inorg. Chem.* **2016**, *55*, 5089−5091.

(14) Ashley, D. C.; Jakubikova, E. Ironing out the Photochemical and Spin-Crossover Behavior of Fe(II) Coordination Compounds with Computational Chemistry. *Coord. Chem. Rev.* **2017**, *337*, 97−111.

(15) Zhang, W. K.; Gaffney, K. J. Mechanistic Studies of Photoinduced Spin Crossover and Electron Transfer in Inorganic Complexes. *Acc. Chem. Res.* **2015**, *48*, 1140−1148.

(16) Carey, M. C.; Adelman, S. L.; McCusker, J. K. Insights into the Excited State Dynamics of Fe(II) Polypyridyl Complexes from Variable-Temperature Ultrafast Spectroscopy. *Chem. Sci.* **2019**, *10*, 134−144.

(17) McCusker, J. K.; Walda, K. N.; Dunn, R. C.; Simon, J. D.; Magde, D.; Hendrickson, D. N. Subpicosecond ^{1}MLCT-^{5}T$_2$

DOI: 10.1021/jacs.9b07373
J. Am. Chem. Soc. 2019, 141, 14394−14402

Intersystem Crossing of Low-Spin Polypyridyl Ferrous Complexes. *J. Am. Chem. Soc.* **1993**, *115*, 298−307.
(18) Auböck, G.; Chergui, M. Sub-50-fs Photoinduced Spin Crossover in $Fe(bpy_3)^{2+}$. *Nat. Chem.* **2015**, *7*, 629−633.
(19) Jamula, L. L.; Brown, A. M.; Guo, D.; McCusker, J. K. Synthesis and Characterization of a High-Symmetry Ferrous Polypyridyl Complex: Approaching the $^5T_2/^3T_1$ Crossing Point for Fe^{II}. *Inorg. Chem.* **2014**, *53*, 15−17.
(20) Shepard, S. G.; Fatur, S. M.; Rappe, A. K.; Damrauer, N. H. Highly Strained Iron(II) Polypyridines: Exploiting the Quintet Manifold To Extend the Lifetime of MLCT Excited States. *J. Am. Chem. Soc.* **2016**, *138*, 2949−2952.
(21) Fatur, S. M.; Shepard, S. G.; Higgins, R. F.; Shores, M. P.; Damrauer, N. H. A Synthetically Tunable System To Control MLCT Excited-State Lifetimes and Spin States in Iron(II) Polypyridines. *J. Am. Chem. Soc.* **2017**, *139*, 4493−4505.
(22) Mengel, A. K. C.; Förster, C.; Breivogel, A.; Mack, K.; Ochsmann, J. R.; Laquai, F.; Ksenofontov, V.; Heinze, K. A Heteroleptic Push-Pull Substituted Iron(II) Bis(tridentate) Complex with Low-Energy Charge-Transfer States. *Chem. - Eur. J.* **2015**, *21*, 704−714.
(23) Mengel, A. K. C.; Bissinger, C.; Dorn, M.; Back, O.; Förster, C.; Heinze, K. Boosting Vis/NIR Charge-Transfer Absorptions of Iron(II) Complexes by N-Alkylation and N-Deprotonation in the Ligand Backbone. *Chem. - Eur. J.* **2017**, *23*, 7920−7931.
(24) Liu, Y. Z.; Harlang, T.; Canton, S. E.; Chabera, P.; Suarez-Alcantara, K.; Fleckhaus, A.; Vithanage, D. A.; Goransson, E.; Corani, A.; Lomoth, R.; Sundström, V.; Wärnmark, K. Towards Longer-Lived Metal-to-Ligand Charge Transfer States of Iron(II) Complexes: An N-Heterocyclic Carbene Approach. *Chem. Commun.* **2013**, *49*, 6412−6414.
(25) Harlang, T. C. B.; Liu, Y. Z.; Gordivska, O.; Fredin, L. A.; Ponseca, C. S.; Huang, P.; Chabera, P.; Kjaer, K. S.; Mateos, H.; Uhlig, J.; Lomoth, R.; Wallenberg, R.; Styring, S.; Persson, P.; Sundström, V.; Wärnmark, K. Iron Sensitizer Converts Light to Electrons with 92% Yield. *Nat. Chem.* **2015**, *7*, 883−889.
(26) Liu, L.; Duchanois, T.; Etienne, T.; Monari, A.; Beley, M.; Assfeld, X.; Haacke, S.; Gros, P. C. A New Record Excited State ^{3}MLCT Lifetime for Metalorganic Iron(II) Complexes. *Phys. Chem. Chem. Phys.* **2016**, *18*, 12550−12556.
(27) Duchanois, T.; Etienne, T.; Beley, M.; Assfeld, X.; Perpete, E. A.; Monari, A.; Gros, P. C. Heteroleptic Pyridyl-Carbene Iron Complexes with Tuneable Electronic Properties. *Eur. J. Inorg. Chem.* **2014**, *2014*, 3747−3753.
(28) Liu, Y. Z.; Kjaer, K. S.; Fredin, L. A.; Chabera, P.; Harlang, T.; Canton, S. E.; Lidin, S.; Zhang, J. X.; Lomoth, R.; Bergquist, K. E.; Persson, P.; Wärnmark, K.; Sundström, V. A Heteroleptic Ferrous Complex with Mesoionic Bis(1,2,3-triazol-5-ylidene) Ligands: Taming the MLCT Excited State of Iron(II). *Chem. - Eur. J.* **2015**, *21*, 3628−3639.
(29) Chábera, P.; Liu, Y.; Prakash, O.; Thyrhaug, E.; El Nahhas, A.; Honarfar, A.; Essén, S.; Fredin, L. A.; Harlang, T. C. B.; Kjaer, K. S.; Handrup, K.; Ericson, F.; Tatsuno, Y.; Morgan, K.; Schnadt, J.; Häggström, L.; Ericsson, T.; Sobkowiak, A.; Lidin, S.; Huang, P.; Styring, S.; Uhlig, J.; Bendix, J.; Lomoth, R.; Sundström, V.; Persson, P.; Wärnmark, K. A Low-Spin Fe(III) Complex with 100-ps Ligand-to-Metal Charge Transfer Photoluminescence. *Nature* **2017**, *543*, 695−699.
(30) Kjær, K. S.; Kaul, N.; Prakash, O.; Chábera, P.; Rosemann, N. W.; Honarfar, A.; Gordivska, O.; Fredin, L. A.; Bergquist, K. E.; Häggström, L.; Ericsson, T.; Lindh, L.; Yartsev, A.; Styring, S.; Huang, P.; Uhlig, J.; Bendix, J.; Strand, D.; Sundström, V.; Persson, P.; Lomoth, R.; Wärnmark, K. Luminescence and Reactivity of a Charge-Transfer Excited Iron Complex with Nanosecond Lifetime. *Science* **2019**, *363*, 249−253.
(31) Chábera, P.; Kjaer, K. S.; Prakash, O.; Honarfar, A.; Liu, Y. Z.; Fredin, L. A.; Harlang, T. C. B.; Lidin, S.; Uhlig, J.; Sundström, V.; Lomoth, R.; Persson, P.; Wärnmark, K. Fe^{II} Hexa N-Heterocyclic Carbene Complex with a 528 ps Metal-to-Ligand Charge-Transfer Excited-State Lifetime. *J. Phys. Chem. Lett.* **2018**, *9*, 459−463.
(32) Mann, K. R.; Cimolino, M.; Geoffroy, G. L.; Hammond, G. S.; Orio, A. A.; Albertin, G.; Gray, H. B. Electronic Structures and Spectra of Hexakisphenylisocyanide Complexes of Cr(0), Mo(0), W(0), Mn(I), and Mn(II). *Inorg. Chim. Acta* **1976**, *16*, 97−101.
(33) Mann, K. R.; Gray, H. B.; Hammond, G. S. Excited-State Reactivity Patterns of Hexakisarylisocyano Complexes of Chromium(0), Molybdenum(0), and Tungsten(0). *J. Am. Chem. Soc.* **1977**, *99*, 306−307.
(34) Sattler, W.; Ener, M. E.; Blakemore, J. D.; Rachford, A. A.; LaBeaume, P. J.; Thackeray, J. W.; Cameron, J. F.; Winkler, J. R.; Gray, H. B. Generation of Powerful Tungsten Reductants by Visible Light Excitation. *J. Am. Chem. Soc.* **2013**, *135*, 10614−10617.
(35) Sattler, W.; Henling, L. M.; Winkler, J. R.; Gray, H. B. Bespoke Photoreductants: Tungsten Arylisocyanides. *J. Am. Chem. Soc.* **2015**, *137*, 1198−1205.
(36) Büldt, L. A.; Wenger, O. S. Chromium(0), Molybdenum(0), and Tungsten(0) Isocyanide Complexes as Luminophores and Photosensitizers with Long-Lived Excited States. *Angew. Chem., Int. Ed.* **2017**, *56*, 5676−5682.
(37) Büldt, L. A.; Guo, X.; Vogel, R.; Prescimone, A.; Wenger, O. S. A Tris(diisocyanide)chromium(0) Complex Is a Luminescent Analog of $Fe(2,2'\text{-Bipyridine})_3^{2+}$. *J. Am. Chem. Soc.* **2017**, *139*, 985−992.
(38) Büldt, L. A.; Guo, X.; Prescimone, A.; Wenger, O. S. A Molybdenum(0) Isocyanide Analogue of $Ru(2,2\text{-Bipyridine})_3^{2+}$: A Strong Reductant for Photoredox Catalysis. *Angew. Chem., Int. Ed.* **2016**, *55*, 11247−11250.
(39) Studer, A.; Curran, D. P. The Electron is a Catalyst. *Nat. Chem.* **2014**, *6*, 765−773.
(40) Hamze, R.; Peltier, J. L.; Sylvinson, D.; Jung, M.; Cardenas, J.; Haiges, R.; Soleilhavoup, M.; Jazzar, R.; Djurovich, P. I.; Bertrand, G.; Thompson, M. E. Eliminating Nonradiative Decay in Cu(I) Emitters: > 99% Quantum Efficiency and Microsecond Lifetime. *Science* **2019**, *363*, 601−606.
(41) Gernert, M.; Müller, U.; Haehnel, M.; Pflaum, J.; Steffen, A. A Cyclic Alkyl(amino)carbene as Two-Atom π-Chromophore Leading to the First Phosphorescent Linear Cu^I Complexes. *Chem. - Eur. J.* **2017**, *23*, 2206−2216.
(42) Di, D. W.; Romanov, A. S.; Yang, L.; Richter, J. M.; Rivett, J. P. H.; Jones, S.; Thomas, T. H.; Abdi Jalebi, M.; Friend, R. H.; Linnolahti, M.; Bochmann, M.; Credgington, D. High-Performance Light-Emitting Diodes based on Carbene-Metal-Amides. *Science* **2017**, *356*, 159−163.
(43) Leoni, E.; Mohanraj, J.; Holler, M.; Mohankumar, M.; Nierengarten, I.; Monti, F.; Sournia-Saquet, A.; Delavaux-Nicot, B.; Nierengarten, J. F.; Armaroli, N. Heteroleptic Copper(I) Complexes Prepared from Phenanthroline and Bis-Phosphine Ligands: Rationalization of the Photophysical and Electrochemical Properties. *Inorg. Chem.* **2018**, *57*, 15537−15549.
(44) Hossain, A.; Bhattacharyya, A.; Reiser, O. Copper's Rapid Ascent in Visible-Light Photoredox Catalysis. *Science* **2019**, *364*, eaav9713.
(45) Hernandez-Perez, A. C.; Collins, S. K. Heteroleptic Cu-Based Sensitizers in Photoredox Catalysis. *Acc. Chem. Res.* **2016**, *49*, 1557−1565.
(46) Michelet, B.; Deldaele, C.; Kajouj, S.; Moucheron, C.; Evano, G. A General Copper Catalyst for Photoredox Transformations of Organic Halides. *Org. Lett.* **2017**, *19*, 3576−3579.
(47) Nicholls, T. P.; Caporale, C.; Massi, M.; Gardiner, M. G.; Bissember, A. C. Synthesis and Characterisation of Homoleptic 2,9-Diaryl-1,10-Phenanthroline Copper(I) Complexes: Influencing Selectivity in Photoredox-Catalysed Atom-Transfer Radical Addition Reactions. *Dalton Trans* **2019**, *48*, 7290−7301.
(48) Lazorski, M. S.; Castellano, F. N. Advances in the Light Conversion Properties of Cu(I)-Based Photosensitizers. *Polyhedron* **2014**, *82*, 57−70.
(49) Czerwieniec, R.; Leitl, M. J.; Homeier, H. H. H.; Yersin, H. Cu(I) Complexes - Thermally Activated Delayed Fluorescence.

DOI: 10.1021/jacs.9b07373
J. Am. Chem. Soc. 2019, 141, 14394−14402

Photophysical Approach and Material Design. *Coord. Chem. Rev.* **2016**, *325*, 2−28.
(50) Mondal, R.; Lozada, I. B.; Davis, R. L.; Williams, J. A. G.; Herbert, D. E. Exploiting Synergy Between Ligand Design and Counterion Interactions to Boost Room Temperature Phosphorescence from Cu(I) Compounds. *J. Mater. Chem. C* **2019**, *7*, 3772−3778.
(51) Wang, C.; Otto, S.; Dorn, M.; Kreidt, E.; Lebon, J.; Srsan, L.; Di Martino-Fumo, P.; Gerhards, M.; Resch-Genger, U.; Seitz, M.; Heinze, K. Deuterated Molecular Ruby with Record Luminescence Quantum Yield. *Angew. Chem., Int. Ed.* **2018**, *57*, 1112−1116.
(52) Jimenez, J. R.; Doistau, B.; Besnard, C.; Piguet, C. Versatile Heteroleptic Bis-Terdentate Cr(III) Chromophores Displaying Room Temperature Millisecond Excited State Lifetimes. *Chem. Commun.* **2018**, *54*, 13228−13231.
(53) Stevenson, S. M.; Shores, M. P.; Ferreira, E. M. Photooxidizing Chromium Catalysts for Promoting Radical Cation Cycloadditions. *Angew. Chem., Int. Ed.* **2015**, *54*, 6506−6510.
(54) Ford, P. C. Metal Complex Strategies for Photo-Uncaging the Small Molecule Bioregulators Nitric Oxide and Carbon Monoxide. *Coord. Chem. Rev.* **2018**, *376*, 548−564.
(55) Pal, A. K.; Li, C. F.; Hanan, G. S.; Zysman-Colman, E. Blue-Emissive Cobalt(III) Complexes and Their Use in the Photocatalytic Trifluoromethylation of Polycyclic Aromatic Hydrocarbons. *Angew. Chem., Int. Ed.* **2018**, *57*, 8027−8031.
(56) Welin, E. R.; Le, C.; Arias-Rotondo, D. M.; McCusker, J. K.; MacMillan, D. W. C. Photosensitized, Energy Transfer-Mediated Organometallic Catalysis through Electronically Excited Nickel(II). *Science* **2017**, *355*, 380−384.
(57) Shields, B. J.; Kudisch, B.; Scholes, G. D.; Doyle, A. G. Long-Lived Charge-Transfer States of Nickel(II) Aryl Halide Complexes Facilitate Bimolecular Photoinduced Electron Transfer. *J. Am. Chem. Soc.* **2018**, *140*, 3035−3039.
(58) Grübel, M.; Bosque, I.; Altmann, P. J.; Bach, T.; Hess, C. R. Redox and Photocatalytic Properties of a Ni^{II} Complex with a Macrocyclic Biquinazoline (Mabiq) Ligand. *Chem. Sci.* **2018**, *9*, 3313−3317.
(59) Zhang, Y.; Lee, T. S.; Petersen, J. L.; Milsmann, C. A Zirconium Photosensitizer with a Long-Lived Excited State: Mechanistic Insight into Photoinduced Single-Electron Transfer. *J. Am. Chem. Soc.* **2018**, *140*, 5934−5947.
(60) Zhang, Y.; Petersen, J. L.; Milsmann, C. Photochemical C-C Bond Formation in Luminescent Zirconium Complexes with CNN Pincer Ligands. *Organometallics* **2018**, *37*, 4488−4499.
(61) Yeung, K. T.; To, W. P.; Sun, C. Y.; Cheng, G.; Ma, C. S.; Tong, G. S. M.; Yang, C.; Che, C. M. Luminescent Tungsten(VI) Complexes: Photophysics and Applicability to Organic Light-Emitting Diodes and Photocatalysis. *Angew. Chem., Int. Ed.* **2017**, *56*, 133−137.
(62) Rudshteyn, B.; Vibbert, H. B.; May, R.; Wasserman, E.; Warnke, I.; Hopkins, M. D.; Batista, V. S. Thermodynamic and Structural Factors That Influence the Redox Potentials of Tungsten-Alkylidyne Complexes. *ACS Catal.* **2017**, *7*, 6134−6143.
(63) Kvapilova, H.; Sattler, W.; Sattler, A.; Sazanovich, I. V.; Clark, I. P.; Towrie, M.; Gray, H. B.; Zalis, S.; Vlcek, A. Electronic Excited States of Tungsten(0) Arylisocyanides. *Inorg. Chem.* **2015**, *54*, 8518−8528.
(64) Qiao, Y. S.; Schelter, E. J. Lanthanide Photocatalysis. *Acc. Chem. Res.* **2018**, *51*, 2926−2936.
(65) Romero, N. A.; Nicewicz, D. A. Organic Photoredox Catalysis. *Chem. Rev.* **2016**, *116*, 10075−10166.
(66) Ghosh, I.; Marzo, L.; Das, A.; Shaikh, R.; König, B. Visible Light Mediated Photoredox Catalytic Arylation Reactions. *Acc. Chem. Res.* **2016**, *49*, 1566−1577.
(67) Speckmeier, E.; Fischer, T. G.; Zeitler, K. A Toolbox Approach to Construct Broadly Applicable Metal-Free Catalysts for Photoredox Chemistry: Deliberate Tuning of Redox Potentials and Importance of Halogens in Donor-Acceptor Cyanoarenes. *J. Am. Chem. Soc.* **2018**, *140*, 15353−15365.
(68) Fischer, C.; Sparr, C. Direct Transformation of Esters into Heterocyclic Fluorophores. *Angew. Chem., Int. Ed.* **2018**, *57*, 2436−2440.
(69) McCarthy, B. G.; Pearson, R. M.; Lim, C. H.; Sartor, S. M.; Damrauer, N. H.; Miyake, G. M. Structure-Property Relationships for Tailoring Phenoxazines as Reducing Photoredox Catalysts. *J. Am. Chem. Soc.* **2018**, *140*, 5088−5101.
(70) Drance, M. J.; Sears, J. D.; Mrse, A. M.; Moore, C. E.; Rheingold, A. L.; Neidig, M. L.; Figueroa, J. S. Terminal Coordination of Diatomic Boron Monofluoride to Iron. *Science* **2019**, *363*, 1203−1205.
(71) Margulieux, G. W.; Weidemann, N.; Lacy, D. C.; Moore, C. E.; Rheingold, A. L.; Figueroa, J. S. Isocyano Analogues of $Co(CO)_4^n$: A Tetraisocyanide of Cobalt Isolated in Three States of Charge. *J. Am. Chem. Soc.* **2010**, *132*, 5033−5035.
(72) Angelici, R. J.; Quick, M. H.; Kraus, G. A.; Plummer, D. T. Synthesis of Chelating Bidentate Isocyano and Cyano Ligands and Their Metal Complexes. *Inorg. Chem.* **1982**, *21*, 2178−2184.
(73) Plummer, D. T.; Angelici, R. J. Synthesis and Characterization of Homoleptic Complexes of the Chelating Bidentate Isocyano Ligand *tert*-BuDiNC. *Inorg. Chem.* **1983**, *22*, 4063−4070.
(74) Plummer, D. T.; Kraus, G. A.; Angelici, R. J. Synthesis of Chelating Bidentate and Tridentate Cyano Ligands and their Complexes with Group 7 Metal Carbonyls. *Inorg. Chem.* **1983**, *22*, 3492−3497.
(75) Hahn, F. E.; Tamm, M. Chelate Complexes with Triisocyanide Ligands. *Angew. Chem., Int. Ed. Engl.* **1991**, *30*, 203−205.
(76) Hahn, F. E. The Coordination Chemistry of Multidentate Isocyanide Ligands. *Angew. Chem., Int. Ed. Engl.* **1993**, *32*, 650−665.
(77) Naik, A.; Maji, T.; Reiser, O. Iron(II)-Bis(isonitrile) Complexes: Novel Catalysts in Asymmetric Transfer Hydrogenations of Aromatic and Heteroaromatic Ketones. *Chem. Commun.* **2010**, *46*, 4475−4477.
(78) Vicenzi, D.; Sgarbossa, P.; Biffis, A.; Tubaro, C.; Basato, M.; Michelin, R. A.; Lanza, A.; Nestola, F.; Bogialli, S.; Pastore, P.; Venzo, A. Platinum(II) Complexes with Novel Diisocyanide Ligands: Catalysts in Alkyne Hydroarylation. *Organometallics* **2013**, *32*, 7153−7162.
(79) Monti, F.; Baschieri, A.; Matteucci, E.; Mazzanti, A.; Sambri, L.; Barbieri, A.; Armaroli, N. A Chelating Diisocyanide Ligand for Cyclometalated Ir(III) Complexes with Strong and Tunable Luminescence. *Faraday Discuss.* **2015**, *185*, 233−248.
(80) Knorn, M.; Rawner, T.; Czerwieniec, R.; Reiser, O. Copper-(phenanthroline)(bisisonitrile)$^+$-Complexes for the Visible-Light-Mediated Atom Transfer Radical Addition and Allylation Reactions. *ACS Catal.* **2015**, *5*, 5186−5193.
(81) Emerich, B. M.; Moore, C. E.; Fox, B. J.; Rheingold, A. L.; Figueroa, J. S. Protecting-Group-Free Access to a Three-Coordinate Nickel(0) Tris-isocyanide. *Organometallics* **2011**, *30*, 2598−2608.
(82) Cotton, F. A.; Zingales, F. Donor-Acceptor Properties of Isonitriles as Estimated by Infrared Study. *J. Am. Chem. Soc.* **1961**, *83*, 351−355.
(83) Bohling, D. A.; Mann, K. R.; Enger, S.; Gennett, T.; Weaver, M. J.; Walton, R. A. Electrochemical Redox Behavior of the Hexakis-(arylisocyanide) Complexes of Molybdenum(0) and Tungsten(0). *Inorg. Chim. Acta* **1985**, *97*, L51−L53.
(84) Arias-Rotondo, D. M.; McCusker, J. K. The Photophysics of Photoredox Catalysis: A Roadmap for Catalyst Design. *Chem. Soc. Rev.* **2016**, *45*, 5803−5820.
(85) Bohling, D. A.; Evans, J. F.; Mann, K. R. Inductive, Steric, and Environmental Effects in the Non-Aqueous Electrochemistry of Hexakis(Aryl Isocyanide) Chromium Complexes. *Inorg. Chem.* **1982**, *21*, 3546−3551.
(86) Suzuki, K.; Kobayashi, A.; Kaneko, S.; Takehira, K.; Yoshihara, T.; Ishida, H.; Shiina, Y.; Oishi, S.; Tobita, S. Reevaluation of Absolute Luminescence Quantum Yields of Standard Solutions Using a Spectrometer with an Integrating Sphere and a Back-Thinned CCD Detector. *Phys. Chem. Chem. Phys.* **2009**, *11*, 9850−9860.

DOI: 10.1021/jacs.9b07373
J. Am. Chem. Soc. 2019, 141, 14394−14402

(87) Cuttell, D. G.; Kuang, S. M.; Fanwick, P. E.; McMillin, D. R.; Walton, R. A. Simple Cu(I) Complexes with Unprecedented Excited-State Lifetimes. *J. Am. Chem. Soc.* **2002**, *124*, 6−7.
(88) Brunner, F.; Babaei, A.; Pertegas, A.; Junquera-Hernandez, J. M.; Prescimone, A.; Constable, E. C.; Bolink, H. J.; Sessolo, M.; Orti, E.; Housecroft, C. E. Phosphane Tuning in Heteroleptic Cu(N^N)(P^P)$^+$ Complexes for Light-Emitting Electrochemical Cells. *Dalton Trans* **2019**, *48*, 446−460.
(89) Armaroli, N. Photoactive Mono- and Polynuclear Cu(I)-Phenanthrolines. A Viable Alternative to Ru(II)-Polypyridines? *Chem. Soc. Rev.* **2001**, *30*, 113−124.
(90) Yoshimura, A.; Hoffman, M. Z.; Sun, H. An Evaluation of the Excited-State Absorption-Spectrum of $Ru(bpy)_3^{2+}$ in Aqueous and Acetonitrile Solutions. *J. Photochem. Photobiol., A* **1993**, *70*, 29−33.
(91) Jarenmark, M.; Carlström, G.; Fredin, L. A.; Hedberg Wallenstein, J.; Doverbratt, I.; Abrahamsson, M.; Persson, P. Diastereomerization Dynamics of a Bistridentate Ru^{II} Complex. *Inorg. Chem.* **2016**, *55*, 3015−3022.
(92) Caspar, J. V.; Meyer, T. J. Application of the Energy-Gap Law to Nonradiative Excited-State Decay. *J. Phys. Chem.* **1983**, *87*, 952−957.
(93) Klendworth, D. D.; Welters, W. W.; Walton, R. A. Redox Chemistry of Hexakis(Phenyl Isocyanide) Complexes of Molybdenum and Tungsten - The Synthesis of the 7-Coordinate Cations $[M(CNPh)_7]^{2+}$ and their Electrochemistry and Substitution Reactions. *Organometallics* **1982**, *1*, 336−343.
(94) Caravana, C.; Giandomenico, C. M.; Lippard, S. J. Electrochemical Studies of 7-Coordinate Isocyanide Complexes of Molybdenum(II) and Tungsten(II). *Inorg. Chem.* **1982**, *21*, 1860−1863.
(95) Yanagisawa, S.; Ueda, K.; Taniguchi, T.; Itami, K. Potassium *t*-Butoxide Alone Can Promote the Biaryl Coupling of Electron-Deficient Nitrogen Heterocycles and Haloarenes. *Org. Lett.* **2008**, *10*, 4673−4676.
(96) Studer, A.; Curran, D. P. Organocatalysis and C-H Activation Meet Radical- and Electron-Transfer Reactions. *Angew. Chem., Int. Ed.* **2011**, *50*, 5018−5022.
(97) Liu, W.; Cao, H.; Zhang, H.; Zhang, H.; Chung, K. H.; He, C. A.; Wang, H. B.; Kwong, F. Y.; Lei, A. W. Organocatalysis in Cross-Coupling: DMEDA-Catalyzed Direct C-H Arylation of Unactivated Benzene. *J. Am. Chem. Soc.* **2010**, *132*, 16737−16740.
(98) Sun, C. L.; Li, H.; Yu, D. G.; Yu, M. A.; Zhou, X. A.; Lu, X. Y.; Huang, K.; Zheng, S. F.; Li, B. J.; Shi, Z. J. An Efficient Organocatalytic Method for Constructing Biaryls through Aromatic C-H Activation. *Nat. Chem.* **2010**, *2*, 1044−1049.
(99) Shirakawa, E.; Itoh, K.; Higashino, T.; Hayashi, T. *tert*-Butoxide-Mediated Arylation of Benzene with Aryl Halides in the Presence of a Catalytic 1,10-Phenanthroline Derivative. *J. Am. Chem. Soc.* **2010**, *132*, 15537−15539.
(100) Zhang, L.; Yang, H.; Jiao, L. Revisiting the Radical Initiation Mechanism of the Diamine-Promoted Transition-Metal-Free Cross-Coupling Reaction. *J. Am. Chem. Soc.* **2016**, *138*, 7151−7160.
(101) Buden, M. E.; Guastavino, J. F.; Rossi, R. A. Room-Temperature Photoinduced Direct C-H-Arylation via Base-Promoted Homolytic Aromatic Substitution. *Org. Lett.* **2013**, *15*, 1174−1177.
(102) Zheng, X. L.; Yang, L.; Du, W. Y.; Ding, A. S.; Guo, H. Amine-Catalyzed Direct Photoarylation of Unactivated Arenes. *Chem. - Asian J.* **2014**, *9*, 439−442.
(103) Kawamoto, T.; Sato, A.; Ryu, I. Cyanoborohydride-Promoted Radical Arylation of Benzene. *Org. Lett.* **2014**, *16*, 2111−2113.
(104) Cheng, Y. N.; Gu, X. Y.; Li, P. X. Visible-Light Photoredox in Homolytic Aromatic Substitution: Direct Arylation of Arenes with Aryl Halides. *Org. Lett.* **2013**, *15*, 2664−2667.
(105) Xu, Z.; Gao, L.; Wang, L. L.; Gong, M. W.; Wang, W. F.; Yuan, R. S. Visible Light Photoredox Catalyzed Biaryl Synthesis Using Nitrogen Heterocycles as Promoter. *ACS Catal.* **2015**, *5*, 45−50.
(106) Ghosh, I.; Ghosh, T.; Bardagi, J. I.; König, B. Reduction of Aryl Halides by Consecutive Visible Light-Induced Electron Transfer Processes. *Science* **2014**, *346*, 725−728.
(107) Pause, L.; Robert, M.; Savéant, J. M. Can Single-Electron Transfer Break an Aromatic Carbon-Heteroatom Bond in One Step? A Novel Example of Transition between Stepwise and Concerted Mechanisms in the Reduction of Aromatic Iodides. *J. Am. Chem. Soc.* **1999**, *121*, 7158−7159.
(108) Nguyen, J. D.; D'Amato, E. M.; Narayanam, J. M. R.; Stephenson, C. R. J. Engaging Unactivated Alkyl, Alkenyl and Aryl Iodides in Visible-Light-Mediated Free Radical Reactions. *Nat. Chem.* **2012**, *4*, 854−859.
(109) Poelma, S. O.; Burnett, G. L.; Discekici, E. H.; Mattson, K. M.; Treat, N. J.; Luo, Y. D.; Hudson, Z. M.; Shankel, S. L.; Clark, P. G.; Kramer, J. W.; Hawker, C. J.; Read de Alaniz, J. Chemoselective Radical Dehalogenation and C-C Bond Formation on Aryl Halide Substrates Using Organic Photoredox Catalysts. *J. Org. Chem.* **2016**, *81*, 7155−7160.
(110) Kim, H.; Lee, C. Visible-Light-Induced Photocatalytic Reductive Transformations of Organohalides. *Angew. Chem., Int. Ed.* **2012**, *51*, 12303−12306.
(111) Shon, J.-H.; Sittel, S.; Teets, T. S. Synthesis and Characterization of Strong Cyclometalating Iridium Photoreductants for Application in Photocatalytic Aryl Bromide Hydrodebromination. *ACS Catal.* **2019**, *9*, 8646−8658.
(112) Devery, J. J.; Nguyen, J. D.; Dai, C. H.; Stephenson, C. R. J. Light-Mediated Reductive Debromination of Unactivated Alkyl and Aryl Bromides. *ACS Catal.* **2016**, *6*, 5962−5967.
(113) Yin, H. L.; Carroll, P. J.; Manor, B. C.; Anna, J. M.; Schelter, E. J. Cerium Photosensitizers: Structure-Function Relationships and Applications in Photocatalytic Aryl Coupling Reactions. *J. Am. Chem. Soc.* **2016**, *138*, 5984−5993.
(114) Ghosh, I.; König, B. Chromoselective Photocatalysis: Controlled Bond Activation through Light-Color Regulation of Redox Potentials. *Angew. Chem., Int. Ed.* **2016**, *55*, 7676−7679.
(115) Neumeier, M.; Sampedro, D.; Májek, M.; de la Peña O'Shea, V. A.; Jacobi von Wangelin, A.; Pérez-Ruiz, R. Dichromatic Photocatalytic Substitutions of Aryl Halides with a Small Organic Dye. *Chem. - Eur. J.* **2018**, *24*, 105−108.
(116) Gritter, R. J.; Chriss, R. J. Free-Radical Reactions of Pyrroles. *J. Org. Chem.* **1964**, *29*, 1163−1167.
(117) Wenger, O. S. Photoactive Complexes with Earth-Abundant Metals. *J. Am. Chem. Soc.* **2018**, *140*, 13522−13533.

DOI: 10.1021/jacs.9b07373
J. Am. Chem. Soc. 2019, 141, 14394−14402

Supporting Information to:

Long-Lived, Strongly Emissive, and Highly Reducing Excited States in Mo(0) Complexes with Chelating Isocyanides

Patrick Herr,† Felix Glaser,† Laura A. Büldt,† Christopher B. Larsen, and Oliver S. Wenger*

† These authors contributed equally.

Department of Chemistry, University of Basel, St. Johanns-Ring 19, 4056 Basel, Switzerland

Table of contents

Syntheses, equipment and methods

The L^{Me} and L^{tBu} ligands and the $[Mo(L^{Me})_3]$ complex were synthesized as reported earlier.[1]

$[Mo(L^{tBu})_3]$. The following method is similar to our previously published synthesis of $[Mo(L^{Me})_3]$,[1] and it is based on a method originally developed for the synthesis of W(0) complexes with monodentate isocyanides.[2,3] Sodium amalgam was prepared by adding small pieces of Na (33 mg, 1.4 mmol) to Hg (0.3 ml, 4.4 g, 22 mmol). A solution of L^{tBu} ligand (86.6 mg, 0.172 mmol) in dry THF (2 ml) was added, followed by addition of a solution of $MoCl_4(THF)_2$ (26 mg, 0.052 mmol) in dry THF (2 ml).[1,4] After adding more THF (2 ml), the reaction mixture was stirred vigorously under Ar at room temperature overnight. The dark red solution was then transferred to a separate Schlenk flask using a syringe, followed by filtration under inert (Ar) gas. The red filtrate was concentrated in vacuo to yield the desired complex as a red crystalline solid in 68% yield. ^{1}H-NMR (600 MHz, C_6D_6): δ = 7.52 (d, J = 2.3 Hz, 2 H), 7.48 (dd, J = 7.7 Hz and 1.7 Hz, 2 H), 7.47 (d, J = 2.3 Hz, 2 H), 7.34-7.28 (m, 2 H), 1.50 (s, 18 H), 1.20 (s, 18 H) ppm. ^{13}C-NMR (150.9 MHz, C_6D_6): δ = 175.3, 152.3, 146.0, 141.8, 139.4, 131.1, 129.4, 128.8, 127.6, 126.5, 123.1, 35.8, 35.2, 31.2, 29.4 ppm. IR ν [cm^{-1}]: 2953 (m), 2923 (m), 2866 (w), 1951 (s, $\nu_{C\equiv N}$), 1593 (w), 1457 (m), 1425 (m), 1389 (m), 1361 (m), 1248 (w), 1203 (w), 880 (w), 841 (w), 797 (w), 719 (w), 696 (m), 537 (m), 506 (w), 447 (w). HRMS (ESI) (*m/z*) calcd. for $C_{108}H_{132}N_6Mo^+$: 1610.9565; found: 1610.9550.

Attempts to obtain C,H,N elemental analyses from three different synthetic batches consistently yielded lower than expected values for all elements, indicating incomplete combustion of the sample.

NMR, mass spectrometry, elemental analysis, cyclic voltammetry, infrared spectroscopy, optical absorption and luminescence spectroscopy, transient absorption and time-resolved luminescence spectroscopy were performed on the experimental set-ups described recently.[1] MALDI-TOF-MS spectra were acquired on a Bruker microflex instrument operating in positive mode. A solution of matrix (DCTB in CH_2Cl_2) was evaporated onto the sample plate, and a solution of analyte evaporated directly onto the matrix. Photochemical experiments were performed as described below. Luminescence quantum yields were determined relative to a solution of $[Ru(bpy)_3]^{2+}$ in aerated CH_3CN (ϕ = 0.018),[5] as described earlier.[1] The energies of the electronic origin (E_{00}) were estimated from the onset of the emission in a frozen 2-methyl-THF matrix at 77 K.

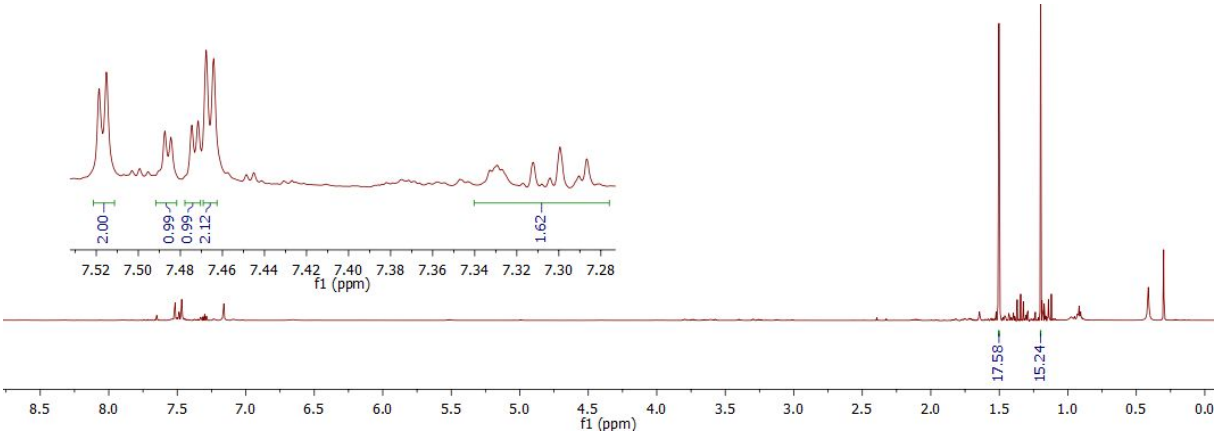

Figure S1. ^{1}H-NMR spectrum of [Mo(L^{tBu})$_3$] in C_6D_6.

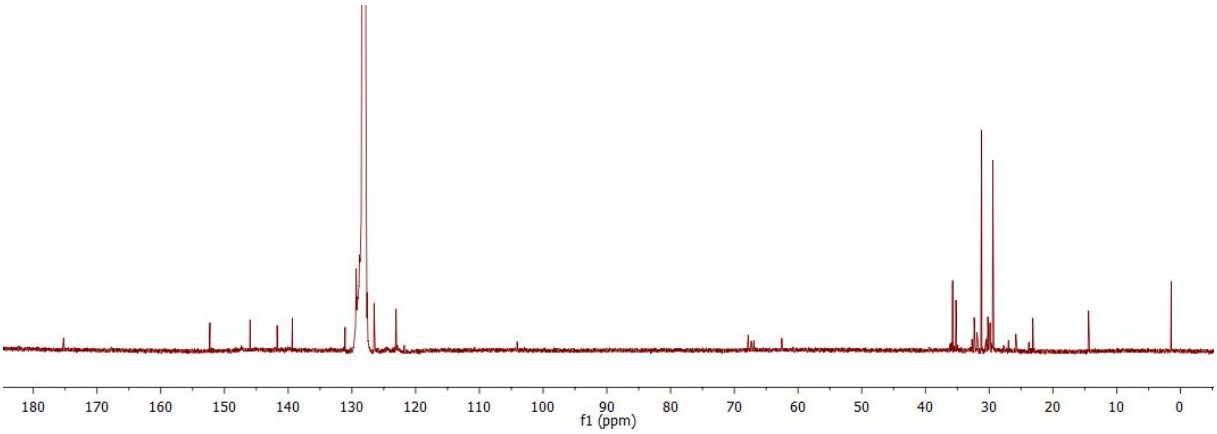

Figure S2. ^{13}C-NMR spectrum of [Mo(L^{tBu})$_3$] in C_6D_6.

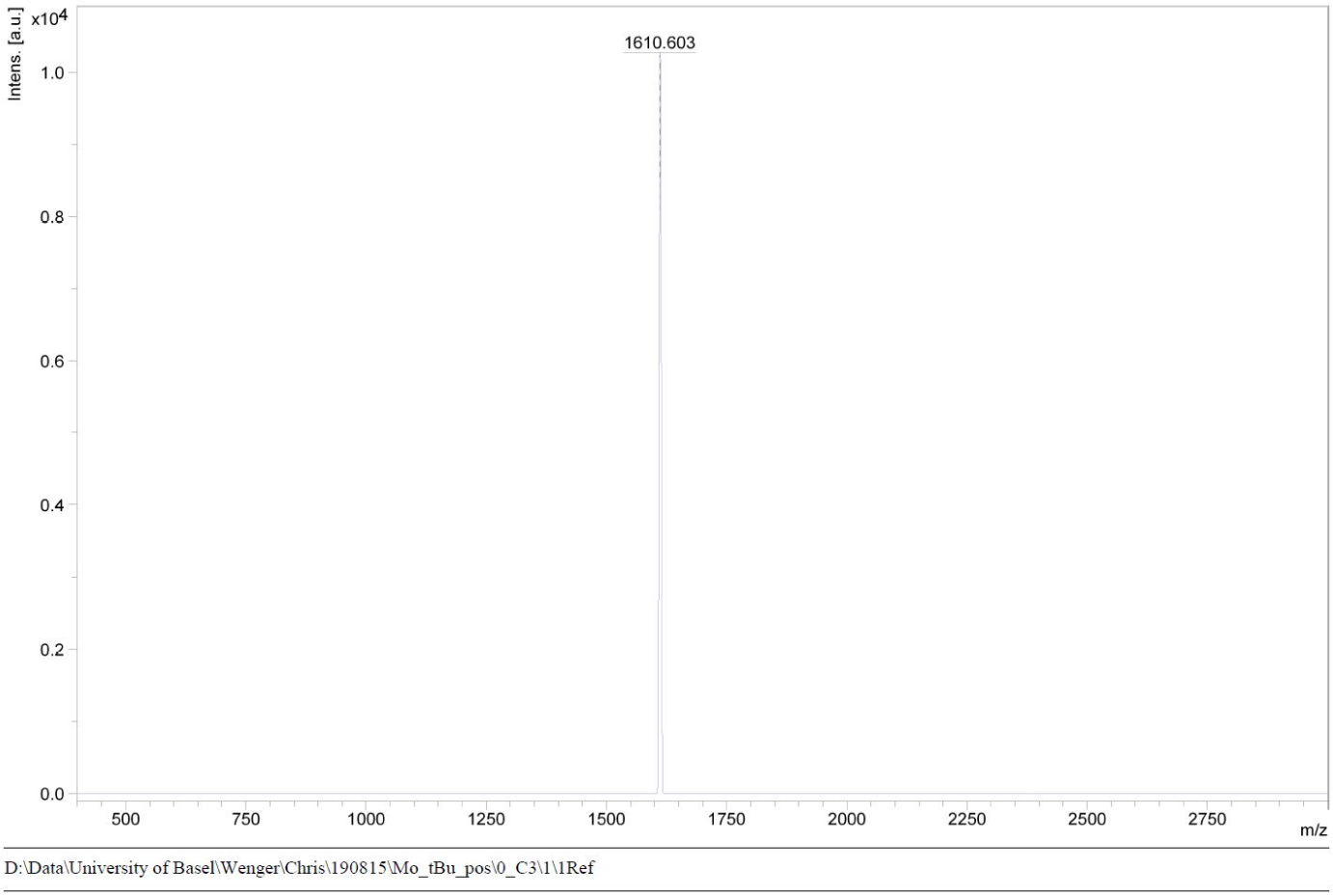

Figure S3. MALDI-TOF mass spectrum of $[Mo(L^{tBu})_3]$.

Infrared spectroscopy

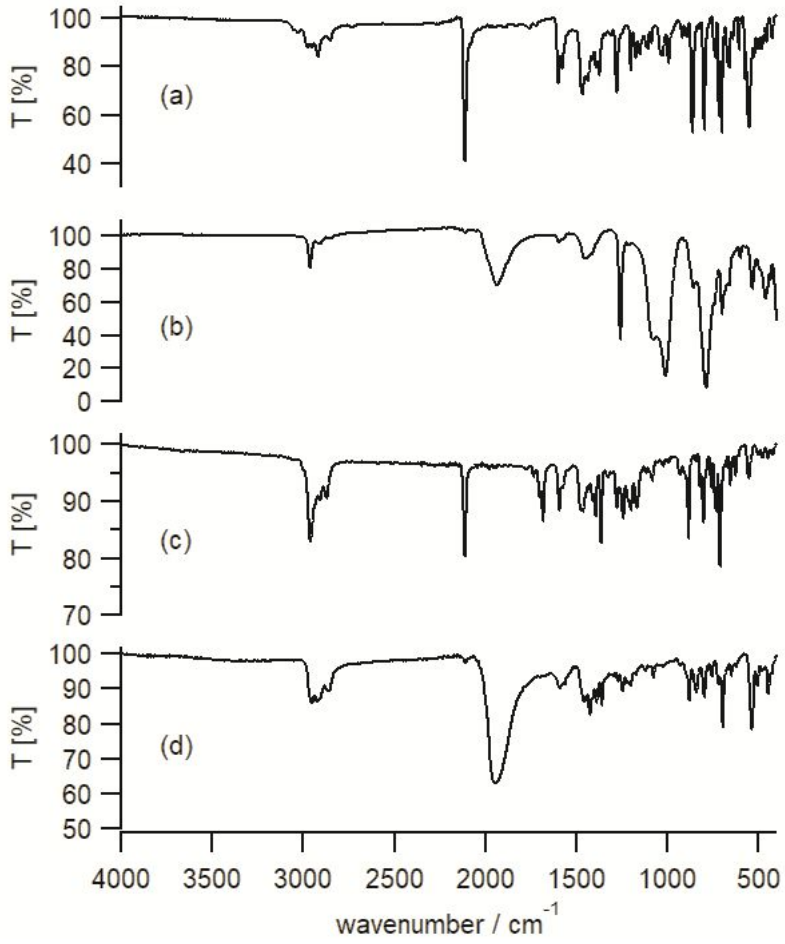

Figure S4. Solid-state IR spectra of (a) free L^{Me} ligand, (b) the $[Mo(L^{Me})_3]$ complex, (c) free L^{tBu} ligand, and (d) the $[Mo(L^{tBu})_3]$ complex.

Electronic absorption spectra in different solvents

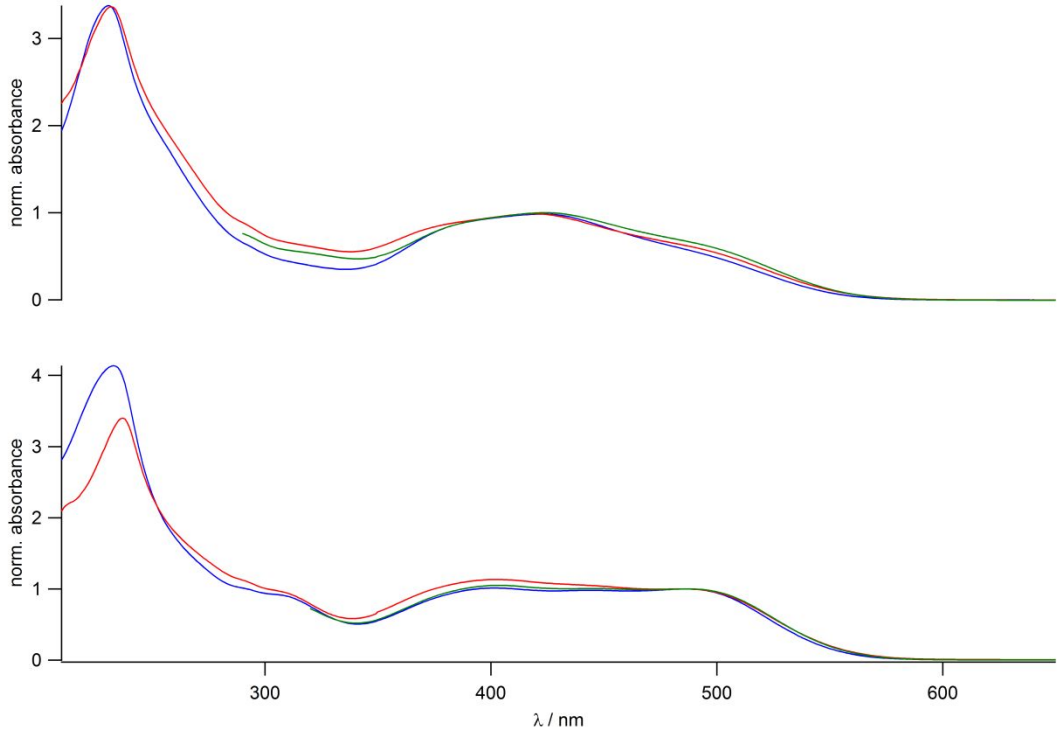

Figure S5. Normalized UV-Vis electronic absorption spectra of $[Mo(L^{Me})_3]$ (above) and $[Mo(L^{tBu})_3]$ (below) in *n*-hexane (blue), toluene (green) and THF (red).

Spectroelectrochemistry

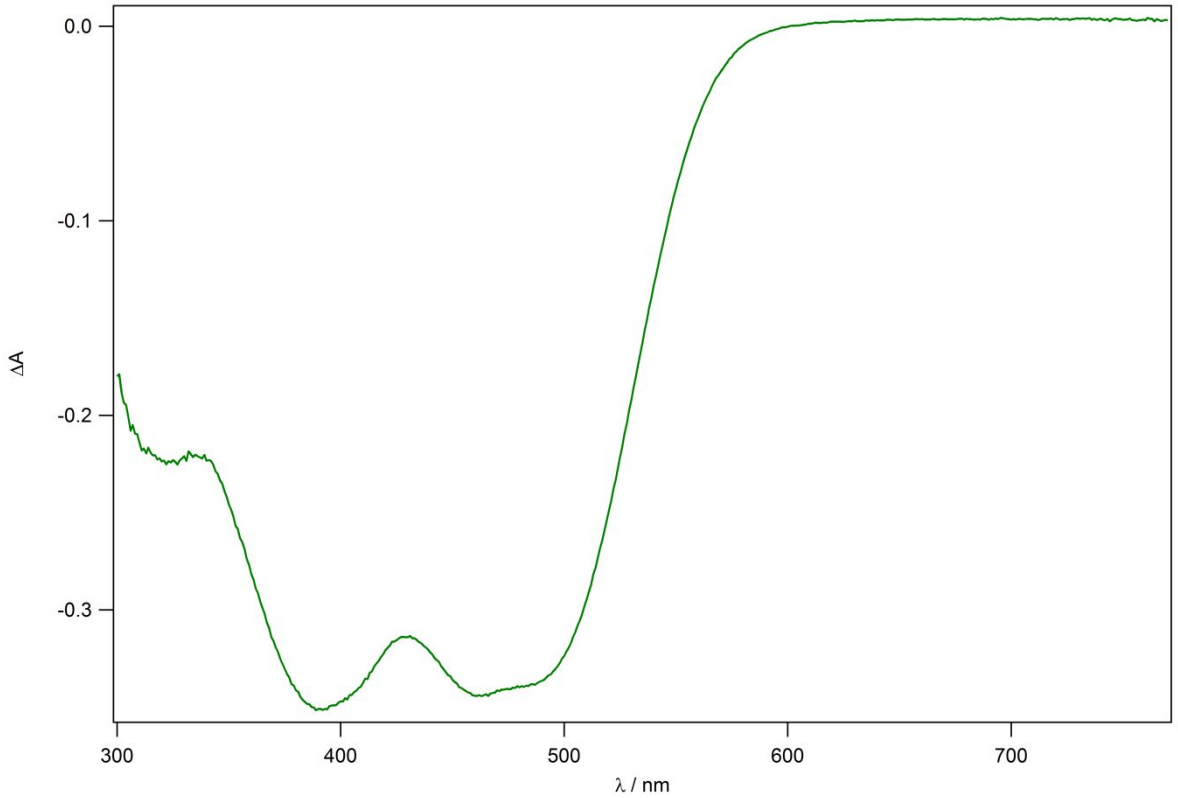

Figure S6. UV-Vis electronic absorbance difference spectrum of $[Mo(L^{tBu})_3]$ obtained upon electrochemical oxidation at 0.3 V vs SCE, recorded in THF in the presence of 0.1 M Bu_4NPF_6.

Low temperature luminescence data

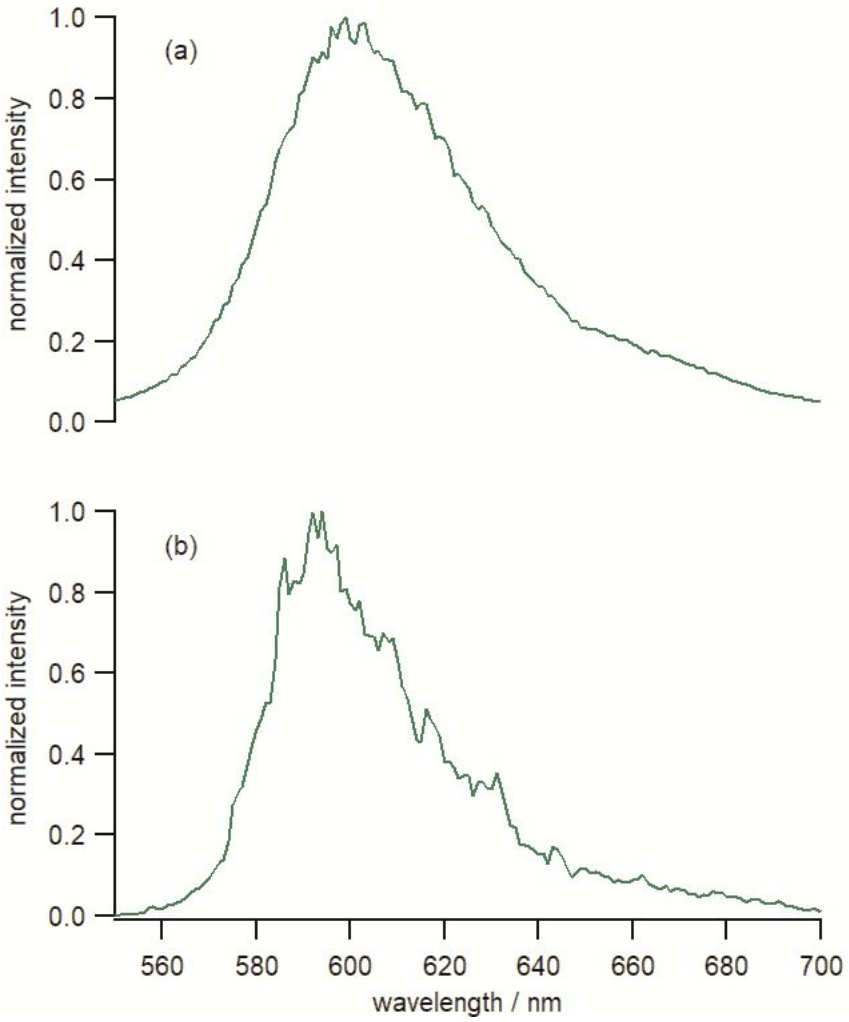

Figure S7. Luminescence spectra of (a) [Mo(L^{Me})$_3$] and (b) [Mo(L^{tBu})$_3$] in a frozen 2-methyl-THF matrix at 77 K. Excitation occurred at 500 nm.

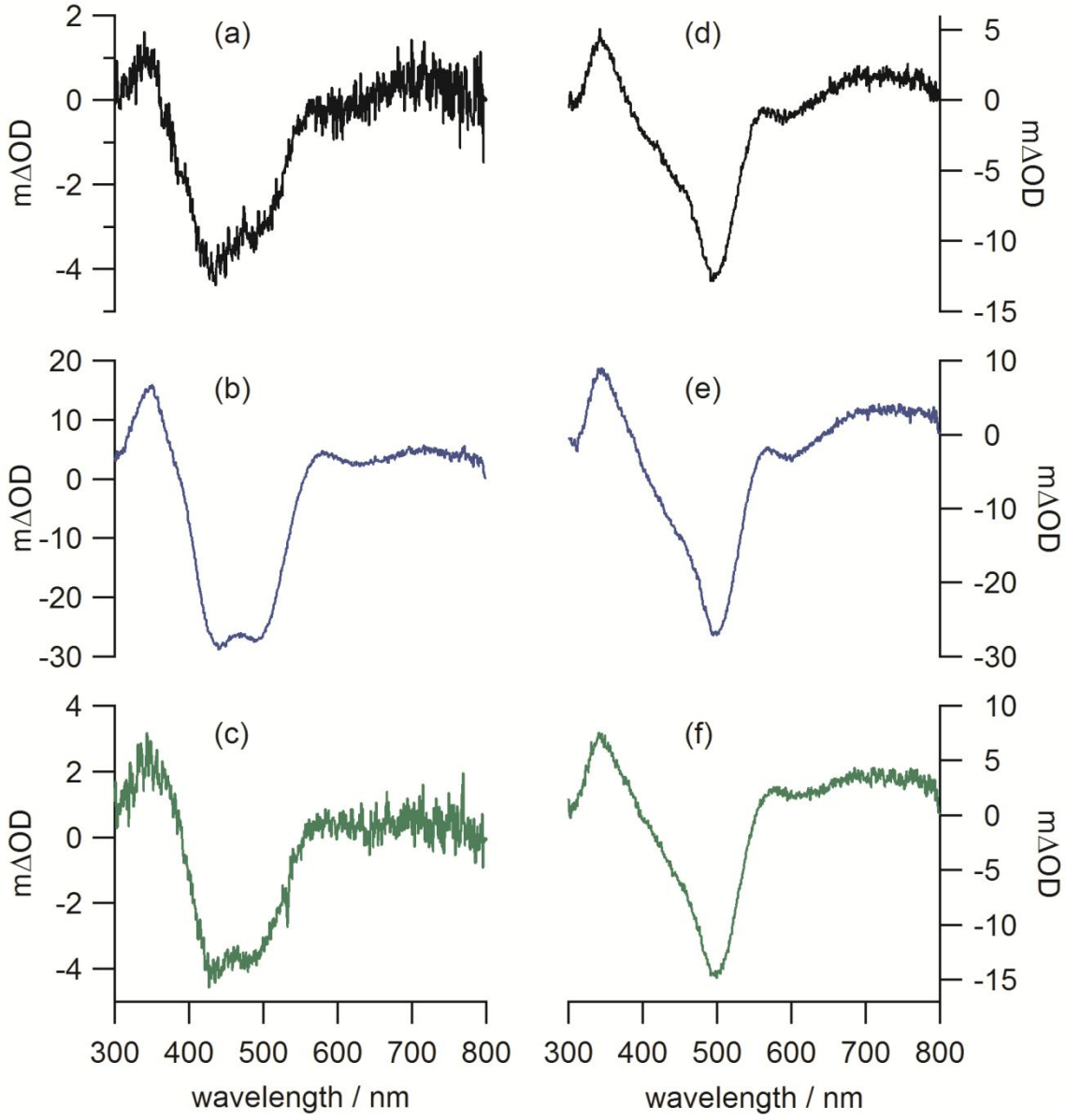

Figure S8. Transient absorption spectra obtained after excitation of 10^{-5} M [Mo(L^{Me})$_3$] (left column) and [Mo(L^{tBu})$_3$] (right column) at 532 nm with laser pulses of ~10 ns duration. Signals were time-integrated over 200 ns immediately after excitation. Black traces: in *n*-hexane (a, d); blue traces: in toluene (b, e); green traces: in THF (c, f) (all de-aerated).

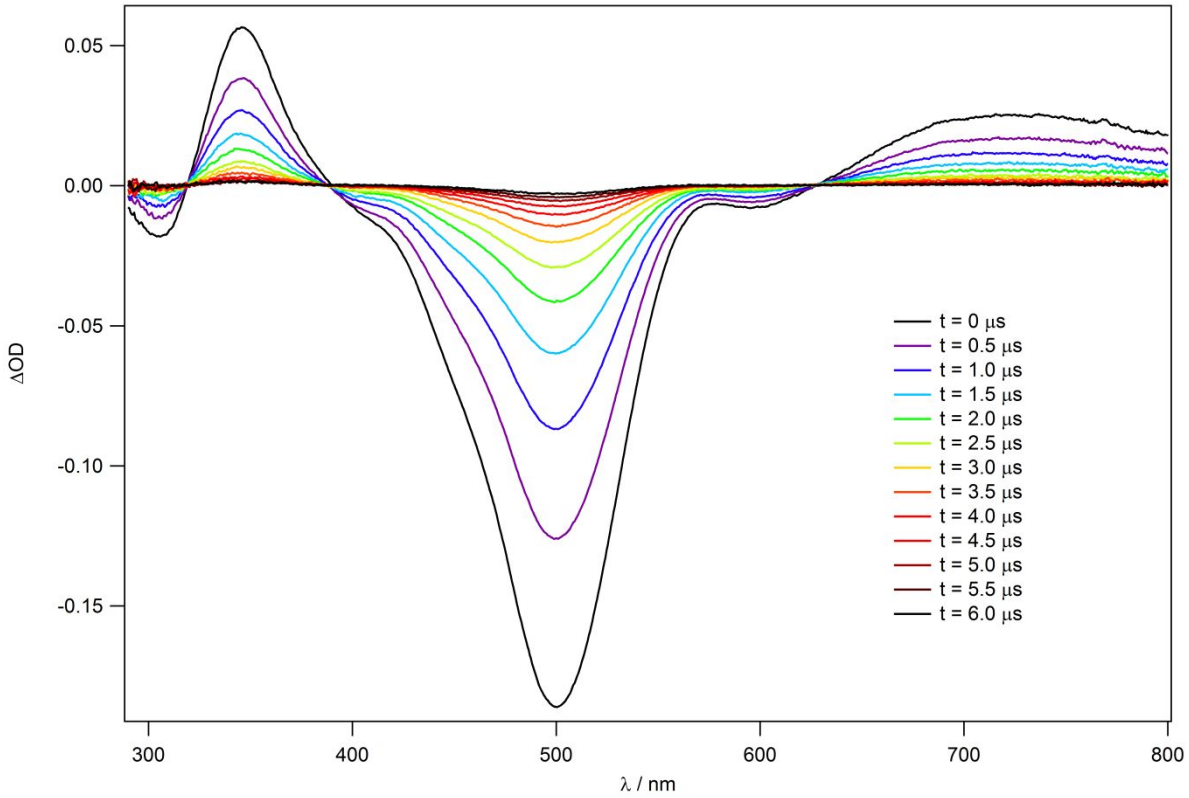

Figure S9. Transient absorption spectra of 50 μM [Mo(L^{tBu})$_3$] in toluene recorded at specified delay times following excitation at 532 nm with laser pulses of ~10 ns duration. Signals were time-integrated over 200 ns.

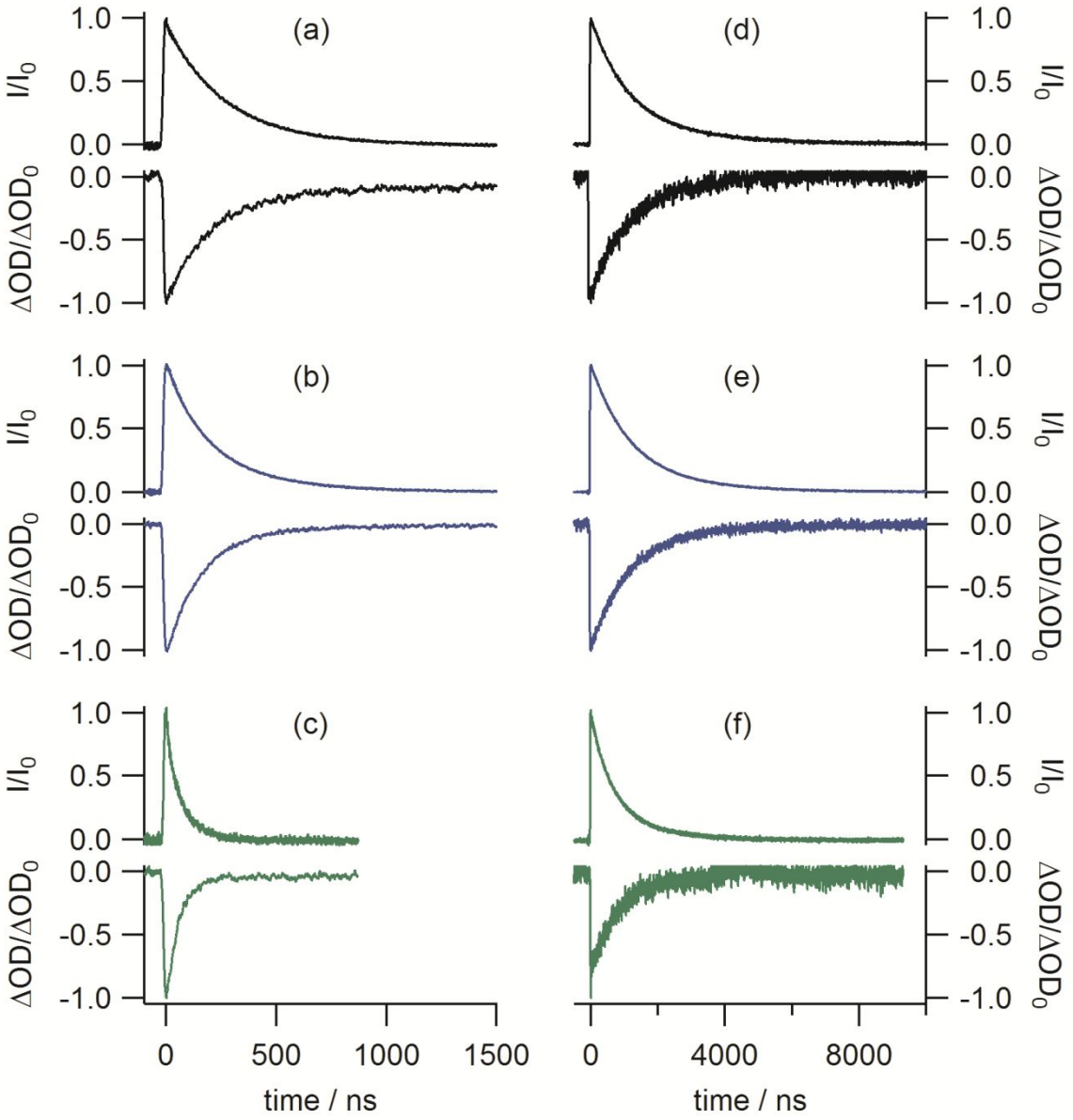

Figure S10. Luminescence decays and MLCT bleach recoveries of 10^{-5} M $[Mo(L^{Me})_3]$ (left column) and $[Mo(L^{tBu})_3]$ (right column) in de-aerated *n*-hexane (black; a, c), toluene (blue; b, d), and THF (green; c, f) at 20 °C. Excitation occurred at 532 nm using laser pulses of ~10 ns duration. Luminescence detection occurred at 580 nm (*n*-hexane), 585 nm (toluene), and at 595 nm (THF). The MLCT bleach recoveries were recorded at 485 nm.

Substrates for photochemical experiments

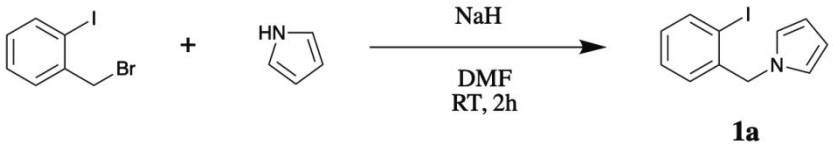

1a

1-(2-Iodobenzyl)-pyrrole, substrate **1a**. Pyrrole (169 µL, 164 mg, 2.44 mmol, 1.1 eq.) was added slowly to a stirred suspension of NaH (60 % in mineral oil, 101 mg, 2.53 mmol, 1.15 eq.) in DMF (5 mL). After 20 min, 2-iodobenzylbromide (652 mg, 2.20 mmol, 1.0 eq.) was added and the mixture stirred for 2.5 h. The reaction was quenched with water (15 mL) and the product extracted into Et_2O. The combined organic phases were dried over Na_2SO_4 and the solvent removed *in vacuo*. The crude product was purified by column chromatography (SiO_2, pentane → pentane/EtOAc 19:1) to afford **1a** (526 mg, 85 %) as a colorless liquid. Spectroscopic data match those reported in the literature.[6] ^{1}H-NMR (400 MHz, acetone-d_6): δ 7.89 (dd, J = 7.9, 1.3 Hz, 1H), 7.34 (td, J = 7.5, 1.3 Hz, 1H), 7.14 – 6.98 (m, 1H), 6.80 (t, J = 2.1 Hz, 2H), 6.77 – 6.65 (m, 1H), 6.11 (t, J = 2.1 Hz, 2H), 5.14 (s, 2H) ppm.

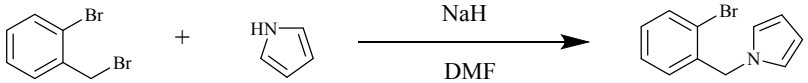

2a

1-(2-Bromobenzyl)-pyrrole, substrate **2a.** Compound **2a** was prepared in the same manner as **1a**, using 2-bromobenzylbromide. The product was purified through distillation (110 °C, 0.8 mbar) to afford **2a** (84%) as a colorless liquid. ^{1}H-NMR (400 MHz, acetone-d_6): δ 7.57 (dd, J = 7.9, 1.3 Hz, 1H), 7.23 (td, J = 7.6, 1.3 Hz, 1H), 7.17 – 7.12 (m, 1H), 6.72 (t, J = 2.0 Hz, 2H), 6.71 – 6.68 (m, 1H), 6.23 (t, J = 2.0 Hz, 2H), 5.16 (s, 2H) ppm.

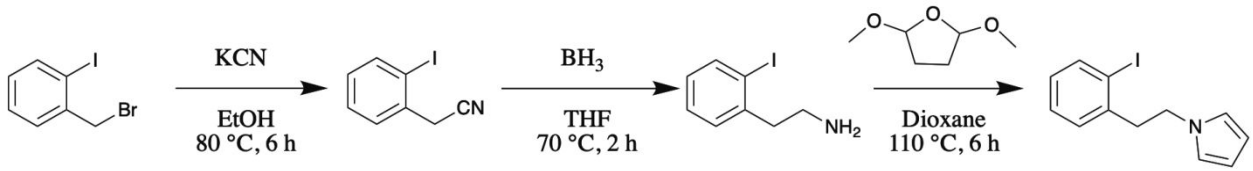

3a

1-(2-Iodobenzyl)-pyrrole, substrate **3a**. This compound was obtained via synthesis of 2-iodobenzyl cyanide and 2-(2-iodophenyl)ethan-1-amine following modified literature procedures.[7]

Step 1: 2-Iodobenzyl cyanide. 2-Iodobenzyl bromide (1.50 g, 5.05 mmol, 1.0 eq.) and KCN (586 mg, 2.20 mmol, 1.1 eq.) were dissolved in EtOH (12,5 mL) and refluxed for 6 h. The solvent was removed under reduced pressure and water (15 mL) was added. The product was extracted into EtOAc (3 × 25 mL) and washed with brine. The combined organic phases were dried over Na_2SO_4 and the solvent removed *in vacuo*. The crude product was purified by column chromatography (SiO_2, pentane → pentane/EtOAc 19:1) to afford 2-iodobenzyl cyanide (971 mg, 79 %) as a colorless liquid. The spectroscopic data match those reported in the literature.[7] ^{1}H-NMR (400 MHz, $CDCl_3$): δ 7.88 (dd, J = 7.9, 1.2 Hz, 1H), 7.54 (dd, J = 7.7, 1.1 Hz, 1H), 7.40 (td, J = 7.6, 1.3 Hz, 1H), 7.05 (td, J = 7.7, 1.6 Hz, 1H), 3.82 (s, 2H) ppm.

Steps 2 & 3: 2-(2-Iodophenyl)ethan-1-amine and 1-(2-iodophenethyl)-1H-pyrrole. A solution of BH_3 in THF (1 M, 10.0 mL, 10.0 mmol, 2.5 eq.) was added to a solution of 2-iodobenzyl cyanide (971 mg, 4.00 mmol, 1.0 eq) in THF (4

mL) and refluxed for 2 h. The reaction mixture was quenched with aqueous HCl (2 M) and brought to a basic pH with NaOH (1 M). The residue was extracted into EtOAc and washed with brine. The combined organic phases were dried over Na_2SO_4 and the solvent removed *in vacuo*. The crude 2-(2- iodophenyl)ethan-1-amine was used without further purification in the next step.

The crude intermediate (520 mg of 950 mg) was dissolved in a mixture of dioxane (1.5 mL) and glacial acetic acid (3.0 mL). 2,5-Dimethoxytetrahydrofuran (300 µL, 305 mg, 2.32 mmol, 1.1 eq.) was then added and the reaction mixture heated to 110 °C for 6 h. The solvent was removed *in vacuo* and the crude product was purified by column chromatography (SiO_2, 16 % DCM in pentane) to afford **3a** (102 mg, 16 %; ~15 % over 2 steps) as a colorless oil. ^{1}H-NMR (400 MHz, $CDCl_3$): δ 7.88 (dd, J = 7.9, 1.3 Hz, 1H), 7.27 (td, J = 7.4, 1.3 Hz, 1H), 7.07 (dd, J = 7.6, 1.7 Hz, 1H), 6.96 (td, J = 7.6, 1.7 Hz, 1H), 6.69 (t, J = 2.1 Hz, 2H), 6.18 (t, J = 2.1 Hz, 2H), 4.12 (t, J = 7.6 Hz, 2H), 3.22 (t, J = 7.7 Hz, 2H) ppm. ^{13}C-NMR (101 MHz, $CDCl_3$): δ 140.94, 139.70, 130.14, 128.67, 128.62, 120.60, 108.24, 100.42, 49.49, 43.31 ppm.

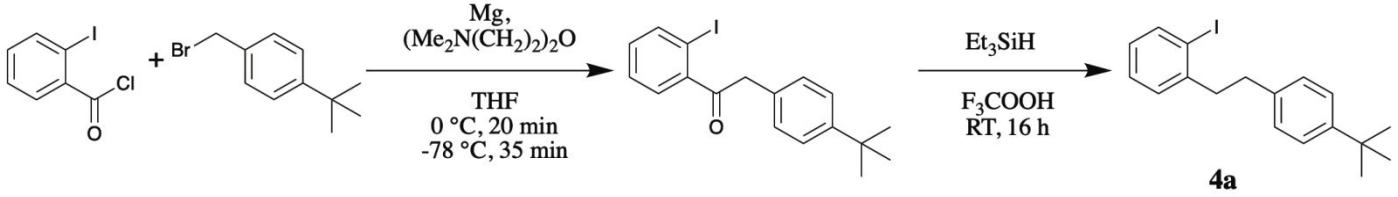

1-(4-(*tert*-Butyl)phenethyl)-2-iodobenzene, substrate **4a**. *Step 1*: 2-(4-(*tert*-butyl)phenyl)-1-(2-iodophenyl)ethan-1-one was prepared following a modified literature procedure.[8] A solution of 4-*tert*-butylbenzyl bromide (735 µL, 909 mg, 4.0 mmol, 1.0 eq.) in THF (8 mL) was added dropwise under an inert atmosphere to magnesium tunings (194 mg, 8.0 mmol, 2.0 eq.) in THF (4 mL) in a three-necked flask equipped with a septum, a reflux condenser and a dropping funnel. The suspension was stirred for an additional hour and then added at 0 °C to a solution of bis[2-(*N*,*N*-dimethylaminoethyl)] ether (762 µL, 641 mg, 4.0 mmol, 1.0 eq.) in THF (3 mL). After stirring for 20 min at 0 °C, the solution was added dropwise over 20 min to a solution of 2-iodobenzoyl chloride (1.49 g, 5.60 mmol, 1.4 eq.) in THF (15 mL) at -78 °C. The solution was again stirred for 40 min at this temperature and quenched afterwards with sat. aq. NH_4Cl (20 mL) and water (20 mL). The product was extracted into EtOAc (2 × 50 mL), the combined organic phases were dried over Na_2SO_4 and the solvent removed *in vacuo*. A side product was separated by recrystallization from methanol (~15 mL). The solvent was removed from the filtrate *in vacuo* and the crude 2-(4-(*tert*-butyl)phenyl)-1-(2-iodophenyl)ethan-1-one was used without further purification in the next step.

Step 2: 1-(4-(*tert*-butyl)phenethyl)-2-iodobenzene. The crude 2-(4-(*tert*-butyl)phenyl)-1-(2-iodophenyl)ethan-1-one from the previous step was dissolved in trifluoroacetic acid (12 mL, 40 eq.), and triethylsilane (1.92 mL, 1.40 g, 12 mmol, 3.0 eq.) was added slowly at 0 °C. The reaction mixture was stirred for 16 h at rt, quenched with aq. NaOH solution (2.5 M, ~60 mL) at 0 °C and extracted into EtOAc. The combined organic phases were washed with brine, dried over Na_2SO_4 and the solvent removed *in vacuo*. The crude product was purified by column chromatography (SiO_2, pentane) to afford **4a** (350 mg, 24 % over 2 steps) as a colorless liquid. ^{1}H-NMR (400 MHz, CD_2Cl_2): δ 7.87 (dd, J = 7.9, 1.3 Hz, 1H), 7.35 (dt, J = 8.4, 2.1 Hz, 2H), 7.29 (dt, J = 7.3, 1.2 Hz, 1H), 7.32 – 7.24 (m, 3H), 7.23 (dt, J = 8.4, 2.1 Hz, 2H), 6.92 (ddd, J = 7.9, 7.1, 2.0 Hz, 1H), 3.04 – 2.96 (m, 2H), 2.89 – 2.82 (m, 2H), 1.36 (s, 9H) ppm.

^{13}C-NMR (101 MHz, CD_2Cl_2): δ 149.50, 145.01, 140.02, 138.92, 130.01, 128.97, 128.59, 128.39, 125.82, 100.92, 43.61, 36.52, 34.84, 31.74 ppm.

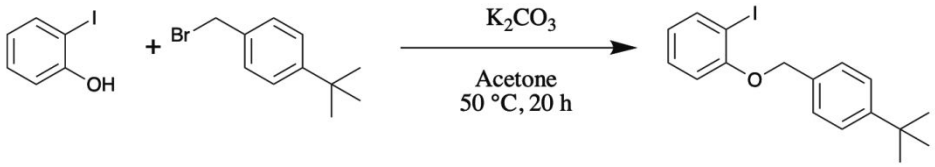

5a

1-((4-(tert-Butyl)benzyl)oxy)-2-iodobenzene, substrate **5a**. 2-Iodophenol (330 mg, 1.5 eq., 1.0 eq.) and K_2CO_3 (866 mg, 6.27 mmol, 4.2 eq.) were dissolved in acetone (7.5 mL) and 4-(*tert*-butyl)benzyl bromide (496 µL, 613 mg, 2.70 mmol, 1.8 eq.) was added. The reaction mixture was refluxed at 65 °C for 16 h. The mixture was allowed to cool to rt, filtered and the solvent removed *in vacuo*. The crude product was purified by column chromatography (SiO_2, pentane → pentane/DCM 9:1) to afford **5a** (553 mg, 100 %) as a white solid. ^{1}H-NMR (400 MHz, CD_2Cl_2): δ 7.80 (dd, J = 7.8, 1.6 Hz, 1H), 7.43 (s, 4H), 7.31 (ddd, J = 8.3, 7.3, 1.6 Hz, 1H), 6.92 (dd, J = 8.3, 1.4 Hz, 1H), 6.73 (td, J = 7.6, 1.4 Hz, 1H), 5.10 (s, 2H), 1.33 (s, 9H) ppm. ^{13}C-NMR (101 MHz, $CDCl_3$): δ 157.45, 150.99, 139.67, 133.64, 129.54, 126.94, 125.62, 122.86, 112.89, 87.00, 70.85, 34.74, 31.51 ppm.

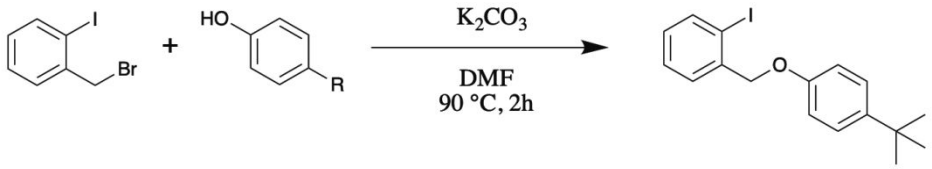

6a

1-((4-(*tert*-Butyl)phenoxy)methyl)-2-iodobenzene, substrate **6a**. Following a published procedure,[9] 2-iodobenzyl bromide (386 mg, 1.30 mmol, 1.0 eq.), 4-*tert*-butylphenol (235 mg, 1.56 mmol, 1.2 eq.) and K_2CO_3 (915 mg, 6.62 mmol, 5.0 eq.) were dissolved in DMF (4 mL) and stirred at 90 °C for 2 h. After cooling to rt the reaction water (30 mL) was added and the product was extracted into Et_2O (3 × 40 mL). The combined organic phases were washed with brine, dried over Na_2SO_4 and the solvent was removed *in vacuo*. The crude product was purified by column chromatography (SiO_2, pentane/DCM 9:1) to afford **6a** (411 mg, 85 %) as a colorless liquid. ^{1}H-NMR (400 MHz, $CDCl_3$): δ 7.87 (dd, J = 7.9, 1.2 Hz, 1H), 7.53 (dd, J = 7.6, 1.8 Hz, 1H), 7.37 (td, J = 7.6, 1.3 Hz, 1H), 7.33 (d, J = 8.9 Hz, 2H), 7.03 (ddd, J = 7.9, 7.3, 1.6 Hz, 1H), 6.93 (d, J = 8.9 Hz, 2H), 5.03 (s, 2H), 1.31 (s, 9H) ppm.

Mechanistic considerations: Thermal vs photochemical BHAS

Thermal BHAS reactions are typically radical chain processes following the mechanism in Figure S11b.[10] After reaction initiation via single electron transfer (SET), reductive dehalogenation leads to an aryl radical ($Ar^1\bullet$) which can add to an aryl coupling partner (Ar^2). The resulting intermediate is deprotonated by strong base (typically ^{t}BuOK), leading to an anionic Ar^1-Ar^2 species that propagates the radical chain via electron donation to Ar^1-X. The sequence of deprotonation followed by re-oxidation is of key importance for the radical chain propagation.

In the photochemical BHAS reaction considered in the present work, only weak base (2,2,6,6-tetramethylpiperidine) is present, leading to a reversed reaction order of re-oxidation followed by deprotonation (Scheme 3 in the main paper). In this scenario, there is no strongly reducing intermediate that could propagate a radical chain mechanism.

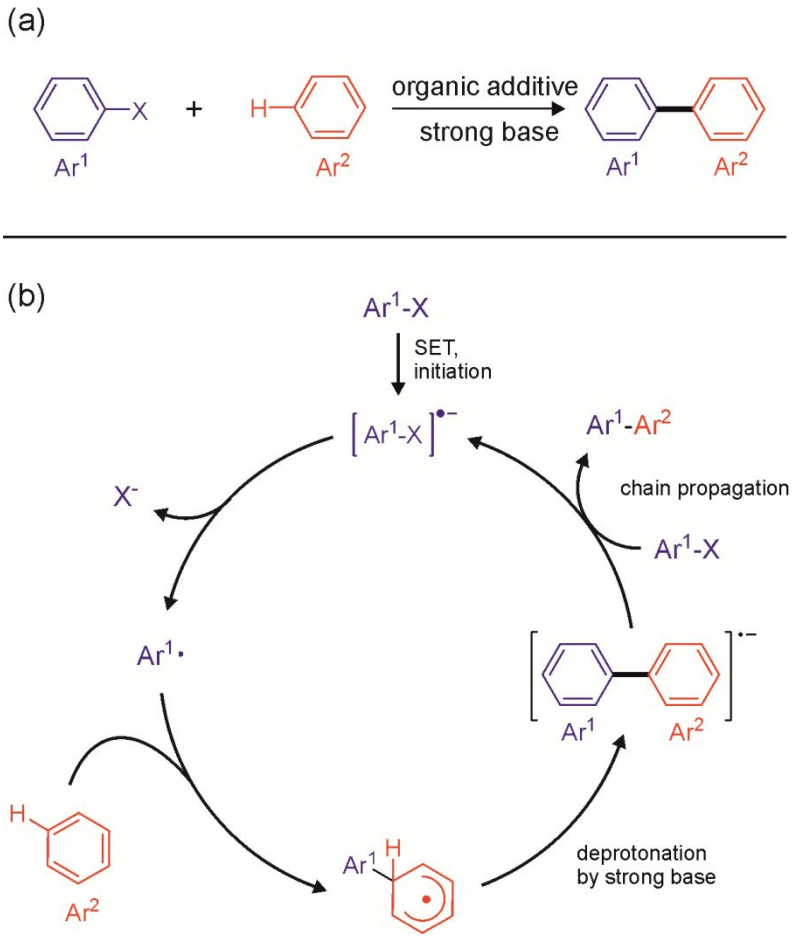

Figure S11. Postulated mechanism for thermal BHAS reactions involving strong base.

Photochemical experiments

Photochemical experiments were all performed using 50 mM of substrate, 5 mol% of photoredox catalyst and 2 eq. TMP in deuterated benzene. Reaction mixtures were de-aerated through three cycles of freeze-pump-thaw, and carried out in NMR tubes flame-sealed under vacuum. Photoirradiation was carried out using one of two home-built photoreactors (Figure S12). Earlier studies were performed using a setup comprised of LED strips (470 nm) set in epoxy resin around the inside of an 80 mm diameter aluminum canister incorporating a 30 mm diameter electric fan, which maintains an operating temperature of ca. 40 °C. In order to perform reactions at room temperature, a second setup incorporating both passive and active water cooling capabilities was built. This setup is comprised of LED strips (470 nm) set in epoxy resin around the outside of a glass beaker, with an external aluminium layer that acts as a heatsink. The beaker is filled with water and incorporates copper tubing through which water is flowed to maintain an operating temperature of ca. 20 °C. The reactor is stirred to maintain even temperature throughout the reactor.
Conversions were determined from relative peak integrals of the benzylic protons. The reactions were determined to be complete when no further conversion was observed (i.e. when the conversions plateaued), with the exception of substrate **2b**, where the reaction did not reach completion after continuous irradiation exceeding two months.

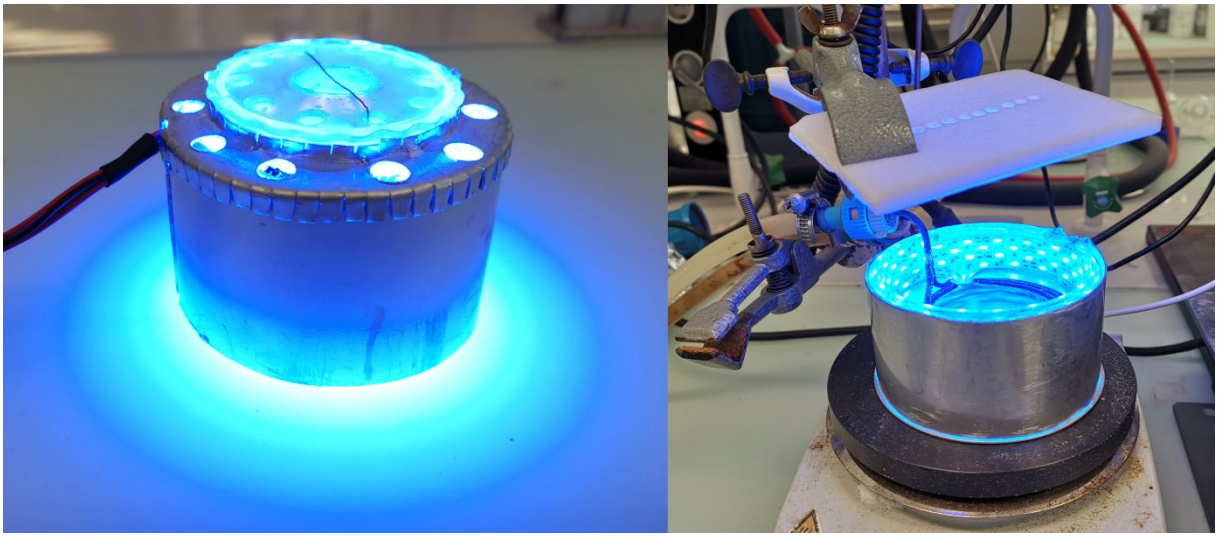

Figure S12. Photoreactors employed within this work (λ_{ex} = 470 nm, ca. 14 W). Left: air-cooled (ca. 40 °C); right: water-cooled (ca. 20 °C).

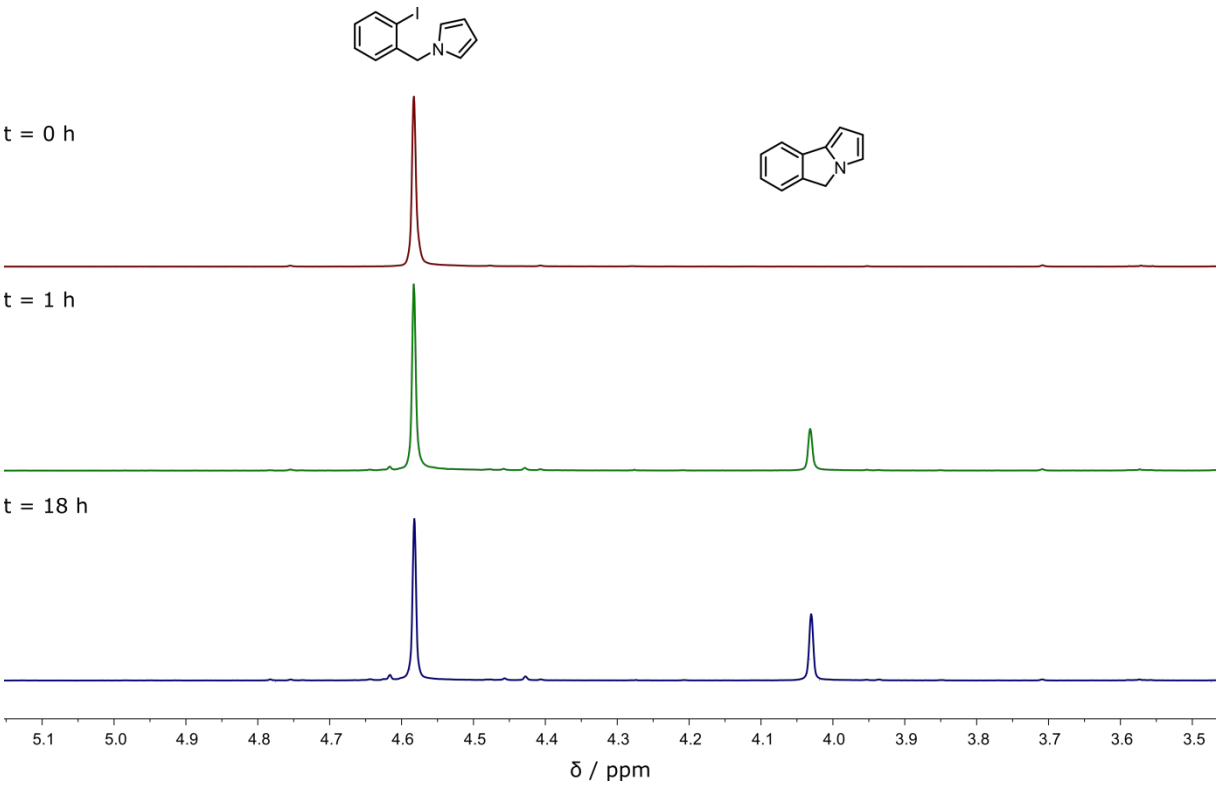

Figure S13. ^{1}H NMR spectra, recorded at 400 MHz in C_6D_6, of 50 mM **1a** with [Mo(L^{Me})$_3$] (5 mol%) and TMP (2 eq.) at various time points under continuous irradiation at 470 nm at ca. 40 °C.

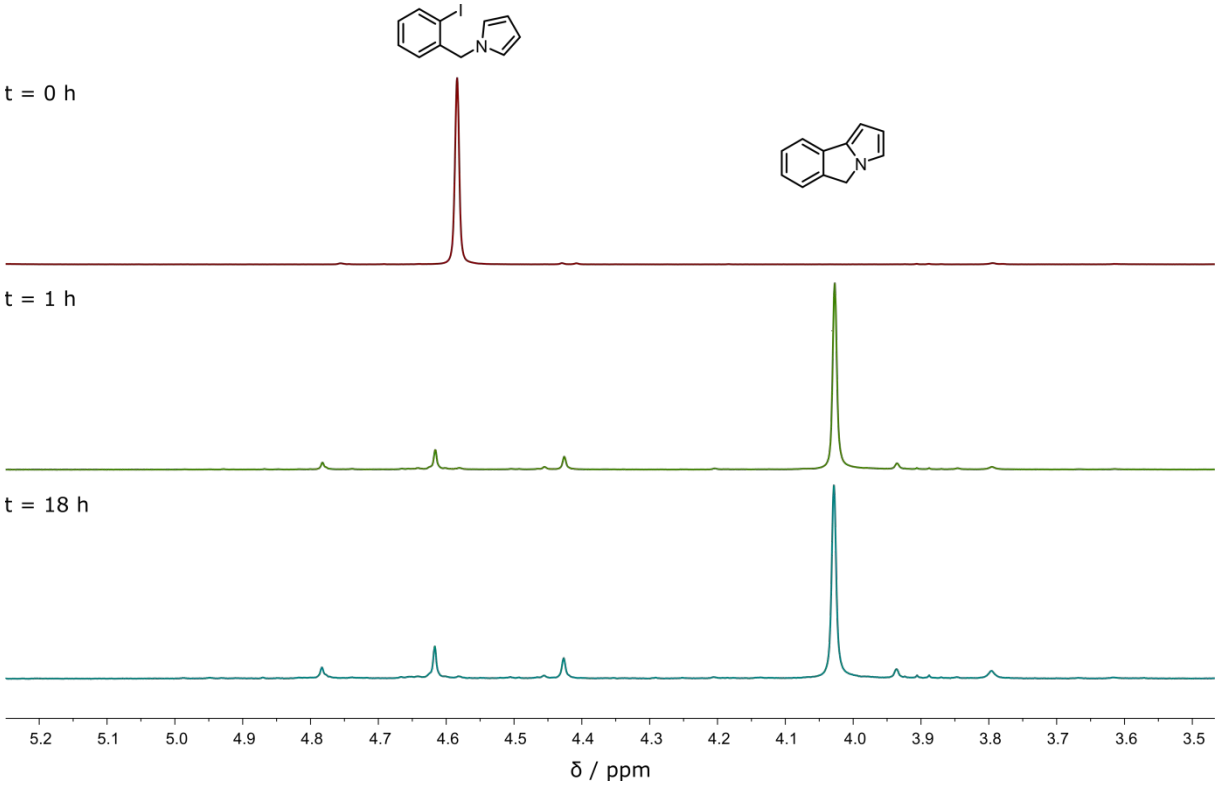

Figure S14. ^{1}H NMR spectra, recorded at 400 MHz in C_6D_6, of 50 mM **1a** with [Mo(L^{tBu})$_3$] (5 mol%) and TMP (2 eq.) at various time points under continuous irradiation at 470 nm at ca. 40 °C.

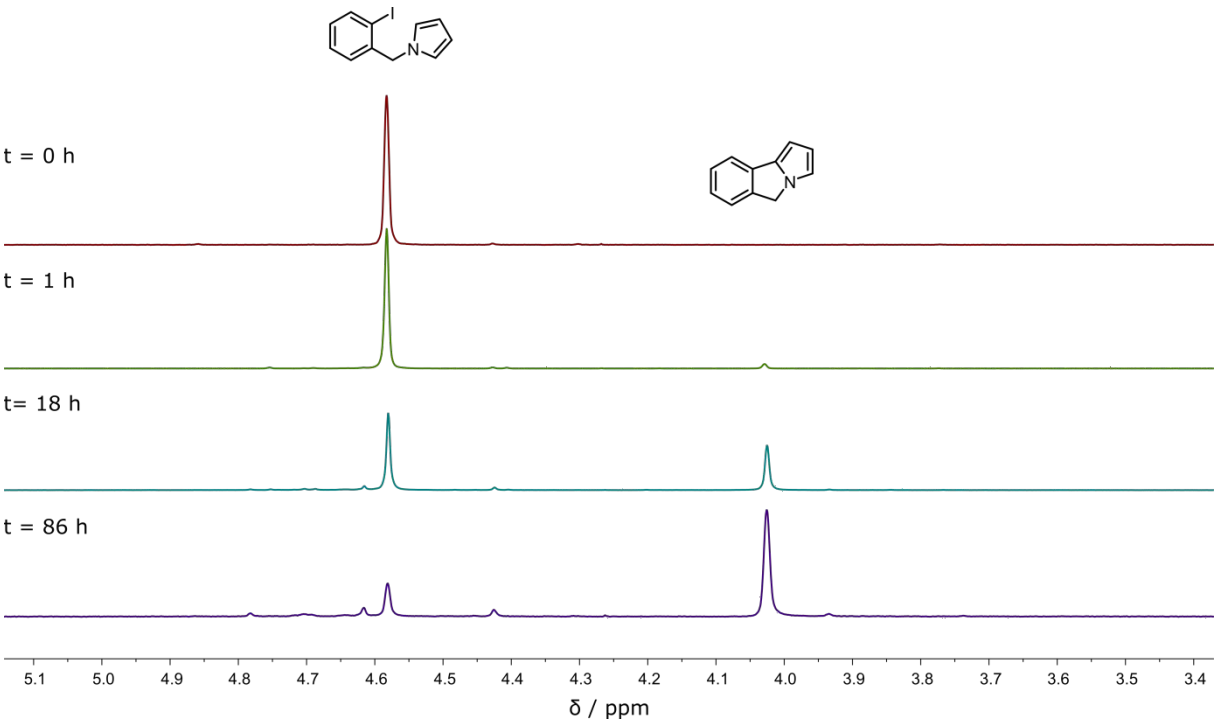

Figure S15. ^{1}H NMR spectra, recorded at 400 MHz in C_6D_6, of 50 mM **1a** with [Ir(ppy)$_3$] (5 mol%) and TMP (2 eq.) at various time points under continuous irradiation at 470 nm at ca. 40 °C.

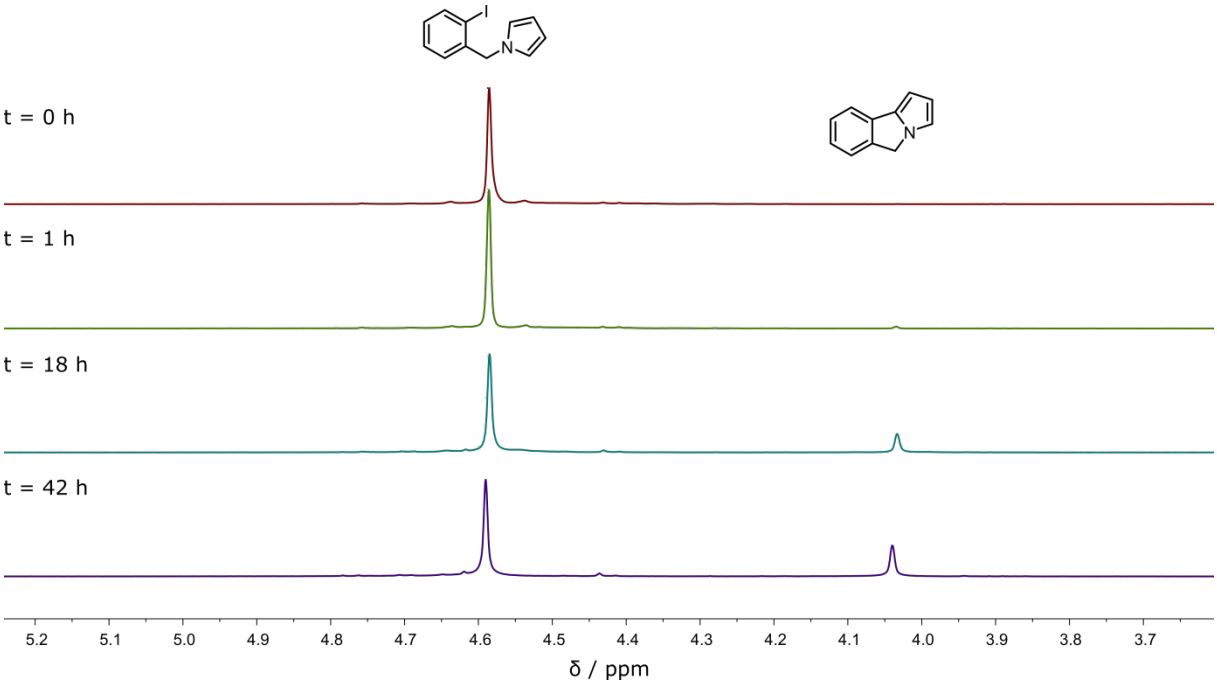

Figure S16. ^{1}H NMR spectra, recorded at 400 MHz in C_6D_6, of 50 mM **1a** with [Ir(ppy)$_3$] (5 mol%) and TMP (2 eq.) at various time points under continuous irradiation at 405 nm at ca. 20 °C.

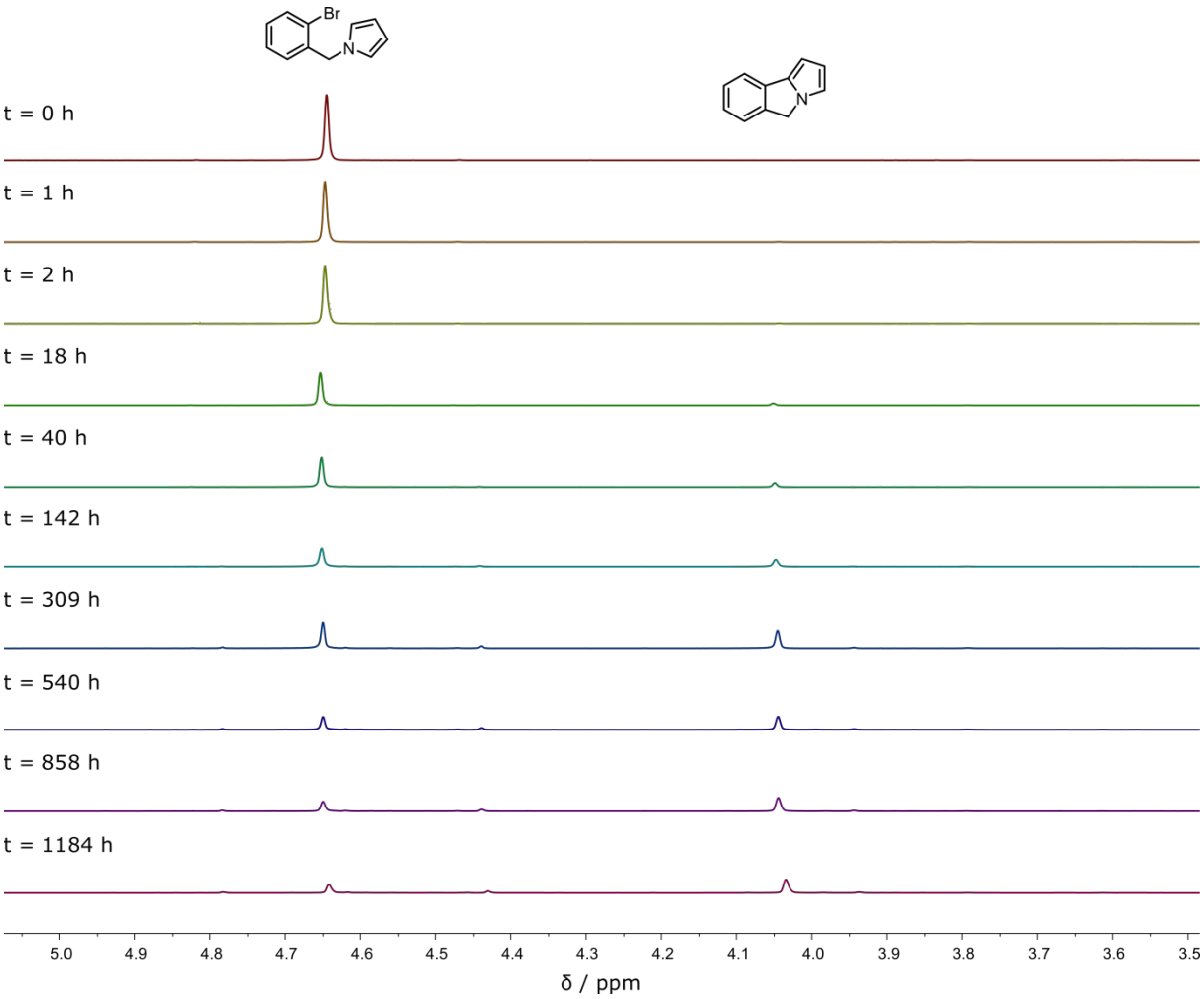

Figure S17. ^{1}H NMR spectra, recorded at 400 MHz in C_6D_6, of 50 mM **2a** with [Mo(L^{tBu})$_3$] (5 mol%) and TMP (2 eq.) at various time points under continuous irradiation at 470 nm at ca. 40 °C.

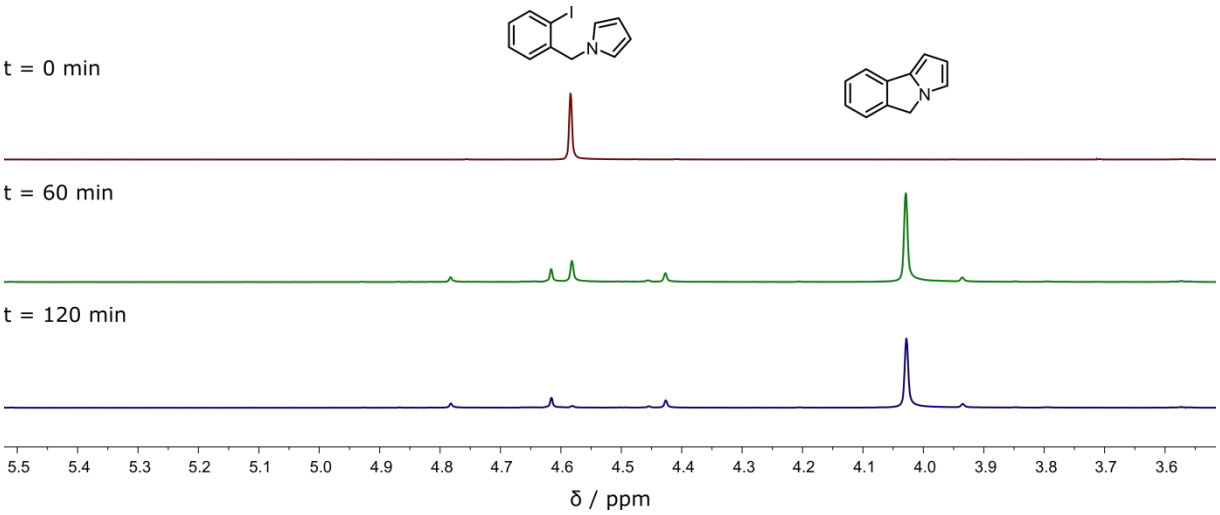

Figure S18. ^{1}H NMR spectra, recorded at 400 MHz in C_6D_6, of 50 mM **1a** with [Mo(L^{tBu})$_3$] (5 mol%) and TMP (2 eq.) at various time points under continuous irradiation at 470 nm at ca. 20 °C.

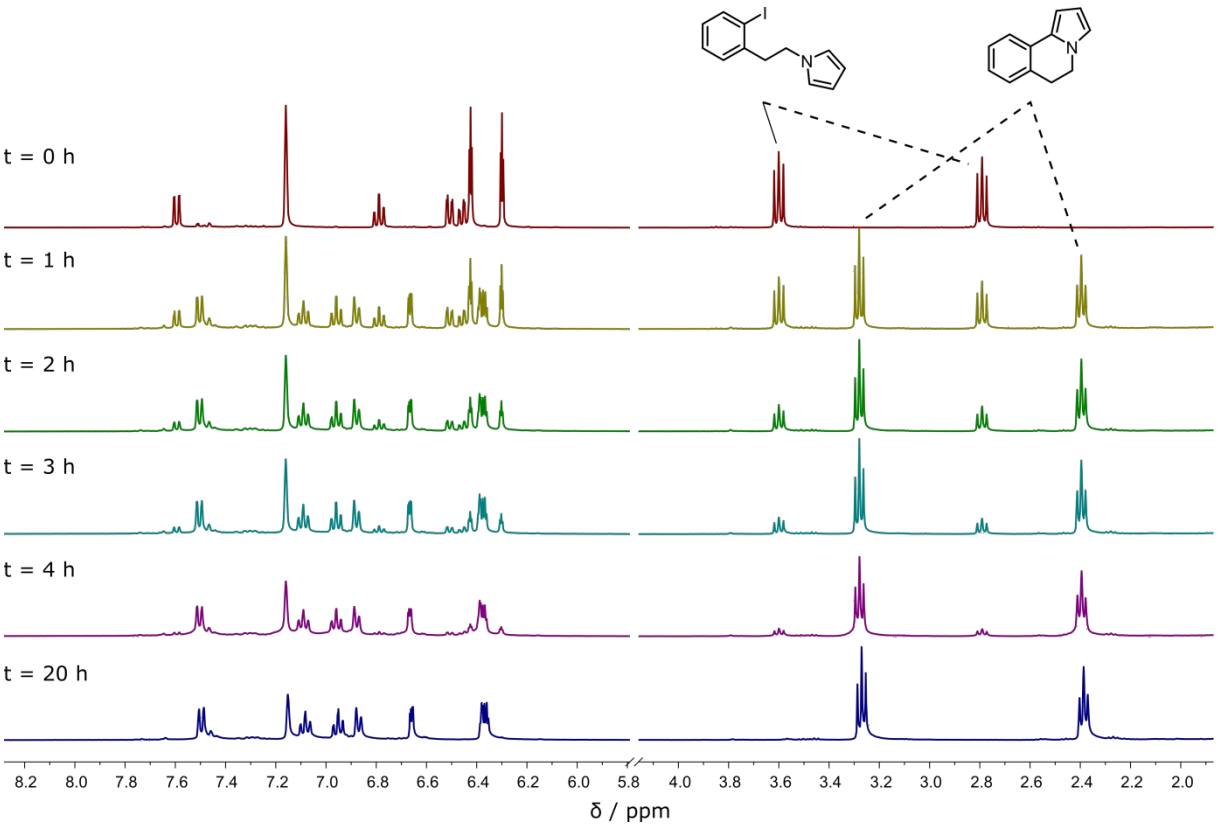

Figure S19. ^{1}H NMR spectra, recorded at 400 MHz in C_6D_6, of 50 mM **3a** with [Mo(L^{tBu})$_3$] (5 mol%) and TMP (2 eq.) at various time points under continuous irradiation at 470 nm at ca. 20 °C.

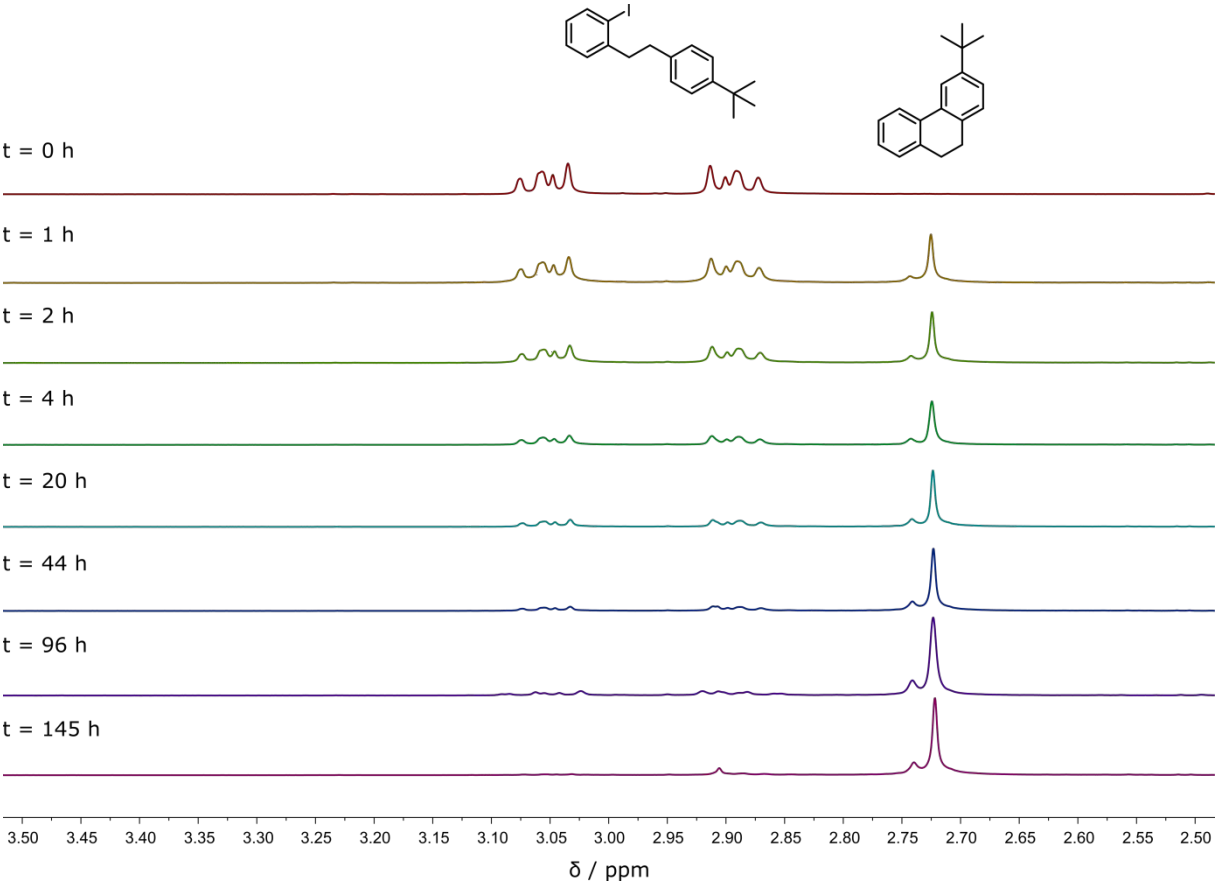

Figure S20. ^{1}H NMR spectra, recorded at 400 MHz in C_6D_6, of 50 mM **4a** with [Mo(L^{tBu})$_3$] (5 mol%) and TMP (2 eq.) at various time points under continuous irradiation at 470 nm at ca. 20 °C.

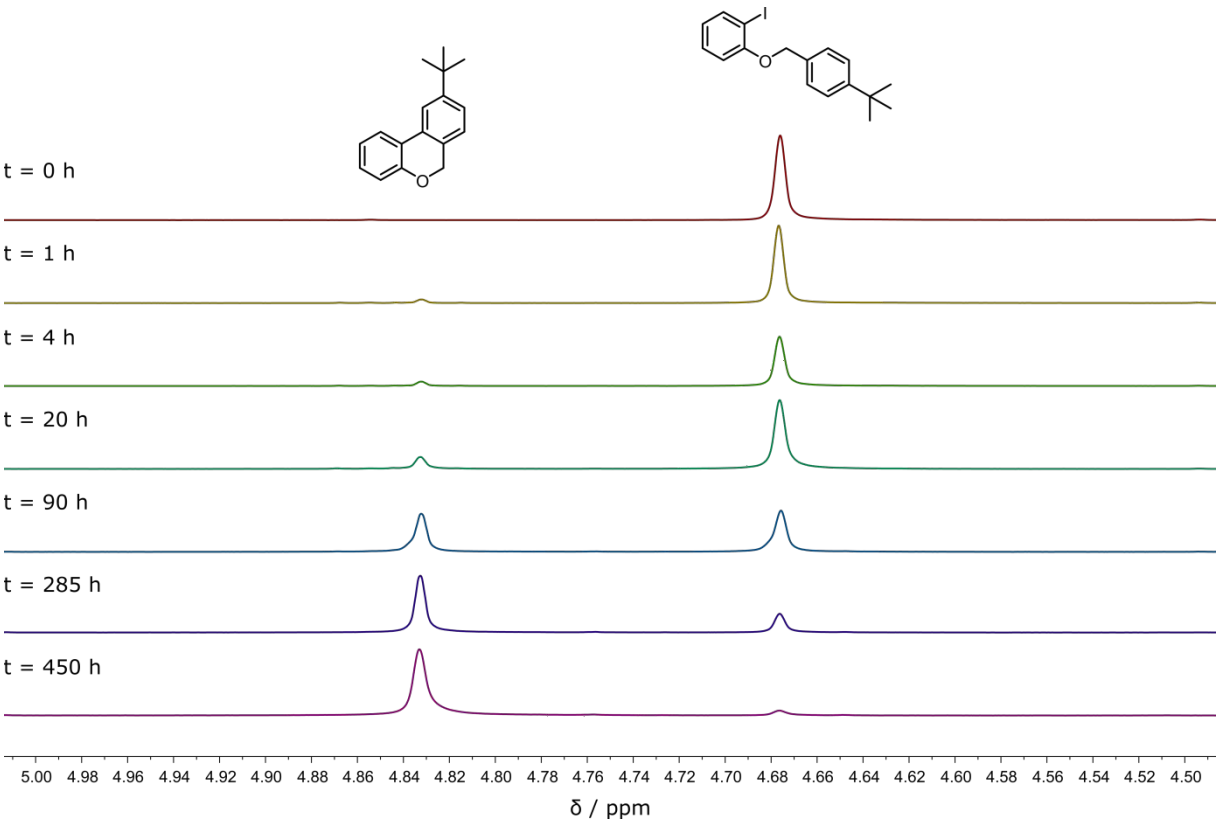

Figure S21. ^{1}H NMR spectra, recorded at 400 MHz in C_6D_6, of 50 mM **5a** with [Mo(L^{tBu})$_3$] (5 mol%) and TMP (2 eq.) at various time points under continuous irradiation at 470 nm at ca. 20 °C.

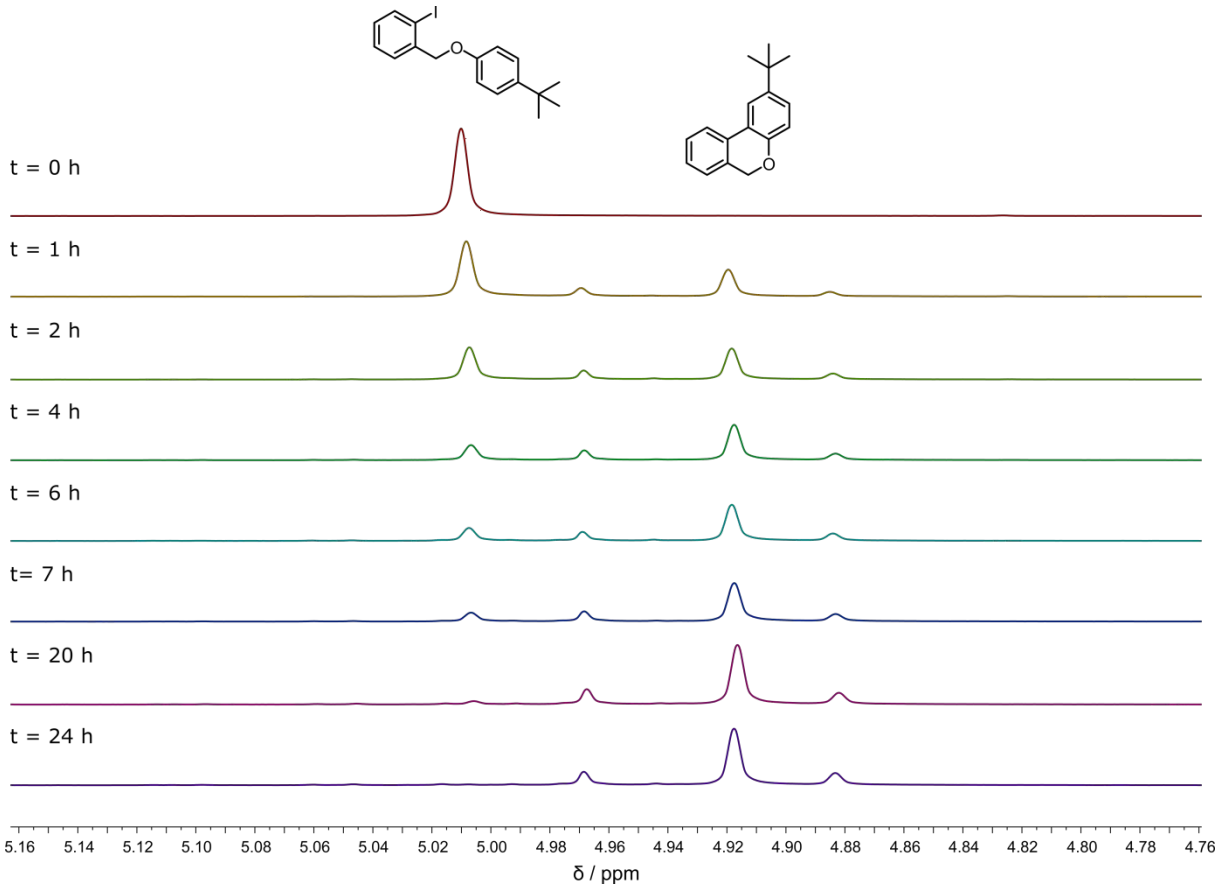

Figure S22. ^{1}H NMR spectra, recorded at 400 MHz in C_6D_6, of 50 mM **6a** with [Mo(L^{tBu})$_3$] (5 mol%) and TMP (2 eq.) at various time points under continuous irradiation at 470 nm at ca. 20 °C.

References

(1) Büldt, L. A.; Guo, X.; Prescimone, A.; Wenger, O. S. A Molybdenum(0) Isocyanide Analogue of Ru(2,2-Bipyridine)$_3^{2+}$: A Strong Reductant for Photoredox Catalysis *Angew. Chem. Int. Ed.* **2016**, *55*, 11247-11250.

(2) Sattler, W.; Ener, M. E.; Blakemore, J. D.; Rachford, A. A.; LaBeaume, P. J.; Thackeray, J. W.; Cameron, J. F.; Winkler, J. R.; Gray, H. B. Generation of Powerful Tungsten Reductants by Visible Light Excitation *J. Am. Chem. Soc.* **2013**, *135*, 10614-10617.

(3) Sattler, W.; Henling, L. M.; Winkler, J. R.; Gray, H. B. Bespoke Photoreductants: Tungsten Arylisocyanides *J. Am. Chem. Soc.* **2015**, *137*, 1198-1205.

(4) Zhang, W.; Lu, Y. Y.; Moore, J. S. Preparation of a Triamidolmolybdenum(VI) Propylidyne Complex - A Highly Active Catalyst Precursor for Alkyne Metathesis *Org. Synth.* **2007**, *84*, 163-176.

(5) Suzuki, K.; Kobayashi, A.; Kaneko, S.; Takehira, K.; Yoshihara, T.; Ishida, H.; Shiina, Y.; Oishic, S.; Tobita, S. Reevaluation of Absolute Luminescence Quantum Yields of Standard Solutions Using a Spectrometer with an Integrating Sphere and a Back-Thinned CCD Detector *Phys. Chem. Chem. Phys.* **2009**, *11*, 9850-9860.

(6) Nayak, M.; Kang, Y. K.; Kim, I. Altering the Cyclization Modes: Temperature-Dependent Intramolecular 7-Endo-Dig vs 6-Endo-Dig Electrophilic Ring Closures *Org. Lett.* **2017**, *19*, 1474-1477.

(7) Landge, K. P.; Jang, K. S.; Lee, S. Y.; Chi, D. Y. Approach to the Synthesis of Indoline Derivatives from Diaryliodonium Salts *J. Org. Chem.* **2012**, *77*, 5705-5713.

(8) Wang, X. J.; Zhang, L.; Sun, X. F.; Xu, Y. B.; Krishnamurthy, D.; Senanayake, C. H. Addition of Grignard Reagents to Aryl Acid Chlorides: An Efficient Synthesis of Aryl Ketones *Org. Lett.* **2005**, *7*, 5593-5595.

(9) Yang, Y. P.; Cui, M. C.; Zhang, X. Y.; Dai, J. P.; Zhang, Z. Y.; Lin, C. P.; Guo, Y. Z.; Liu, B. L. Radioiodinated Benzyloxybenzene Derivatives: A Class of Flexible Ligands Target to beta-Amyloid Plaques in Alzheimer's Brains *J. Med. Chem.* **2014**, *57*, 6030-6042.

(10) Zhang, L.; Yang, H.; Jiao, L. Revisiting the Radical Initiation Mechanism of the Diamine-Promoted Transition-Metal-Free Cross-Coupling Reaction *J. Am. Chem. Soc.* **2016**, *138*, 7151-7160.

4.2 Luminescence Band Shape Analysis and Temperature Dependent Emission Studies of Mo(0) Isocyanide Complexes

In addition to the studies presented in chapter 4.1, luminescence band shape analysis and simulations, as previously reported for polypyridine complexes of Os(II),[91] were performed for $[Mo(L^{Me})_3]$ and $[Mo(L^{tBu})_3]$. The results of such calculations can give further insight into excited-state distortions and nonradiative relaxation pathways of these two compounds. We found that in both complexes, the ^{3}MLCT relaxation is coupled to ligand backbone ring stretch vibrations at around 1300 cm^{-1}, comparable to structurally related tris(*α*-diimine)ruthenium(II) complexes. However, the Mo(0) isocyanide complexes show higher average frequencies between 1600-1650 cm^{-1}, likely due to additional coupling to C≡N vibrations. In combination with results from temperature-dependent emission experiments, these new findings can explain the factor of 10 difference in non-radiative relaxation between $[Mo(L^{Me})_3]$ and $[Mo(L^{tBu})_3]$. These studies were published in:

- P. Herr, O. S. Wenger "Excited-State Relaxation in Luminescent Molybdenum(0) Complexes with Isocyanide Chelate Ligands" *Inorganics*, **2020**, *8*, 14.

Author Contributions

- P.H. performed research, analysed data, and wrote the manuscript.
- O.S.W. conceived research, analysed data, and wrote the manuscript

inorganics

MDPI

Article

Excited-State Relaxation in Luminescent Molybdenum(0) Complexes with Isocyanide Chelate Ligands

Patrick Herr and Oliver S. Wenger *

Department of Chemistry, University of Basel, St. Johanns-Ring 19, 4056 Basel, Switzerland; patrick.herr@unibas.ch

* Correspondence: oliver.wenger@unibas.ch

Received: 20 January 2020; Accepted: 14 February 2020; Published: 17 February 2020

Abstract: Diisocyanide ligands with a *m*-terphenyl backbone provide access to Mo^0 complexes exhibiting the same type of metal-to-ligand charge transfer (MLCT) luminescence as the well-known class of isoelectronic Ru^{II} polypyridines. The luminescence quantum yields and lifetimes of the homoleptic tris(diisocyanide) Mo^0 complexes depend strongly on whether methyl- or *tert*-butyl substituents are placed in α-position to the isocyanide groups. The bulkier *tert*-butyl substituents lead to a molecular structure in which the three individual diisocyanides ligated to one Mo^0 center are interlocked more strongly into one another than the ligands with the sterically less demanding methyl substituents. This rigidification limits the distortion of the complex in the emissive excited-state, causing a decrease of the nonradiative relaxation rate by one order of magnitude. Compared to Ru^{II} polypyridines, the molecular distortions in the luminescent ^{3}MLCT state relative to the electronic ground state seem to be smaller in the Mo^0 complexes, presumably due to delocalization of the MLCT-excited electron over greater portions of the ligands. Temperature-dependent studies indicate that thermally activated nonradiative relaxation via metal-centered excited states is more significant in these homoleptic Mo^0 tris(diisocyanide) complexes than in $[Ru(2,2'\text{-bipyridine})_3]^{2+}$.

Keywords: luminescence; photophysics; metal-to-ligand charge transfer; ligand field; electron transfer

1. Introduction

Hexacarbonyl complexes of Cr^0, Mo^0, and W^0 are prototypical coordination compounds obeying the 18-electron rule with a low-spin d^6 valence electron configuration. Isocyanides (CNR) are formally isoelectronic with CO, and consequently it is unsurprising that hexakis(isocyanide) complexes of the abovementioned d^6 metals as well as some heteroleptic complexes comprising both CO and CNR ligands have long been known [1–7]. The isocyanides are less π-accepting than CO, yet the ligand field remains very strong (even in the Cr^0 complexes), and all 6 d-electrons are paired in the t_{2g}-set of d-orbitals, which represent the HOMO in octahedral symmetry. In arylisocyanides, there is some π-conjugation between the C≡N group and the aryl π-system, and consequently antibonding ligand-based orbitals become the LUMO in hexakis(arylisocyanide) complexes of Cr^0, Mo^0, and W^0 [1,2]. The resulting electronic structure with a metal-based HOMO and a ligand-centered LUMO is closely related to that encountered for isoelectronic Ru^{II} and Os^{II} polypyridine complexes. Thus, in analogy to this well-known class of precious metal-based complexes, arylisocyanide complexes of Cr^0, Mo^0, and W^0 have energetically low-lying metal-to-ligand charge transfer (MLCT) absorptions. An early investigation already reported luminescence from a ^{3}MLCT state in W^0 arylisocyanide complexes [2], and more recent work demonstrated that high luminescence quantum yields and long excited-state lifetimes are achievable by optimizing the ligand design [8–10]. Moreover, these W^0

complexes with monodentate arylisocyanide ligands are very strong photoreductants, capable, for example, of reducing anthracene to its radical anion form. Many different kinds of metal complexes with isocyanide ligands have been explored over the past few decades [11–15], but metals with the d^6 or d^{10} electron configurations are unique in their ability to show luminescence from a ^{3}MLCT excited state.

Whilst structurally more flexible, multidentate isocyanide chelate ligands had been known for some time [16], we found that chelating diisocyanide ligands based on a *m*-terphenyl backbone permit the synthesis of homoleptic tris(diisocyanide) complexes of Cr^0 and Mo^0 that luminesce from ^{3}MLCT excited states (Figure 1) [17]. The molecular and the electronic structures of these compounds are reminiscent of Fe^{II} and Ru^{II} polypyridine complexes, which have been investigated extensively in the past. Until now, no convincing case of steady-state MLCT luminescence from a Fe^{II} complex has been reported despite significant advances in extending their ^{3}MLCT lifetimes in recent years [18–23]; hence, our Cr^0 complex currently seems to be the only example of a first-row d^6-metal complex showing MLCT luminescence in solution at room temperature under steady-state photo-irradiation [24]. The Mo^0 diisocyanide complexes are not only emissive, but they can furthermore be employed in photoredox catalysis of thermodynamically challenging reductions, which cannot be performed with more widely known photoreductants such as *fac*-[Ir(ppy)$_3$] (ppy = 2-phenylpyridine) [25]. Thus, the Mo^0 diisocyanide complexes represent Earth-abundant alternatives to precious-metal based luminophores and photoredox catalysts, and in our view, there is interesting fundamental photophysics and photochemistry to be explored in this field [26].

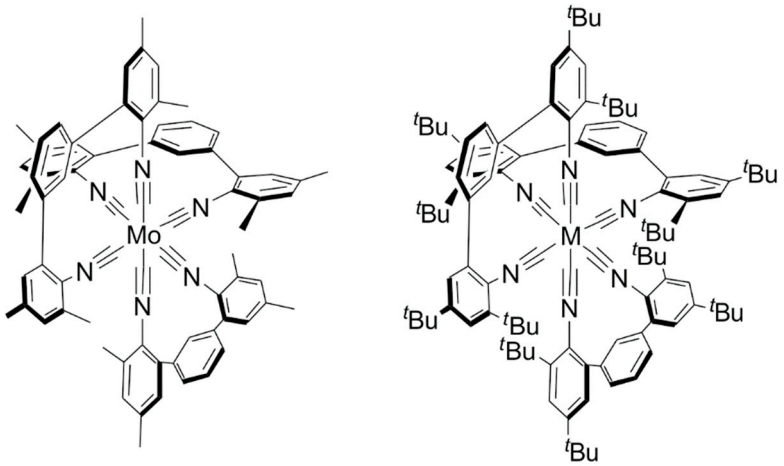

Figure 1. Molecular structures of Cr^0 and Mo^0 complexes with diisocyanide chelate ligands [17,24,25,27].

Recently we reported that the [Mo(L$^{t\mathrm{Bu}}$)$_3$] complex exhibits much more favorable photophysical properties than the closely related [Mo(L$^{\mathrm{Me}}$)$_3$] compound, and we demonstrated that [Mo(L$^{t\mathrm{Bu}}$)$_3$] is more widely applicable in photoredox catalysis due to greater photo-robustness [27]. The present article focuses on the origin of the photophysical differences between these two complexes and attempts to identify possible reasons for the very favorable luminescence behavior of [Mo(L$^{t\mathrm{Bu}}$)$_3$] in comparison to $[Ru(bpy)_3]^{2+}$ (bpy = 2,2′-bipyridine) and related Ru^{II} polypyridines. Herein, we provide the first analysis of relevant ^{3}MLCT excited-state distortions in tris(diisocyanide) Mo^0 complexes, and new temperature-dependent luminescence lifetime data give insight into thermally activated nonradiative relaxation via metal-centered excited states.

2. Results and Discussion

The $[Mo(L^{Me})_3]$ and $[Mo(L^{tBu})_3]$ complexes differ only by the substituents in *ortho*- and *para*-position to the isocyanide groups, yet their photoluminescence properties are very disparate (Table 1) [27]. Whilst the emissive excited state is of ^{3}MLCT-type in both cases, the luminescence quantum yield (φ_{em}) for $[Mo(L^{tBu})_3]$ (in de-aerated solution at 20 °C) is an order of magnitude higher than for $[Mo(L^{Me})_3]$ under identical conditions. Similarly, the ^{3}MLCT lifetime (τ) is roughly a factor of 10 longer for $[Mo(L^{tBu})_3]$ compared to $[Mo(L^{Me})_3]$. (In a prior study we already noted that the *tert*-butyl decorated complex exhibits bi-exponential luminescence decays and transient absorption kinetics in all solvents investigated, and this is likely due to conformational equilibria in solution [27]).

Table 1. Emission band maxima (λ_{max}), luminescence quantum yields (φ_{em}), and ^{3}MLCT lifetimes (τ) in de-aerated toluene at 20 °C [27].

Compound	λ_{max}/nm	φ_{em}	τ/ns
$[Mo(L^{Me})_3]$	607	0.023	166
$[Mo(L^{tBu})_3]$	585	0.203	1110 (85%)/2330 (15%) [1]

[1] Bi-exponential decays are observed in all investigated solvents; see text for details.

The parallel combined trends in luminescence quantum yields and lifetimes indicate that the rate for nonradiative ^{3}MLCT relaxation (k_{nr}) decreases by circa a factor of 10 between $[Mo(L^{Me})_3]$ and $[Mo(L^{tBu})_3]$, whereas the radiative relaxation rate (k_r) remains similar. Using Equations (1) and (2), this effect can be quantified and the resulting rate constants can be compared to $[Ru(dmb)_3]^{2+}$ (dmb = 4,4′-dimethyl-2,2′-bipyridine) [28], which is an isoelectronic analogue of our molybdenum complexes (Table 2).

$$\tau^{-1} = k_r + k_{nr} \quad (1)$$

$$\varphi_{em} = k_r/(k_r + k_{nr}) \quad (2)$$

Table 2. Rate constants for radiative (k_r) and nonradiative (k_{nr}) ^{3}MLCT excited-state relaxation in solution at room temperature.

Compound	$k_r/10^5$ s^{-1}	$k_{nr}/10^5$ s^{-1}
$[Mo(L^{Me})_3]$ [1]	1.39	58.9
$[Mo(L^{tBu})_3]$ [1,2]	1.78	5.95
$[Ru(dmb)_3]^{2+}$ [3,4]	0.83	10.6

[1] In toluene. [2] Weighted average of lifetime values (τ) used for the calculation (0.85 × 1110 ns + 0.15 × 2330 ns) [27]. [3] In acetonitrile. [4] From [28].

The radiative rate constants of the two Mo^0 complexes are roughly a factor of 2 larger than for the Ru^{II} complex. This is in line with more strongly absorbing MLCT features for $[Mo(L^{Me})_3]$ and $[Mo(L^{tBu})_3]$ (with ε_{max} up to 27,000 M^{-1} cm^{-1}) compared to $[Ru(dmb)_3]^{2+}$ ($\varepsilon_{max} \approx$ 16,500 M^{-1} cm^{-1}, ε_{max} is the extinction coefficient at the ^{1}MLCT absorption band maximum) [27]. However, it should be kept in mind that these are ^{1}MLCT absorption bands whereas the k_r values are for ^{3}MLCT relaxation. As anticipated above, k_{nr} is indeed 10 times smaller for $[Mo(L^{tBu})_3]$ than for $[Mo(L^{Me})_3]$ (last column in Table 2). In principle, a slower rate for nonradiative relaxation in the *tert*-butyl decorated complex is in line with the energy gap law [29], because this complex emits at somewhat shorter wavelengths (λ_{max} = 585 nm, Table 1) than the methyl-substituted congener (λ_{max} = 607 nm, Table 1). Yet, the factor of 10 difference in k_{nr} seems large in relation to the difference in ^{3}MLCT excited-state energies (ca. 600 cm^{-1} when using the emission band maxima as a proxy).

Mere consideration of energy gaps is a very simplified view, and it is clear that the molecular distortions occurring in an excited state have a big influence on the rates for nonradiative relaxation [29].

The analysis of luminescence band shapes can provide deeper insight into excited-state distortions and nonradiative relaxation [30], and consequently it seemed meaningful to perform such analyses with the emission spectra of [Mo(L^{Me})$_3$] and [Mo(L^{tBu})$_3$] (Figure 2); such analyses had not been performed before on our Mo^0 complexes. Ideally, vibrational fine structure would directly indicate the relevant distortion modes [31], but the lack thereof is common for MLCT luminescence and does not preclude emission band shape analysis [28].

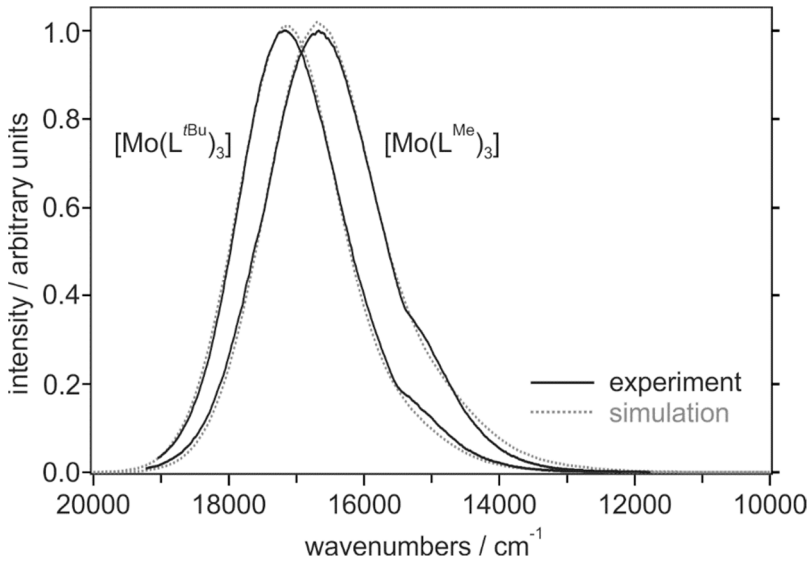

Figure 2. Luminescence spectra of [Mo(L^{Me})$_3$] and [Mo(L^{tBu})$_3$] in *n*-hexane at 20 °C following excitation at 500 nm (solid black trace) [25,27], along with simulated emission spectra according to Equation (3) (dotted gray traces).

Suitable models describe the emission spectrum as a superposition of vertical transitions between the electronically excited state and the ground state [32]. The intensity of each transition is determined by the Franck–Condon factor, which quantifies the overlap between the vibrational wave functions of the initial and the final state (Figure 3a). In this picture, the integral over all relevant vibronic transitions then makes up the experimentally observable emission band shape. Whilst several vibrations can in principle couple to an electronic transition [33], it is common to use single configurational coordinate models in which only one (weighted average) vibrational mode is considered, particularly when vibrationally unresolved (MLCT) luminescence spectra (at room temperature) are analyzed. In this limit, the emission intensity $I(\nu)$ at a given energy ν is described by Equation (3), where $\hbar{\cdot}\omega_M$ is the average energy of the vibrational mode that couples to the luminescence transition [28,34].

$$I(\upsilon) = \sum_{\nu_M=0}^{n} \left\{ \left(\frac{E_0 - \nu_M{\cdot}\hbar\omega_M}{E_0} \right)^3 \times \left(\frac{S_M}{\nu_M!} \right) \times exp\left[-4{\cdot}ln(2){\cdot}\left(\frac{\nu - E_0 + \nu_M{\cdot}\hbar\omega_M}{\Delta\upsilon_{1/2}} \right)^2 \right] \right\} \quad (3)$$

E_0 is the difference between the zero-point energies of the ground and the excited state, whereas S_M is the Huang–Rhys parameter describing the extent of molecular distortion occurring between the two respective electronic states. The term $\Delta\nu_{1/2}$ is the homogeneously broadened bandwidth associated with the vibronic transitions. For the simulation of the spectra, the quantum number ν_M runs over the number of relevant vibrational levels of $\hbar{\cdot}\omega_M$, which serve as final states in the electronic ground state.

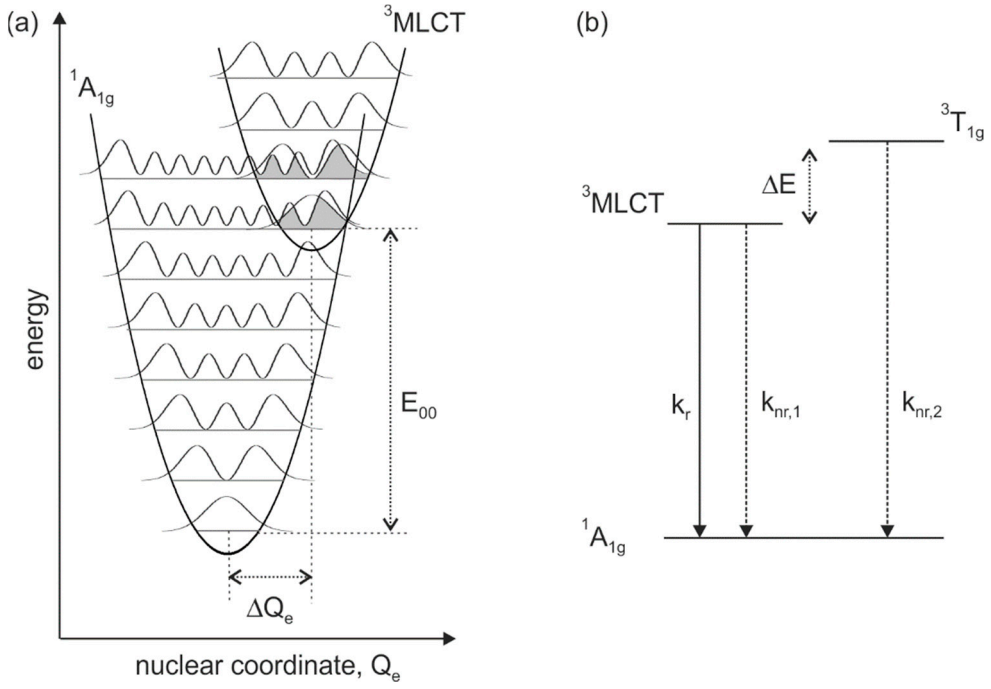

Figure 3. (**a**) Vibrational overlap (gray shaded areas) leading to nonradiative excited-state decay. (**b**) Nonradiative deactivation of the ^{3}MLCT excited state via thermal population of the $^3T_{1g}$ (metal-centered) excited state.

For the simulations in Figure 2, we summed over ν_M values from 0 to 3 and adapted E_0, S_M and $\hbar\cdot\omega_M$ to match the experimentally observed emission spectra as closely as possible. The outcomes are included in Figure 2 as dotted gray traces, and the fitting parameters are summarized in Table 3 along with those reported previously for the $[Ru(dmb)_3]^{2+}$ complex [28]. The experimental emission spectra are somewhat affected by an instrumental artefact at 15,400 cm^{-1} [24], which renders the simulations on the low energy side of the luminescence bands imperfect. Of key interest in this analysis are the Huang–Rhys parameter (S_M) and the (average) vibrational frequency ($\hbar\cdot\omega_M$). The respective values for the $[Ru(dmb)_3]^{2+}$ complex are quite typical for Ru^{II} and Os^{II} polypyridines [28,30,32,34,35]. The vibrational frequency $\hbar\cdot\omega_M$ of ca. 1300 cm^{-1} for this class of compounds is usually interpreted as a dominance of polypyridine ring stretching modes in defining the relevant excited-state distortion of the emissive ^{3}MLCT state relative to the electronic ground state. Huang–Rhys parameters in the range of 0.6 to 1.2 are very common for Ru^{II} and Os^{II} polypyridines [28,30,32,34]. By contrast, our isoelectronic Mo^0 complexes yield markedly lower Huang–Rhys parameters combined with a significantly higher average vibrational frequency (Table 3).

Table 3. Emission spectral fitting parameters.

Compound	E_0/cm^{-1}	E_{00}/cm^{-1}	$\hbar\cdot\omega_M$/cm^{-1}	S_M	$\Delta\nu_{1/2}$/cm^{-1}
$[Mo(L^{Me})_3]$ [1]	16,700	18,100	1650	0.23	1800
$[Mo(L^{tBu})_3]$ [1]	17,150	18,400	1600	0.15	1700
$[Ru(dmb)_3]^{2+}$ [2,3]	15,980	17,310	1330	1.05	1750

[1] In toluene. [2] In acetonitrile. [3] From [28].

Specifically, our simulations provide $\hbar\cdot\omega_M$ values near 1600 cm^{-1}, suggesting that isocyanide C≡N stretch vibrations (ca. 1950 cm^{-1}) [25,27] contribute substantially to the weighted average of all modes that are responsible for the excited-state distortion, presumably along with lower frequency aryl ring stretch modes. This interpretation is compatible with recent computational work on W^0

complexes with monodentate arylisocyanide ligands, which demonstrated that distortion along a normal coordinate involving the C≡N stretch is important [10]. Furthermore, previous work discussed the coupling of the C≡N group to the aromatic π-system of arylisocyanides [1,2], and it seems plausible that any distortion along the C≡N coordinate will automatically also affect the aromatic π-system and associated ring stretching vibrations. On this basis, $\hbar \cdot \omega_M$ values near 1600 cm^{-1} for the Mo^0 complexes can be rationalized.

The Huang-Rhys parameters obtained for $[Mo(L^{Me})_3]$ and $[Mo(L^{tBu})_3]$ are considerably lower than that for $[Ru(dmb)_3]^{2+}$ (Table 3) and for many other Ru^{II} polypyridines [35]. This is a somewhat surprising finding, which presumably reflects the fundamentally dissimilar molecular structures of the diisocyanide and α-diimine ligands. Thus, in the Mo^0 complexes, the ^{3}MLCT excited-state distortion seems considerably weaker than in the Ru^{II} and Os^{II} polypyridines, but this distortion occurs along vibrational modes with significantly higher average frequency. The combination of these two opposing effects results in rate constants for nonradiative relaxation (k_{nr}) that are within one order of magnitude the same for the Mo^0 and $[Ru(dmb)_3]^{2+}$ complexes (last column of Table 2).

The energy gap E_0 corresponds to the peak maximum of the first member of the vibrational progression in the $\hbar \cdot \omega_M$ distortion mode [30], and as such does not strictly correspond to the ^{3}MLCT energy (E_{00}) used, for example, for the estimation of excited-state redox potentials from ground-state potentials [36]. However, the two quantities are related to one another by Equation (4), in which k_B is Boltzmann's constant and T is temperature [28].

$$E_{00} = E_0 + \frac{(\Delta \upsilon_{1/2})^2}{16 \cdot ln(2) \cdot k_B \cdot T} \quad (4)$$

This relationship yields E_{00} values (Table 3, third column) that are in line with those determined previously for $[Mo(L^{Me})_3]$ and $[Mo(L^{tBu})_3]$ using other methods (ca. 2.2 eV) [25,27]. Lastly, we note that the $\Delta\nu_{1/2}$ values for our Mo^0 diisocyanide complexes are similar to those obtained for the previously investigated Ru^{II} and Os^{II} polypyridines [28,30,32,34,35].

Aside from the comparison between the spectral band fitting parameters obtained for the Mo^0 and Ru^{II} complexes (Table 3), the comparison between the obtained parameter sets for $[Mo(L^{Me})_3]$ and $[Mo(L^{tBu})_3]$ is interesting. The emissive ^{3}MLCT excited state is at slightly higher energy in the complex with *tert*-butyl-substituted ligands (ca. 300 cm^{-1}) and its Huang–Rhys parameter is 35% lower than that of the complex with methyl-substituted ligands (Table 3). Both of these findings are in line with the higher luminescence quantum yield for $[Mo(L^{tBu})_3]$ compared to $[Mo(L^{Me})_3]$ (Table 1). The lower Huang–Rhys parameter for $[Mo(L^{tBu})_3]$ translates into a smaller distortion of the ^{3}MLCT excited state relative to the $^1A_{1g}$ ground state along the nuclear coordinate Q_e (Figure 3a), which in turn leads to weaker overlaps between vibrational functions of the ^{3}MLCT and $^1A_{1g}$ states (grey shaded areas in Figure 3a). This makes nonradiative relaxation less efficient than in $[Mo(L^{Me})_3]$, where the excited-state distortion is stronger. The magnitude of the (equilibrium) distortion, ΔQ_e, is related to the Huang–Rhys parameter by Equation (5), where M is the reduced mass of the oscillator and ω_M is the vibrational frequency.

$$S_M = \frac{1}{2} \cdot \left(\frac{M \cdot \omega_M}{\hbar} \right) \cdot (\Delta Q_e)^2 \quad (5)$$

Since multiple normal coordinates contribute to S_M in our Mo^0 complexes, and because we are lacking information regarding their relative importance, the ΔQ_e values for the relevant individual normal coordinates cannot be calculated here. If vibrational fine structure were observable in the emission spectra, this would be possible [33].

The above emission band shape analysis serves to rationalize nonradiative relaxation occurring directly from the emissive ^{3}MLCT manifold to the electronic ground state. However, in Ru^{II} polypyridine complexes there is usually additional nonradiative relaxation from the ^{3}MLCT via the $^3T_{1g}$ excited state (Figure 3b) [37,38]. Depending on ligand design [39], this metal-centered state can be energetically very close and nonradiative relaxation becomes very rapid, and this is the

reason why $[Ru(tpy)_2]^{2+}$ (tpy = 2,2′:6′,2″-terpyridine) is essentially non-emissive in solution at room temperature [40]. Conversely, when the $^3T_{1g}$ state is located energetically sufficiently above the ^{3}MLCT manifold, high luminescence quantum yields and long excited state lifetimes are achievable [41]. In $[Ru(bpy)_3]^{2+}$ that energy difference amounts to ca. 3600 cm^{-1} [42], but for emissive Mo^0 isocyanide complexes this important aspect has not been explored before.

In order to gain insight into thermally activated ^{3}MLCT relaxation via the $^3T_{1g}$ state, we therefore performed temperature-dependent luminescence lifetime studies (τ(T), open circles in Figure 4). The ^{3}MLCT lifetimes of both $[Mo(L^{Me})_3]$ and $[Mo(L^{tBu})_3]$ decrease by roughly a factor of 4 between 283 and 338 K, in line with a thermally activated nonradiative decay process. The luminescence decays of $[Mo(L^{tBu})_3]$ remain bi-exponential at all temperatures measured (see above), and the τ(T)-values reported in Figure 4 are weighted averages from bi-exponential fits. Equation (6) and the simplified model illustrated by Figure 3b have been used previously to determine the ^{3}MLCT-$^3T_{1g}$ energy gap ΔE for $[Ru(bpy)_3]^{2+}$ [42], and the solid lines in Figure 4a,b is fits with the same model to the experimental data for our Mo^0 complexes.

$$\tau(T) = [k_r + k_{nr,1} + k_{nr,2} \cdot \exp(-\Delta E/k \cdot T)]^{-1} \quad (6)$$

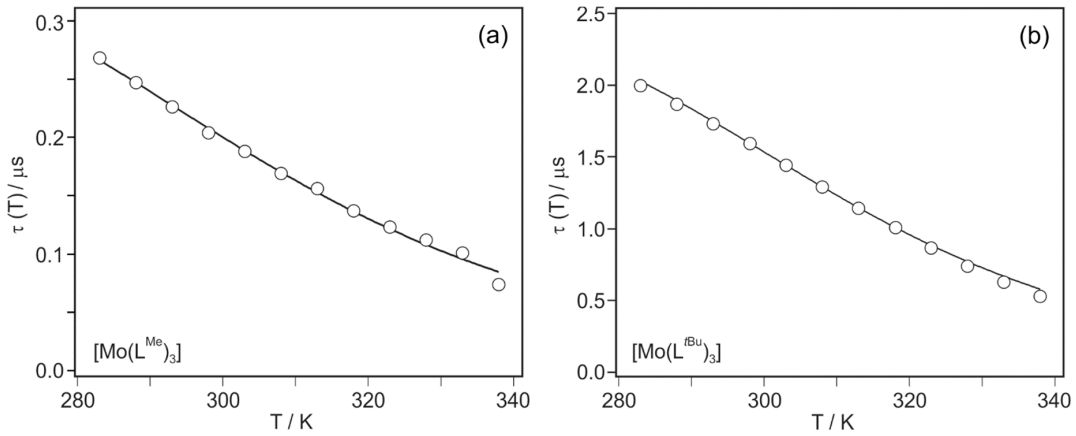

Figure 4. Temperature-dependent luminescence lifetimes (circles) and fits with Equation (6) (solid lines) for (**a**) $[Mo(L^{Me})_3]$ and (**b**) $[Mo(L^{tBu})_3]$ in toluene. See text for further details.

The sum $k_r + k_{nr,1}$ (reflecting the total ^{3}MLCT decay rate constant, Figure 3b) was fitted along with $k_{nr,2}$ and ΔE. The results from such 3-parameter fits are listed in Table 4 along with those reported previously for $[Ru(bpy)_3]^{2+}$ [42]. Of key interest is the comparison of ΔE-values. The ^{3}MLCT-$^3T_{1g}$ energy gap is largest in $[Ru(bpy)_3]^{2+}$ (3559 cm^{-1}); hence, that compound features the highest barrier for thermally activated nonradiative relaxation via a metal-centered excited state. For the more strongly emissive $[Mo(L^{tBu})_3]$ complex ΔE is ca. 19% larger than for $[Mo(L^{Me})_3]$ (2934 vs. 2472 cm^{-1}, last column in Table 4). Thus, the Mo^0 complex with the *tert*-butylated ligand features less efficient nonradiative relaxation than the Mo^0 complex with the methylated ligand, both via direct ^{3}MLCT relaxation to the electronic ground state (Figure 3a) and via thermal activation of metal-centered excited states (Figure 3b). It seems plausible that the greater overall rigidity of the $[Mo(L^{tBu})_3]$ complex compared to $[Mo(L^{Me})_3]$ is responsible for that. An X-ray crystal structure of $[Mo(L^{tBu})_3]$ is not available, but when considering the X-ray structure of the analogous Cr^0 compound in Figure 5b, it seems evident that the bulkier *tert*-butyl-substituents lead to a mutually more interlocked ligand framework than in the case of $[Mo(L^{Me})_3]$ (Figure 5a).

Table 4. Results from fits with Equation (6) to the temperature-dependent luminescence lifetime data in Figure 4.

Compound	$k_r + k_{nr,1}/s^{-1}$	$k_{nr,2}/s^{-1}$	$\Delta E/cm^{-1}$
$[Mo(L^{Me})_3]$	2.57×10^6	3.4×10^{11}	2472
$[Mo(L^{tBu})_3]$	3.74×10^5	3.6×10^{11}	2934
$[Ru(bpy)_3]^{2+}$ [1]	1.29×10^6	1.0×10^{13}	3559

[1] From [42].

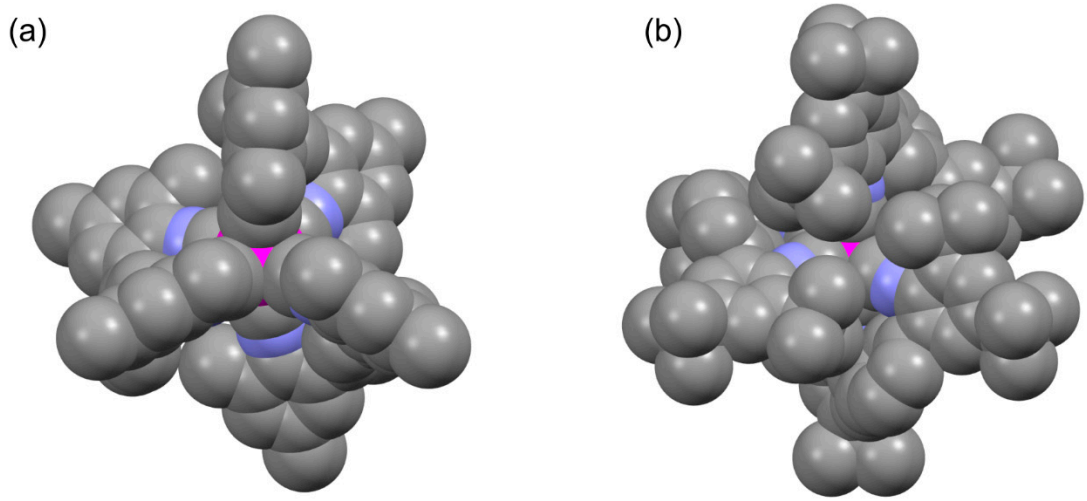

Figure 5. Space-filling representations of X-ray crystal structures of (**a**) $[Mo(L^{Me})_3]$ and (**b**) $[Cr(L^{tBu})_3]$ [24,25]. An X-ray structure of $[Mo(L^{tBu})_3]$ is not available; hence, the Cr^0 structure in (**b**) is used for comparison with $[Mo(L^{Me})_3]$.

3. Materials and Methods

The $[Mo(L^{Me})_3]$ and $[Mo(L^{tBu})_3]$ complexes were available from two recent studies and were stored under an Argon atmosphere at 4 °C [25,27]. Samples of both complexes (25 µM in dry toluene) were degassed by three freeze-pump-thaw cycles prior to measurements. The new temperature-dependent luminescence lifetime data were obtained using an LP920-KS spectrometer from Edinburgh Instruments, employing a Nd:YAG laser (Quantel Brilliant b) with an OPO (Opotek) as excitation source. The excitation wavelength was 500 nm with a typical pulse energy of 7 mJ. Single-wavelength kinetics were recorded using a photomultiplier tube. Spectral band shape analysis occurred with the Igor Pro software (version 6.3.7.2). The method by Parker and Rees was applied when converting the emission spectra from wavelength to wavenumbers [43].

4. Conclusions

The new analyses and additional temperature-dependent lifetime data reported herein are useful to understand why $[Mo(L^{tBu})_3]$ exhibits much more favorable photophysical properties than $[Mo(L^{Me})_3]$. Furthermore, the direct comparison between these tris(diisocyanide)molybdenum(0) complexes and the isoelectronic and structurally related tris(α-diimine)ruthenium(II) compounds made herein is insightful.

In both compound classes the ^{3}MLCT relaxation is coupled to ring stretch vibrations (ca. 1300 cm^{-1}) of the ligand backbone, but in the Mo^0 diisocyanides there seems to be additional coupling to C≡N vibrations, manifesting in a higher average frequency (1600–1650 cm^{-1}) of all modes responsible for excited-state distortion. The disadvantage of coupling to a higher frequency mode in the Mo^0 complexes seems to be compensated by significantly smaller Huang–Rhys factors compared to Ru^{II} polypyridines. Thus, the combination of weaker distortion along higher frequency modes is likely

responsible for the finding that the Mo^0 diisocyanide complexes have similarly favorable luminescence properties as the $[Ru(bpy)_3]^{2+}$ parent compound. In future work, it will be desirable to complement these findings by time-dependent density functional theory calculations to get clearer insight into the relevant excited-state distortions.

The barrier for thermal ^{3}MLCT deactivation via metal-centered excited states is 18–30% smaller in the two investigated Mo^0 complexes than in $[Ru(bpy)_3]^{2+}$. For $[Mo(L^{Me})_3]$ that barrier is 19% lower than for $[Mo(L^{tBu})_3]$, and the spectral band shape analysis points to a significantly greater ^{3}MLCT excited-state distortion in $[Mo(L^{Me})_3]$ relative to $[Mo(L^{tBu})_3]$. These two new findings can explain why nonradiative relaxation is roughly 10 times slower in the *tert*-butylated than in the methylated complex. Differences in the rigidity of the molecular structures of these two complexes provide a plausible rationale for this behavior. The sterically more demanding *tert*-butyl substituents lead to a molecular structure of $[Mo(L^{tBu})_3]$, in which the three individual ligands are considerably more interlocked into one another than in $[Mo(L^{Me})_3]$ where only methyl-groups are present. The use of sterically demanding substituents at the ligand periphery that lead to a compact molecular structure could represent a more generally valid design principle for minimizing undesirable excited state distortions, particularly in photoactive complexes of Earth-abundant metals [44,45].

Author Contributions: P.H. performed research, analyzed data, and wrote the paper, O.S.W. conceived research, analyzed data, and wrote the paper. All authors have read and agreed to the published version of the manuscript.

Funding: This work was funded by the Swiss National Science Foundation through grant number 200021_178760.

Conflicts of Interest: The authors declare no conflict of interest. The funders had no role in the design of the study; in the collection, analyses, or interpretation of data; in the writing of the manuscript, or in the decision to publish the results.

References

1. Mann, K.R.; Cimolino, M.; Geoffroy, G.L.; Hammond, G.S.; Orio, A.A.; Albertin, G.; Gray, H.B. Electronic Structures and Spectra of Hexakisphenylisocyanide Complexes of Cr^0, Mo^0, W^0, Mn^I, and Mn^{II}. *Inorg. Chim. Acta* **1976**, *16*, 97–101. [CrossRef]
2. Mann, K.R.; Gray, H.B.; Hammond, G.S. Excited-State Reactivity Patterns of Hexakisarylisocyano Complexes of Chromium(0), Molybdenum(0), and Tungsten(0). *J. Am. Chem. Soc.* **1977**, *99*, 306–307. [CrossRef]
3. King, R.B.; Saran, M.S. Isocyanide-Metal Complexes. II. CO and CN Stretching Modes in tert-Butyl Isocyanide Derivatives of Octahedral Metal-Carbonyls. *Inorg. Chem.* **1974**, *13*, 74–78. [CrossRef]
4. Coville, N.J.; Albers, M.O. A Synthetic Route to $M(CO)_{6-n}(RNC)_n$ (M = Cr, Mo, W; n = 1–6) from $M(CO)_6$ and Isonitriles. *Inorg. Chim. Acta* **1982**, *65*, L7–L8. [CrossRef]
5. Lyons, L.J.; Pitz, S.L.; Boyd, D.C. Electrochemical and IR Spectroelectrochemical Investigations of the Series $Mo(CO)_{6-n}(CNR)_n$ (n = 1–6) (R = 2,8-Dimethylphenyl): In-situ Observation of fac-mer and cis-trans Isomerizations. *Inorg. Chem.* **1995**, *34*, 316–322. [CrossRef]
6. Angelici, R.J.; Quick, M.H.; Kraus, G.A.; Plummer, D.T. Synthesis of Chelating Bidentate Isocyano and Cyano Ligands and Their Metal Complexes. *Inorg. Chem.* **1982**, *21*, 2178–2184. [CrossRef]
7. Treichel, P.M.; Firsich, D.W.; Essenmacher, G.P. Manganese(I) and Chromium(0) Complexes of Phenyl Isocyanide. *Inorg. Chem.* **1979**, *18*, 2405–2409. [CrossRef]
8. Sattler, W.; Henling, L.M.; Winkler, J.R.; Gray, H.B. Bespoke Photoreductants: Tungsten Arylisocyanides. *J. Am. Chem. Soc.* **2015**, *137*, 1198–1205. [CrossRef] [PubMed]
9. Sattler, W.; Ener, M.E.; Blakemore, J.D.; Rachford, A.A.; LaBeaume, P.J.; Thackeray, J.W.; Cameron, J.F.; Winkler, J.R.; Gray, H.B. Generation of Powerful Tungsten Reductants by Visible Light Excitation. *J. Am. Chem. Soc.* **2013**, *135*, 10614–10617. [CrossRef] [PubMed]
10. Kvapilova, H.; Sattler, W.; Sattler, A.; Sazanovich, I.V.; Clark, I.P.; Towrie, M.; Gray, H.B.; Zalis, S.; Vlcek, A. Electronic Excited States of Tungsten(0) Arylisocyanides. *Inorg. Chem.* **2015**, *54*, 8518–8528. [CrossRef] [PubMed]
11. Margulieux, G.W.; Weidemann, N.; Lacy, D.C.; Moore, C.E.; Rheingold, A.L.; Figueroa, J.S. Isocyano Analogues of $[Co(CO)]_4^n$: A Tetraisocyanide of Cobalt Isolated in Three States of Charge. *J. Am. Chem. Soc.* **2010**, *132*, 5033–5035. [CrossRef] [PubMed]

12. Monti, F.; Baschieri, A.; Matteucci, E.; Mazzanti, A.; Sambri, L.; Barbieri, A.; Armaroli, N. A Chelating Diisocyanide Ligand for Cyclometalated Ir(III) Complexes with Strong and Tunable Luminescence. *Faraday Discuss.* **2015**, *185*, 233–248. [CrossRef] [PubMed]
13. Knorn, M.; Rawner, T.; Czerwieniec, R.; Reiser, O. Copper(phenanthroline)(bisisonitrile)$^{+}$-Complexes for the Visible-Light-Mediated Atom Transfer Radical Addition and Allylation Reactions. *ACS Catal.* **2015**, *5*, 5186–5193. [CrossRef]
14. Drance, M.J.; Sears, J.D.; Mrse, A.M.; Moore, C.E.; Rheingold, A.L.; Neidig, M.L.; Figueroa, J.S. Terminal Coordination of Diatomic Boron Monofluoride to Iron. *Science* **2019**, *363*, 1203–1205. [CrossRef] [PubMed]
15. Cañada, L.M.; Kölling, J.; Teets, T.S. Blue-Phosphorescent Bis-Cyclometalated Iridium Complexes with Arylisocyanide Ancillary Ligands. *Polyhedron* **2020**, *178*, 114332. [CrossRef]
16. Hahn, F.E. The Coordination Chemistry of Multidentate Isocyanide Ligands. *Angew. Chem. Int. Ed.* **1993**, *32*, 650–665. [CrossRef]
17. Büldt, L.A.; Wenger, O.S. Chromium(0), Molybdenum(0), and Tungsten(0) Isocyanide Complexes as Luminophores and Photosensitizers with Long-Lived Excited States. *Angew. Chem. Int. Ed.* **2017**, *56*, 5676–5682. [CrossRef]
18. Braun, J.D.; Lozada, I.B.; Kolodziej, C.; Burda, C.; Newman, K.M.E.; van Lierop, J.; Davis, R.L.; Herbert, D.E. Iron(II) Coordination Complexes with Panchromatic Absorption and Nanosecond Charge-Transfer Excited State Lifetimes. *Nat. Chem.* **2019**, *11*, 1144–1150. [CrossRef]
19. Chábera, P.; Kjaer, K.S.; Prakash, O.; Honarfar, A.; Liu, Y.Z.; Fredin, L.A.; Harlang, T.C.B.; Lidin, S.; Uhlig, J.; Sundström, V.; et al. Fe-II Hexa *N*-Heterocyclic Carbene Complex with a 528 ps Metal-to-Ligand Charge-Transfer Excited-State Lifetime. *J. Phys. Chem. Lett.* **2018**, *9*, 459–463. [CrossRef]
20. Steube, J.; Burkhardt, L.; Päpcke, A.; Moll, J.; Zimmer, P.; Schoch, R.; Wölper, C.; Heinze, K.; Lochbrunner, S.; Bauer, M. Excited-State Kinetics of an Air-Stable Cyclometalated Iron(II) Complex. *Chem. Eur. J.* **2019**, *25*, 11826–11830. [CrossRef]
21. Duchanois, T.; Liu, L.; Pastore, M.; Monari, A.; Cebrian, C.; Trolez, Y.; Darari, M.; Magra, K.; Frances-Monerris, A.; Domenichini, E.; et al. NHC-Based Iron Sensitizers for DSSCs. *Inorganics* **2018**, *6*, 63. [CrossRef]
22. Carey, M.C.; Adelman, S.L.; McCusker, J.K. Insights into the Excited State Dynamics of Fe(II) Polypyridyl Complexes from Variable-Temperature Ultrafast Spectroscopy. *Chem. Sci.* **2019**, *10*, 134–144. [CrossRef] [PubMed]
23. Wenger, O.S. Is Iron the New Ruthenium? *Chem. Eur. J.* **2019**, *25*, 6043–6052. [CrossRef] [PubMed]
24. Büldt, L.A.; Guo, X.; Vogel, R.; Prescimone, A.; Wenger, O.S. A Tris(diisocyanide)chromium(0) Complex Is a Luminescent Analog of Fe(2,2′-Bipyridine)$_3^{2+}$. *J. Am. Chem. Soc.* **2017**, *139*, 985–992. [CrossRef]
25. Büldt, L.A.; Guo, X.; Prescimone, A.; Wenger, O.S. A Molybdenum(0) Isocyanide Analogue of Ru(2,2′-Bipyridine)$_3^{2+}$: A Strong Reductant for Photoredox Catalysis. *Angew. Chem. Int. Ed.* **2016**, *55*, 11247–11250. [CrossRef]
26. Büldt, L.A.; Wenger, O.S. Luminescent Complexes Made from Chelating Isocyanide Ligands and Earth-Abundant Metals. *Dalton Trans.* **2017**, *46*, 15175–15177. [CrossRef]
27. Herr, P.; Glaser, F.; Büldt, L.A.; Larsen, C.B.; Wenger, O.S. Long-Lived, Strongly Emissive, and Highly Reducing Excited States in Mo(0) Complexes with Chelating Isocyanides. *J. Am. Chem. Soc.* **2019**, *141*, 14394–14402. [CrossRef]
28. Damrauer, N.H.; Boussie, T.R.; Devenney, M.; McCusker, J.K. Effects of Intraligand Electron Delocalization, Steric Tuning, and Excited-State Vibronic Coupling on the Photophysics of Aryl-Substituted Bipyridyl Complexes of Ru(II). *J. Am. Chem. Soc.* **1997**, *119*, 8253–8268. [CrossRef]
29. Caspar, J.V.; Meyer, T.J. Application of the Energy-Gap Law to Nonradiative Excited-State Decay. *J. Phys. Chem.* **1983**, *87*, 952–957. [CrossRef]
30. Kober, E.M.; Caspar, J.V.; Lumpkin, R.S.; Meyer, T.J. Application of the Energy-Gap Law to Excited-State Decay of Osmium(II) Polypyridine Complexes: Calculation of Relative Nonradiative Decay-Rates from Emission Spectral Profiles. *J. Phys. Chem.* **1986**, *90*, 3722–3734. [CrossRef]
31. Hauser, A.; Reber, C. Spectroscopy and Chemical Bonding in Transition Metal Complexes. *Struct. Bond.* **2016**, *172*, 291–312.
32. Claude, J.P.; Meyer, T.J. Temperature-Dependence of Nonradiative Decay. *J. Phys. Chem.* **1995**, *99*, 51–54. [CrossRef]

33. Wenger, O.S.; Güdel, H.U. Optical Spectroscopy of $CrCl_6^{3-}$ Doped $Cs_2NaScCl_6$: Broadband Near-Infrared Luminescence and Jahn-Teller Effect. *J. Chem. Phys.* **2001**, *114*, 5832–5841. [CrossRef]
34. Treadway, J.A.; Strouse, G.F.; Ruminski, R.R.; Meyer, T.J. Long-Lived Near-Infrared MLCT Emitters. *Inorg. Chem.* **2001**, *40*, 4508–4509. [CrossRef]
35. Ashford, D.L.; Glasson, C.R.K.; Norris, M.R.; Concepcion, J.J.; Keinan, S.; Brennaman, M.K.; Templeton, J.L.; Meyer, T.J. Controlling Ground and Excited State Properties through Ligand Changes in Ruthenium Polypyridyl Complexes. *Inorg. Chem.* **2014**, *53*, 5637–5646. [CrossRef]
36. Roundhill, D.M. *Photochemistry and Photophysics of Metal Complexes*; Plenum Press: New York, NY, USA, 1994.
37. Medlycott, E.A.; Hanan, G.S. Designing Tridentate Ligands for Ruthenium(II) Complexes with Prolonged Room Temperature Luminescence Lifetimes. *Chem. Soc. Rev.* **2005**, *34*, 133–142. [CrossRef]
38. Dixon, I.M.; Heully, J.L.; Alary, F.; Elliott, P.I.P. Theoretical Illumination of Highly Original Photoreactive ^{3}MC States and the Mechanism of the Photochemistry of Ru(II) Tris(Bidentate) Complexes. *Phys. Chem. Chem. Phys.* **2017**, *19*, 27765–27778. [CrossRef]
39. Sun, Q.C.; Dereka, B.; Vauthey, E.; Daku, L.M.L.; Hauser, A. Ultrafast Transient IR Spectroscopy and DFT Calculations of Ruthenium(II) Polypyridyl Complexes. *Chem. Sci.* **2017**, *8*, 223–230. [CrossRef]
40. Ponce, A.; Gray, H.B.; Winkler, J.R. Electron Tunneling Through Water: Oxidative Quenching of Electronically Excited $Ru(tpy)_2^{2+}$ (tpy = 2,2′:6,2″-terpyridine) by Ferric Ions in Aqueous Glasses at 77 K. *J. Am. Chem. Soc.* **2000**, *122*, 8187–8191. [CrossRef]
41. Abrahamsson, M.; Jäger, M.; Osterman, T.; Eriksson, L.; Persson, P.; Becker, H.C.; Johansson, O.; Hammarström, L. A 3.0 ms Room Temperature Excited State Lifetime of a Bistridentate Ru^{II}-polypyridine Complex for Rod-Like Molecular Arrays. *J. Am. Chem. Soc.* **2006**, *128*, 12616–12617. [CrossRef]
42. Van Houten, J.; Watts, R.J. Temperature-Dependence of Photophysical and Photochemical Properties of Tris(2,2′-bipyridyl)ruthenium(II) Ion in Aqueous-Solution. *J. Am. Chem. Soc.* **1976**, *98*, 4853–4858. [CrossRef]
43. Parker, C.A.; Rees, W.T. Correction of Fluorescence Spectra and Measurement of Fluorescence Quantum Efficiency. *Analyst* **1960**, *85*, 587–600. [CrossRef]
44. Wenger, O.S. Photoactive Complexes with Earth-Abundant Metals. *J. Am. Chem. Soc.* **2018**, *140*, 13522–13533. [CrossRef] [PubMed]
45. Förster, C.; Heinze, K. Photophysics and Photochemistry with Earth-abundant Metals—Fundamentals and Concepts. *Chem. Soc. Rev.* **2020**. [CrossRef]

5 Conclusion and Future Directions

Multidentate isocyanide complexes of cheap, earth-abundant first- and second-row transition metals with d^6 electronic configuration are a new class of photosensitizers that offer unique excited-state properties and reactivity. One such case are isocyanide complexes of Mo(0), which show long luminescence lifetimes and high photoluminescence quantum yields, if the metal centre is properly shielded from the chemical surrounding. Their high excited-state oxidation potentials allow such complexes to catalyse challenging photoreactions that are not possible with common Ru- or Ir-based complexes.

Another example is a new set of homoleptic isocyanide complexes of Mn(I), which is among the first examples of first-row transition metals exhibiting MLCT luminescence in solution at room temperature (apart from complexes of Cu(I), whose electronic configuration makes luminescent MLCT states more accessible). The finding that these compounds have two different excited states that can both be accessed for photoreactions makes them stand out from the typical behaviour of second- and third-row transition metal complexes. These new insights into the photophysical properties of first-row transition metal complexes complement recent discoveries, such as luminescent LMCT states in Fe(III) complexes.[55] Further research on low-valent complexes of earth-abundant metals is needed to better understand and reveal more of the interesting characteristics of this class of compounds.

For a better understanding of the electronic and steric influence of multidentate isocyanide ligands, an obvious next step is the synthesis and characterisation of Mo(0) complexes with the bi- and tridentate thienyl ligands discussed in chapter 3. With regard to the structurally similar complexes used in reference [85], these new complexes should help to quantify the effects stemming from the thienyl linkers versus the extended π-system. *Vice versa*, Mn(I) complexes with the phenylene linked ligands could also give further insight on this matter.

Furthermore, a detailed analysis of the inherent weaknesses of these complexes is also required. These drawbacks include the difficulties to regenerate the initial state after photo-oxidation in Mo(0) complexes or the poor photostability of the Mn(I) complexes. A combination of the Mo(0) photocatalyst with either an electrochemical setup or novel methods like dehydrogenation reactions to produce the required electrons, as described in reference [92], could improve the versatility of this system. Structural modifications of the ligands can address problems in complexes of both metals. Especially for the new type of Mn(I) complexes, structural improvements could help resolve the poor photostability while revealing possible new and interesting characteristics.

The ligand scaffold employed in this thesis is extremely versatile and can be modified in various ways:

1) The steric demand of the linker can be modulated by the size of the aromatic ring (Figure 22). The main condition that the resulting ligand needs to fulfil is a bite angle, which matches the requirements for coordination with the desired metal centre.

Figure 22: Possible linker sizes for new multidentate isocyanide ligands. X is a heteroatom such as S, O, or NH.

2) The electronic properties of the linker can be modulated by functionalisation with electron-donating or withdrawing groups (Figure 23a). Incorporation of heteroatoms other than sulphur is another option (Figure 23b). Reference [85] already described the changes observed in complexes of Mo(0) after replacement of phenylene linkers with thienyl groups. Possible heterocycle linkers include, but are not limited to, pyrrole, imidazole, furane, pyridine, pyrimidine, or pyrazine. A third option to alter the electronic properties of the linker is the introduction of polycyclic aromatic structures (Figure 23c). Combinations of polycyclic linkers with the introduction of heteroatoms gives a variety of possible, and synthetically accessible, new ligand structures.

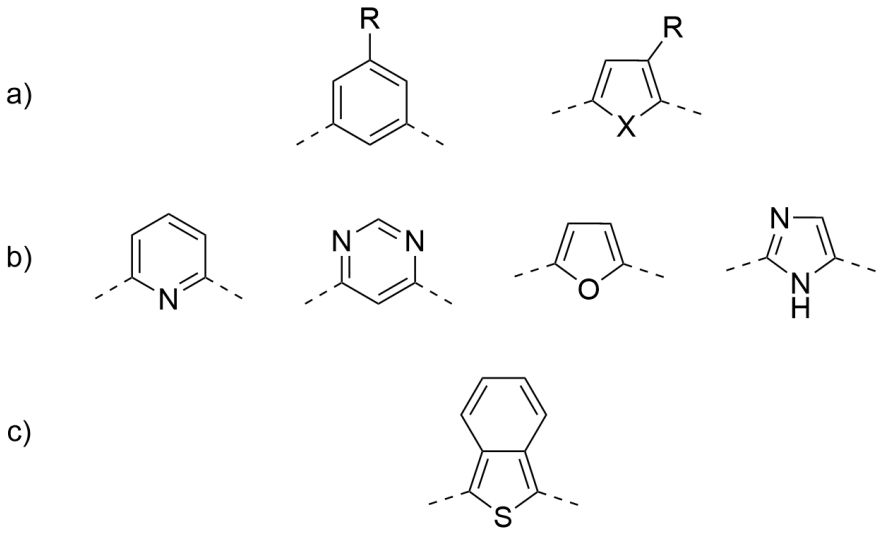

Figure 23: The electronic properties of the linker group can be modified with electron donating and/or withdrawing R groups (a), introduction of heteroatoms (b) or polycycles (c) as well as combinations thereof.

3) Functionalisation of the peripheral aromatic rings can also modulate the electronic properties of new ligands. A variety of changes similar to the aforementioned linker modulations are possible (Figure 24). However, a sterically demanding group in *ortho*-position to the isocyanide group is necessary to preserve the shielding of the metal centre.

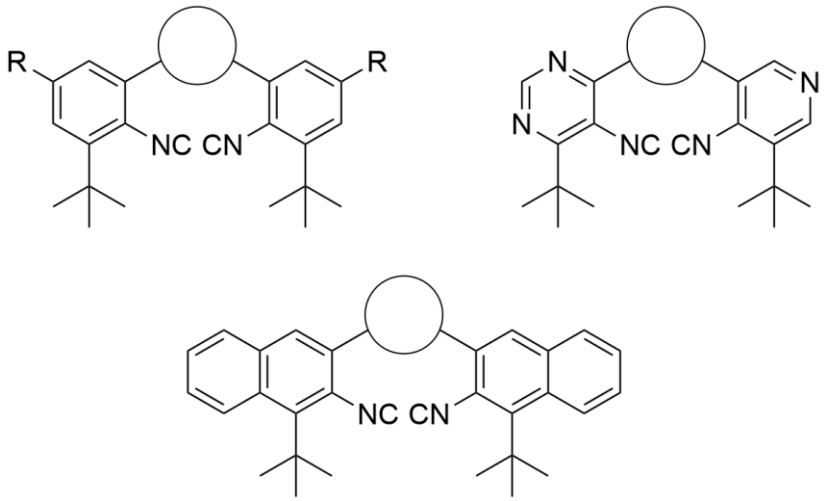

Figure 24: The electronic properties of the peripheral aromatic rings can be modified with electron donating and/or withdrawing R groups, introduction of heteroatoms or polycycles as well as combinations thereof.

4) A structurally more rigid ligand would prevent the linker units from forming conformers that cause the multiexponential luminescence decay discussed in chapter 3. Ligand rigidity can be achieved through benzannulation, bridging the peripheral with the central aromatic unit (Figure 25). The resulting large π-system of such a ligand likely shifts the absorption (and possibly emission) properties of corresponding complexes further into the red spectral region, which is beneficial, especially for Mn(I) complexes. In addition, the extended π-system could make the ^{3}π- π* states discussed in chapter 3 more accessible, for increased reactivity from these states.

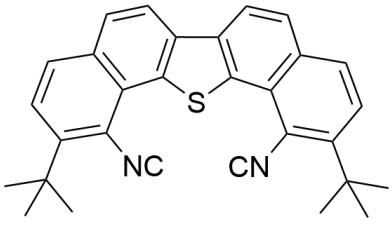

Figure 25: Example of a ligand with increased rigidity due to bridged peripheral and linker units.

All these structural changes are applicable for a bi- as well as a tridentate ligand scaffold with one and two linker units, respectively.

While changes in the ligand structure, which expand the absorption of corresponding complexes into the red spectral region are beneficial for Mn(I) complexes, the opposite

approach seems necessary for Mo(0). Due to the extension of the spectral absorption over a large part of the visible spectrum, luminescence lifetime and quantum yield drop drastically in the complexes described in reference [85], compared to the complex discussed in chapter 4. This is likely an effect of the energy gap law. Using ligands that shift the absorption properties of Mo(0) complexes to higher energies, even more reducing excited states could get accessible.

A synthetically more challenging change is the development of heteroleptic complexes – for example a combination of isocyanide ligands with NHC ligands. Another example that is accessible with heteroleptic complexes are push-pull systems, as already shown for Fe(II) complexes.[93] If successful, the range of possible properties of such complexes could be increased tremendously.

Finally, complexes of other metals can be synthesised. With the insights gained from the synthesis and analysis only of some of the aforementioned new ligands as well as a reliable synthetic route for heteroleptic complexes at hand, even luminescent isocyanide complexes of Fe(II) could be within reach.

6 Appendix: Donor-Acceptor Interactions through a Helical Oligo-1,2-naphthylene Bridge

The miniaturisation of electrical circuits has been following MOORE's law for the last 50 years.[94] However, conventional electronic devices made from bulk materials have an inherent limit to their minimal size. Therefore, the field of molecular electronics, in which researchers built single molecules with the properties of e.g. wires, switches or transistors, has gained increasing interest in recent decades.[95]

Most research on molecular wires is focused on two-dimensional, linear rod-like compounds such as oligo-*p*-phenylenes, as these structures have well-defined geometries and good donor-acceptor separation.[96,97] In contrast, the field of multidimensional electron transfer only started to receive increased interest in recent years. One major hindrance in the research of three-dimensional electronic wires is that of lacking configurational stability. The Sparr group recently developed helical oligo-1,2-naphthylenes that are composed of biaryls with a defined configuration of stereogenic axes.[98] This configurational stability enables the investigation of electron transfer through these molecular wires without the problem of interconversion between different conformers that prior studies had.

A donor-bridge-acceptor system was synthesised with varying lengths of the oligo-1,2-naphthylene bridge (Figure 26).

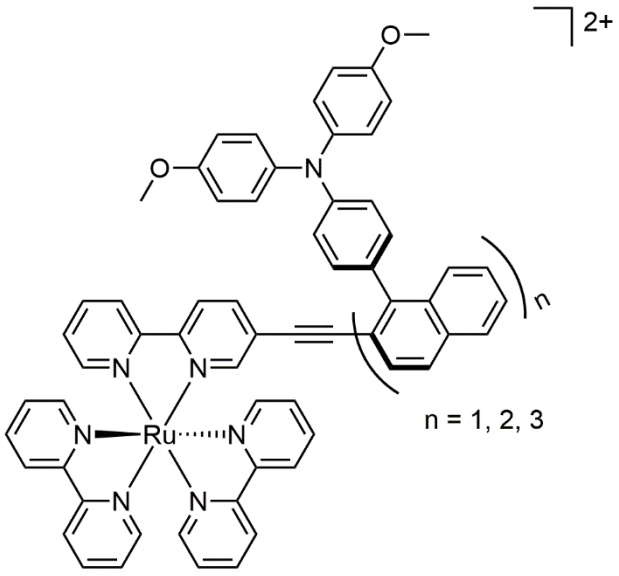

Figure 26: Structure of the donor-bridge-acceptor system used to study electron transfer through a helical, three-dimensional 1,2-naphthylene bridge of varying length.

Due to their favourable and distinguishable electrochemical and optical spectroscopic properties, $[Ru(bpy)_3]^{2+}$ was used as a photosensitizer and electron acceptor and a

triarylamine unit was used as electron donor. The bridge consists of one to three naphthalene units, to study changes of the electron transfer route and rate with increasing length of the molecular wire.

We found that the electron transfer rate surprisingly depends only very weakly on the bridge length. We attributed this to the unique molecular architecture of the oligo-1,2-naphthylene bridge, which allows a combination of electron transfer paths through covalent and noncovalent contacts. Despite the rigidity of the helical bridge structure, several close contacts exist that are possible secondary structure shortcuts for electron transfer. All results of this study were published in:

- A. Castrogiovanni, P. Herr, C. B. Larsen, X. Guo, C. Sparr, O. S. Wenger "Shortcuts for Electron-Transfer through the Secondary Structure of Helical Oligo-1,2-Naphthylenes" *Chem. Eur. J.*, **2019**, *25*, 16748-16754.

Author Contributions

- A.C. synthesised and characterised all compounds and contributed equally to data analysis and preparation of the manuscript.
- P.H. performed all the spectroscopic and electrochemical measurements and contributed equally to data analysis and preparation of the manuscript.
- C.B.L. fitted the temperature dependence of k_{ET} (Figure 3) and contributed equally to data analysis and preparation of the manuscript.
- X.G. performed the DFT calculations and contributed equally to data analysis and preparation of the manuscript.
- C.S. conceived research and contributed equally to data analysis and preparation of the manuscript.
- O.S.W. conceived research and contributed equally to data analysis and preparation of the manuscript.

COMMUNICATION

Shortcuts for Electron-Transfer through the Secondary Structure of Helical Oligo-1,2-naphthylenes

Alessandro Castrogiovanni,[†] Patrick Herr,[†] Christopher B. Larsen, Xingwei Guo,[‡] Christof Sparr,* and Oliver S. Wenger*

Abstract: Atropisomeric 1,2-naphthylene scaffolds provide access to donor-acceptor compounds with helical oligomer-based bridges, and transient absorption studies reveal a highly unusual dependence of the electron transfer rate on oligomer length, which is due to their well-defined secondary structure. Close non-covalent intramolecular contacts enable shortcuts for electron transfer that would otherwise have to occur over longer distances along covalent pathways, reminiscent of the behavior seen for certain proteins. The simplistic picture of tube-like electron transfer can describe this superposition of different pathways including both the covalent helical backbone as well as non-covalent contacts, contrasting the wire-like behavior reported many times before for more conventional molecular bridges. The exquisite control over the molecular architecture, achievable with the configurationally stable and topologically defined 1,2-naphthylene-based scaffolds, is of key importance for the tube-like electron transfer behavior. Our insights are relevant for the emerging field of multi-dimensional electron transfer and for possible future applications in molecular electronics.

1. Introduction

Photoinduced electron transfer (PET) in artificial systems typically relies on linear, rigid rod-like compounds in which the conformational degrees of freedom are restricted, leading to relatively well-defined molecular geometries and donor-acceptor separations (Scheme 1a). Such design simplifies investigations of the influence of driving-force,[1] donor-acceptor distance,[2] or bridge structure [3] on electron transfer rates (k_{ET}). Oligo-*p*-phenylenes are a prototypical class of molecular wires,[4] but recently oligo-*o*-phenylenes emerged as isomeric alternatives with intriguing properties because of their possible folding into helical secondary structures.[5] In such helical foldamers, multiple electron transfer pathways begin to compete with one another. On the one hand, electron transfer can still occur along the covalent backbone of the wire (Scheme 1b) like in the linear oligo-*p*-phenylenes, but on the other hand there can now be pathways involving non-covalent contacts between structural elements that are close in three-dimensional space but not directly connected to one another (Scheme 1d). As long as such conformationally dynamic systems are considered, it remains extremely difficult to distinguish between different pathways (Scheme 1c) because different interconverting conformers can be present on the timescale of the electron transfer event. For this reason, a prior study of dynamic oligo-*o*-phenylene bridged donor-acceptor compounds provided entangled results with limited insight into the actual electron transfer pathways.[6]

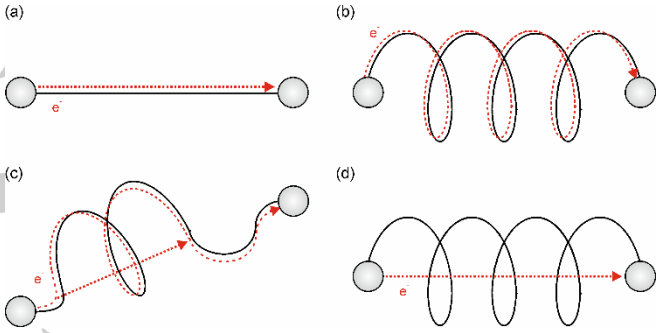

Scheme 1. (a) Electron transfer (ET) through linear wires; (b) ET across the covalent backbone of a helical structure; (c) conformational flexibility complicates the assessment of the relative importance of covalent versus non-covalently pathways; (d) ET pathway involving non-covalent contacts in a helical structure.

Recently, some of us discovered a stereoselective aldol condensation leading to configurationally stable, atropisomeric oligo-1,2-naphthylenes which do not suffer from the problem of rapid interconversion between different wire conformers on the electron transfer timescale, because they are composed of biaryls with defined configuration of stereogenic axes.[7]

As the understanding of one-dimensional electron transfer (Scheme 1a) gets increasingly complete, there is now growing interest in multi-dimensional electron transfer (Scheme 1b-d), for example in foldamers,[8] π-stacked,[9] forked [10] or circular structures.[11] The motivations for such research are diverse and include for example the ambition to construct light-harvesting and charge-separating systems that emulate natural photosynthesis, to enhance the efficiency of organic light emitting diodes (OLEDs), or the desire to control electron transfer pathways in future molecular electronics applications. Donor-bridge-acceptor compounds with well-defined molecular structures are ideally suited to explore the fundamentals of multi-dimensional electron transfer, and in our oligo-1,2-naphthylenes the type of unfolding illustrated in Scheme 1c is impossible. Consequently, we are able to get unusually direct insight into the combination of the

[*] A. Castrogiovanni, P. Herr, Dr. C. B. Larsen, Dr. X. Guo, Prof. Dr. C. Sparr, Prof. Dr. O. S. Wenger
Department of Chemistry, University of Basel
St. Johanns-Ring 19, 4056 Basel (Switzerland)
E-mail: christof.sparr@unibas.ch, oliver.wenger@unibas.ch
[†] These two authors contributed equally.
[‡] Current address: Center of Basic Molecular Science (CBMS), Department of Chemistry, Tsinghua University, Beijing 100084 (China).

Supporting information for this article is given via a link at the end of the document.

pathways illustrated in Scheme 1b/d, which are of significant interest for the abovementioned applications in solar energy conversion, lighting, and molecular electronics.

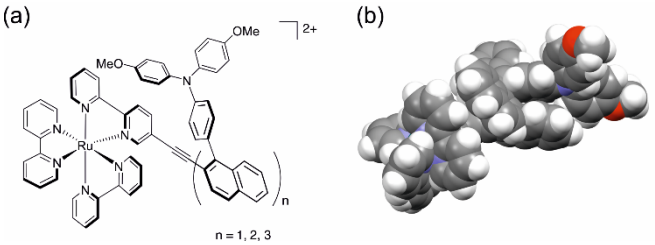

Scheme 2. (a) Donor-acceptor dyads synthesized and investigated in this work. (b) Space-filling model of the dyad with n = 3 (compound **W3**).

Quantitative information on electron transfer pathways is often extractable from distance dependence studies of electron transfer rates,[12] and therefore we synthesized three donor-acceptor dyads (Scheme 2a) comprised of variable-length 1,2-naphthylene bridges (n = 1, 2, 3). The choice of triarylamine (TAA) and $[Ru(bpy)_3]^{2+}$ as electron donor and electron acceptor units was mainly motivated by their favorable electrochemical and optical spectroscopic properties, providing unambiguous observables in time-resolved laser spectroscopy.[6, 13] A space-filling molecular model of the dyad with n = 3 (Scheme 2b) illustrates the steric congestion caused by the 1,2-naphthylene based wire backbone, and it becomes evident that pathways involving non-covalent contacts can potentially contribute to electron transfer between TAA and $[Ru(bpy)_3]^{2+}$ in such structures. To some extent, the situation in our dyads resembles that encountered in proteins, where electron transfer along the covalent primary structure is often preferable, but where individual steps involving non-covalent contacts across the tertiary structure can make important contributions.[14] In artificial systems, such events are yet hardly explored for the reasons outlined above (Scheme 1).

2. Synthesis

Using an iterative oligo-1,2-naphthylene synthesis by the addition of a building block **BB** followed by a catalyst-induced formation of a naphthaldehyde,[6] precursor **A1** was readily accessible (Scheme 2). The shortest dyad **W1** (n = 1) was in turn prepared by conversion of the aldehyde of **A1** to a terminal alkyne by using the Ohira-Bestmann reagent, allowing the subsequent installation of the bipyridine moiety through a Sonogashira cross-coupling. The free ligand was complexed with $[Ru(bpy)_2Cl_2]$, delivering the molecular dyad **W1** (n = 1) with a covalent distance between the triarylamine (TAA) *N*-atom and the Ru(II) center of 17.5 Å and notably, a drastically shorter spatial separation (7.0 Å). In order to study the impact of covalent and through-space separation on the PET properties, we next synthesized a homologous system with a longer donor-acceptor distance. We thus converted aldehyde **A2** to the corresponding alkyne under the conditions employed for the synthesis of **W1**, but found that the following Sonogashira cross-coupling was ineffective, presumably due to competitive oxidative pathways. However, this complication could be obviated by performing the cross-coupling under copper-free conditions to access the bipyridine ligand poised for ensuing complexation to provide **W2** (n = 2) as a 1 : 1 mixture of (S_a)-Δ and (S_a)-Λ diastereomers. Compared to **W1**, the homologous dyad **W2** contains a configurationally stable stereogenic axis, resulting in an increased covalent distance of 21.7 Å, which is about twice the length of spatial separation of the donor *N*-atom and Ru (10.3 Å). The possibility of controlling the configuration and the secondary structure of oligo-1,2-naphthylenes to govern the spatial relationship of substituents prompted us to devise a wire with two stereogenic axes. Following the synthetic approach for the preparation of dyad **W2**, the enantio- and diastereoisomerically-defined aldehyde **A3** could be converted to the corresponding dyad **W3** with three naphthylene repeating units. The (S_a,S_a) configuration of the stereogenic axes ensures a maximal covalent separation of 26.2 Å, which is approximately 10 Å longer than the through-space distance. The $[Ru(bpy)_3]^{2+}$ photosensitizer unit in all three dyads is present as a mixture of Δ and Λ stereoisomers.

3. Electron transfer

The $[Ru(bpy)_3]^{2+}$ photosensitizer of all dyads can be selectively excited at 532 nm (Fig. S1), and transient absorption spectra recorded immediately after the 10-ns laser pulses (Fig. 1a) are essentially a superposition of $[Ru(bpy)_3]^{+}$ (Fig. 1b) and $TAA^{\bullet+}$ (Fig. 1c) as is evident from UV-Vis spectroelectrochemical measurements. This observation indicates that electron transfer from TAA to photoexcited $[Ru(bpy)_3]^{2+}$ occurs on a timescale faster than 10 ns. The redox properties of the TAA donor and the $[Ru(bpy)_3]^{2+}$ photosensitizer are insensitive to bridge elongation (Fig. S2-S4), and cyclic voltammetry yields potentials around 0.70 V vs SCE for the $TAA^{\bullet+/0}$ and -1.15 V vs SCE for the $[Ru(bpy)_3]^{2+/+}$ redox couples in all three dyads. Given an excited-state energy of 2.03 eV (based on the ^{3}MLCT luminescence of the **W2** dyad in butyronitrile at 77 K, Fig. S5), we therefore estimate that one-electron reduction of the ^{3}MLCT-excited $[Ru(bpy)_3]^{2+}$ units of our dyads occurs at potentials near 0.88 V vs SCE. Consequently, the reaction free energy (ΔG_{ET}^0) for electron transfer from TAA to ^{3}MLCT-excited $[Ru(bpy)_3]^{2+}$ is around -0.2 eV for all dyads (Table S1), because TAA is oxidized near 0.7 V and photoexcited $[Ru(bpy)_3]^{2+}$ is reduced near 0.9 V vs SCE. As noted above, this process occurs within the duration of the excitation laser pulses (Fig. S6), and therefore cannot be temporally resolved by nanosecond laser flash photolysis.

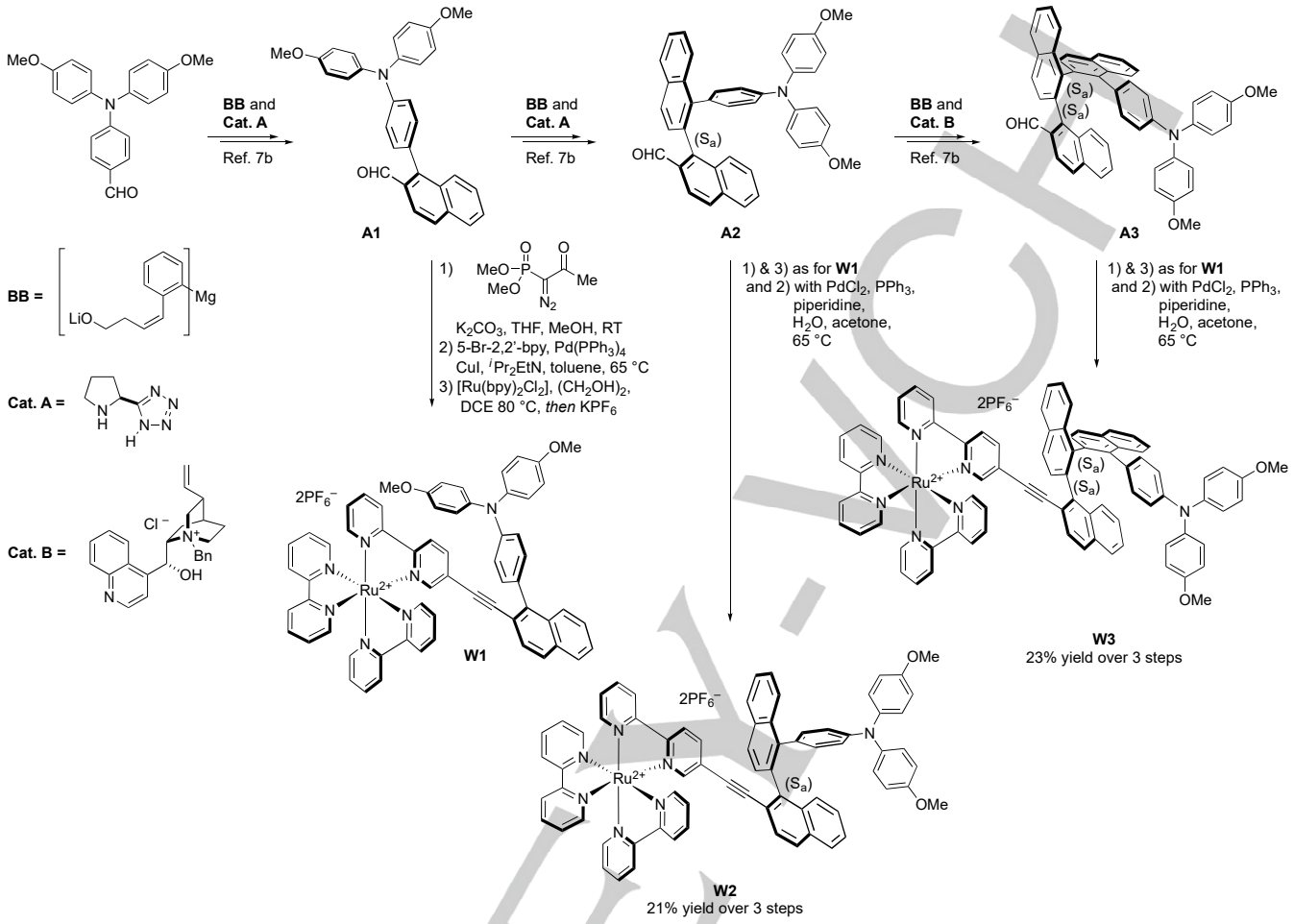

Scheme 3. Synthesis of donor-acceptor dyads **W1**-**3**.

The transient absorption signals of the observable $[Ru(bpy)_3]^+$ and $TAA^{\bullet+}$ photoproducts (Fig. 1a) start to decay immediately after the end of the pulses (Fig. 2a-c) as a result of the spontaneously occurring thermal reverse electron transfer from reduced acceptor to oxidized donor. All decays are mono-exponential, and for a given dyad they are exactly alike irrespective of whether $[Ru(bpy)_3]^+$ (red traces in Fig. 2a) or $TAA^{\bullet+}$ is monitored (blue traces in Fig. 2a), diagnostic of intramolecular reverse electron transfer, in the course of which the reduced acceptor and the oxidized donor disappear with identical kinetics. Based on the potentials for the $TAA^{\bullet+/0}$ and $[Ru(bpy)_3]^{2+/+}$ redox couples given above, this thermal reverse reaction is associated with ΔG_{ET}^0 of ca. -1.8 eV. Evidently, the thermal reverse electron transfer from $[Ru(bpy)_3]^+$ to $TAA^{\bullet+}$ has a far greater driving-force (1.8 eV) than the initial electron transfer from TAA to photoexcited $[Ru(bpy)_3]^{2+}$ (0.2 eV), yet the thermal reverse process occurs on a much slower timescale (ca. 1 µs, Fig. 2a) than the initial photoinduced reaction (< 10 ns, see above). This is not an uncommon observation in molecular dyads and triads of this type, and it is often attributed to the inverted driving-force regime of Marcus theory, in which electron transfer rates decrease with increasing driving-force.[1d, 2a, 15]

Single-exponential fits to the decay data in Fig. 2 yield rate constants (k_{ET}) decreasing from $(8.2\pm0.4)\times10^6$ s^{-1} for **W1** to $(6.3\pm0.3)\times10^6$ s^{-1} for **W2** and finally $(5.2\pm0.3)\times10^6$ s^{-1} for **W3** (Table 1). Thus, k_{ET} depends very weakly on dyad length, exhibiting a decrease by only a factor of 1.6 between **W1** and **W3**. This finding is highly unusual as becomes evident by comparison to previously disclosed distance dependence data obtained from dyads with oligo-*p*-phenylene bridges, where each additional phenylene unit typically causes a decrease of k_{ET} by a factor of 10.[16] The elongation by two *o*-naphthyl units when going from **W1** to **W3** therefore causes a decrease of k_{ET} that is roughly a factor of 60 lower than the expectable decrease associated with the elongation by two *p*-phenylene units. Thus, our oligo-1,2-naphthylene bridges mediate long-range electron transfer with much faster rates than the prototypical oligo-*p*-phenylene wires. This is a remarkable finding, which could not be anticipated at the outset of this project.

Energy minimized ground-state DFT calculations were used to estimate the donor-acceptor distances in our dyads (Fig. S8; see

SI page S29 for details), leading to values between 17.5 (n = 1) and 26.2 Å (n = 3) when measuring the distance between the TAA *N*-atom and the Ru(II) center along the shortest covalent pathway through all naphthylene units ($r_{DA,cov}$). Alternatively, values ranging from 7.0 (n = 1) to 15.7 Å (n = 3) are obtained when determining the distance between the two respective atoms directly through space ($r_{DA,ts}$). Semi-logarithmic plots of k_{ET} versus distance are linear (Fig. 2d), in line with the commonly observed exponential distance dependence of k_{ET} in the tunneling regime, where the bridge imposes a barrier through which the electrons tunnel from the donor to the acceptor. The distance decay constant (β) in eq. 1 describes the steepness of the exponential decrease of k_{ET}, and $k_{ET}^{(0)}$ is the electron transfer rate when the donor and the acceptor are in van der Waals contact distance.[14d] The physical origin of the exponential function in eq. 1 are exponentially decreasing orbital overlaps as described by superexchange theory.[17] Regardless of whether the $r_{DA,cov}$ or the $r_{DA,ts}$ values from above are used, a β value of 0.05 Å^{-1} is obtained for our dyads (Fig. 2d), which is much lower than the typical β-values of oligo-*p*-phenylenes and closely related bridges (0.5 – 0.8 Å^{-1}).[16] In principle, β is not a bridge-specific parameter, but instead depends on the entire combination of donor, bridge, and acceptor,[2c, 18] but nevertheless this comparison between β values is meaningful because some of the previously investigated phenylene-bridged systems involved similar $[Ru(bpy)_3]^{2+}$ and tertiary amine donors as in dyads **W1**-**W3**.[19] Given β values that are lower by a factor of 10-16 in oligo-1,2-naphthylenes than in oligo-*p*-phenylenes, one can argue that our new wires perform by at least an order of magnitude better.

$$k_{ET}(d) = k_{ET}^{(0)} \cdot \exp[-\beta \cdot d] \qquad \text{(eq. 1)}$$

With a β value as low as 0.05 Å^{-1}, a hopping rather than tunneling mechanism could in principle be operative.[12, 20] In the electron hopping process, individual bridge units are temporarily reduced before the transferring electron reaches the thermodynamic sink at the acceptor. Alternatively, in the hole hopping picture, the bridge units are transiently oxidized before the hole reaches the donor. The electron reduction potential of naphthalene is -2.49 V vs SCE [21] and the $[Ru(bpy)_3]^{2+/+}$ potential is -1.15 V vs SCE (see above), hence the temporary reduction of a naphthalene unit by $[Ru(bpy)_3]^{+}$ is endergonic by ca. 1.3 eV. The one-electron oxidation of naphthalene requires a potential of 1.54 V vs SCE,[21] whereas the $TAA^{\bullet+/0}$ potential is 0.70 V vs SCE, and consequently the hole transfer from $TAA^{\bullet+}$ to naphthalene is endergonic by ca. 0.8 eV. On this basis, both electron and hole hopping processes are unlikely, and we conclude that the unusually shallow distance dependence observable for our oligo-1,2-naphthylenes is likely due to an unusually efficient tunneling process.

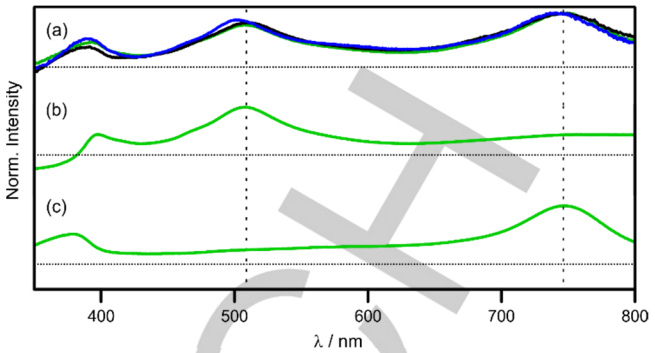

Figure 1. (a) Transient absorption spectra recorded after excitation of 20 μM solutions of the dyads from Scheme 1 in acetonitrile (blue, n = 1; green, n = 2; black, n = 3). Excitation occurred at 532 nm with laser pulses of ca. 10 ns duration, spectra were recorded by integration over 200 ns without delay. (b) Spectro-electrochemical UV-Vis difference spectrum recorded from a de-aerated 1 mM solution of the dyad with n = 2 in acetonitrile while applying a potential of -1.3 V vs. SCE. (c) Spectro-electrochemical UV-Vis difference spectrum obtained from the same solution while applying a potential of 0.9 V vs. SCE. The UV-Vis spectra prior to applying any potential served as baselines in (b) and (c).

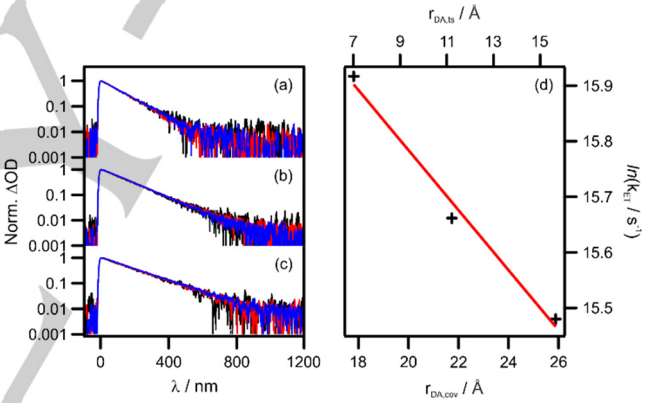

Figure 2. Decay of the transient absorption signals at ca. 390 (black), 510 (red) and 745 (blue) nm, for (a) n = 1, (b) n = 2 and (c) n = 3 in de-aerated acetonitrile after excitation at 532 nm with laser pulses of ca. 10 ns duration (T = 20 °C). (d) ET rates (k_{ET}) as a function of donor-acceptor distance measured through the covalent bridge backbone ($r_{DA,cov}$) and through space ($r_{DA,ts}$) in energy-minimized ground-state conformers of the three dyads from Scheme 1.

To gain further insight, we performed temperature-dependent transient absorption studies, from which we determined k_{ET} for the thermal reverse electron transfer from $[Ru(bpy)_3]^{+}$ to $TAA^{\bullet+}$ in all three dyads between 0 and 50 °C (Figure S27). Fitting the temperature dependence of k_{ET} to the semiclassical Marcus-Hush equation (eq. 2) is a common procedure to determine the reorganization energy (λ) and the electronic coupling between the donor and the acceptor (H_{DA}).[3a] We used the reaction free energies (ΔG_{ET}^0) extracted from cyclic voltammetry (Table S1) as input values, and fitted λ and H_{DA} to the kinetic data in Fig. 3 (see SI page S27 for details).

$$k_{ET} = \sqrt{\frac{\pi}{\hbar^2 \cdot \lambda \cdot k_B \cdot T}} \cdot {H_{DA}}^2 \cdot \exp\left[-\frac{(\lambda + \Delta G_{ET}^0)^2}{4 \cdot \lambda \cdot k_B \cdot T}\right] \qquad \text{(eq. 2)}$$

Table 1. Electron-transfer parameters for the dyads from Scheme 1: Donor-acceptor distances measured through the covalent bridge backbone ($r_{DA,cov}$) and through-space in low-energy conformers ($r_{DA,ts}$), rate constants for ET (k_{ET}) at 20 °C, (negative) reaction free energies (ΔG_{ET}^0), activation free energies ($\Delta G_{ET}^{\ddagger}$), reorganization energies (λ), and electronic coupling (H_{DA}) between donor and acceptor.

cmpd	$r_{DA,cov}$ [Å]	$r_{DA,ts}$ [Å]	k_{ET} [s^{-1}]	$-\Delta G_{ET}^0$ [eV]	$\Delta G_{ET}^{\ddagger}$ [meV]	λ [eV]	H_{DA} [cm^{-1}]
n = 1	17.5	7.0	$(8.2\pm0.4)\cdot10^6$	1.81±0.05	110±10	1.12±0.04	1.5±0.1
n = 2	21.7	10.3	$(6.3\pm0.3)\cdot10^6$	1.79±0.05	120±10	1.07±0.04	1.7±0.1
n = 3	26.2	15.7	$(5.2\pm0.3)\cdot10^6$	1.82±0.05	140±10	1.06±0.04	2.1±0.1

The obtained λ values for the three dyads are all within experimental error at ca. 1.1 eV (Table 1), in line with numerous previously investigated systems, including many ET enzymes.[14c] A λ value of 1.1 eV is furthermore compatible with a simple model [15a] which treats the donor and the acceptor as two charged spheres (with radii of 4 Å) interacting with each other in electrostatic fashion through CH_3CN (with a dielectric constant of 35.7 and a refractive index of 1.3441).[22] Thus, there is no unusual behavior of λ in our dyads. The striking finding is that H_{DA} is nearly insensitive to bridge elongation and even slightly increases from 1.5±0.1 cm^{-1} to 2.1±0.1 cm^{-1} between **W1** and **W3** (Table 1). For superexchange tunneling, a decrease of H_{DA} with increasing r_{DA} is usually observed, typically by factors of 1.2 – 3.0 per Å distance elongation depending on whether saturated or π-conjugated bridges are present.[14c, 14d, 23] Thus, the unusually shallow distance dependence of k_{ET} in our dyads (Fig. 2d) can be attributed to an uncommon behavior of electronic coupling between donor and acceptor, whereas the reorganization energy shows no unusual effects.

Since the peculiar distance dependence of H_{DA} in our dyads cannot be reconciled in the common framework of electron transfer along the covalent backbone of the molecular bridge, we began to consider the possibility of additional tunneling pathways along non-covalent contacts within the helical oligo-1,2-naphthalene structure. Prior work on C-clamp or U-shaped molecules demonstrated that electron transfer through space and through solvent molecules is typically much slower than along covalent pathways.[24] However, our oligo-1,2-naphthalene structures are very compact (Scheme 2b), with much shorter non-covalent contacts than in previously investigated model systems, and it is conceivable that these short contacts contribute significantly to H_{DA}. As the length of the molecular bridge increases, the number of such non-covalent contacts increases, and this could explain the peculiar distance dependence of H_{DA} uncovered above.

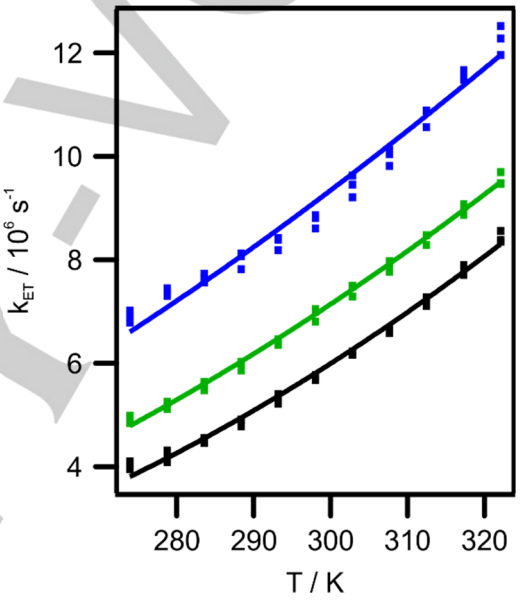

Figure 3. Temperature dependence of k_{ET} for all three dyads recorded at three wavelengths each, fitted to eq. 1.

Ground-state energy-minimized DFT calculations afford qualitative evidence of non-covalent interactions providing possible shortcuts for electron-transfer in our dyads. For instance, there is a short through-space donor-acceptor contact for the **W1** dyad (Fig. 4, top) with a distance of only 7.0 Å between the *N*-atom of TAA and the Ru(II) center, and there are π-interactions between TAA and a naphthylene unit for the **W3** dyad (Fig. 4, bottom). Given that the calculations are on ground-state energy-minimized structures, there are likely many such non-covalent interactions in solution. However, the conformational degrees of freedom of the investigated atropisomeric oligo-1,2-naphthylene dyads **W1-3** are essentially reduced to librational motions between adjacent naphthylene units as well as rotation around the C≡C triple bond, but unfolding of the helical structures is not possible as discussed above (Scheme 1). Nevertheless, it remains impossible to pinpoint exact transfer paths. The key point here is that the helical oligo-1,2-naphthalene structures impose short non-covalent contacts, and relatively minor thermal fluctuations can readily enable electron transfer across these non-

covalent contacts, complementing the transfer along the covalent backbone.

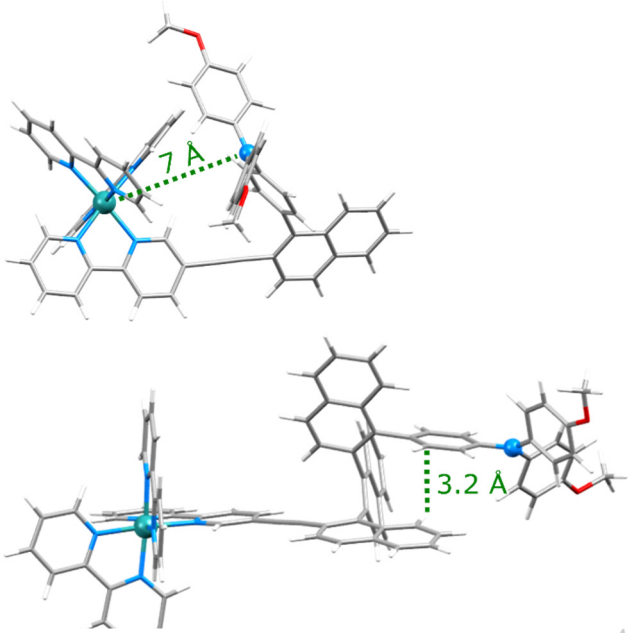

Figure 4. Ground-state geometry-optimized structures of n = 1 (top), and n = 3 (bottom), obtained from B3LYP/6-31G(d) DFT calculations, highlighting examples of non-covalent short-contacts as possible secondary structure shortcuts for electron-transfer.

4. Summary and conclusions

The electronic coupling (H_{DA}) between the donor and acceptor units in our dyads exhibits a fundamentally different dependence on distance than in the vast majority of previously investigated systems. One-dimensional donor-bridge-acceptor compounds (Scheme 1a) typically exhibit an exponential decrease of H_{DA} in the tunneling regime, whilst electron (or hole) hopping can give rise to more shallow decreases.[12, 14c, 14d] However, an *in*crease of H_{DA} with distance elongation as for the dyads in Scheme 2a (even though weak, from 1.5±0.1 to 2.1±0.1 cm^{-1}) is very rare.[16b, 25] This suggests that the unusually congested molecular architecture of the oligo-1,2-naphthylene bridges (Scheme 2b) imparts uncommon electronic coupling pathways, likely involving a mixture of covalent and non-covalent contacts present in their three-dimensional structure. Reorganization energies (λ) and reaction free energies (ΔG_{ET}^0) remain essentially constant in all our dyads, supporting the view that the observable weak distance dependence of electron transfer rates (k_{ET}) is indeed caused by unusual electronic coupling effects.

In a somewhat simplistic picture, the atropisomeric and configurationally stable oligo-1,2-naphthylene bridges with their helical structures can be regarded as tube-like objects (Scheme 4a/c), in which the transferring electrons do not strictly follow the circular path of the covalent helical coil, but additionally can also follow shorter paths along the donor-acceptor direction. This is in contrast to previously investigated linear donor-bridge-acceptor compounds for which the traditional wire-like and strictly one-dimensional picture (Scheme 4b/d) is sufficient.

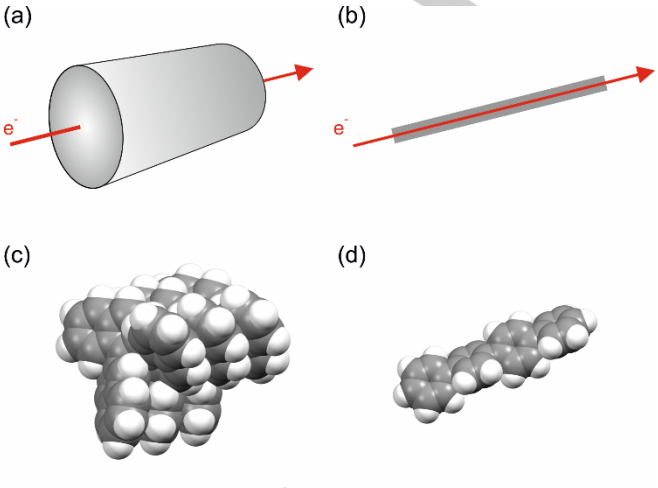

Scheme 4. (a) Illustration of the tube-like nature of electron transfer in helical oligo-1,2-naphthalene structures; (b) wire-like nature of electron transfer in traditional systems; (c) space-filling model of an oligo-1,2-naphthalene compound comprised of 9 monomer units to illustrate the tube-like nature of the structure; (d) space-filling model of a *p*-phenylene tetramer as a representative wire-like system.

Whilst the oligo-1,2-naphthylene bridges cannot unfold to completely open structures and are forced into the tube-like shape, some conformational fluctuations remain possible, for example librational motions between individual bridge units, or rotation of the photosensitizer around the alkynyl-linker. Thus, it remains impossible to pinpoint exact pathways even in these comparatively rigid structures, but possible shortcuts can readily be identified (Figure 4) without the need for major computational efforts. Similar shortcuts could occur in many other artificial systems where long-range electron transfer takes place, for example in compounds with stacked structures or polymer systems used for organic solar cells.[26] With conformationally more flexible wires such as for example 1,2-phenylenes, unfolding would readily occur (Scheme 1c), and a far greater ensemble of conformers would be probed on the electron transfer timescale.[6] Under these conditions, the insights gained above regarding the unusual distance dependence of electronic coupling, shortcuts along non-covalent contacts, and tube-like electron transfer would not be attainable.[6, 27]

In conclusion, the unique molecular architecture of our new oligo-1,2-naphthylenes leads a combination of electron transfer paths involving both covalent and non-covalent contacts, the superposition of which can be described by the simplistic picture of electron transfer within a tube-like object. This manifests in very weakly distant-dependent electron transfer rates. We are unaware of prior studies that reported similar behavior for other types of artificial molecular bridges.

Current studies are devoted to approaches for increasing 3D topological definition to more clearly disentangle the underlying

contributions of hopping and tunneling pathways to long-range electron transfer.

Acknowledgements

This work was funded by the Swiss NSF through grant numbers 200021_178760 and BSSGI0-155902/1 and the NCCR Molecular Systems Engineering. We thank Dr. D. Lotter for initial studies and PD Dr. D. Häussinger for NMR support.

Keywords: electron transfer • donor-acceptor systems • time-resolved spectroscopy • molecular electronics • photochemistry

[1] a) G. N. Lim, C. O. Obondi, F. D'Souza, Angew. Chem. Int. Ed. 2016, 55, 11517-11521; b) L. Favereau, A. Makhal, Y. Pellegrin, E. Blart, J. Petersson, E. Goransson, L. Hammarström, F. Odobel, J. Am. Chem. Soc. 2016, 138, 3752-3760; c) M. M. Waskasi, G. Kodis, A. L. Moore, T. A. Moore, D. Gust, D. V. Matyushov, J. Am. Chem. Soc. 2016, 138, 9251-9257; d) B. Geiss, C. Lambert, Chem. Commun. 2009, 1670-1672; e) M. Wolf, C. Villegas, O. Trukhina, J. L. Delgado, T. Torres, N. Martin, T. Clark, D. M. Guldi, J. Am. Chem. Soc. 2017, 139, 17474-17483.

[2] a) M. Kuss-Petermann, O. S. Wenger, J. Am. Chem. Soc. 2016, 138, 1349-1358; b) K. Hu, A. D. Blair, E. J. Piechota, P. A. Schauer, R. N. Sampaio, F. G. L. Parlane, G. J. Meyer, C. P. Berlinguette, Nat. Chem. 2016, 8, 853-859; c) B. Albinsson, M. P. Eng, K. Pettersson, M. U. Winters, Phys. Chem. Chem. Phys. 2007, 9, 5847-5864; d) K. E. Linton, M. A. Fox, L. O. Palsson, M. R. Bryce, Chem.-Eur. J. 2015, 21, 3997-4007; e) P. M. Burrezo, N. T. Lin, K. Nakabayashi, S. Ohkoshi, E. M. Calzado, P. G. Boj, M. A. D. Garcia, C. Franco, C. Rovira, J. Veciana, M. Moos, C. Lambert, J. T. L. Navarrete, H. Tsuji, E. Nakamura, J. Casado, Angew. Chem. Int. Ed. 2017, 56, 2898-2902.

[3] a) J. Sukegawa, C. Schubert, X. Z. Zhu, H. Tsuji, D. M. Guldi, E. Nakamura, Nat. Chem. 2014, 6, 899-905; b) R. H. Goldsmith, L. E. Sinks, R. F. Kelley, L. J. Betzen, W. H. Liu, E. A. Weiss, M. A. Ratner, M. R. Wasielewski, Proc. Natl. Acad. Sci. U. S. A. 2005, 102, 3540-3545; c) Y. S. Luo, M. Wächtler, K. Barthelmes, A. Winter, U. S. Schubert, B. Dietzek, Chem. Commun. 2019, 55, 5251-5254; d) A. Arrigo, A. Santoro, F. Puntoriero, P. P. Lainé, S. Campagna, Coord. Chem. Rev. 2015, 304, 109-116; e) M. Krzeszewski, E. M. Espinoza, C. Cervinka, J. B. Derr, J. A. Clark, D. Borchardt, G. J. O. Beran, D. T. Gryko, V. I. Vullev, Angew. Chem. Int. Ed. 2018, 57, 12365-12369.

[4] a) B. Schlicke, P. Belser, L. De Cola, E. Sabbioni, V. Balzani, J. Am. Chem. Soc. 1999, 121, 4207-4214; b) A. C. Benniston, A. Harriman, Chem. Soc. Rev. 2006, 35, 169-179.

[5] a) E. Ohta, H. Sato, S. Ando, A. Kosaka, T. Fukushima, D. Hashizume, M. Yamasaki, K. Hasegawa, A. Muraoka, H. Ushiyama, K. Yamashita, T. Aida, Nat. Chem. 2011, 3, 68-73; b) C. S. Hartley, Acc. Chem. Res. 2016, 49, 646-654; c) M. Rickhaus, M. Mayor, M. Juricek, Chem. Soc. Rev. 2016, 45, 1542-1556.

[6] S. Malzkuhn, X. Guo, D. Häussinger, O. S. Wenger, J. Phys. Chem. A 2019, 123, 96-102.

[7] a) D. Lotter, M. Neuburger, M. Rickhaus, D. Häussinger, C. Sparr, Angew. Chem. Int. Ed. 2016, 55, 2930-2933; b) A. Link, C. Sparr, Chem. Soc. Rev. 2018, 47, 3804-3815.

[8] a) A. Méndez-Ardoy, N. Markandeya, X. S. Li, Y. T. Tsai, G. Pecastaings, T. Buffeteau, V. Maurizot, L. Muccioli, F. Castet, I. Huc, D. M. Bassani, Chem. Sci. 2017, 8, 7251-7257; b) X. S. Li, N. Markandeya, G. Jonusauskas, N. D. McClenaghan, V. Maurizot, S. A. Denisov, I. Huc, J. Am. Chem. Soc. 2016, 138, 13568-13578; c) M. Wolffs, N. Delsuc, D. Veldman, N. Van Anh, R. M. Williams, S. C. J. Meskers, R. A. J. Janssen, I. Huc, A. P. H. J. Schenning, J. Am. Chem. Soc. 2009, 131, 4819-4829.

[9] a) A. R. Mallia, P. S. Salini, M. Hariharan, J. Am. Chem. Soc. 2015, 137, 15604-15607; b) Y. L. Wu, N. S. Bobbitt, J. L. Logsdon, N. E. Powers-Riggs, J. N. Nelson, X. L. Liu, T. C. Wang, R. Q. Snurr, J. T. Hupp, O. K. Farha, M. C. Hersam, M. R. Wasielewski, Angew. Chem. Int. Ed. 2018, 57, 3985-3989; c) S. Bhosale, A. L. Sisson, P. Talukdar, A. Furstenberg, N. Banerji, E. Vauthey, G. Bollot, J. Mareda, C. Roger, F. Wurthner, N. Sakai, S. Matile, Science 2006, 313, 84-86.

[10] M. Delor, S. A. Archer, T. Keane, A. Meijer, I. V. Sazanovich, G. M. Greetham, M. Towrie, J. A. Weinstein, Nat. Chem. 2017, 9, 1099-1104.

[11] C. B. Larsen, O. S. Wenger, Angew. Chem. Int. Ed. 2018, 57, 841-845.

[12] M. Cordes, B. Giese, Chem. Soc. Rev. 2009, 38, 892-901.

[13] H. C. Schmidt, C. B. Larsen, O. S. Wenger, Angew. Chem. Int. Ed. 2018, 57, 6696-6700.

[14] a) T. R. Prytkova, V. V. Shunaev, O. E. Glukhova, I. V. Kurnikov, J. Phys. Chem. B 2015, 119, 1288-1294; b) J. J. Regan, S. M. Risser, D. N. Beratan, J. N. Onuchic, J. Phys. Chem. B 1993, 97, 13083-13088; c) J. R. Winkler, H. B. Gray, J. Am. Chem. Soc. 2014, 136, 2930-2939; d) H. B. Gray, J. R. Winkler, Proc. Natl. Acad. Sci. U. S. A. 2005, 102, 3534-3539.

[15] a) R. A. Marcus, N. Sutin, Biochim. Biophys. Acta 1985, 811, 265-322; b) P. Y. Chen, T. D. Westmoreland, E. Danielson, K. S. Schanze, D. Anthon, P. E. Neveux, T. J. Meyer, Inorg. Chem. 1987, 26, 1116-1126.

[16] a) E. A. Weiss, M. J. Ahrens, L. E. Sinks, M. A. Ratner, M. R. Wasielewski, J. Am. Chem. Soc. 2004, 126, 9510-9511; b) O. S. Wenger, Chem. Soc. Rev. 2011, 40, 3538-3550; c) J. J. Shen, Y. W. Zhong, Sci Rep 2015, 5, doi: 10.1038/srep13835; d) S. Welter, N. Salluce, P. Belser, M. Groeneveld, L. De Cola, Coord. Chem. Rev. 2005, 249, 1360-1371; e) M. T. Indelli, C. Chiorboli, L. Flamigni, L. De Cola, F. Scandola, Inorg. Chem. 2007, 46, 5630-5641.

[17] a) H. M. McConnell, J. Chem. Phys. 1961, 35, 508-515; b) M. Natali, S. Campagna, F. Scandola, Chem. Soc. Rev. 2014, 43, 4005-4018.

[18] a) F. D. Lewis, J. Q. Liu, W. Weigel, W. Rettig, I. V. Kurnikov, D. N. Beratan, Proc. Natl. Acad. Sci. U. S. A. 2002, 99, 12536-12541; b) O. S. Wenger, Acc. Chem. Res. 2011, 44, 25-35.

[19] a) D. Hanss, O. S. Wenger, Inorg. Chem. 2008, 47, 9081-9084; b) D. Hanss, O. S. Wenger, Inorg. Chem. 2009, 48, 671-680.

[20] a) S. Welter, F. Lafolet, E. Cecchetto, F. Vergeer, L. De Cola, ChemPhysChem 2005, 6, 2417-2427; b) E. A. Weiss, M. J. Tauber, R. F. Kelley, M. J. Ahrens, M. A. Ratner, M. R. Wasielewski, J. Am. Chem. Soc. 2005, 127, 11842-11850; c) W. B. Davis, W. A. Svec, M. A. Ratner, M. R. Wasielewski, Nature 1998, 396, 60-63.

[21] M. Montalti, A. Credi, L. Prodi, M. T. Gandom, Handbook of photochemistry, 3rd edition, CRC/Taylor & Francis, Boca Raton, 2006.

[22] M. Kuss-Petermann, O. S. Wenger, Phys. Chem. Chem. Phys. 2016, 18, 18657-18664.

[23] P. J. Low, Coord. Chem. Rev. 2013, 257, 1507-1532.

[24] a) K. Kumar, Z. Lin, D. H. Waldeck, M. B. Zimmt, J. Am. Chem. Soc. 1996, 118, 243-244; b) J. M. Nadeau, M. Liu, D. H. Waldeck, M. B. Zimmt, J. Am. Chem. Soc. 2003, 125, 15964-15973; c) B. M. Graff, D. N. Lamont, M. F. L. Parker, B. P. Bloom, C. E. Schafmeister, D. H. Waldeck, J. Phys. Chem. A 2016, 120, 6004-6013.

[25] a) C. Stangel, C. Schubert, S. Kuhri, G. Rotas, J. T. Margraf, E. Regulska, T. Clark, T. Torres, N. Tagmatarchis, A. G. Coutsolelos, D. M. Guldi, Nanoscale 2015, 7, 2597-2608; b) E. A. Weiss, M. J. Ahrens, L. E. Sinks, A. V. Gusev, M. A. Ratner, M. R. Wasielewski, J. Am. Chem. Soc. 2004, 126, 5577-5584.

[26] a) G. Li, R. Zhu, Y. Yang, Nat. Photonics 2012, 6, 153-161; b) A. Mishra, P. Bäuerle, Angew. Chem. Int. Ed. 2012, 51, 2020-2067; c) F. C. Grozema, L. D. A. Siebbeles, Int. Rev. Phys. Chem. 2008, 27, 87-138.

[27] E. H. Yonemoto, G. B. Saupe, R. H. Schmehl, S. M. Hubig, R. L. Riley, B. L. Iverson, T. E. Mallouk, J. Am. Chem. Soc. 1994, 116, 4786-4795.

Entry for the Table of Contents

COMMUNICATION

Taking shortcuts: Phototriggered electron transfer between a triarylamine unit and a ruthenium complex follows shortcuts in the secondary structure of a naphthylene-based molecular bridge, leading to a particularly low distance dependence of reaction rates and overall faster electron transfer.

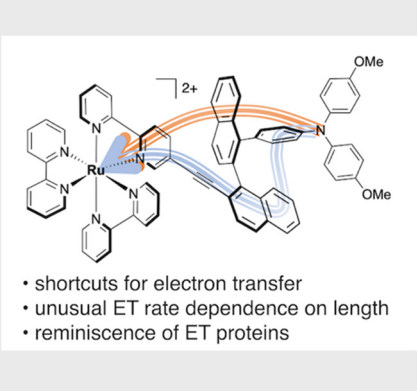

Alessandro Castrogiovanni,[†] Patrick Herr,[†] Christopher B. Larsen, Xingwei Guo, Christof Sparr, and Oliver S. Wenger**

Page No. – Page No.

Shortcuts for Electron-Transfer through the Secondary Structure of Helical Oligo-1,2-naphthylenes

Bibliography

[1] International Energy Agency (IEA), *Key World Energy Statistics 2019*, **2019**.

[2] J. T. Kiehl, K. E. Trenberth, *Bull. Am. Meteorol. Soc.* **1997**, *78*, 197–208.

[3] European Energy Agency (EEA), *Global and European Temperature*, **2019**.

[4] M. Wahlström, P. Kocyba, M. de Vydt, J. De Moor, *Protest for a Future: Composition, Mobilization and Motives of the Participants in Fridays For Future Climate Protests on 15 March, 2019 in 13 European Cities*, **2019**.

[5] United Nations (UN), *Paris Agreement*, **2015**.

[6] Q. Schiermeier, J. Tollefson, T. Scully, A. Witze, O. Morton, *Nature* **2008**, *454*, 816–823.

[7] United Nations Development Programme, *World Energy Assesment 2000*, **2000**.

[8] Bundesministerium für Wirtschaft und Technologie (BMWi), *Zeitreihen Zur Entwicklung Der Erneuerbaren Energien in Deutschland*, **2020**.

[9] European Energy Agency (EEA), *Final Energy Consumption by Sector and Fuel in Europe*, **2020**.

[10] N. Armaroli, V. Balzani, *Chem. Asian J.* **2011**, *6*, 768–784.

[11] Y. Tachibana, L. Vayssieres, J. R. Durrant, *Nat. Photonics* **2012**, *6*, 511–518.

[12] K. Jiang, S. Siahrostami, A. J. Akey, Y. Li, Z. Lu, J. Lattimer, Y. Hu, C. Stokes, M. Gangishetty, G. Chen, Y. Zhou, W. Hill, W. Bin Cai, D. Bell, K. Chan, J. K. Nørskov, Y. Cui, H. Wang, *Chem* **2017**, *3*, 950–960.

[13] M. A. Cismesia, T. P. Yoon, *Chem. Sci.* **2015**, *6*, 5426–5434.

[14] J. K. McCusker, *Science* **2019**, *363*, 484–488.

[15] D. M. Arias-Rotondo, J. K. McCusker, *Chem. Soc. Rev.* **2016**, *45*, 5803–5820.

[16] C. Förster, K. Heinze, *Chem. Soc. Rev.* **2020**, *49*, 1057–1070.

[17] O. S. Wenger, *Chem. Eur. J.* **2019**, *25*, 6043–6052.

[18] A. Hagfeldt, G. Boschloo, L. Sun, L. Kloo, H. Pettersson, *Chem. Rev.* **2010**, *110*, 6595–6663.

[19] R. D. Costa, E. Ortí, H. J. Bolink, F. Monti, G. Accorsi, N. Armaroli, *Angew. Chem. Int. Ed.* **2012**, *51*, 8178–8211.

[20] J. Twilton, C. C. Le, P. Zhang, M. H. Shaw, R. W. Evans, D. W. C. MacMillan, *Nat. Rev. Chem.* **2017**, *1*, 1-18.

[21] A. Magnuson, M. Anderlund, O. Johansson, P. Lindblad, R. Lomoth, T. Polivka, S. Ott, K. Stensjö, S. Styring, V. Sundström, L. Hammarström, *Acc. Chem. Res.* **2009**, *42*, 1899–1909.

[22] F. Heinemann, J. Karges, G. Gasser, *Acc. Chem. Res.* **2017**, *50*, 2727–2736.

[23] Y. Liu, T. Harlang, S. E. Canton, P. Chábera, K. Suárez-Alcántara, A. Fleckhaus, D. A. Vithanage, E. Göransson, A. Corani, R. Lomoth, V. Sundström, K. Wärnmark, *Chem. Commun.* **2013**, *49*, 6412–6414.

[24] J. D. Braun, I. B. Lozada, C. Kolodziej, C. Burda, K. M. E. Newman, J. van Lierop, R. L. Davis, D. E. Herbert, *Nat. Chem.* **2019**, *11*, 1144–1150.

[25] Y. Liu, P. Persson, V. Sundström, K. Wärnmark, *Acc. Chem. Res.* **2016**, *49*, 1477–1485.

[26] P. S. Wagenknecht, P. C. Ford, *Coord. Chem. Rev.* **2011**, *255*, 591–616.

[27] O. S. Wenger, *J. Am. Chem. Soc.* **2018**, *140*, 13522–13533.

[28] A. J. Lees, D. M. Manuta, *Inorg. Chem.* **1986**, *25*, 1354–1359.

[29] L. A. Büldt, X. Guo, R. Vogel, A. Prescimone, O. S. Wenger, *J. Am. Chem. Soc.* **2017**, *139*, 985–992.

[30] L. A. Büldt, X. Guo, A. Prescimone, O. S. Wenger, *Angew. Chem. Int. Ed.* **2016**, *55*, 11247–11250.

[31] Y. J. Yuan, Z. T. Yu, D. Q. Chen, Z. G. Zou, *Chem. Soc. Rev.* **2017**, *46*, 603–631.

[32] V. Balzani, P. Ceroni, A. Juris, *Photochemistry and Photophysics 1st Ed.*, WILEY-VCH, Weinheim, **2014**.

[33] C. E. Housecroft, A. G. Sharpe, *Inorganic Chemistry, Fourth Edition*, Pearson Education Limited, Harlow, **2012**.

[34] Y. C. Wei, S. F. Wang, Y. Hu, L. S. Liao, D. G. Chen, K. H. Chang, C. W. Wang, S. H. Liu, W. H. Chan, J. L. Liao, W. Y. Hung, T. H. Wang, P. T. Chen, H. F. Hsu, Y. Chi, P. T. Chou, *Nat. Photonics* **2020**, *14*, 570–577.

[35] M. Bixon, J. Jortner, *J. Chem. Phys.* **1968**, *48*, 715.

[36] M. Montalti, A. Credi, L. Prodi, M. T. Gandolfi, *Handbook of Photochemistry, 3rd Ed.*, CRC Press, Boca Raton, **2006**.

[37] M. Gisin, J. Wirz, *Helv. Chim. Acta* **1976**, *59*, 2273–2277.

[38] B. Dick, B. König, *Chemical Photocatalysis*, De Gruyter, Berlin/Boston, **2013**.

[39] C. K. Prier, D. A. Rankic, D. W. C. Macmillan, *Chem. Rev.* **2013**, *113*, 5322–5363.

[40] A. Studer, D. P. Curran, *Nat. Chem.* **2014**, *6*, 765–773.

[41] M. H. Shaw, J. Twilton, D. W. C. Macmillan, *J. Org. Chem.* **2016**, *81*, 6898–6926.

[42] C. R. Bock, J. A. Connor, A. R. Gutierrez, T. J. Meyer, D. G. Whitten, B. P. Sullivan, J. K. Nagle, *J. Am. Chem. Soc.* **1979**, *101*, 4815–4824.

[43] A. F. Hollemann, N. Wiberg, *Lehrbuch Der Anorganischen Chemie, 102th Ed.*, De Gruyter, Berlin, **2007**.

[44] A. K. Pal, C. Li, G. S. Hanan, E. Zysman-Colman, *Angew. Chem. Int. Ed.* **2018**, *130*, 8159–8163.

[45] C. F. Harris, C. S. Kuehner, J. Bacsa, J. D. Soper, *Angew. Chem. Int. Ed.* **2018**, *130*, 1325–1329.

[46] S. Kaufhold, N. W. Rosemann, P. Chábera, L. Lindh, I. Bolaño Losada, J. Uhlig, T. Pascher, D. Strand, K. Wärnmark, A. Yartsev, P. Persson, *J. Am. Chem. Soc.* **2021**, *143*, 1307–1312.

[47] C. Conti, F. Castelli, L. S. Forster, *J. Phys. Chem.* **1979**, *83*, 2371–2376.

[48] L. Viaene, J. D'Olieslager, *Inorg. Chem.* **1987**, *26*, 960–962.

[49] G. Auböck, M. Chergui, *Nat. Chem.* **2015**, *7*, 629–633.

[50] S. Mukherjee, D. N. Bowman, E. Jakubikova, *Inorg. Chem.* **2015**, *54*, 560–569.

[51] A. Francés-Monerris, K. Magra, M. Darari, C. Cebrián, M. Beley, E. Domenichini, S. Haacke, M. Pastore, X. Assfeld, P. C. Gros, A. Monari, *Inorg. Chem.* **2018**, *57*, 10431–10441.

[52] I. M. Dixon, F. Alary, M. Boggio-Pasqua, J. L. Heully, *Inorg. Chem.* **2013**, *52*, 13369–13374.

[53] P. Zimmer, L. Burkhardt, A. Friedrich, J. Steube, A. Neuba, R. Schepper, P. Müller, U. Flörke, M. Huber, S. Lochbrunner, M. Bauer, *Inorg. Chem.* **2018**, *57*, 360–373.

[54] P. Chábera, K. S. Kjaer, O. Prakash, A. Honarfar, Y. Liu, L. A. Fredin, T. C. B. Harlang, S. Lidin, J. Uhlig, V. Sundström, R. Lomoth, P. Persson, K. Wärnmark, *J. Phys. Chem. Lett.* **2018**, *9*, 459–463.

[55] K. S. Kjær, N. Kaul, O. Prakash, P. Chábera, N. W. Rosemann, A. Honarfar, O. Gordivska, L. A. Fredin, K. E. Bergquist, L. Häggström, T. Ericsson, L. Lindh, A. Yartsev, S. Styring, P. Huang, J. Uhlig, J. Bendix, D. Strand, V. Sundström, P. Persson, R. Lomoth, K. Wärnmark, *Science* **2019**, *363*, 249–253.

[56] P. Chábera, Y. Liu, O. Prakash, E. Thyrhaug, A. El Nahhas, A. Honarfar, S. Essén, L. A. Fredin, T. C. B. Harlang, K. S. Kjær, K. Handrup, F. Ericson, H. Tatsuno, K. Morgan, J. Schnadt, L. Häggström, T. Ericsson, A. Sobkowiak, S. Lidin, P. Huang, S. Styring, J. Uhlig, J. Bendix, R. Lomoth, V. Sundström, P. Persson, K. Wärnmark, *Nature* **2017**, *543*, 695–699.

[57] V. Baslon, J. P. Harris, C. Reber, H. E. Colmer, T. A. Jackson, A. P. Forshaw, J. M. Smith, R. A. Kinney, J. Telser, *Can. J. Chem.* **2017**, *195*, 547–552.

[58] H. Wu, C. Wang, F. Wang, H. Peng, H. Zhang, Y. Bai, *J. Chinese Chem. Soc.* **2015**, *62*, 1028–1034.

[59] A. S. Berezin, K. A. Vinogradova, V. A. Nadolinny, T. S. Sukhikh, V. P. Krivopalov, E. B. Nikolaenkova, M. B. Bushuev, *Dalton Trans.* **2018**, *47*, 1657–1665.

[60] Y. Suffren, N. O'Toole, A. Hauser, E. Jeanneau, A. Brioude, C. Desroches, *Dalton Trans.* **2015**, *44*, 7991–8000.

[61] Y. Kim, F. W. M. Vanhelmont, C. L. Stern, J. T. Hupp, *Inorg. Chim. Acta* **2001**, *318*, 53–60.

[62] P. C. Ford, *Chem. Sci.* **2016**, *7*, 2964–2986.

[63] L. A. Büldt, O. S. Wenger, *Chem. Sci.* **2017**, *8*, 7359–7367.

[64] S. Otto, M. Grabolle, C. Förster, C. Kreitner, U. Resch-Genger, K. Heinze, *Angew. Chem. Int. Ed.* **2015**, *54*, 11572–11576.

[65] C. Wang, S. Otto, M. Dorn, E. Kreidt, J. Lebon, L. Sršan, P. Di Martino-Fumo, M. Gerhards, U. Resch-Genger, M. Seitz, K. Heinze, *Angew. Chem. Int. Ed.* **2018**, *57*, 1112–1116.

[66] S. Otto, C. Förster, C. Wang, U. Resch-Genger, K. Heinze, *Chem. Eur. J.* **2018**, *24*, 12555–12563.

[67] S. Otto, J. P. Harris, K. Heinze, C. Reber, *Angew. Chem. Int. Ed.* **2018**, *57*, 11069–11073.

[68] P. M. Becker, C. Förster, L. M. Carrella, P. Boden, D. Hunger, J. van Slageren, M. Gerhards, E. Rentschler, K. Heinze, *Chem. Eur. J.* **2020**, *26*, 7199–7204.

[69] D. M. Arias-Rotondo, J. K. Mccusker, *Chem. Soc. Rev.* **2016**, *45*, 5797–6080.

[70] A. E. Carpenter, C. C. Mokhtarzadeh, D. S. Ripatti, I. Havrylyuk, R. Kamezawa, C. E. Moore, A. L. Rheingold, J. S. Figueroa, *Inorg. Chem.* **2015**, *2*, 2936–2944.

[71] J. F. Hartwig, *Organotransition Metal Chemistry - From Bonding to Catalysis 1st Ed.*, University Science Books, Mill Valley, **2010**.

[72] K. R. Mann, M. Cimolino, G. L. Geoffroy, G. S. Hammond, A. A. Orio, G. Albertin, H. B. Gray, *Inorg. Chim. Acta* **1976**, *16*, 97–101.

[73] G. S. Hammond, K. R. Mann, H. B. Gray, *J. Am. Chem. Soc.* **1977**, *99*, 306–307.

[74] W. Sattler, M. E. Ener, J. D. Blakemore, A. A. Rachford, P. J. Labeaume, J. W. Thackeray, J. F. Cameron, J. R. Winkler, H. B. Gray, *J. Am. Chem. Soc.* **2013**, *135*, 10614–10617.

[75] W. Sattler, L. M. Henling, J. R. Winkler, H. B. Gray, *J. Am. Chem. Soc.* **2015**, *137*, 1198–1205.

[76] F. Hahn, *Angew. Chem. Int. Ed.* **1993**, *33*, 650–665.

[77] D. T. Plummer, R. J. Angelici, *Inorg. Chem.* **1983**, *22*, 4063–4070.

[78] D. T. Plummer, *Synthesis of Multidentate Nitrile and Isonitrile Ligands and Their Transition-Metal Complexes*, Doctoral Dissertation, Iowa State University, **1983**.

[79] F. E. Hahn, M. Tamm, *Angew. Chem. Int. Ed.* **1992**, *31*, 1212–1214.

[80] Y. Ito, K. Kobayashi, T. Saegusa, *J. Organomet. Chem.* **1986**, *303*, 301–308.

[81] K. Sakata, Y. Yamaguchi, X. Shen, M. Hashimoto, A. Tsuge, *Synth. React. Inorg. M.* **2005**, *35*, 545–551.

[82] K. Sakata, K. Matsumoto, M. Hashimoto, *Inorg. Chim. Acta* **1994**, *227*, 113–118.

[83] A. Naik, *Synthesis and Application of Chiral Novel Bis(Isonitrile) Ligands in Catalysis*, Doctoral Dissertation, University Regensburg, **2010**.

[84] F. Monti, A. Baschieri, E. Matteucci, A. Mazzanti, L. Sambri, A. Barbieri, N. Armaroli, *Faraday Discuss.* **2015**, *185*, 233–248.

[85] J. B. Bilger, C. Kerzig, C. B. Larsen, O. S. Wenger, *J. Am. Chem. Soc.* **2021**, *143*, 1651–1663.

[86] L. Büldt, *Powerful Low-Valent Photocatalysts and Luminophores Based on Earth-Abundant Metals*, Doctoral Dissertation, University Basel, **2016**.

[87] C. B. Larsen, O. S. Wenger, *Chem. Eur. J.* **2018**, *24*, 2039–2058.

[88] F. Glaser, O. S. Wenger, *Coord. Chem. Rev.* **2020**, *405*, 213129.

[89] T. Koike, M. Akita, *Inorg. Chem. Front.* **2014**, *1*, 562–576.

[90] K. Suzuki, A. Kobayashi, S. Kaneko, K. Takehira, T. Yoshihara, H. Ishida, Y. Shiina, S. Oishi, S. Tobita, *Phys. Chem. Chem. Phys.* **2009**, *11*, 9850–9860.

[91] E. M. Kober, J. V. Caspar, R. S. Lumpkin, T. J. Meyer, *J. Phys. Chem.* **1986**, *90*, 3722–3734.

[92] H. Yu, E. Haviv, R. Neumann, *Angew. Chem. Int. Ed.* **2020**, *59*, 6219–6223.

[93] A. K. C. Mengel, C. Förster, A. Breivogel, K. Mack, J. R. Ochsmann, F. Laquai, V. Ksenofontov, K. Heinze, *Chem. Eur. J.* **2015**, *21*, 704–714.

[94] R. R. Schaller, *IEEE Spectr.* **1997**, *June*, 53–59.

[95] R. L. Carroll, C. B. Gorman, *Angew. Chem. Int. Ed.* **2002**, *41*, 4378–4400.

[96] B. Schlicke, P. Belser, L. De Cola, E. Sabbioni, V. Balzani, *J. Am. Chem. Soc.* **1999**, *121*, 4207–4214.

[97] A. Nitzan, M. A. Ratner, *Science* **2003**, *300*, 1384–1389.

[98] D. Lotter, M. Neuburger, M. Rickhaus, D. Häussinger, C. Sparr, *Angew. Chem. Int. Ed.* **2016**, *55*, 2920–2923.

Curriculum Vitae

Surname: Herr
First Name: Patrick Sebastian
Date of Birth: 08.09.1989
Mail: patrick.herr@unibas.ch

Education

since 11/2016	PhD Student in the Group of Prof. Oliver S. Wenger, University of Basel (CH)
2016	MSc in Chemistry, Group of Prof. Stefan Mecking, University of Konstanz (DE)
2012	Internship at Universidade Estadual Paulista (UNESP), Campus Ilha Solteira (BR)
2012	BSc in Chemistry, Group of Prof. Stefan Mecking, University of Konstanz (DE)
2009	Allgemeine Hochschulreife, Gymnasium Kenzingen, Kenzingen (DE)

Scientific Membership and Honorary Office

Since 11/2016	Member of the Swiss Chemical Society since 2016
12/2016 - 02.2020	Member of the PhD Chemistry Community at University of Basel

Publications

[4]	P. Herr, C. Kerzig, C. B. Larsen, D. Häussinger, O. S. Wenger «Manganese(I) complexes with metal-to-ligand charge transfer luminescence and photoreactivity» submitted 2020
[3]	P. Herr, O. S. Wenger *«Excited-State Relaxation in Luminescent Molybdenum(0) Complexes with Isocyanide Chelate Ligands»* *Inorganics* **2020**, *26*, 3119-3128
[2]	A. Castrogiovanni, P. Herr, C. B. Larsen, X. Guo, C. Sparr, O. S. Wenger *«Shortcuts for Electron-Transfer through the Secondary Structure of Helical Oligo-1,2-Naphthylenes»* *Chem. Eur. J.* **2019**, *25*, 16748-16754

[1] P. Herr, F. Glaser, L. A. Büldt, C. B. Larsen, O. S. Wenger *«Long-Lived, Strongly Emissive, and Highly Reducing Excited States in Mo(0) Complexes with Chelating Isocyanides»*
J. Am. Chem. Soc **2019**, *141*, 14394-14402

Poster Presentations

7/2019	23rd ISPPCC, Hong Kong (HKG) *Luminescent complexes made from earth-abundant d^6 metals and chelating isocyanides*
6/2019	1st SCS Photochemistry Symposium, Fribourg (CH) *Photophysics of a Bidentate Mo(0) Isocyanide Complex and its Application as a Photoreductant*
8/2018	43rd ICCC, Sendai (JP) *Luminescent complexes made from earth-abundant d^6 metals and chelating isocyanides*
8/2017	SCS Fall Meeting, Bern (CH) *A Bidentate Mo(0) Isocyanide Complex is a Powerful Photoredox Catalyst*
7/2017	22nd ISPPCC, Oxford (GB) *Photoredox Catalysis with a Powerful Mo(0) Isocyanide Photoreductant*